

# Microscopic Imaging in Turbid Media

A thesis submitted

by

Steven Paul Schilders

for the degree of

DOCTOR OF PHILOSOPHY



Optical Technology Research Laboratory  
School of Communications and Informatics  
Victoria University of Technology

FTS THESIS  
570.282 SCH  
30001005872173  
Schilders, Steven Paul  
Microscopic imaging in  
turbid media

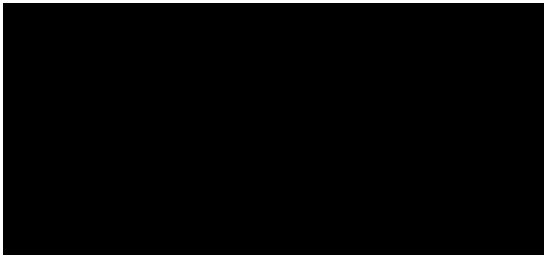
This PhD thesis is dedicated to my wife, Michelle

# Declaration

I, Steven Paul Schilders, declare that this thesis entitled

*“Microscopic imaging in turbid media”*

is my own work (except for figures 3.7, 4.2, 4.14, 4.20, 5.13 and 5.14) and has not been submitted previously, in whole or in part, in respect of any other academic award.



Steven Schilders

Optical Technology Research Laboratory  
School of Communications and Informatics  
Victoria University of Technology  
Australia

Dated the 1<sup>st</sup> of October, 1999

## Acknowledgement

There are a number of people whom I wish to thank for assistance throughout my PhD study. Firstly I would like to thank my PhD supervisor Professor Min Gu for his guidance, invaluable advice and assistance given throughout my course of study. Special thanks should also be given to the postdoctoral fellow Dr. Xiaosong Gan for his assistance.

I would also like to personally thank the other PhD students of the Optoelectronic Imaging Group, Mr. Pu Chun Ke and Mr. Daniel Day for their assistance and discussions. In addition, I would like to thank St. Vincent's Institute of Medical Research and in particular Dr. Mark Lam for providing the experimental biological samples used in this work.

Without the help of the technical staff my project would have not been a success. Therefore I would like to thank the Laboratory Manager Mr. Alex Shelamoff, the technical staff, Mr. Hayrettin Arisoy and Mr. Abdurrahman Kuzucu, and the mechanical workshop staff, Mr. Donald Ermel and Mr. Mark Kivenen, for their assistance in designing and machining parts for the microscopes.

Extended thanks are also given to Professor David Booth for his valuable advice and Dr. Andrew Stevenson for many discussions and light hearted moments. I would also like to thank all the remaining staff and postgraduate students in the Optical Technology Research Laboratory for making my time at Victoria University pleasant and enjoyable.

Last and probably most important, I would like to thank my wife Michelle and the members of the Ackermann family, for their endless support and encouragement throughout the course of my study.

## Abstract

This thesis is concerned with the understanding of photon propagation within turbid media with different characteristics (e.g. scattering anisotropy, optical thickness and geometric thickness). The turbid media (samples) used in the work presented in this thesis consist of polystyrene microspheres (0.107, 0.202, 0.48 and 1.056  $\mu\text{m}$  in diameter) and semi-skimmed milk suspensions. The imaged objects embedded within the turbid media consist of polystyrene microspheres (10 or 22  $\mu\text{m}$  in diameter) and a series of test bars. The 10 and 22  $\mu\text{m}$  polystyrene microspheres can be considered an approximate model for imaging a small tumour embedded within a biological tissue structure.

In particular the work presented in this thesis is concerned with the development of novel microscopic imaging techniques that allow high quality (i.e. micrometer scale resolution, high contrast and have a high signal-to-noise ratio) imaging through turbid media. The work presented in this thesis differs from previously published work in that the techniques developed are primarily designed for microscopic imaging systems.

This thesis discusses three independent techniques to increase image quality and resolution when they are used for imaging through turbid media in a microscopic imaging system. The first technique presented in this thesis is a newly developed angle-gating technique that relies on the difference in spatial deviation between unscattered and scattered photons. The angle-gating mechanism is implemented by the use of annular illumination and annular collection objectives. An in-depth

experimental investigation is performed to demonstrate the performance of the annular illumination and collection objectives in suppressing scattered photons in both a transmission and a reflection microscope. In addition the effect of the numerical aperture of the imaging objectives on suppressing scattered photons is presented.

It is also shown that a three-dimensional object embedded within turbid media can be misinterpreted, due to an inversion of image contrast, when imaged with a conventional imaging system. This misinterpretation can be overcome by using an angle-gating mechanism since it suppresses scattered photons that contribute to the image. In addition image resolution is also improved when the angle-gating mechanism is used.

The second technique presented in this thesis is based on the difference in polarisation states between unscattered and scattered photons. The polarisation-gating methods experimentally investigated include conventional polarisation-gating and differential polarisation-gating. The effect of the scattering particle size (i.e. scattering anisotropy) and the geometric thickness of turbid media on transverse resolution for a bar object is experimentally studied for the first time in a reflection microscope.

It is demonstrated that polarisation-gating, in particular differential polarisation-gating, can provide a significant improvement in transverse resolution when compared with no-gating (i.e. the collection of both unscattered and scattered

photons). The improvement in transverse resolution is due to the suppression of scattered photons, which lose their initial state of polarisation.

The third technique studied in this thesis is based on fluorescence microscopy. An in-depth experimental investigation into transverse resolution achievable when single-photon and two-photon excitation is used to image through turbid media consisting of different sized scatterers is presented for a reflection microscope.

It is demonstrated that two-photon microscopy can provide a significant improvement in penetration depth and transverse resolution in imaging through turbid media. The limiting factor in obtaining high quality images for single-photon excitation is the degradation of resolution caused by scattering experienced by the illumination source. For two-photon excitation the limiting factor in obtaining high quality images is demonstrated to be the signal-to-noise ratio of the detected fluorescence signal.

The work on two-photon fluorescence microscopy is extended to show that this technical tool can be applied to three-dimensional spectroscopy (chemical state) of biological tissue samples by measuring their autofluorescence signatures.

A modified Monte-Carlo simulation model is used to verify the experimental trends seen for angle-gating and polarisation-gating mechanisms used in imaging through turbid media.

# Table of contents

Declaration.....	ii
Acknowledgement.....	iii
Abstract.....	v
Table of contents.....	viii

## Chapter 1 Imaging in turbid media

1.1 Introduction.....	1
1.2 Physical processes of light in turbid media.....	4
1.2.1 Classification of photons.....	4
1.2.2 Physical properties of photons.....	5
1.3 Objective of this work.....	9
1.4 Preview of the thesis.....	12

## Chapter 2 Review of imaging techniques

2.1 Introduction.....	15
2.2 Detection techniques.....	16
2.2.1 Temporal imaging techniques.....	16
2.2.1.1 Streak camera.....	17
2.2.1.2 Optical cross-correlation.....	19
2.2.1.3 Kerr-gating.....	21
2.2.1.4 Optical coherence-gating.....	23

2.2.2 Spatially resolved techniques.....	24
2.2.2.1 Confocal imaging.....	25
2.2.2.2 Optical heterodyning.....	28
2.2.3 Polarisation-gating techniques.....	29
2.2.4 Combined gating techniques.....	30
2.3 Fluorescence microscopy.....	32
2.3.1 Principal differences between single-photon and two-photon excitation.....	32
2.3.1 A comparison of single-photon and two-photon excitation.....	33
2.3.2.1 Laser source.....	33
2.3.2.2 Excitation volume.....	34
2.3.2.3 Scattering.....	37
2.4 Macroscopic imaging versus microscopic imaging.....	39
2.5 Summary.....	40

## **Chapter 3 Theoretical simulation of photon propagation in turbid media**

3.1 Introduction.....	42
3.2 Scattering by a sphere: Mie theory.....	43
3.2.1 Scattering coefficients for spherical particles.....	44
3.2.2 Scattering cross-sections and anisotropy value.....	45
3.2.3 Calculation of the scattering-mean-free-path length.....	47
3.3 Monte-Carlo simulation method.....	49
3.3.1 General theory.....	49

3.3.2 Microscopic imaging.....	51
3.3.2.1 Theoretical formulation.....	51
3.3.2.2 Modelled microscope systems.....	56
3.3.3 Polarisation.....	58
3.3.4 Pulse propagation.....	62
3.3.5 General simulation properties.....	66
3.4 Application of the Monte-Carlo model.....	68
3.5 Summary.....	72

## **Chapter 4 Angle-gating in turbid media**

4.1 Introduction.....	73
4.2 Principle of angle-gating in microscopic imaging.....	74
4.3 Angle-gating in a transmission optical microscope.....	78
4.3.1 Experimental details.....	78
4.3.1.1 Experimental setup.....	78
4.3.1.2 Sample preparation.....	82
4.3.2 Effect of the annular illumination and collection objectives.....	86
4.3.2.1 Effect of an annular illumination objective.....	86
4.3.2.2 Effect of an annular collection objective.....	89
4.3.2.3 Effect of identical illumination and collection objectives.....	92
4.3.3 Effect of the numerical aperture of the matching objectives.....	95
4.3.4 Imaging with circular and annular objectives.....	98
4.3.5 Discussion.....	106

4.3.5.1 Diffraction effect.....	107
4.3.5.2 Polarisation-gating.....	108
4.3.5.3 Theoretical comparison.....	109
4.4 Angle-gating in a reflection optical microscope.....	111
4.4.1 Experimental details.....	111
4.4.1.1 Experimental setup.....	111
4.4.1.2 Sample preparation.....	114
4.4.2 Effect of a annular imaging objective.....	115
4.4.3 Imaging with circular and annular objectives.....	118
4.4.4 Discussion.....	121
4.5 General discussion.....	125
4.6 Conclusion.....	126

## **Chapter 5 Polarisation-gating in turbid media**

5.1 Introduction.....	129
5.2 Principles of polarisation-gating.....	131
5.3 Polarisation-gating in a reflection optical microscope.....	134
5.3.1 Experimental details.....	134
5.3.1.1 Experimental setup.....	134
5.3.1.2 Sample preparation.....	135
5.3.2 Effect of the optical thickness and scatterer size on resolution .....	139
5.3.2.1 Scattering suspensions of 0.107 $\mu\text{m}$ polystyrene microspheres.....	139
5.3.2.2 Scattering suspensions of 0.202 $\mu\text{m}$ polystyrene	

microspheres.....	144
5.3.2.3 Scattering suspensions of 0.48 $\mu\text{m}$ polystyrene	
microspheres.....	148
5.3.2.4 Scattering suspensions of semi-skimmed milk.....	150
5.3.3 Effect of pinhole-gating and polarisation-gating.....	153
5.3.4 Discussion.....	156
5.4 Theoretical comparison.....	166
5.5 Conclusion.....	169

## **Chapter 6 Fluorescence imaging in turbid media**

6.1 Introduction.....	170
6.2 Fluorescence imaging in a reflection optical microscope.....	172
6.2.1 Experimental details.....	172
6.2.1.1 Experimental setup.....	172
6.2.1.2 Sample preparation.....	174
6.2.2 Effect of scatterer size on image quality for fluorescent	
microspheres.....	178
6.2.2.1 Scattering suspensions of 0.107 $\mu\text{m}$ polystyrene	
microspheres.....	180
6.2.2.2 Scattering suspensions of 0.202 $\mu\text{m}$ polystyrene	
microspheres.....	182
6.2.3 Effect of scatterer size on image quality for a fluorescent bar.....	184
6.2.3.1 Scattering suspensions of 0.107 $\mu\text{m}$ polystyrene	
microspheres.....	185

---

6.2.3.2 Scattering suspensions of 0.202 $\mu\text{m}$ polystyrene microspheres.....	188
6.2.3.3 Scattering suspensions of 0.48 $\mu\text{m}$ polystyrene microspheres.....	191
6.2.3.1 Scattering suspensions of 1.056 $\mu\text{m}$ polystyrene microspheres.....	193
6.2.4 Discussion.....	195
6.3 Application of two-photon fluorescence imaging .....	199
6.3.1 Introduction.....	199
6.3.2 Imaging with cellular autofluorescence.....	199
6.3.3 Experimental details.....	201
6.3.3.1 Experimental setup.....	201
6.3.3.2 Sample preparation.....	201
6.3.4 Three-dimensional microscopy and spectroscopy.....	203
6.3.5 Discussion.....	208
6.4 Conclusion.....	209
 <b>Chapter 7 Conclusion</b>	
7.1 Thesis conclusion.....	210
7.2 Future work.....	217
References.....	219
List of symbols.....	228
List of figures.....	232

List of tables.....243

List of author's publications.....245

# Chapter 1

## Imaging in turbid media

### 1.1 Introduction

This chapter outlines the importance and general problems associated with laser based imaging in turbid media and discusses the characteristics of the light emerging from turbid media. This chapter is organised into the following sections: Section 1.2 characterises and discusses the physical characteristics of the light propagating in turbid media. Section 1.3 outlines the general objectives and novelty of the work presented in this thesis and section 1.4 describes the content of this thesis. The remainder of this section discusses the motives behind the work presented in this thesis.

In recent years there has been an increased interest in research into imaging with non-ionising radiation. This is partly due to fears from the medical fraternity that recurrent exposure to ionising radiation used in x-ray tomography may, in the minority of cases, be the cause of some patient tumours (Recommendations of the International Commission on Radiological Protection, 1990). Therefore there is an effort to develop safe, cost-effective and accurate techniques to compliment these existing techniques (magnetic resonance imaging and x-ray tomography). Most of

the laser development work done in this area is based on transillumination imaging systems (Morgan *et al.*, 1994; de Haller, 1996). Transillumination imaging systems use parallel beams to probe the sample under inspection, which allows three-dimensional optical tomographic images to be obtained (Hebden and Wong, 1993), in somewhat of an analogous way to MRI and x-ray tomography.

In addition to the demand for safe and accurate imaging systems for biomedical applications, laser based imaging systems have become an increasingly important research topic due their potential use in the fields of photodynamic therapy (Moore *et al.*, 1997), dermatology (Schmitt *et al.*, 1995; Rajadhyaksha *et al.*, 1995) and eye research (Masters, 1995). These applications become possible because laser based imaging systems can confine the illumination beam probe to selected localised areas.

Another reason for the increased interest in research into imaging with laser technology is in the area of spectroscopy. Alfano *et al.* (1984) demonstrated the possibility that healthy and cancerous tissue could be distinguished on the basis of their chemical composition, which was determined from spectroscopic analysis. Since this development numerous authors (Alfano *et al.*, 1987; Lohmann *et al.*, 1989; Schomacker *et al.*, 1992) have studied different tissue cultures (e.g. lung, breast, colon and cervix) in the hope that the spectroscopic signatures of biological tissue can be used in conjunction with laser based imaging techniques to more accurately distinguish between healthy and cancerous tissue. It should be noted that the information obtained with laser spectroscopy is currently unavailable with

conventional x-ray imaging techniques. Therefore laser spectroscopy opens up a new level of knowledge that until recently has not been used to its full potential.

The advantages of laser based spectroscopy analysis of biological tissue has been demonstrated by Alfano *et al.* (1984) and Masters (1996) who have used spectroscopic analysis to develop non-invasive *in vivo* imaging instrumentation to replace biopsies in dermatology. A biopsy requires the removal of tissue from the patient. This removal of tissue can cause unnecessary trauma and problems for the patient (wounds and scarring) due to its invasive nature. Thus techniques that can image the tissue *in situ* are highly desirable for the patient. High resolution images are usually required in this area of research; thus microscopic imaging techniques (e.g. confocal microscopy) instead of transillumination imaging systems are typically used for imaging.

To date most laser based spectroscopic analysis of biological tissue has been based on single-photon excitation. However Guo *et al.* (1997) and Masters *et al.* (1997) have demonstrated that multi-photon excitation (Denk *et al.*, 1990) can be used to obtain spectroscopic information of the biological tissue under inspection. Imaging systems employing multi-photon excitation can provide improved imaging performance of the sample under inspection due to its added advantages over single-photon excitation (refer to section 2.3).

Therefore due to the potential of laser based imaging systems in medical applications a large number of researchers are currently trying to develop imaging

techniques and theoretical models to help in the imaging and characterisation of small tumours (micrometer to millimeter scale) embedded in optically thick layers of biological tissue. However, tissue is highly diffusive and therefore acts as a turbid medium, which creates problems in detecting the necessary light to obtain an informative image with the resolution and contrast required.

## **1.2 Physical processes of light in turbid media**

### **1.2.1 Classification of photons**

One of the most challenging problems in the fields of physics, biology and medical diagnostics is to obtain an image of structures embedded within or behind turbid media. This is due to the nature of the detected illumination photons once they have propagated through turbid media.

It is well known that the detected illumination photons propagating through turbid media consist of unscattered (or ballistic), snake (or weakly scattered), and multiply scattered components (de Haller, 1996). The unscattered component (figure 1.1(a)) travels in a straight line and traverses the shortest distance through turbid media. Unscattered photons retain the characteristics of the incident light and carry the maximum information about the structures embedded within or behind turbid media. The snake component (figure 1.1(b)) consists of photons that propagate along zig-zag paths slightly off the straight-line unscattered path. The snake photons retain significant properties of the incident light and information on structures embedded within or behind turbid media. The multiply scattered component (figure 1.1(c)) consists of photons randomly scattered at various angles

in turbid media. Multiple scattered photons travel long distances through the turbid media and emerge later in time and in all directions. These photons lose many of their initial physical characteristics and carry little information about structures embedded within or behind turbid media. Multiply scattered photons are the source of image blurring and resolution deterioration that make it difficult to obtain the necessary information needed for high contrast and high resolution imaging. The degradation of the image quality can become so severe in turbid media that the embedded structures are completely hidden from view.

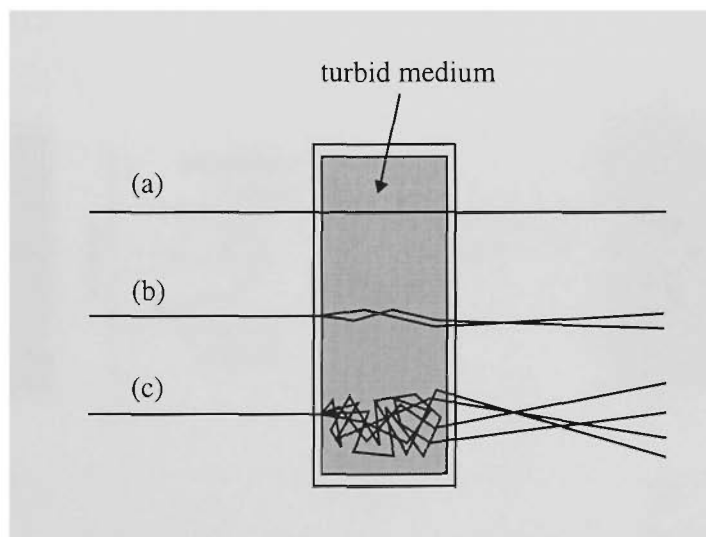


Figure 1.1: Photon propagation within turbid media. For a clear description, the three components are depicted separately: (a) unscattered photons; (b) snake photons; (c) multiply scattered photons.

### 1.2.2 Physical properties of photons

There are a few physical effects that need to be considered regarding the above mentioned components (see figure 1.2). These effects are associated with the spatial, polarisation, temporal and spectral properties of the illumination light propagating through turbid media. The deviation (spreading) of the illumination

photon flux in space is described by the spatial property (figure 1.2(a)). The polarisation property of scattered photons (figure 1.2(b)) is related to the polarisation state of individual photons in the illumination photon flux. The temporal property (figure 1.2(c)) describes the time-induced delay (pulse spreading) of the illumination photon flux. The spectral property (figure 1.2(d)) describes the frequency shift of the illumination photon flux. All these effects are mutually connected and are independent of the light source used except for the temporal effect which cannot be detected with a continuous-wave laser source (i.e. a pulse light source is needed)

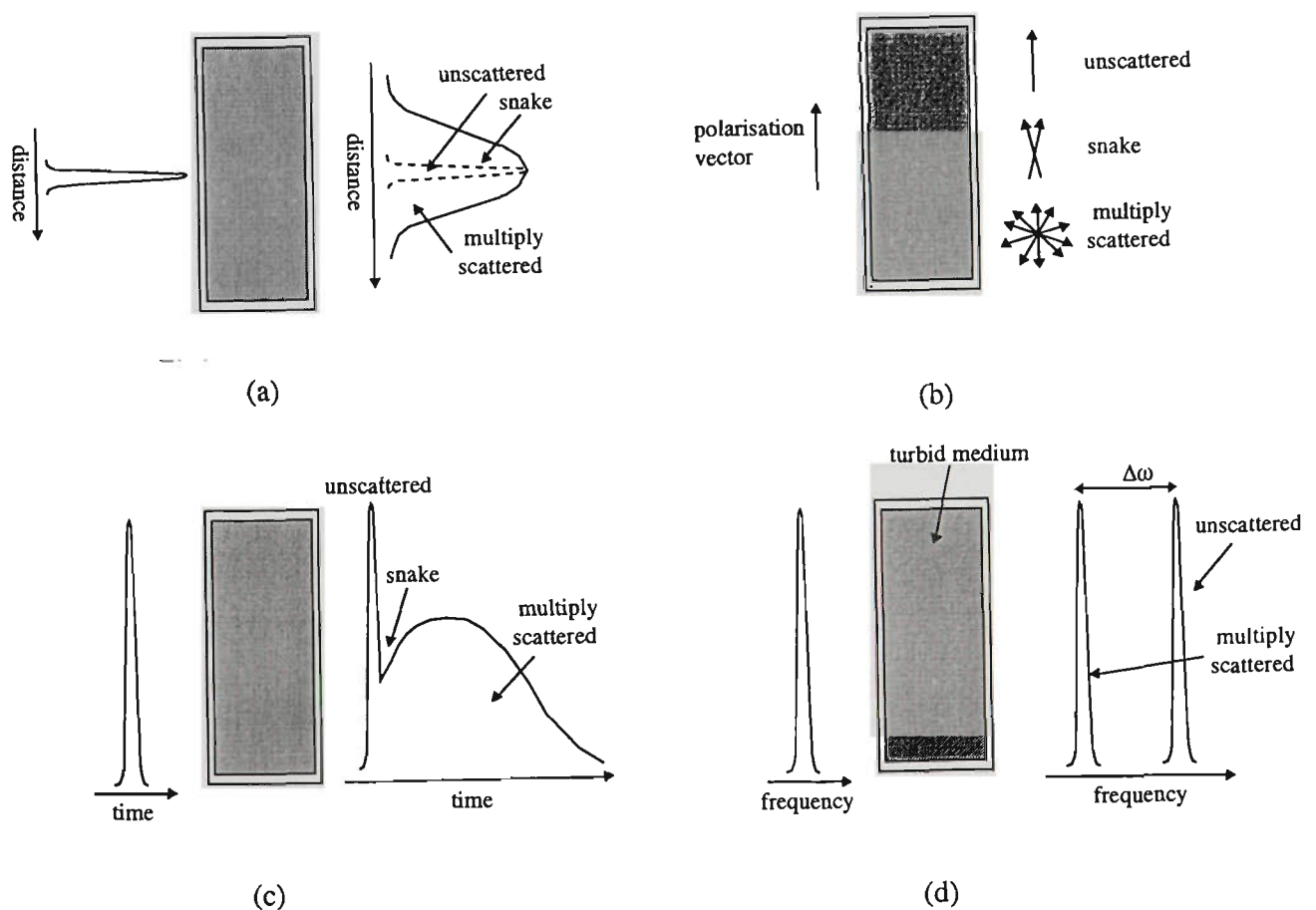


Fig. 1.2: Four physical effects of photons propagating through turbid media: (a) spatial broadening; (b) polarisation degradation; (c) temporal broadening; (a) spectral shift.

The spatial spreading of an incident beam with a Gaussian beam profile is illustrated in figure 1.2(a). Dashed lines illustrate the collected unscattered portion of the illumination beam. Snake and multiply scattered photons cause the diffraction pattern generated by the unscattered photons to broaden, since they travel along paths that are different from the unscattered straight through path (see figure 1.1). The amount of spatial broadening of the illumination beam is determined by the characteristics of the turbid media at the wavelength of illumination. The statistically different propagation paths of unscattered and scattered photons are the bases of the angle-gating principle discussed in chapter 4.

Figure 1.2(b) demonstrates the change in the polarisation vector of an illumination beam propagating through turbid media. The state of polarisation for the illumination beam (for example, defined by the vertical polarisation vector in figure 1.2(b)) is maintained with unscattered photons. Snake photons lose some degree of the illumination polarisation state, and the multiply scattered photons suffer substantial depolarisation. That is, the orientation of the polarisation vector is partially or completely random. The magnitude of the direction change in the polarisation vector is determined by the characteristics of turbid media at the wavelength of illumination.

The temporal properties can only be considered when a pulsed illumination beam is considered (figure 1.2(c)). An incident pulse can broaden (in the time domain) when the pulse undergoes its transition through turbid media. The unscattered photons are the first to arrive, followed closely by the snake photons, and at a later time the multiply scattered photons arrive. The turbid media characteristics at the

wavelength of illumination determines the amount of delay (temporal pulse broadening) induced between the unscattered, snake and scattered photons.

The spectral effect is demonstrated in figure 1.2(d) for an illumination pulse. The spectral effect can only be considered if inelastic collisions take place. After the illumination pulse passes through the turbid media the snake and multiply scattered photons will have their frequencies shifted from the unscattered component. The magnitude of the spectral shift,  $\Delta\omega$ , induced depends on the number of scattering events experienced by an individual photon. That is, the larger the number of scattering events experience the larger the spectral shift incurred. Most of the present research tends to treat collisions as an elastic process, which means that there is no energy transfer from photons to scattering particles, so no spectral change occurs (i.e.  $\Delta\omega = 0$ ). This situation simplifies the problem of modeling, since it ignores scattering phenomena such as Mandel'stam-Brillouin and Raman scattering (Bohern and Huffman, 1983). Although no scattering event is purely elastic, in most situations this is a good and reasonable approximation to be made since the frequency shift,  $\Delta\omega$ , is small.

These four effects (spatial broadening, polarisation degradation, temporal broadening and spectral shift) provide direct distinguishable differences between the unscattered, snake and scattered components, which can be taken advantage of when a particular detection scheme is used (refer to chapter 2).

One can assume that unscattered photons and snake photons are those necessary to create an informative high resolution and high contrast image. Thus methods for

detecting only unscattered and snake photons (the coherent component of the illumination beam) that carry more information of the embedded object, while the multiply scattered photons (the incoherent component of the illumination beam) are suppressed, have been used in imaging through turbid media (refer to section 2.2). Although, it should be noted that images may be reconstructed from the multiply scattered photons if the phase and amplitude of the scattered photons are known at many points in space. However, the reconstruction of images from multiply scattered photons, known as the inverse scattering problem (Baltes, 1978), remains a difficult experimental and theoretical problem to be overcome in imaging through turbid media.

The detection methods (gating mechanisms) that are currently used to suppress the multiply scattered photons (incoherent component) are discussed in detail in chapter 2.

### **1.3 Objective of this work**

As stated in section 1.1 there is a need for high resolution imaging systems that can image through biological tissue samples (i.e. turbid media). Typically to achieve this high resolution objective one needs to employ a microscopic imaging system. However, as stated in section 1.2 high quality (i.e. high resolution, high contrast, low noise etc) images are only possible if scattered photons are removed from the detected signal in imaging through turbid media. That is, gating techniques that remove a large proportion of the scattered photons are required in imaging through turbid media.

Currently there are only a couple of techniques available to suppress scattered photons when microscopic imaging systems are used (refer to section 2.2). The objective of this thesis is to extend the current knowledge by understanding the principles behind photon propagation through turbid media (with different scattering properties) when microscopic imaging systems are used. In particular the objective of the work presented in this thesis is concerned with the development of microscopic imaging techniques that allow high quality imaging through turbid media.

This thesis is aimed at understanding three independent novel techniques to increase the image quality and resolution in imaging through turbid media with microscopic imaging systems.

The first technique presented in this thesis is a newly developed angle-gating technique that relies on the spatial deviation difference between unscattered and scattered photons (refer to chapter 4). The angle-gating mechanism is implemented by the use of annular illumination and collection objectives. The effect of the angle-gating components (annular illumination and collection objectives) on suppressing scattered photons needs to be understood so that an imaging criterion can be established in imaging through turbid media.

The second technique presented in this thesis is based on the difference in polarisation states between unscattered and scattered photons (refer to chapter 5). The polarisation-gating methods investigated include conventional polarisation-gating and differential polarisation-gating. The suppression of scattered photons

by polarisation-gating depends on the characteristics of the turbid media. Therefore, this thesis systematically investigates the characteristics of turbid media that determine the effectiveness of the polarisation-gating mechanism in imaging through turbid media in a microscopic system.

The third technique presented in this thesis is based on fluorescence microscopy (refer to chapter 6). It is well known that multi-photon microscopy has added advantages of single-photon microscopy in imaging biological tissue (refer to section 2.3). However the advantage of using multi-photon excitation (e.g. two-photon excitation in this thesis) instead of single-photon excitation in turbid media has not been extensively studied. This thesis experimentally demonstrates for the first time (to the author's knowledge) a study into the effect that scattering particle size has on penetration depth, image quality and resolution achievable in imaging through turbid media. From this investigation the limiting factors in obtaining high quality images for single-photon and two-photon excitation have been determined.

This thesis provides both qualitative and quantitative data to demonstrate the performance of all three gating-techniques used in imaging through turbid media with different characteristics including, for example, scattering particle size (i.e. scattering anisotropy), optical thickness and geometric thickness.

## **1.4 Preview of the thesis**

So far this chapter has outlined the principles of obtaining high quality images of structures embedded within or behind turbid media. It has also outlined the objective of the work presented in this thesis. This section discusses the content of the remaining chapters in this thesis.

Chapter 2 reviews the current imaging techniques used to suppress scattered photons in imaging through turbid media and discusses their implementation to obtain high quality images. Temporally resolved imaging techniques, spatially resolved techniques and polarisation-gating techniques which are based on the photon properties outlined in section 1.2 are discussed. A discussion on fluorescence microscopy outlining the fundamental differences between single-photon and multi-photon excitation is also presented. In addition a discussion of macroscopic imaging versus microscopic imaging is presented. This discussion highlights the problems associated with certain imaging techniques when they are applied to microscopic imaging systems.

A series of theoretical simulations were performed to validate the experimental trends presented in this thesis (refer to chapters 4 and 5). A Monte-Carlo simulation program that has been developed for microscopic imaging through turbid media by Professor Gu and Dr. Gan was used to perform the theoretical simulations. The formulation of the model is based on scattering from a spherical particle developed from Mie theory. The details of the theoretical development and Monte-Carlo model are presented in chapter 3. Chapter 3 further discusses

and demonstrates the limitation of some current gating mechanisms (i.e. gating mechanisms based on time-of-flight) when they are applied to a microscopic imaging system.

Chapters 4, 5 and 6 in this thesis are dedicated to the new results on microscopic imaging techniques in turbid media. Chapter 4 is dedicated to a newly developed angle-gating mechanism for imaging through turbid media. This gating technique is based on the difference in the propagation direction between unscattered and scattered photons propagating through turbid media. An in-depth experimental investigation into the effects of the angle-gating mechanism on image quality for transmission and reflection microscopes is presented. As a comparison the effect of conventional polarisation-gating on image quality is also presented in this chapter.

Chapter 5 discusses the effects of different polarisation-gating (conventional polarisation-gating and differential polarisation-gating) mechanisms when they are applied to a reflection optical microscope. A comparative study of the resolution achievable between no-gating and the different polarisation-gating mechanisms is presented when various turbid media are imaged. The performance of polarisation-gating mechanisms is also demonstrated qualitatively through various turbid media. The effect of the polarisation-gating mechanisms with additional pinhole-gating on image quality is also experimentally investigated.

Chapter 4 and chapter 5 include both experimental and theoretical results to demonstrate and validate the gating principle under investigation.

Chapter 6 is dedicated to fluorescence imaging in turbid media. An experimental investigation into the imaging performance of single-photon and two-photon excitation in turbid media with different properties (i.e. scatterer size, optical thickness and geometric thickness) is presented. The investigation into fluorescence imaging with two-photon excitation is then extended and applied to imaging of biological tissue.

A thesis conclusion and a list of possible future work that can be undertaken are presented in chapter 7.

# Chapter 2

## Review of imaging techniques

### 2.1 Introduction

This chapter reviews and discusses the principles of current detection techniques (gating mechanisms) used to separate the useful unscattered and snake photons (the coherent component of the illumination beam) from the highly scattered photons (the incoherent component of the illumination beam). The gating techniques discussed in this chapter rely on the characteristic differences between unscattered and scattered photons outlined in section 1.2. In addition this chapter also discusses fluorescence microscopy. In particular it outlines the fundamental differences between single-photon excitation and multi-photon (i.e. two-photon) excitation.

This chapter is organised into the following sections: Section 2.2 discusses the principles of current detection techniques. Section 2.3 discusses the principles of fluorescence microscopy. Section 2.4 discusses the use of the gating techniques in a microscopic imaging system and a chapter summary is given in section 2.5.

## **2.2 Detection techniques**

A number of approaches have been proposed to obtain useful images through certain depths of turbid media. The useful unscattered and/or snake photons may be selected by gating in the temporal domain, by filtering in the spatial domain or by the use of a polarisation gate. It should be noted that all three detection techniques may be used together to maximise the suppression of scattered photons, since they rely on different aspects of light.

Gating techniques rely on the effective detection of unscattered photons, which directly relates to the resolution limit attainable for a given turbid sample. This means that as turbid media become optically thick the attenuation of the unscattered component increases and in most cases the unscattered component disappears, so the detected signal in this situation comprises solely snake and highly scattered photons. In addition, the gating period (temporal techniques) or the gating area (spatial techniques) required to obtain enough signal (i.e. high signal-to-noise ratio) needs to be broadened as the turbid medium becomes optically thick. These two effects can substantially degrade the resolvability/resolution of an imaging system, which thereby limits the image quality achievable.

### **2.2.1 Temporal imaging techniques**

Temporal imaging techniques all rely on the fact that unscattered photons are the first light to arrive at the detection apparatus of an imaging system, while the scattered component is delayed, providing the necessary rejection (refer to figure 1.2(c)). The induced delay between unscattered and scattered components depends

directly on the characteristics of turbid media. As mentioned in section 1.2 the implementation of temporal imaging techniques usually requires the use of a pulsed laser. Various time-resolved detection schemes have been used, including the use of a streak camera (Martin *et al.*, 1980; Ho *et al.*, 1989; Yoo and Alfano, 1990; Hebden *et al.*, 1991, Hebden, 1993; Andersson-Engels *et al.*, 1993; Hebden and Wong, 1993; Liu *et al.*, 1994; Anderson *et al.*, 1994; Wang *et al.*, 1995; Bruce *et al.*, 1995), optical cross-correlation (Fujimoto *et al.*, 1986; Liu *et al.*, 1991; Yoo *et al.*, 1991; Faris and Banks, 1994; Watson *et al.*, 1995), Kerr gating (Wang *et al.*, 1991; 1993a; 1993b; 1993c; Kalpaxis *et al.*, 1993; Xiang *et al.*, 1997) and optical coherence-gating, e.g. optical coherence tomography (OCT), (Hee *et al.*, 1993; Swanson *et al.*, 1993; Bouma *et al.*, 1995; Yadlowsky *et al.*, 1995; de Boer *et al.*, 1997; Pan *et al.*, 1997; Schmitt *et al.*, 1997; Schmitt and Hiang, 1998).

#### 2.2.1.1 Streak camera

A streak camera is a fast electronic gating device that controls the detection of the temporally delayed photons with a variable shutter and exposure time. A simple schematic diagram of an imaging system employing a streak camera as a gating mechanism is illustrated in figure 2.1. The ultrafast laser source is split by beamsplitter  $B_1$  into an illumination beam and a reference beam. The illumination beam provides the diagnostic pulse, which is delivered to the surface of an object embedded within a turbid medium under inspection. The reference beam does not traverse through the turbid medium. The reference beam is further split via beamsplitter  $B_2$  into a synchronisation pulse and a zero reference pulse. The synchronisation pulse is directed onto a photodiode of a synchronising unit, while the zero reference pulse is delivered directly to the streak camera. The

synchronising unit synchronises the repetition frequency of the train of pulses with the scanning frequency of the streak camera. Photons originating from the turbid medium under inspection are collected via a lens L, and are directed onto the streak camera entrance. Photons collected via the streak camera can then be gated according to their time of arrival relative to the detected zero reference pulse. The gating point is adjusted by delaying the zero reference pulse via the reference delay mirror  $M_3$ .

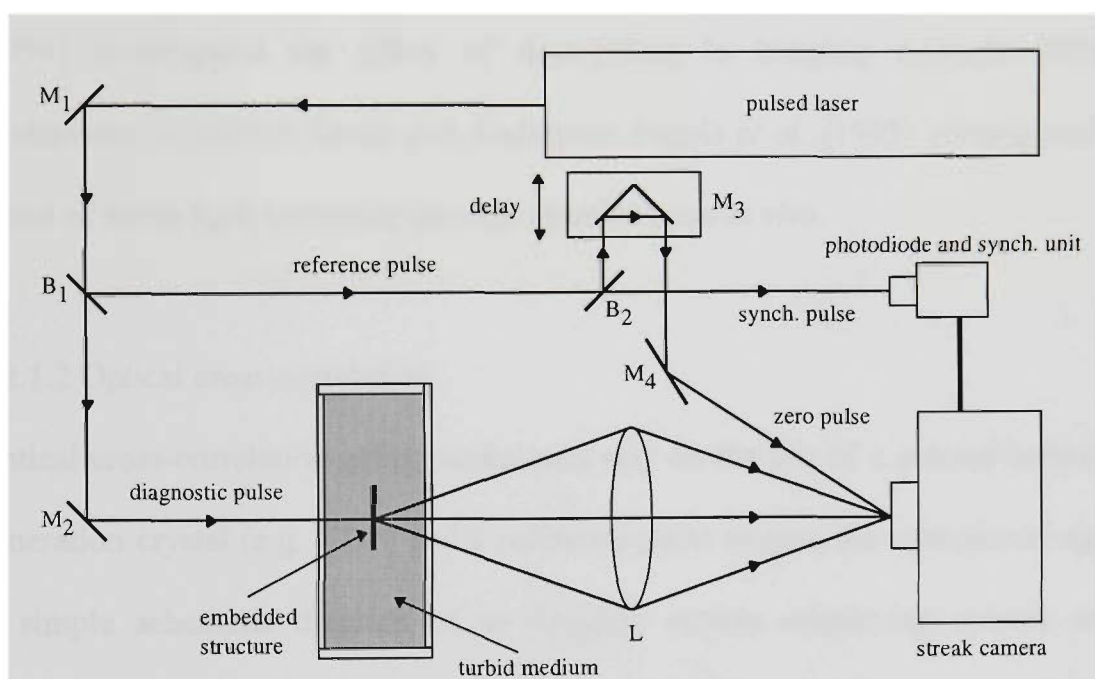


Figure 2.1: Schematic diagram for an imaging system employing a streak camera. B: beamsplitter; L: lens; M: mirror.

The limitations of the streak camera are its very high price and the minimum gating time which is usually in the picosecond range and is an order of magnitude larger than the pulse width of a femtosecond pulsed beam. This minimum gating period makes it hard to discriminate between the unscattered and scattered

photons. Thus the image quality can be reduced depending purely on the characteristics of the turbid media under inspection.

Ho *et al.* (1989) and Yoo *et al.* (1990) performed extensive analyses on the delay induced between unscattered and scattered photons in imaging through different turbid media composed of polystyrene microspheres. Hebden *et al.* (1991; 1993) demonstrated the effect of different gating periods on image quality for millimetre scaled objects embedded within an optically dense turbid medium. Liu *et al.* (1994) investigated the effect of time-gating in imaging through different thicknesses of chicken breast and Andersson-Engels *et al.* (1993) investigated the effect of white light scattering through muscle tissue *in vivo*.

#### 2.2.1.2 Optical cross-correlation

Optical cross-correlation gating techniques rely on the use of a second-harmonic-generation crystal (e.g. KDP) and a reference pulse to gate the unscattered signal. A simple schematic diagram of an imaging system employing optical cross-correlation gating is illustrated in figure 2.2. The ultrafast laser source is split by a beamsplitter B into an illumination beam and a reference beam. The illumination beam provides the diagnostic pulse, which is delivered to the surface of an embedded object within a turbid medium being imaged via lens  $L_1$ . Lens  $L_1$  is also used to collimate the reflected/backscattered signal originating from the turbid medium under inspection. The reference beam is retro-reflected by mirror M placed on a mechanical stage so that a variable delay can be introduced. Photons originating from the turbid medium under inspection and the reference pulse are focused onto a second-harmonic-generation crystal via lens  $L_2$ . The second-

harmonic signal produced at the focus of lens  $L_2$  is then passed through a narrow band filter to block the residual excitation light. The second-harmonic signal is then collected via a detector employing a lock-in amplifier (not shown in figure 2.2) to increase the detection sensitivity. The measurement of the integrated second-harmonic signal as a function of the temporal delay, introduced by the variable path length mirror M for the reference pulse, determines the contribution of scattered photons.

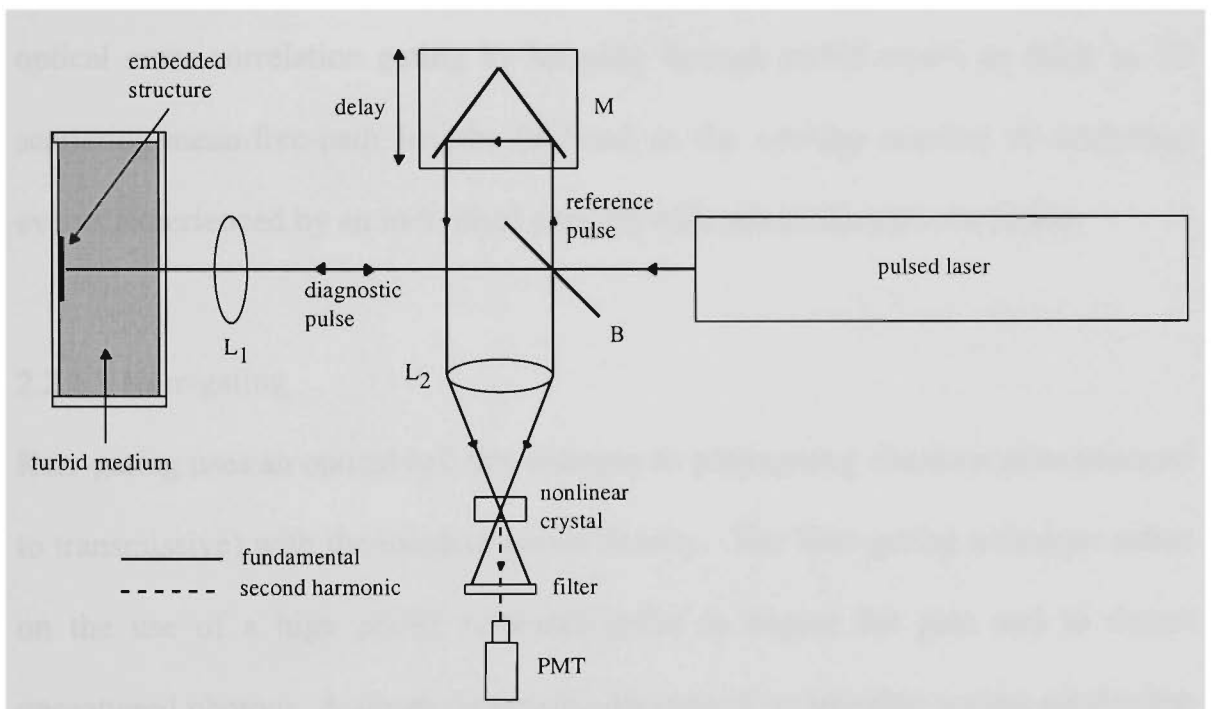


Figure 2.2: Schematic diagram for an imaging system employing the optical cross-correlation technique. B: beamsplitter; L: lens; M: mirror.

It should be noted that a second-harmonic signal is generated only when both the reference and collected unscattered photons fall on the second-harmonic-generation crystal simultaneously. When the scattered photons and highly scattered photons arrive at the second-harmonic-generation crystal the reference pulse has

already moved off; thus no second-harmonic signal can be generated. This technique allows a short gating time to be obtained (e.g. in a femtosecond range, which is comparable to the pulse width of the excitation laser light).

Fujimoto *et al.* (1986) demonstrated the principle of optical cross-correlation and applied it to the imaging of a rabbit eye cornea and skin samples. Liu *et al.* (1991) investigated the effect of turbid media consisting of polystyrene microspheres on the detection of unscattered photons. Yoo *et al.* (1991) illustrated the potential of optical cross-correlation gating by imaging through turbid media as thick as 28 scattering-mean-free-path lengths (defined as the average number of scattering events experienced by an individual photon) with sub-millimetre resolution.

### 2.2.1.3 Kerr-gating

Kerr-gating uses an optical cell that changes its propagating characteristics (opaque to transmissive) with the incident power density. The Kerr-gating technique relies on the use of a high power reference pulse to trigger the gate and to detect unscattered photons. A simple schematic diagram of an imaging system employing a Kerr-gate is illustrated in figure 2.3. A laser pulse is sent through a nonlinear crystal and a second harmonic pulse is produced. A dichroic mirror DM is then used to reflect the fundamental pulse to the embedded object under inspection, while the second-harmonic pulse is directed to the Kerr cell via mirror M<sub>2</sub>. The second-harmonic pulse is then used to trigger the Kerr gate. Photons originating from the turbid media under inspection are collected via a lens L and are directed onto the Kerr cell. Only the unscattered photons that arrive at the Kerr cell at the same time as the reference second-harmonic pulse are detected. However when

the snake photons and highly scattered photons arrive at the Kerr cell the reference second-harmonic pulse has already moved off; thus the gating mechanism is closed. This technique allows short gating times to be obtained since the gating period depends on the pulse width of excitation and the material response of the Kerr cell.

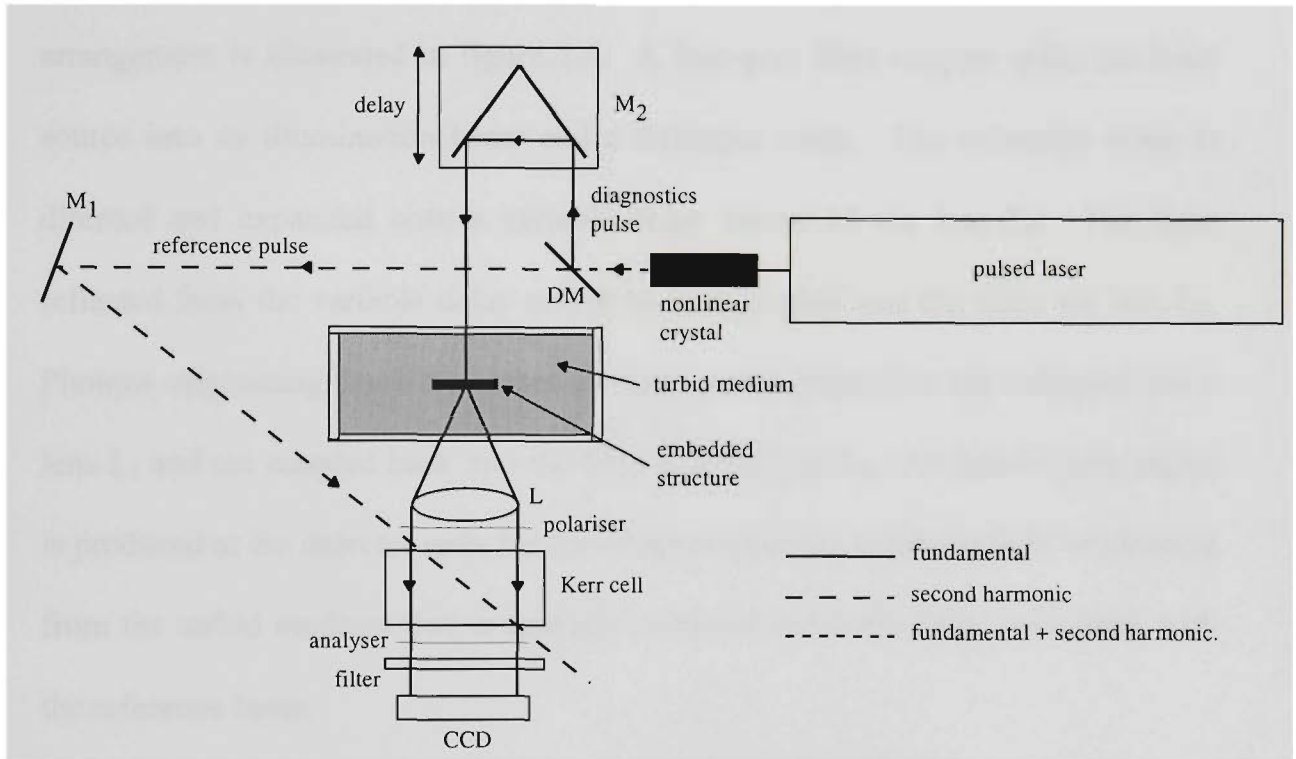


Figure 2.3: Schematic diagram for an imaging system employing a Kerr cell. DM: dichroic mirror; L: lens; M: mirror.

Wang *et al.* (1993c) demonstrated the performance of a Kerr cell on image quality for a  $250\ \mu\text{m}$  bar object embedded in turbid samples of intralipid. Wang *et al.* (1993a) also showed that the use of a double stage Kerr gate can significantly improve the signal-to-noise ratio of the recorded signal due to an increase in the attainable shutter speed.

#### 2.2.1.4 Optical coherence-gating

Optical coherence-gating use either coherent or incoherent sources (e.g. a pulsed laser a pulsed laser or a low coherence laser/laser diode) in an interferometer arrangement, since these sources have a broad bandwidth. A simple schematic diagram of an imaging system employing a fibre optic coherence-gating arrangement is illustrated in figure 2.4. A four-port fibre coupler splits the laser source into an illumination beam and a reference beam. The reference beam is directed and expanded onto a variable delay mirror M via lens  $L_3$ . The light reflected from the variable delay mirror M is recoupled into the fibre via lens  $L_3$ . Photons originating from the turbid medium under inspection are collected via a lens  $L_1$  and are coupled back into the fibre arm via lens  $L_2$ . An interference signal is produced at the detector only for the component of the collected light originating from the turbid medium that is spatially coherent and temporally coincident with the reference beam.

Images are formed by selectively gating the quasi-coherent constituent of the early arriving portion of the photons originating from the turbid medium under inspection. Optical coherence-gating allows deeper penetration than the previously mentioned techniques since it has higher detection sensitivity through the use of narrowband heterodyne detection. This technique is highly dependent on the turbid medium thickness and the coherence length of the laser source. That is, the coherence length of the laser should be as short as possible, since the image is formed from the point in the sample from which back-scattered photons experience an equal delay to those traversing the reference arm.

Hee *et al.* (1993) demonstrated the performance of optical coherence-gating by imaging test bars. Swanson *et al.* (1993) investigated the use of optical coherence-gating by measuring *in vivo* the retina of a human eye. Pan *et al.* (1997) determined the contrast limits for optical coherence-gating in turbid media, while Schmitt *et al.*, (1995; 1997; 1998) has performed extensive studies of the use of OCT in biological imaging.

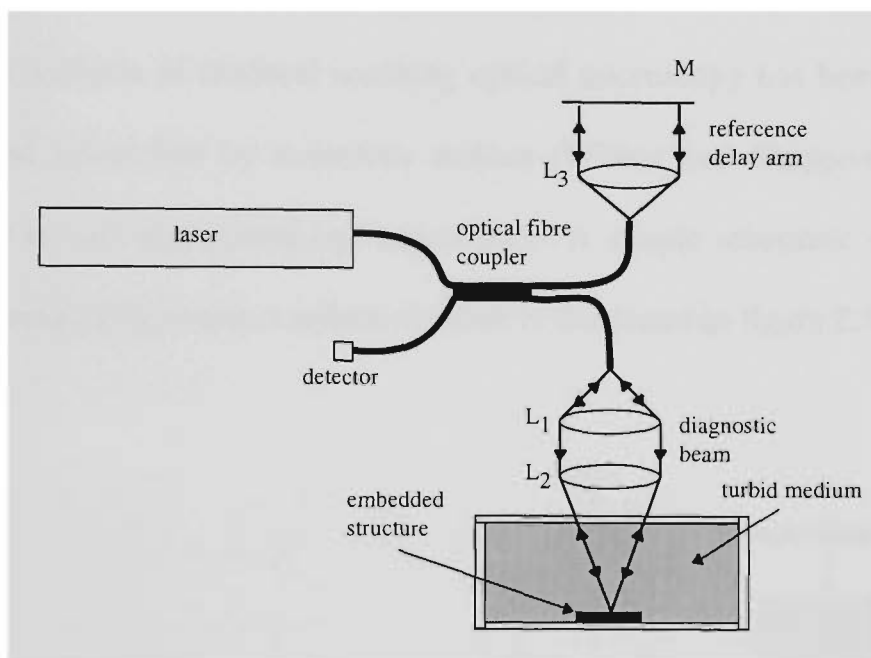


Figure 2.4: Schematic diagram for an imaging system employing a fibre optic coherence-gate. B: beamsplitter; L: lens; M: mirror.

### 2.2.2 Spatially resolved techniques

In contrast to temporally resolved methods, spatially resolved techniques rely on the directional selectivity to suppress the scattered component of the light originating from turbid media. Although effective, spatially resolved techniques may have difficulty rejecting light that has been multiply scattered back into the propagation direction of unscattered photons. The spatially resolved techniques that have been studied include confocal imaging (Dilworth *et al.*, 1991; Schmitt *et*

*al.*, 1994; Smithpeter *et al.*, 1998; Gan *et al.*, 1998) and optical heterodyning (Schmidt *et al.*, 1995).

### 2.2.2.1 Confocal imaging

Various authors (Kino and Corle, 1989; Anderson, 1994) have described the principle of confocal scanning optical microscopy, invented by Minsky (1955), which is an important tool in biological imaging and industrial inspection. The theoretical analysis of confocal scanning optical microscopy has been extensively studied and researched by numerous authors (Wilson and Shepperd, 1984; Gu, 1996) and is well established and understood. A simple schematic diagram of a confocal imaging system in a reflection mode is illustrated in figure 2.5.

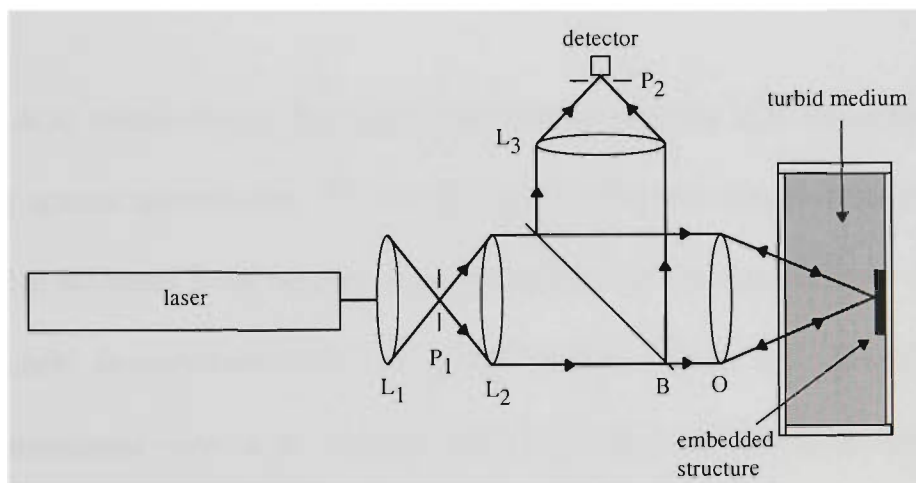


Figure 2.5: Schematic diagram of a reflection confocal scanning optical microscope. B: beamsplitter; L: lens; O: objective; P: pinhole.

A confocal scanning optical microscope differs from a conventional optical microscope in that it illuminates and images one point on the sample using a point source that is achieved using a spatial filter (pinhole)  $P_1$ . Light passes through

pinhole  $P_1$  to an objective  $O$  that forms a sharply focused diffraction-limited spot on an object. Light reflected from the object passes back through the objective  $O$  and back through another pinhole  $P_2$  so that the viewing area is isolated to an area that is exactly coincident with the illumination spot. Thus the illumination and detection peaks are optically conjugated with each other. Light originating from out-of-focus planes of the imaging lens is rejected, which effectively provides a small depth of field (termed the optical sectioning property) in a reflection confocal scanning optical microscope. A photodetector then measures the intensity of the light reflected by the sample, and a high-contrast image can be produced, formed mainly by the in-focus light. It should be noted that a confocal scanning optical microscope reduces to a conventional scanning optical microscope by removing the detection pinhole  $P_2$ .

Figure 2.6(a) demonstrates the optical sectioning property of a reflection confocal scanning optical microscope. Shown in figure 2.6(a) is a series of optical sections recorded at different focal heights from the surface on the sample under inspection. Figure 2.6(b) demonstrates how the optical sections can be recombined to form a three-dimensional view of the sample under inspection. It should be noted that the images in figure 2.6 are recorded without turbid media.

Scattered photons are suppressed when a confocal scanning optical microscope is used to image through a turbid medium since they statistically travel at angles not along the illumination path (refer to figure 1.1) predicted by geometric optics and therefore are not intersected at the spatial filter (pinhole)  $P_2$ .

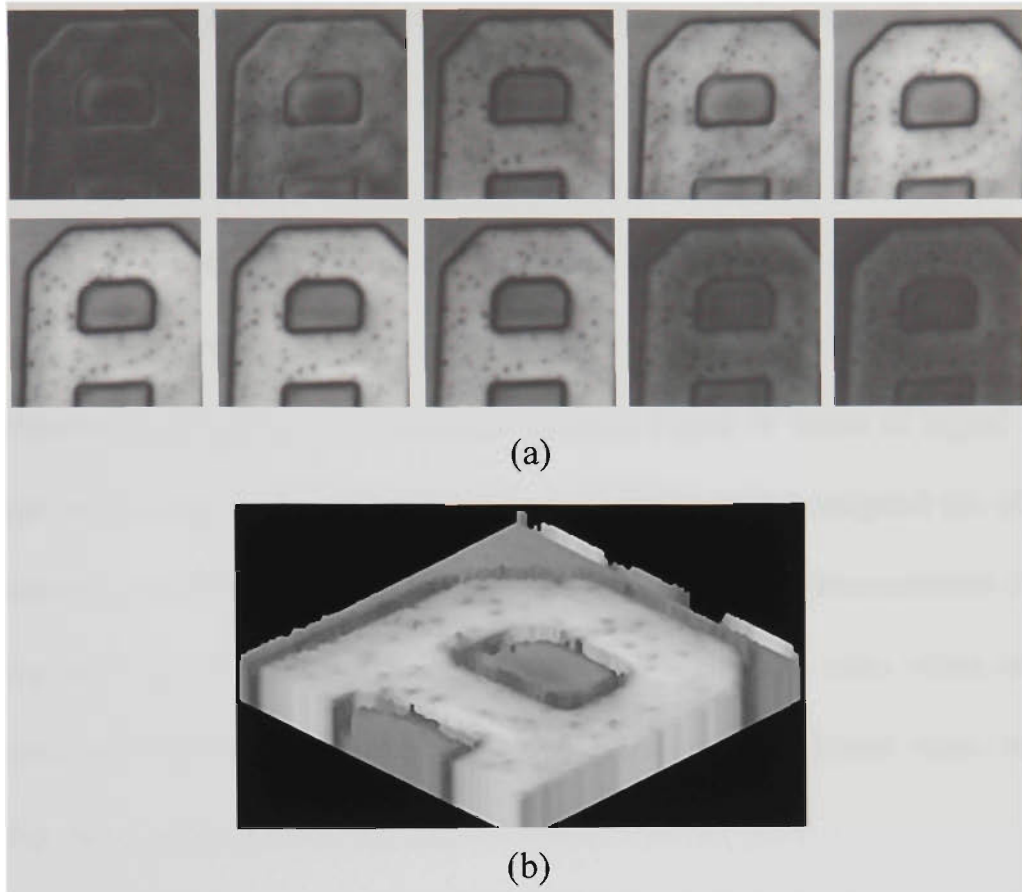


Figure 2.6: (a) Confocal image sections of the letter 'A' recorded from the surface of an integrated circuit; (b) three-dimensional reconstruction of the letter 'A' from the image sections shown in (a). Images were recorded with a 7 mW He-Ne laser, while the confocal microscope employed 20  $\mu\text{m}$  illumination and collection pinholes.

Schmitt *et al.* (1994) examined the performance of confocal microscopes designed for probing structures embedded in turbid media. They particularly studied the variables that affect confocal microscopy in turbid media, which include the size of pinhole, the numerical aperture of the imaging objective, and the concentration and scattering anisotropy of the particles in turbid media. These effects were both

theoretically and experimentally investigated. Their experimental confocal microscope employed a He-Ne laser and a photomultiplier tube (Schmitt *et al.*, 1994).

Smithpeter *et al.* (1998) examined the maximum penetration depth of *in vivo* confocal reflectance imaging of amelanotic tissue. Their experimental investigation (Smithpeter *et al.*, 1998) examined the detected signal in terms of signal source strength and source depth. Smithpeter *et al.* (1998) also investigated the effect of the scattering coefficient for different turbid media. It was demonstrated that the limiting factor in penetration depth was the signal-to-noise ratio when an ideal confocal microscope was used, while the signal-to-background ratio was the limiting factor when a large pinhole was used.

Gan *et al.* (1998) studied the effect of scattered photons that experience different numbers of scattering events on image resolution. Gan *et al.* (1998) also investigated the effect of the numerical aperture and the pinhole size on the photon distribution and resolution. A criterion for determining the efficiency of a gating method was proposed, which is based on the relationship between resolution and signal strength.

#### 2.2.2.2 Optical heterodyning

Optical heterodyning uses an interferometer (Schmidt *et al.*, 1995), which has in one arm the turbid media, illuminated with a continuous wave or pulse laser source, while in the other arm there is a modulator which shifts the frequency of the laser source. A compensation cell is used to match the optical path length of

the unscattered light traversing through the turbid medium. The reference arm signal is detected in a reference lock-in amplifier, which then moves the turbid medium detection pinhole into the appropriate position using translation stages, to detect the unscattered light. The multiply scattered light is not detected since the detection pinhole is not aligned properly.

### **2.2.3 Polarisation-gating techniques**

The state of polarisation of light provides another characteristic difference between unscattered and scattered photons, which can be used as an efficient gating mechanism. The conventional polarisation technique (MacKintosh *et al.*, 1989; McCormick, 1990; Schmitt *et al.*, 1992; Hielscher *et al.*, 1997; Morgan *et al.*, 1997) uses the principle that depolarisation only occurs when the incident polarised light hits a scattering object (refer to figure 1.1). That is, the degree of incident polarisation is maintained during free flight. Thus the more a photon experiences scattering, the stronger the depolarisation. Conventional polarisation-gating establishes a cheap gating mechanism, which primarily enables only the information-carrying (unscattered) photons to be detected.

The conventional polarisation-gating mechanism is implemented by polarising the incident light and detecting the portion of light originating from a turbid medium that has the same polarisation state as the incident light. This operation is achieved by placing an analyser in front of the detection apparatus.

Schmitt *et al.* (1992) theoretical and experimentally demonstrated the effect of conventional polarisation gating for different sized scatterers and optical

thicknesses for a parallel beam probe employed in a transmission system. Hielscher *et al.* (1997) experimentally illustrated the effect of particle size and concentration for a parallel beam probe employed in a backward scattering arrangement.

It has been illustrated by Horinaka *et al.* (1995) and visually demonstrated by Morgan *et al.* (1997), Schmitt and Hiang (1998), Demos *et al.* (1998) that further improvement in the suppression of scattered photons (therefore leading to higher resolution) is possible if the differential polarisation-gated signal is used to construct an image. The differential polarisation-gated signal is obtained by subtracting the detected signal measured with the analyser perpendicular to the incident polarisation direction from the conventional polarisation intensity. Morgan *et al.* (1997) also outlined the regimes where differential polarisation-gating is most effective in a transillumination imaging system.

#### **2.2.4 Combined gating techniques**

So far this chapter has only discussed independent gating techniques that have been used to gate unscattered photons in imaging through turbid media. Since the gating mechanism outlined in sections 2.2.1, 2.2.2 and 2.2.3 all rely on different physical aspects of scattered and unscattered photons, numerous authors (Wang *et al.*, 1993b; Anderson *et al.*, 1994; Wang *et al.*, 1995; Gu *et al.*, 1996; Gan *et al.*, 1997; Kempe *et al.*, 1994; 1996; Kempe and Rudolph, 1994; Izatt *et al.*, 1994; Liang *et al.*, 1997; de Boer *et al.*, 1997; Schmitt and Hiang, 1998) have applied multiple gating techniques to more effectively gate unscattered photons in turbid media. This section discusses some of these multiple gating methods.

Wang *et al.* (1993b) used a pinhole filter in Fourier space in conjunction with an optical Kerr cell to reduce the contribution of scattered photons being detected. Anderson *et al.* (1994) and Wang *et al.* (1995) combined the spatial gate (a pinhole in the Fourier domain) with a streak camera to further gate unscattered photons. Gu *et al.* (1996) demonstrated the effect of an annular filter on image quality for different turbid media and different sized detectors when a confocal imaging system is used. Gan *et al.* (1997) demonstrated that an annular filter could be used as a method of confining and gating unscattered photons when a microscopic imaging system is employed.

Kempe *et al.* (1994; 1996) and Izatt *et al.* (1994) demonstrated that the performance of a confocal microscope could be improved in terms of penetration depth and resolvability with the additional implementation of an optical coherence gate in imaging through turbid media.

The performance of the combination of polarisation-gating and Kerr-gating has been demonstrated by Liang *et al.* (1997) for different concentrations of turbid media.

Both de Boer *et al.* (1997) and Schmitt and Hiang (1998) demonstrated the effect of the combination of polarisation-gating and optical coherence-gating on image quality for biological tissue.

## 2.3 Fluorescence microscopy

### 2.3.1 Principal differences between single-photon and two-photon excitation

The principle of fluorescence is illustrated in figure 2.7 for single-photon (figure 2.7(a)) and two-photon (figure 2.7(b)) excitation. For single-photon excitation a fluorophore absorbs a single photon of the illumination light (typically in the visible spectrum), which results in transition of the electrons occupying the ground state ( $S_0$ ) to a higher electronic state ( $S_1$ ). The energy of each photon absorbed is given by,

$$E = h\nu \quad (2.1)$$

where  $h$  is Planck's constant and  $\nu$  is the frequency of an illumination photon.

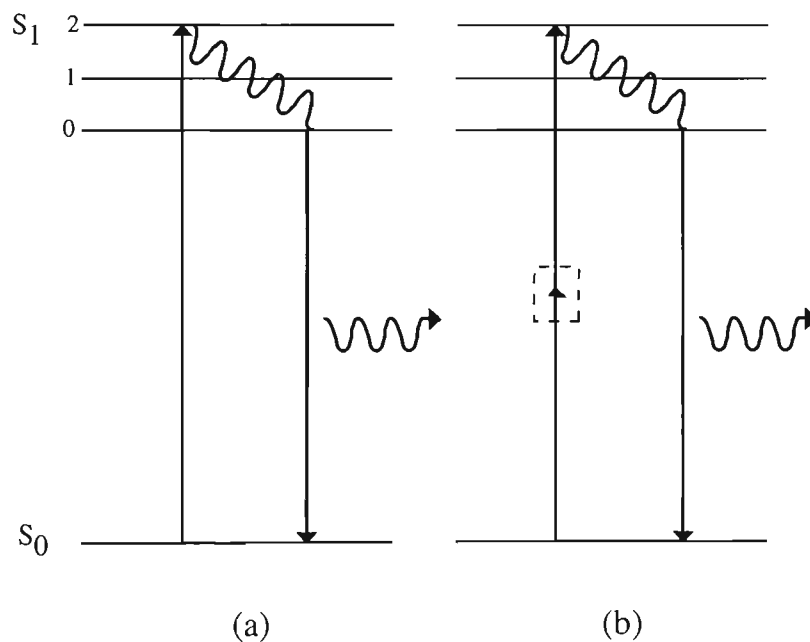


Figure 2.7: Energy level diagram for (a) single-photon and (b) two-photon excitation.

Excited states are metastable and have typical lifetimes of the order of  $10^{-9}$  seconds (Shen, 1984). Therefore after absorption, electrons at excited states ( $S_1$ ) return to

the ground state via a relaxation process. The relaxation of excited electrons is a multi-step process. First the excited electrons rapidly relax to the lowest vibrational state of the excited level ( $S_{1(0)}$ ) by a radiationless transition. Secondly the electrons undergo a transition from the excited level ( $S_{1(0)}$ ) to a vibrational state of the ground state ( $S_0$ ), with the energy lost in the transition given off in the form of light.

The fundamental difference between single-photon and two-photon excitation is in the ground-to-excited state transition. In the two-photon excitation process (Denk, 1990) two photons, each photon having an energy of  $E/2$ , need to be absorbed simultaneously to excite an electron from the ground state ( $S_0$ ) to a higher energy state ( $S_1$ ). There is a requirement that the photons be both spatially and temporally coincident for the transition to occur.

### **2.3.2 A comparison of single-photon and two-photon excitation**

The previous section demonstrated the basic principle between single-photon and two-photon excitation. This section gives further characteristic differences between the two forms of excitation when they are applied to microscopic imaging.

#### **2.3.2.1 Laser source**

Typically single-photon excitation uses ultra-violet (UV) to visible laser sources for excitation, since the majority of biological fluorophores have absorption bands within these regions. For single-photon excitation, the wavelength of the fluorescence emission is longer than the wavelength of excitation, with a typical Stokes shift between 10-100 nm, due to the loss of energy in the radiationless

transitions (see figure 2.7). As a result it may be difficult to design filters to efficiently separate the fluorescence emission from the excitation light if the Stokes shift is small. Another disadvantage of using UV excitation is that the optics required are very expensive due to the high UV absorption in glass.

Two-photon excitation does not have these problems since it typically uses wavelengths in the infrared (IR) region. Therefore the difference between the fluorescence and excitation wavelengths is substantially greater allowing more efficient separation. Another advantage of using IR excitation wavelengths is that it allows UV excitation without the need for an UV light source.

The probability for two-photon excitation is significantly lower than that for single-photon excitation because two-photon excitation is a second order process of polarisation (Shen, 1984), which leads to the requirement that excitation photons be spatially and temporally coincident (see section 2.3.1). Therefore to increase the efficiency of the two-photon excitation process a pulsed laser source with a typical pulse width of a few hundred femtoseconds is usually used for excitation, although it should be noted that two-photon imaging with the use of a continuous wave source has been successfully demonstrated by Hanninen *et al.* (1994).

#### 2.3.2.2 Excitation volume

The excitation volume for an objective lens employing single-photon and two-photon excitation is illustrated in figures 2.8(a) and 2.8(b), respectively (Tatterson, 1997). It is seen from figure 2.8(a) that single-photon fluorescence is excited almost at all points within the focal volume, due to the linear excitation probability.

For two-photon excitation fluorescence is excited only in the focal region of the imaging objective. This phenomenon is due to the quadratic dependence on the excitation intensity (Chen, 1984; Denk, *et al.*, 1990).

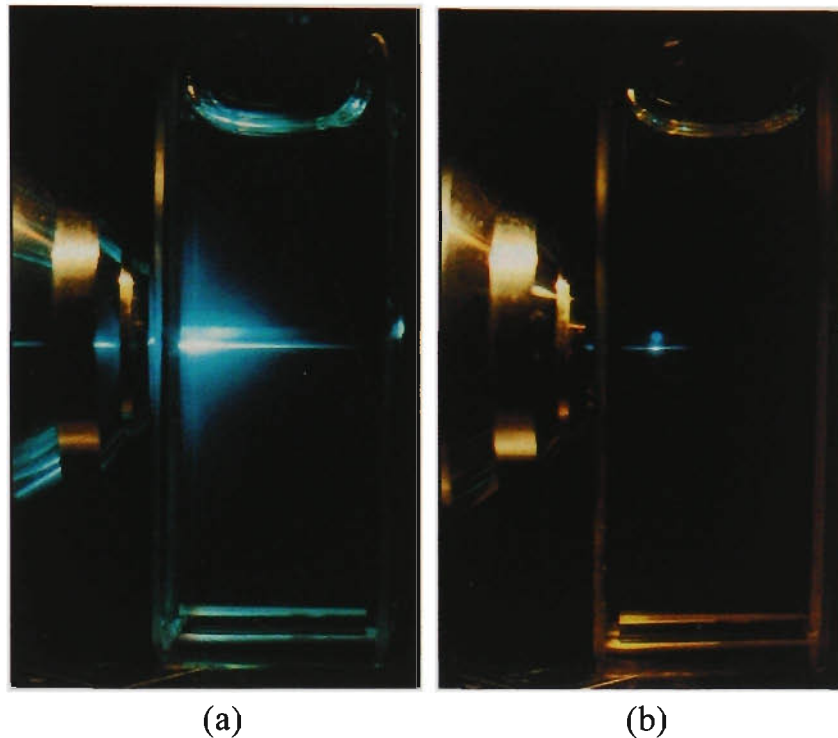


Figure 2.8: Focal volume under single-photon (a) and two-photon (b) excitation (Tatterson, 1997).

Two-photon excitation has a number of significant advantages over single-photon excitation due to the quadratic dependence of the excitation intensity.

- (a) Two-photon excitation has an inherent optical sectioning property. Therefore it removes the requirement of inserting a pinhole in front of the detector to obtain three-dimensional imaging capability (see section 2.2.2.1). Although it should be noted that the resolution can be improved further with the introduction of a finite sized pinhole (Gu and Gan, 1996).

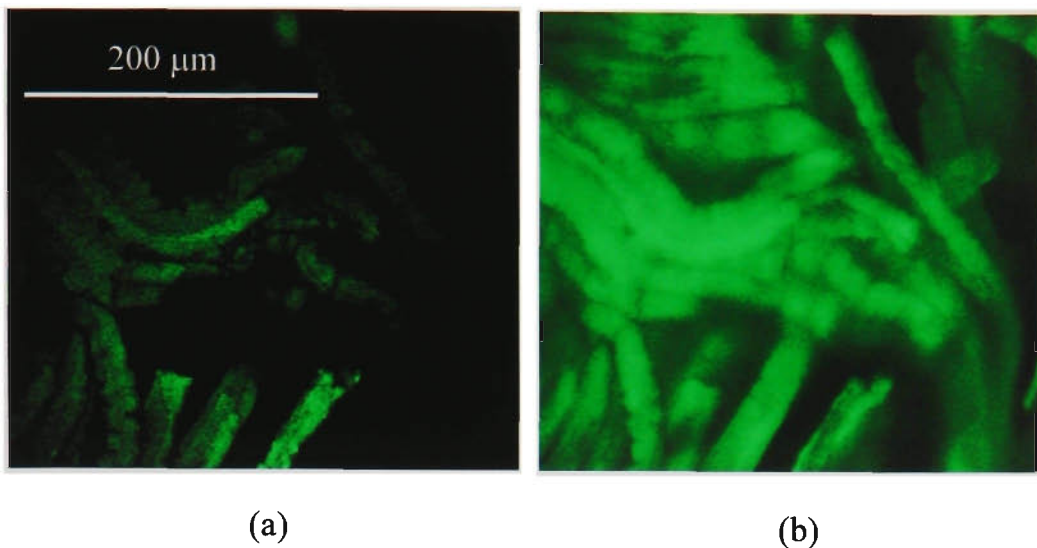


Figure 2.9: Images of rat skeletal muscle tissue recorded from autofluorescence excited by (a) two-photon ( $\lambda = 800$  nm) and (b) single-photon ( $\lambda = 488$  nm) excitation in a conventional scanning optical microscope. The numerical aperture of the imaging objective is 0.75.

Figure 2.9 demonstrates the optical sectioning property associated with two-photon excitation. A comparison is given between autofluorescence images recorded with single-photon and two-photon excitation in a scanning optical microscope (i.e. no detection pinhole is employed). In the case of single-photon excitation the image is blurred (figure 2.9(b)) due to the contribution from out-of-focus information which results from the extended excitation volume (see figure 2.8(a)). The image recorded with two-photon excitation demonstrates that only the information that is in the focal plane of the imaging objective contributes to the image.

(b) Two-photon excitation can confine photon-bleaching, photo-toxicity and photo-damage due to the confinement of the excitation volume, while in the case of single-photon excitation these phenomena occur at all points within the cone of excitation. The advantages of two-photon excitation are of primary importance in imaging through biological tissue, since it leads to an increased exposure time and therefore analysis time.

### 2.3.2.3 Scattering

According to Mie scattering theory (Bohern and Huffman, 1983) a shorter wavelength has a larger scattering cross-section which results in stronger scattering (refer to table 6.1). This implies that two-photon excitation has an advantage over single-photon excitation in terms of penetration depth in imaging through turbid media. Figure 2.10 demonstrates that although the transverse resolution for single-photon (figure 2.10(a)) and two-photon (figure 2.10(b)) excitation is almost indistinguishable the penetration depth for two-photon excitation (figure 2.10(d)) exceeds that for single-photon excitation (figure 2.10(c)) due to reduced scattering in two-photon excitation. The increase in penetration depth demonstrated for two-photon excitation in figure 2.10(b).

Numerous authors have undertaken studies into the imaging potential and applications of non-linear excitation (Hell, 1996; So, 1998). However, there has been little work done in determining the effect of scattering on the performance of fluorescence imaging through turbid media. The effect of scattering on the

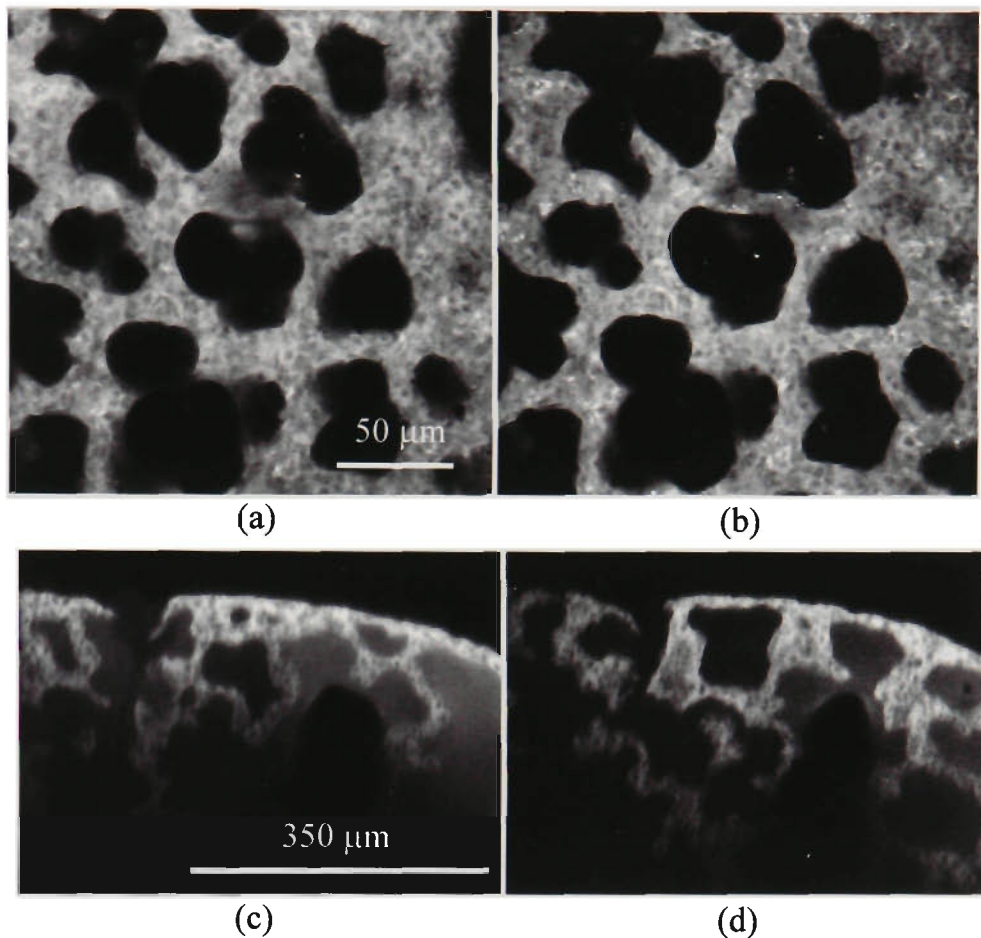


Figure 2.10: Transverse ((a) and (b)) and vertical ((c) and (d)) image section of rat lung tissue recorded from autofluorescence excited by single-photon ( $\lambda = 488 \text{ nm}$  @  $3 \text{ mW}$ ) with a  $100 \text{ }\mu\text{m}$  detection pinhole ((a) and (c)) and two-photon ( $\lambda = 900 \text{ nm}$  @  $< 10 \text{ mW}$ ) without a detection pinhole ((b) and (d)). The numerical aperture of the imaging objective is 0.9 (water immersion).

performance of fluorescence imaging for both single-photon and two-photon excitation was theoretically investigated by Blanca and Saloma (1998). Blanca and Saloma (1998) concluded that two-photon excitation is much more robust to degradations caused by scattering when compared with single-photon confocal imaging, due to reduced scattering of the illumination source. Indebetouw *et al.*,

(1998) investigated the use of holographic imaging to localise fluorescence inhomogeneities in turbid media. Saloma *et al.* (1998) combined site-specific applications of multiple fluorescent markers with confocal fluorescence imaging to obtain clear images of internal organs inside a whole-mount embryo which is an optically-thick sample that is of considerable importance in development biology research. Recently Ying *et al.*, (1999) investigated the spatial distribution of two-photon-excited fluorescence in scattering media. Ying *et al.*, (1999) demonstrated that the distribution of two-photon excited fluorescence is not necessarily confined to the focal region when scattering is present. This effect causes a loss of the optical sectioning property of two-photon microscopy.

## **2.4 Macroscopic imaging versus microscopic imaging**

It should be pointed out that most of the imaging techniques described in this chapter are designed primarily for transillumination imaging systems and not for microscopic imaging systems. Therefore, when some of these gating mechanisms, specifically temporal imaging techniques (see section 2.2.1), are applied to a microscopic imaging system (e.g. a confocal microscope) they may be less effective due to the large range of illumination angles of an imaging lens (refer to section 3.4). Therefore, gating techniques that can be incorporated into microscopes need to be understood and then developed, before high quality images can be obtained through significant depths of turbid media.

Of the characteristic differences remaining between unscattered and scattered photons illustrated in section 1.2; gating methods based on the difference in

propagation path and the difference in polarisation states between unscattered and scattered photons appear to be the most efficient way to suppress scattered photons when imaging through significant depths of turbid media in a microscopic imaging system.

Angle-gating (Gan *et al.*, 1997) is one possible gating method that can be used to suppress scattered photons based on the path deviation of scattered photons. Gan *et al.*, (1997) theoretically demonstrated that the use of annular illumination and collection lenses can efficiently suppress scattered photons, resulting in significantly improved image quality.

The polarisation-gating mechanisms (conventional polarisation-gating and differential polarisation-gating) are very simple to implement and more importantly can be incorporated/combined with spatially resolved techniques (e.g. confocal microscopy and angle-gating).

## 2.5 Summary

This chapter discusses the current status of gating mechanisms that are used to suppress scattered photons in imaging through turbid media. The gating mechanisms can be effectively broken down into three classes,

class (1) Temporal gating techniques, which rely on, the time-of-flight of photons (see section 2.2.1). Time-of-flight imaging techniques encompass the use

of a streak camera, optical cross correlation, Kerr-gating and optical coherence-gating:

class (2) Spatially resolved gating techniques that rely on the path deviation of scattered photons (see section 2.2.2). Spatially resolved techniques include confocal imaging, optical heterodyning and angle-gating;

class (3) Polarisation-gating that relies on the polarisation state of the illumination light (see section 2.2.3). Both conventional polarisation-gating and differential polarisation-gating have been studied.

It has also been illustrated that gating techniques from these three independent classes, time-gating, spatial-gating and polarisation-gating, can be combined to further improve the suppression of scattered light, thereby increasing the image resolution.

This chapter has also discussed the principles behind single-photon and two-photon excitation and demonstrated the advantages in imaging performance achieved with two-photon excitation.

# Chapter 3

## Theoretical simulation of photon propagation in turbid media

### 3.1 Introduction

This chapter gives a detailed presentation of the theoretical formulation and methods used in the simulation of photon propagation in turbid media for microscopic imaging systems. The theoretical formulations presented in this chapter are only applicable for simulating elastic scattering in an absorption free turbid media. It should be noted that only the necessary formulations needed to perform the calculations are given. The implementation of these formulations into a scanning microscope have been conducted by Professor Gu and Dr. Gan in the Optoelectronic Imaging Group at Victoria University (Gu and Gan, 1997; Gan and Gu, 1998; Gan *et al.*, 1997; 1998).

The chapter is organised into the following sections: Section 3.2 outlines the principle of scattering by spherical objects based on Mie theory (Bohern and Huffman, 1983). Section 3.3 outlines the implementation of the theoretical model based on Monte-Carlo simulation (Flock *et al.*, 1989; Hasegawa *et al.*, 1991; Key *et al.*, 1991; Graff *et al.*, 1993). This section includes the implementation of lenses for microscopic imaging (Schmitt *et al.*, 1994; Schmitt and Ben-Letaief, 1996; Gu and Gan, 1997; Gan and Gu, 1998; Gan *et al.*, 1997), polarisation (Gan *et al.*, 1997; 1999; Brusaglioni *et al.*, 1997) and pulse propagation (Hebden and Kruger, 1990; Zaccanti and Donelli, 1994; Gan *et al.*, 1997; Gan and Gu, 1998). Section 3.3 also includes the general constraints placed on the Monte-Carlo simulation. In section 3.4 the Monte-Carlo simulation model is used to calculate the temporal and angular distributions of photons originating from a given turbid media illuminated by a lens system. A summary of the work presented in this chapter is given in section 3.5.

### **3.2 Scattering by a sphere: Mie theory**

There are many methods to describe the interaction of light and matter. However, in this work Mie theory is chosen to describe the scattering processes because it gives an insight into the collision process between photons and scattering particles.

When a beam of light with specified characteristics illuminates a given small particle, the amount of the light scattered by the particle along with its angular distribution depends directly on the characteristics of the particle, including its

shape, size, and the materials of which it is composed (Bohern and Huffman, 1983).

The physics and mathematics for the interaction of an electromagnetic wave with a sphere is complicated and cumbersome. Therefore, only the Mie theory formulations that are needed to calculate the scattering parameters are presented.

### 3.2.1 Scattering coefficients for spherical particles

For a spherical particle of a given particle size, the size parameter,  $x$ , and the relative refractive index,  $m$ , are given by (Bohern and Huffman, 1983)

$$x = k_2 a = \frac{2\pi N_2 a}{\lambda} = 2\pi N_2 A, \quad (3.1)$$

$$m = \frac{k_2}{k_1} = \frac{N_2}{N_1}, \quad (3.2)$$

where  $k$  is the wave vector,  $a$  is the radius of the spherical particle,  $N$  is the refractive index and  $A = a/\lambda$  is the relative particle size. Here the subscripts 1 and 2 represent the surrounding medium and the scattering particle, respectively.

The Mie theory scattering coefficients,  $a_i$  and  $b_i$ , which represent the weighting parameters for the electromagnetic normal modes scattered by a spherical particle defined by equation 3.1, are given by (Bohern and Huffman, 1983)

$$a_i = \frac{\mu_1 m^2 j_i(mx) [x j_i(x)]' - \mu_2 j_i(x) [mx j_i(mx)]'}{\mu_1 m^2 j_i(mx) [x h_i^{(1)}(x)]' - \mu_2 h_i^{(1)}(x) [mx j_i(mx)]'}, \quad (3.3)$$

$$b_i = \frac{\mu_2 j_i(mx) [x j_i(x)]' - \mu_1 j_i(x) [mx j_i(mx)]'}{\mu_2 j_i(mx) [x h_i^{(1)}(x)]' - \mu_1 h_i^{(1)}(x) [mx j_i(mx)]'}, \quad (3.4)$$

where  $\mu_1$  and  $\mu_2$  are permeabilities of the scattering scatterers and the surrounding medium, respectively. The prime indicates differentiation with respect to the argument in the parenthesis,  $j_i(mx)$  is a spherical Bessel function of the first kind,

$$j_i(mx) = \sqrt{\frac{\pi}{2mx}} J_{i+1/2}(mx), \quad (3.5)$$

and  $h_i^{(1)}(x)$  is a spherical Bessel function of the third kind,

$$h_i^{(1)}(x) = j_i(x) + iy_i(x), \quad (3.6)$$

where  $y_i(x)$  is a spherical Bessel function of the second kind,

$$y_i(x) = \sqrt{\frac{\pi}{2x}} Y_{i+1/2}(x). \quad (3.7)$$

Here  $i$  denotes the  $i$ -th mode of an electromagnetic wave.

### 3.2.2 Scattering cross-sections and anisotropy value

The scattering cross-section,  $\sigma_s$ , represents the cross-sectional area that can interact with the illumination light. The scattering cross-section,  $\sigma_s$ , for a spherical particle, defined by equation 3.1, is given by (Bohern and Huffman, 1983)

$$\sigma_s = \frac{2\pi}{k^2} \sum_{i=1}^{\infty} (2i+1) (|a_i|^2 + |b_i|^2). \quad (3.8)$$

The anisotropy value (or the asymmetry parameter),  $g$  ( $= \langle \cos\theta \rangle$ ), which defines the directional change of the scattered light, is given by (Bohern and Huffman, 1983)

$$gQ_s = \frac{4}{x^2} \left[ \sum_{i=1}^{\infty} \frac{i(i+2)}{i+1} \operatorname{Re}\{a_i a_{i+1}^* + b_i b_{i+1}^*\} + \sum_{i=1}^{\infty} \frac{2i+1}{i(i+1)} \operatorname{Re}\{a_i b_i^*\} \right], \quad (3.9)$$

where  $Q_s$  is the scattering efficiency defined as

$$Q_s = \frac{\sigma_s}{\sigma_g}, \quad (3.10)$$

and  $\sigma_g$  is the geometric cross-sectional area projected onto a plane perpendicular to the incident beam (i.e.  $\sigma_g = \pi a^2$  for a spherical particle). It should be noted that the anisotropy value,  $g$ , ranges from 0 to 1, where  $g = 0$  represents isotropic scattering and  $g = 1$  represents forward scattering for all photons.

Consider scattering media consisting of polystyrene microspheres suspended in water. The refractive indices of the polystyrene microspheres and the surrounding medium,  $N_2$  and  $N_1$ , are 1.59 and 1.33, respectively. The scattering efficiency,  $Q_s$ , and the anisotropy value,  $g$ , as a function of the relative particle size,  $A$ , are shown in figure 3.1 (Gan *et al.*, 1997).

The scattering efficiency,  $Q_s$ , increases rapidly for a relative particle size,  $A$ , between 0.2 to 1.2, and then reaches the maximum value when the relative particle size,  $A$ , is approximately 1.25 (figure 3.1). The anisotropy value,  $g$ , increases rapidly when the relative particle size,  $A$ , is less than 0.4, and reaches a fairly steady region when the relative particle size,  $A$ , is larger than 0.5 (figure 3.1). The

maximum value of  $g$  is not equal to unity because it is impossible for all scattered photons to propagate in the forward direction.

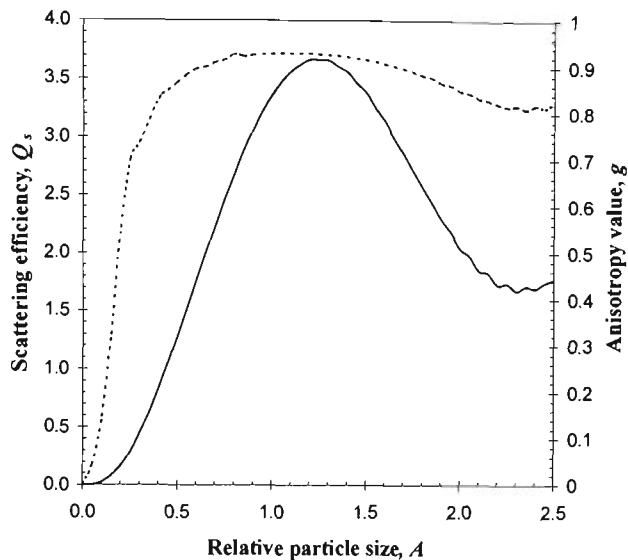


Figure 3.1: Scattering efficiency,  $Q_s$ , (solid curve) and anisotropy value,  $g$ , (dashed curve) as a function of the relative particle size,  $A$ . ( $N_1 = 1.33$  and  $N_2 = 1.59$ ).

### 3.2.3 Calculation of the scattering-mean-free-path length

This section determines the scattering-mean-free-path (smfp) length,  $l_s$ , for the polystyrene microspheres (PolyScience Inc.) used in this thesis. In terms of the theory of light propagation in turbid media, the scattering-mean-free-path length,  $l_s$ , is a measure of the average free-path-length that a photon travels before it is scattered. The scattering-mean-free-path length,  $l_s$ , is determined via

$$l_s = \frac{1}{\sigma_s \rho}, \quad (3.11)$$

where  $\rho$  is the concentration of particles per cubic micrometer and is given by (PolyScience Inc., 1998)

$$\rho = \frac{6W}{p\pi\kappa^3}, \quad (3.12)$$

where  $p$  is the density of polystyrene (1.05),  $W$  is the weight percentage of polystyrene microspheres in the bulk solution (standard solution 2.5%) and  $\kappa$  is the diameter of the polystyrene microspheres ( $\mu\text{m}$ ).

Sphere diameter, $\kappa$ ( $\mu\text{m}$ )	Geometric cross-section, $\sigma_g$ ( $\mu\text{m}^2$ )	Concent. $\rho$ (part./ $\mu\text{m}^3$ )	Relative particle size, $A$ ( $a/\lambda$ )	Scattering efficiency, $Q_s = \sigma_s/\sigma_g$	Scattering cross-section, $\sigma_s$ ( $\mu\text{m}^2$ )	smfp length, $l_s$ ( $\mu\text{m}$ )	Anisotropy value, $g$
0.107	0.009	37.11	0.0845	0.0037	$7.19 \times 10^{-3}$	416.4	0.076
0.202	0.032	5.52	0.1596	0.0805	$2.58 \times 10^{-3}$	70.2	0.31
0.48	0.181	0.411	0.3793	0.7002	$1.27 \times 10^{-1}$	19.2	0.81
1.056	0.876	0.038	0.8342	2.7784	2.42	10.8	0.92

Table 3.1: Calculation of the scattering-mean-free-path length,  $l_s$ , and the anisotropy value,  $g$ , for the polystyrene microspheres used in this work for an excitation wavelength,  $\lambda$ , of 632.8 nm.

Table 3.1 shows the parameters for the four types of polystyrene microspheres used in this work (see chapters 4 and 5) for a wavelength,  $\lambda$ , of 632.8 nm. From the results illustrated in table 3.1 it is seen that larger polystyrene microspheres have shorter scattering-mean-free-path lengths and higher anisotropy values. This result indicates that increasing the scattering microsphere diameter,  $\kappa$ , for a given sample geometric thickness and a given weight percentage of a scattering solution, has the effect of increasing the average number of scattering events experienced by an individual photon since the free-path-length is significantly shorter. An increase in the scattering microsphere diameter,  $\kappa$ , also significantly changes the angular distribution of the scattered photons, since more scattered photons travel in the

forward direction as the anisotropy value,  $g$ , approaches unity. These two effects play an important and significant role in determining the success of a gating mechanism and are discussed/investigated in more detail in chapters 4 and 5.

### 3.3 Monte-Carlo simulation method

#### 3.3.1 General theory

Monte-Carlo simulation is an important tool in studying photon propagation through turbid media since it allows the efficient tracking of photon states (direction, polarisation etc.) at each scattering event experienced within turbid media (see for example Flock *et al.*, 1989; Schmitt *et al.*, 1994; Gan and Gu, 1998).

In the previous section the scattering-mean-free-path length,  $l_s$ , has been defined as a measure of the average free-path length before a photon is scattered. The decay in the number of unscattered photons after propagating through a depth,  $d$ , in turbid media, for a collimated beam, can be represented by Beer's law (Born and Wolf, 1975) and is equal to the probability  $P(d)$  that a photon has a free-path length,  $d$ , for a given scattering mean-free-path length,  $l_s$ ,

$$P(d) = N(d) / N(0) = \exp(-d/l_s), \quad (3.13)$$

where  $N(d)$  is the number of the unscattered photons at depth  $d$ , and  $N(0)$  is the number of incident photons (Gan and Gu, 1998).

For a given number of photons incident to a turbid medium the free-path length between two consecutive interactions of the photons is given by (Gan and Gu, 1998)

$$l_t = l_s \ln \beta, \quad (3.14)$$

where  $l_s = \langle l_t \rangle$  is the time averaged scattering-mean-free-path length, and  $\beta$  is a random number which is evenly chosen between 0 and 1 and satisfies the probability function in equation 3.13.

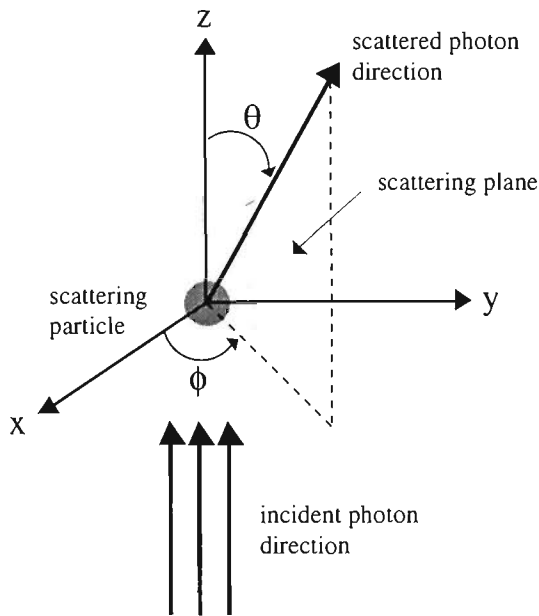


Figure 3.2: Scattering by a spherical particle.

In the Monte-Carlo model developed by Gan and Gu (1998) five independent variables are needed in order to simulate a multi-dimensional photon distribution; these include three spatial coordinates  $x$ ,  $y$  and  $z$ , and two angular coordinates (a polar angle,  $\theta$ , and an azimuthal angle,  $\phi$ ). Figure 3.2 illustrates the coordinate system for a spherical scattering particle. These five independent variables are not

necessarily set to zero for a microscopic imaging system and the method used for determining their initial values is outlined in section 3.3.2.

Each time when a photon interacts with a scattering particle in the simulation model, new coordinates are determined. The new polar angle,  $\theta$ , is equated to the scattering angle,  $\theta_s$ , which is chosen based on the Henyey-Greenstein (H-G) probability distribution (Flock *et al.*, 1987)

$$p_{\theta}(\theta) = \frac{1-g^2}{2(1+g^2-2g\cos\theta)^{3/2}} \sin\theta, \quad (3.15)$$

where  $g$  is the anisotropy value, calculated from equation 3.9. The scattering polar angle,  $\theta_s$ , can therefore be obtained from (Flock *et al.*, 1987)

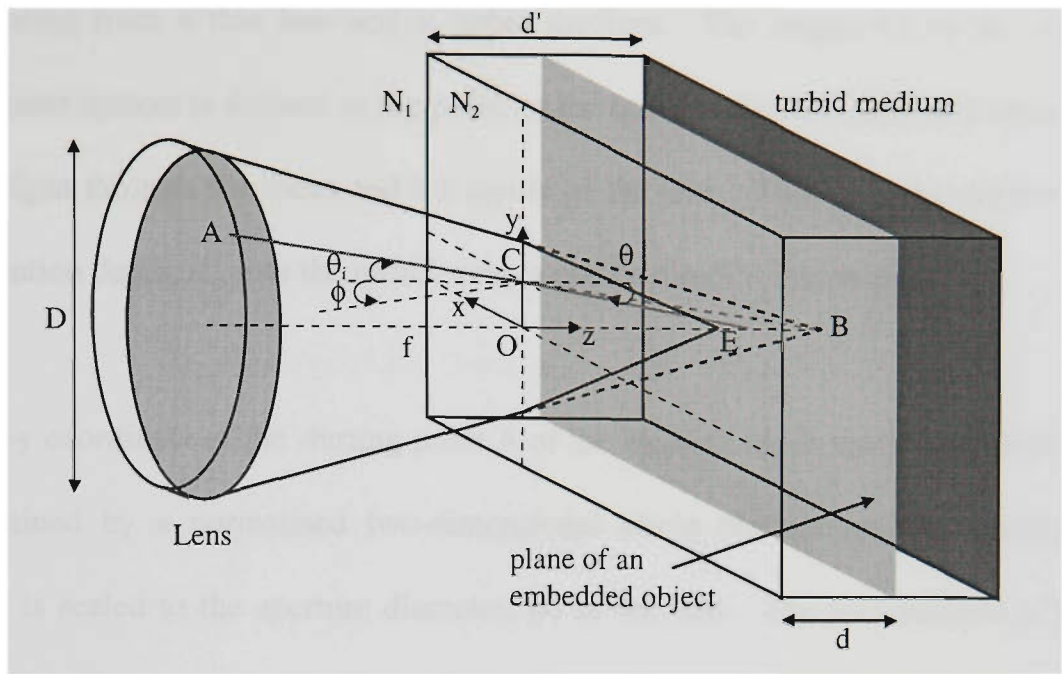
$$\cos\theta_s = \frac{1+g^2}{2g} - \frac{(1-g^2)^2}{2g(1-g+2g\delta)^2}, \quad (3.16)$$

where  $\delta$  is another evenly distributed random number from 0 to 1. The new azimuthal angle,  $\phi$ , is randomly chosen between 0 to  $2\pi$ , while the spatial coordinates,  $x$ ,  $y$  and  $z$ , are determined by the sample and illumination conditions.

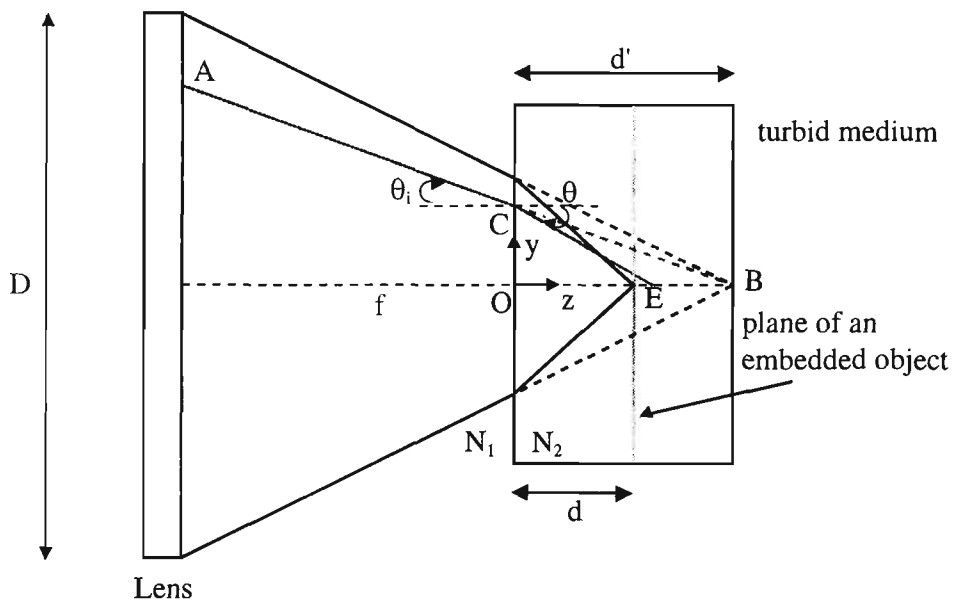
### 3.3.2 Microscopic imaging

#### 3.3.2.1 Theoretical formulation

As briefly mentioned in the previous section the initial values of the three spatial coordinates  $x$ ,  $y$ ,  $z$  and two angular coordinates  $\theta$  and  $\phi$  for a photon entering a turbid medium are not necessarily set to be 0, due to the angular distribution of propagating photons for a lens (see figure 3.3).



(a)



(b)

Figure 3.3: Geometric arrangement for a lens system. (a) Three-dimensional view; (b) two-dimensional view in the meridian plane. The full projection space for photons is illustrated in black, while the incident projection of a single photon is given in grey. The figure illustrates the case when  $N_1 > N_2$ .

Figure 3.3 illustrates the geometric arrangement between the incident photons originating from a thin lens and a turbid medium. The origin,  $O$ , of the  $x$ - $y$ - $z$  coordinate system is defined as the point on the outer surface of the turbid medium that aligns through the focus and the centre of the lens. With this convention the penetration depth,  $d'$ , into the turbid sample can be directly determined.

The  $x$ - $y$  coordinate of the starting point  $A$  of the incident ray in the lens aperture is determined by a normalised two-dimensional circle random number generator which is scaled to the aperture diameter,  $D$ , of the lens. The  $z$ -coordinate of the starting point  $A$  is given by the difference between the penetration depth,  $d'$ , and the focal length,  $f$ , of the lens, which is derived for a given lens of numerical aperture (NA) and aperture diameter,  $D$  (i.e.  $f \approx D/2NA$ ). It should be noted the  $z$ -coordinate of point  $A$  is a constant less than 0, for a given lens, since all photons originate from the same  $x$ - $y$  plane in the lens (see shaded grey plane on the lens in figure 3.3). The ending point of the incident ray is given by point  $B$ , with its  $x$ - $y$ - $z$  coordinate defined as the geometric focus of the imaging lens (i.e. coordinates  $(0, 0, d')$ ).

Due to a change in refractive index between the surrounding and turbid media, the focal plane defined by point  $B$  (see dark grey plane in the turbid medium in figure 3.3) only represents the imaginary depth,  $d'$ , into the turbid medium. This means that, the true focal plane,  $d$ , defined by point  $E$ , into the turbid sample must be determined with the aid of Snell's law (Born and Wolf, 1980)

$$N_1 \sin \theta_i = N_2 \sin \theta, \quad (3.17)$$

where  $N_1$  and  $N_2$  are the refractive indices of the surrounding and turbid media, respectively.  $\theta_i$  is the incident angle at which the ray of a projected photon, defined by points A and B, intersects with the turbid medium boundary at position C (see figure 3.3). It should be noted that in the Monte-Carlo model spherical aberration is ignored. The convergent focal spot is determined from the maximum incident angle,  $\theta_i$  i.e. the marginal ray of the imaging lens.

Reflection and transmission on the interface between a turbid medium and its surrounding medium (see point C in figure 3.3) are also considered in this simulation. A weighting factor,  $f_p$ , is assigned to each photon to represent its contribution weighting. Initially the weighting factor,  $f_p$ , is equal to 1. When a photon passes through a dielectric interface, the weighting of the photon in the transmitted (T) and reflected (R) directions are decided according to the Fresnel formulae (Born and Wolf, 1980)

$$T_p = \frac{2N_1 \cos\theta_i}{N_2 \cos\theta_i + N_1 \cos\theta}, \quad (3.18)$$

$$T_s = \frac{2N_1 \cos\theta_i}{N_1 \cos\theta_i + N_2 \cos\theta}, \quad (3.19)$$

$$R_p = \frac{N_2 \cos\theta_i - N_1 \cos\theta}{N_2 \cos\theta_i + N_1 \cos\theta}, \quad (3.20)$$

$$R_s = \frac{N_1 \cos\theta_i - N_2 \cos\theta}{N_2 \cos\theta_i + N_1 \cos\theta}, \quad (3.21)$$

where the subscripts  $p$  and  $s$  represent parallel and perpendicular polarisation components respectively, while subscripts 1 and 2 represent the surrounding and turbid media, respectively.

The initial values of the five parameters for a single photon (ray) incident to the turbid medium at point C are therefore obtained as follows: the spatial coordinates,  $x$  and  $y$ , and the angular coordinate,  $\phi$ , are derived from the geometry in figure 3.3, while  $\theta$  is obtained from Snell's law (equation 3.17). The spatial coordinate,  $z$ , is set to zero since all photons originate from the same boundary surface ( $z$ -plane) of the turbid medium.

It should be noted for transillumination modelling the values of  $z$ , and  $\theta$  are initially set to zero, since a parallel beam probe with respect to the turbid media is used.

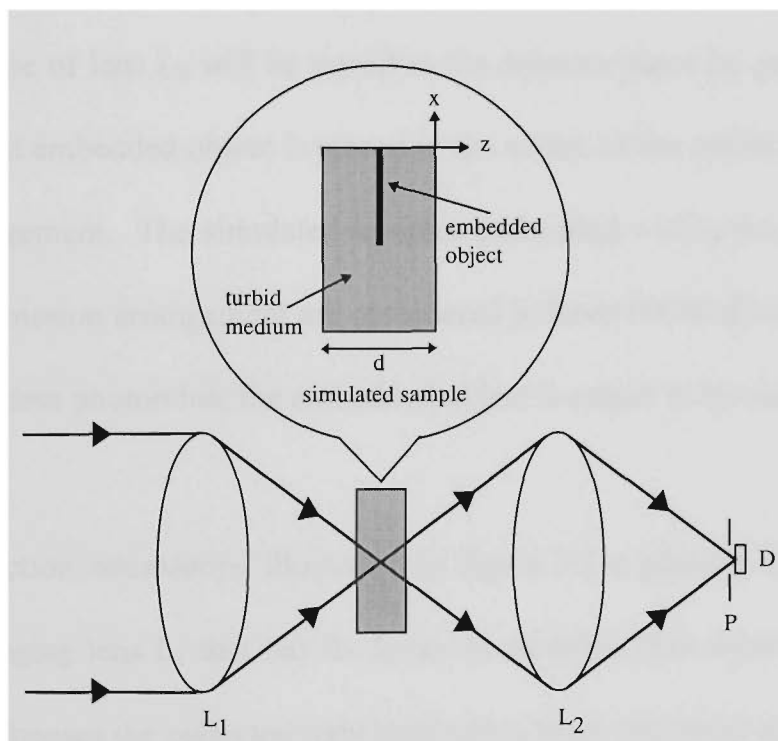


Figure 3.4: Schematic diagram of the modelled transmission scanning optical microscope. D: detector; L: lenses; P: pinhole.

### 3.3.2.2 Modelled microscopic systems

Two scanning optical microscope arrangements are used in this thesis and therefore simulated using the Monte-Carlo model in section 3.3.2.1. They are the transmission scanning optical microscope (figure 3.4) and the reflection scanning optical microscope (figure 3.5). For the transmission optical microscope illustrated in figure 3.4, a parallel beam is incident upon the imaging lens  $L_1$  that has its focus on the embedded object. A separate collection lens  $L_2$  that has its focus overlapped with the imaging lens  $L_1$  is used to collect the light originating from a simulated turbid medium. The collection lens  $L_2$  is also used to focus the collected light onto the detector D. It should be noted that only the photons that fall within the collection cone of lens  $L_2$  will be traced to the detector plane by geometric optics. The simulated embedded object is placed in the centre of the turbid medium in this optical arrangement. The simulated samples embedded within the turbid medium for the transmission arrangement are considered to have 100% absorption. That is, when an incident photon hits the embedded object it ceases to be simulated.

For the reflection microscope illustrated in figure 3.5 a parallel beam is incident upon the imaging lens  $L_1$  that has its focus on an embedded object. A collection lens  $L_2$  then focuses the collected light originating from the turbid medium onto the detector D. It should be noted that only the photons that fall within the collection cone of lens  $L_2$  will be traced to the detector plane by geometric optics. In this arrangement the embedded object is placed on the back surface of the turbid medium. The simulated samples embedded within the turbid medium for the reflection arrangement are considered to have 100% reflectivity.

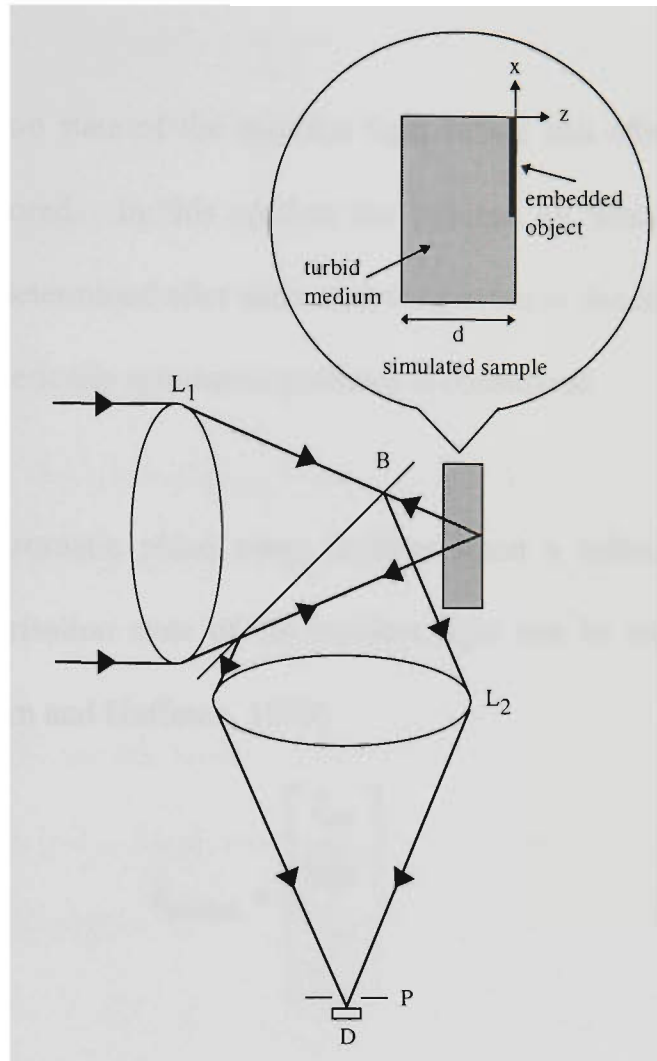


Figure 3.5: Schematic diagram of the modelled reflection scanning optical microscope. B: beamsplitter; D: detector; L: lenses; P: pinhole.

With this arrangement the reflection microscope is equivalent to folding the transmission microscope arrangement, at the embedded object, onto itself.

It should be noted that the size of the detector used in the detection of the light originating from the simulated turbid media is determined by the effective size of the pinhole, P, used (see figures 3.4 and 3.5).

### 3.3.3 Polarisation

So far the polarisation state of the incident light before and after each scattering event has been ignored. In this section the process by which the change in polarisation can be determined after each scattering event is described. Once again only the case for spherically symmetric particles is considered.

Consider a monochromatic plane wave incident upon a spherically symmetric scatterer. The polarisation state of the incident light can be represented by the Stokes vector (Bohern and Huffman, 1983)

$$I_{incident} = \begin{bmatrix} I_{inc} \\ Q_{inc} \\ U_{inc} \\ V_{inc} \end{bmatrix}, \quad (3.22)$$

where

$$I_{inc} = \langle E_x E_x^* + E_y E_y^* \rangle, \quad (3.23)$$

$$Q_{inc} = \langle E_x E_x^* - E_y E_y^* \rangle, \quad (3.24)$$

$$U_{inc} = \langle E_x E_y^* + E_y E_x^* \rangle, \quad (3.25)$$

$$V_{inc} = \langle E_x E_y^* - E_y E_x^* \rangle, \quad (3.26)$$

where  $E_x$  and  $E_y$  represent the orthogonal components of the incident electric field along the x and y axes.  $\langle \rangle$  denotes the time average of the bracketed quantity.

Note that in an optical microscope, the illumination beam on the sample is a convergent beam from an objective lens. Assume that the incident beam before an

illumination objective is a linearly polarised plane wave. After the light propagates through the objective, its polarisation vector changes. Therefore a new Stokes vector,  $I'_{incident}$ , of photons after the objective is determined by geometric optics (Gan *et al.*, 1998).

The relationship of the polarisation state between the incident light and the scattered light can be represented as (Gan *et al.*, 1998)

$$I_{scat}^{after} = MI_{scat}^{before}, \quad (3.27)$$

where  $I_{scat}^{before}$  and  $I_{scat}^{after}$  are the Stokes vectors before and after the scattering event, respectively and  $M$  is a  $4 \times 4$  scattering matrix for a spherical symmetric particle (Bohern and Huffman, 1983)

$$M = \begin{bmatrix} S_{11}(\theta) & S_{12}(\theta) & 0 & 0 \\ S_{12}(\theta) & S_{11}(\theta) & 0 & 0 \\ 0 & 0 & S_{33}(\theta) & S_{34}(\theta) \\ 0 & 0 & -S_{34}(\theta) & S_{33}(\theta) \end{bmatrix}, \quad (3.28)$$

where the matrix elements are given by

$$S_{11}(\theta) = \frac{1}{2} \left( |S_2(\theta)|^2 + |S_1(\theta)|^2 \right), \quad (3.29)$$

$$S_{12}(\theta) = \frac{1}{2} \left( |S_2(\theta)|^2 - |S_1(\theta)|^2 \right), \quad (3.30)$$

$$S_{33}(\theta) = \frac{1}{2} \left( S_2^*(\theta)S_1(\theta) + S_2(\theta)S_1^*(\theta) \right), \quad (3.31)$$

$$S_{34}(\theta) = \frac{1}{2} \left( S_1(\theta)S_2^*(\theta) - S_2(\theta)S_1^*(\theta) \right). \quad (3.32)$$

Here

$$S_1(\theta) = \sum_{i=1}^{\infty} \frac{2i+1}{i(i+1)} (a_i \pi_i + b_i \tau_i), \quad (3.33)$$

$$S_2(\theta) = \sum_{i=1}^{\infty} \frac{2i+1}{i(i+1)} (a_i \tau_i + b_i \pi_i), \quad (3.34)$$

where  $a_i$  and  $b_i$  are the scattering coefficients defined by equations 3.3 and 3.4, respectively, and  $\pi_i$  and  $\tau_i$  are angle dependent functions defined as (Bohern and Huffman, 1983)

$$\pi_i = \frac{P_i^1}{\sin \theta}, \quad (3.35)$$

$$\tau_i = \frac{dP_i^1}{d\theta}, \quad (3.36)$$

where  $P_i^1$  is the associated Legendre function. Both  $\pi_i$  and  $\tau_i$  can be calculated from the upward recursion relations given by (Bohern and Huffman, 1983)

$$\pi_i = \left( \frac{2i-1}{i-1} \pi_{i-1} \right) \cos \theta - \left( \frac{i}{i-1} \pi_{i-2} \right), \quad (3.37)$$

and

$$\tau_i = (i \cos \theta) \pi_i - (i+1) \pi_{i-1}, \quad (3.38)$$

where  $\pi_0 = 0$  and  $\pi_1 = 1$ .

Therefore once the scattering parameters,  $S_1(\theta)$  and  $S_2(\theta)$  (equation 3.34) are known, all elements of the scattering matrix,  $M$ , (equation 3.28) can be calculated. Since calculating the scattering parameters,  $S_1(\theta)$  and  $S_2(\theta)$ , is a time consuming task, an approximation is used in the calculation of the scattering matrix,  $M$ , at each scattering event. Before simulation starts (Gan *et al.*, 1998), the scattering

angle,  $\theta$ , between 0 and  $\pi$  is first divided into 1000 equal intervals and the scattering parameters,  $S_1(\theta)$  and  $S_2(\theta)$ , corresponding to those scattering angles are calculated. All the calculated scattering angles,  $\theta$ , and the scattering parameters,  $S_1(\theta)$  and  $S_2(\theta)$ , are stored in a database file.

To employ polarisation-gating in the Monte-Carlo simulation, Stokes parameters are defined for each incident photon in addition to the five existing parameters ( $x$ ,  $y$ ,  $z$ ,  $\theta$  and  $\phi$ ). At each scattering event in the Monte-Carlo simulation (Gan *et al.*, 1998) the scattering parameters,  $S_1(\theta)$  and  $S_2(\theta)$ , are obtained by matching the scattering angle,  $\theta_s$  (determined by the Henyey-Greenstein probability distribution (equation 3.15)), with the closest scattering angle,  $\theta$ , stored in the look-up database file. Then according to the chosen scattering angle,  $\theta$ , and its corresponding scattering parameters,  $S_1(\theta)$  and  $S_2(\theta)$ , all the elements of the scattering matrix,  $M$ , are calculated using equations 3.28 to 3.32. Therefore a new Stokes vector can be calculated from equations 3.27.

By monitoring the change of the polarisation state of each photon at every scattering event, the depolarisation of the light propagating through a turbid medium can be evaluated.

The degree of polarisation,  $\gamma$ , of the detected scattered light in this thesis is defined as

$$\gamma = \frac{I_p - I_s}{I_p + I_s}, \quad (3.39)$$

where  $I_p$  and  $I_s$  are the light intensity detected with the analyser parallel and perpendicular to the incident polarisation direction, respectively.

Assuming that the incident light is linearly polarised in the x-direction, the parallel polarisation intensity,  $I_p$ , and the perpendicular polarisation intensity,  $I_s$ , can be calculated by

$$I_p = I_{scat} \cdot [1 \ 1 \ 0 \ 0], \quad (3.40)$$

and

$$I_s = I_{scat} \cdot [1 \ -1 \ 0 \ 0]. \quad (3.41)$$

The polarisation gating mechanisms used in this work are parallel (conventional) polarisation-gating, based on the signal intensity ( $I_p$ ) detected with an analyser parallel to the direction of the incident polarisation, and perpendicular polarisation-gating, based on the signal intensity ( $I_s$ ) detected with an analyser perpendicular to the direction of the incident polarisation. The third method of polarisation-gating considered is differential polarisation gating which is based on the subtraction of the conventional polarisation-gated intensity,  $I_p$ , and the perpendicular polarisation-gated intensity,  $I_s$  (refer to chapter 5 for further details).

### 3.3.4 Pulse propagation

This section describes the process by which pulse propagation through a turbid medium is implemented in the Monte-Carlo model (Gan *et al.*, 1997; Gan and Gu, 1998). The inclusion of pulse propagation into the Monte-Carlo model is important to demonstrate the inability of time-of-flight based imaging systems

(refer to section 2.2.1) too effectively suppress scattered photons in microscopic imaging systems.

An ultrashort pulsed beam with pulse width,  $\Delta\tau_0$ , has a finite distribution of wavelength (frequency) components. According to Mie scattering theory (see section 3.2), the scattering coefficients,  $a_i$  and  $b_i$ , are related to the ratio between the radius of a scattering particle,  $a$ , and the wavelength of light,  $\lambda$  (see equations 3.1 to 3.4). Therefore, for a given scattering particle radius,  $a$ , the scattering coefficients,  $a_i$  and  $b_i$ , for each wavelength component,  $\lambda$ , are different. Hence the scattering cross-section,  $\sigma_s$ , and the anisotropy value,  $g$ , need to be determined for each individual wavelength component,  $\lambda$ , for an illumination pulse.

The effect of the broad spectrum of an ultrashort pulse on the scattering efficiency,  $Q_s$ , and the anisotropy value,  $g$ , becomes more pronounced as the pulse width,  $\Delta\tau_0$ , becomes shorter. Let us consider that the intensity of an illumination source is a Gaussian-shaped pulse given by (Gu, 1996)

$$U_0(t) = \exp(-i\omega_0 t) \exp\left[-\left(\frac{t}{T}\right)^2\right], \quad (3.42)$$

where  $t$  is the local time coordinate,  $T$  is related to the pulse width  $\Delta\tau_0$  via  $\Delta\tau_0 = 2T\sqrt{\ln 2}$  and  $\omega_0$  is the central frequency.

The corresponding Fourier spectrum for the Gaussian-shaped pulse (equation 3.42) is then given by (Gu, 1996)

$$V_0(\Delta\Omega) = \sqrt{\pi}T \exp\left[-\left(\frac{T\Delta\Omega}{2}\right)^2\right], \quad (3.43)$$

where  $\Delta\Omega$  is the spectral width, which is defined as the total bandwidth between two positions at which the intensity drops to one half of its peak value.

The relationship between the pulse width  $\Delta\tau_0$ , and the spectral width  $\Delta\Omega$  for the pulse is then given by (Gu, 1996)

$$\Delta\Omega = \frac{8 \ln 2}{\Delta\tau_0}. \quad (3.44)$$

For example a 10-fs pulse with a central wavelength,  $\lambda_0$ , of 700 nm, has a corresponding spectral width,  $\Delta\Omega$ , of approximately 0.206. Note that in this case the spectral width,  $\Delta\Omega$ , is normalised by the central frequency,  $\omega_0$  ( $\omega_0 = 2\pi c/\lambda_0$ , where  $c = 3 \times 10^8$  m/s).

To understand the effect of the spectral width,  $\Delta\Omega$ , on the scattering efficiency,  $Q_s$ , and the anisotropy value,  $g$ , we define two parameters,

$$\Delta Q_s = Q_s(\omega + 0.5\Delta\Omega) - Q_s(\omega - 0.5\Delta\Omega), \quad (3.45)$$

and

$$\Delta g = g(\omega + 0.5\Delta\Omega) - g(\omega - 0.5\Delta\Omega). \quad (3.46)$$

Since the pulse width,  $\Delta\tau_0$ , can be directly related to the frequency bandwidth,  $\Delta\Omega$ , (see equation 3.44) we can plot the difference in the scattering efficiency,  $\Delta Q_s$  and the difference in the anisotropy value,  $\Delta g$ , as a function of the pulse width  $\Delta\tau_0$ .

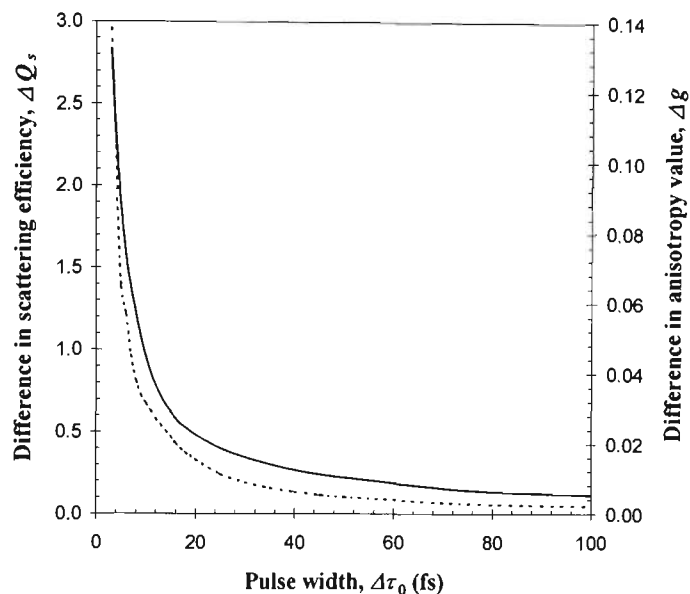


Figure 3.6: Difference in the scattering efficiency,  $\Delta Q_s$ , (solid curve) and the difference in the anisotropy value,  $\Delta g$ , (dashed curve) as a function of the pulse width,  $\Delta\tau_0$  ( $N_1 = 1.33$  and  $N_2 = 1.59$ ).

Shown in figure 3.6 is the effect of the pulse width,  $\Delta\tau_0$ , on the difference in scattering efficiency,  $\Delta Q_s$  and the difference in anisotropy value,  $\Delta g$ , for a central wavelength,  $\lambda_0$ , of 700 nm and a scattering particle radius,  $a$ , of 0.518  $\mu\text{m}$  (Gan *et al.*, 1997). It is seen that the difference in the scattering efficiency,  $\Delta Q_s$ , and the difference in the anisotropy value,  $\Delta g$ , both increase as the pulse width,  $\Delta\tau_0$ , decreases. For the pulse width,  $\Delta\tau_0$ , less than 20 fs the difference in the scattering efficiency,  $\Delta Q_s$ , and the difference in the anisotropy value,  $\Delta g$ , become more

pronounced, indicating that the effect of the frequency bandwidth is more significant in this region. Thus, this effect will rarely be of importance in practice in the near future because the shortest pulse width produced from current commercial pulsed lasers is approximately 40 fs.

The illumination of an ultrashort pulse has been incorporated into the Monte Carlo simulation by describing the temporal distribution of incident photons is given by the following Gaussian profile (Gan and Gu, 1998)

$$f(t_0) = \exp\left(-\frac{t_0^2}{T^2}\right), \quad (3.47)$$

where  $t_0$  is the departure time of a photon. The departure time,  $t_0$ , of photons in the pulse is randomly chosen according to the temporal distribution in equation 3.47.

The effect of the pulse width of the illumination source on the scattering cross-section,  $\sigma_s$ , and the anisotropy value,  $g$ , has been taken into account in the Monte-Carlo simulation when ultrashort pulses are used.

### 3.3.5 General simulation properties

So far only the individual techniques of photon migration in the Monte-Carlo simulation have been dealt with. This section discusses the constraints placed on the propagation of an individual photon, the determination of the number of photons used in a particular simulation process, and the process behind the detection of the simulated photons.

The theory and techniques presented so far in this chapter have not included the transfer and/or loss of photon energy i.e. an absorption free medium and elastic scattering have been assumed. In other words a photon in this model can propagate indefinitely. To overcome this problem the following constraints have been placed on the simulation model (Schmitt *et al.*, 1994; Gan *et al.* 1999).

- (a) Turbid media simulated in the Monte-Carlo model are given finite dimensions.
  
- (b) A scattered photon that interacts with the boundaries of a turbid medium that are not related to imaging processes ceases to be simulated. In the case of a reflection system they include the side walls of a turbid medium and the area of the turbid medium that is not covered by the embedded sample. For the case of a transmission system the boundaries are the side walls and the entry surface of a turbid medium.
  
- (c) Photons cease to exist once specific cut-off points are reached. The cut-off points are defined as (i) the point when the Fresnel weighting factor,  $f_p$ , (see section 3.3.2.1) is less than one tenth of its initial weighting and/or (ii) the point when the number of scattering events experienced by an individual photon is 10 times the average number of scattering events defined for a given turbid medium. For example if the average number of scattering events is 10, the cut-off number of scattering events is 100.

- (d) All available photons that fall within the acceptance cone of the imaging lens (refer  $L_2$  in figures 3.4 and 3.5) are assumed to be collected. These available photons are traced to the detector plane by geometric optics. An additional option is included that defines the size of the detection aperture (i.e. pinhole). Therefore only photons that fall within this aperture contribute to an image.
- (e) The number of photons that are used in the simulation process varies with a turbid medium and the characteristics of an imaging system used. The number of simulation photons chosen is determined by the condition that an increase in the number of simulation photons does not significantly improve the quality or accuracy of the simulated result.

### 3.4 Application of the Monte-Carlo model

In chapter 2, two major classes of the available gating techniques for imaging through turbid media have been discussed. The two classes rely either on the time-of-flight (temporal imaging techniques, refer to section 2.2.1) or path deviation (spatially resolved techniques, refer to section 2.2.2) between unscattered and scattered photons. To determine the effectiveness of these gating techniques in microscopic imaging the developed Monte-Carlo model has been used to simulate the photon distribution in the time-domain and the angle domain.

In this simulation an ultrashort pulsed beam with a temporal width,  $\Delta\tau_0$ , of 20 fs and a central wavelength,  $\lambda_0$ , of 700 nm is used. The turbid medium chosen has a cell geometric thickness,  $d$ , of 160  $\mu\text{m}$ , a scattering-mean-free-path length,  $l_s$ , of 40

$\mu\text{m}$  and an anisotropy value,  $g$ , of 0.9, for the central wavelength,  $\lambda_0$ . The incident pulsed beam is focused onto the turbid medium via an objective of numerical aperture 0.25.

Figure 3.7 Illustrates the angular-temporal photon distribution after the incident pulsed beam has propagated through the turbid medium (Gan *et al.*, 1997). The angular resolution in figure 3.7 is 0.5 degrees and the temporal resolution is one-tenth of the pulse width.

In figure 3.7(a), the turbid medium is illumination by an objective with a circular aperture ( $\varepsilon = 0$ , where  $\varepsilon$  is defined in this thesis as the radius of the central obstruction normalised by the radius of the objective). It is seen that photons propagating at higher angles arrive later than those propagating at lower angles through the objective. It is also noted that there is no clear separation between unscattered and scattered photons in the time domain. This phenomenon demonstrates that time-gating methods are ineffective in suppressing scattered photons. It is also illustrated in figure 3.7(a) that there are no distinguishable unscattered components shown in the angle domain. This phenomenon can also reduce the effectiveness of angle-gating methods that rely on the directional selectivity to suppress scattered photons. These two phenomena arise from the large range of illumination angles produced by the utilisation of a high numerical aperture objective in the imaging process. But high numerical aperture objectives are necessary for high-resolution imaging.

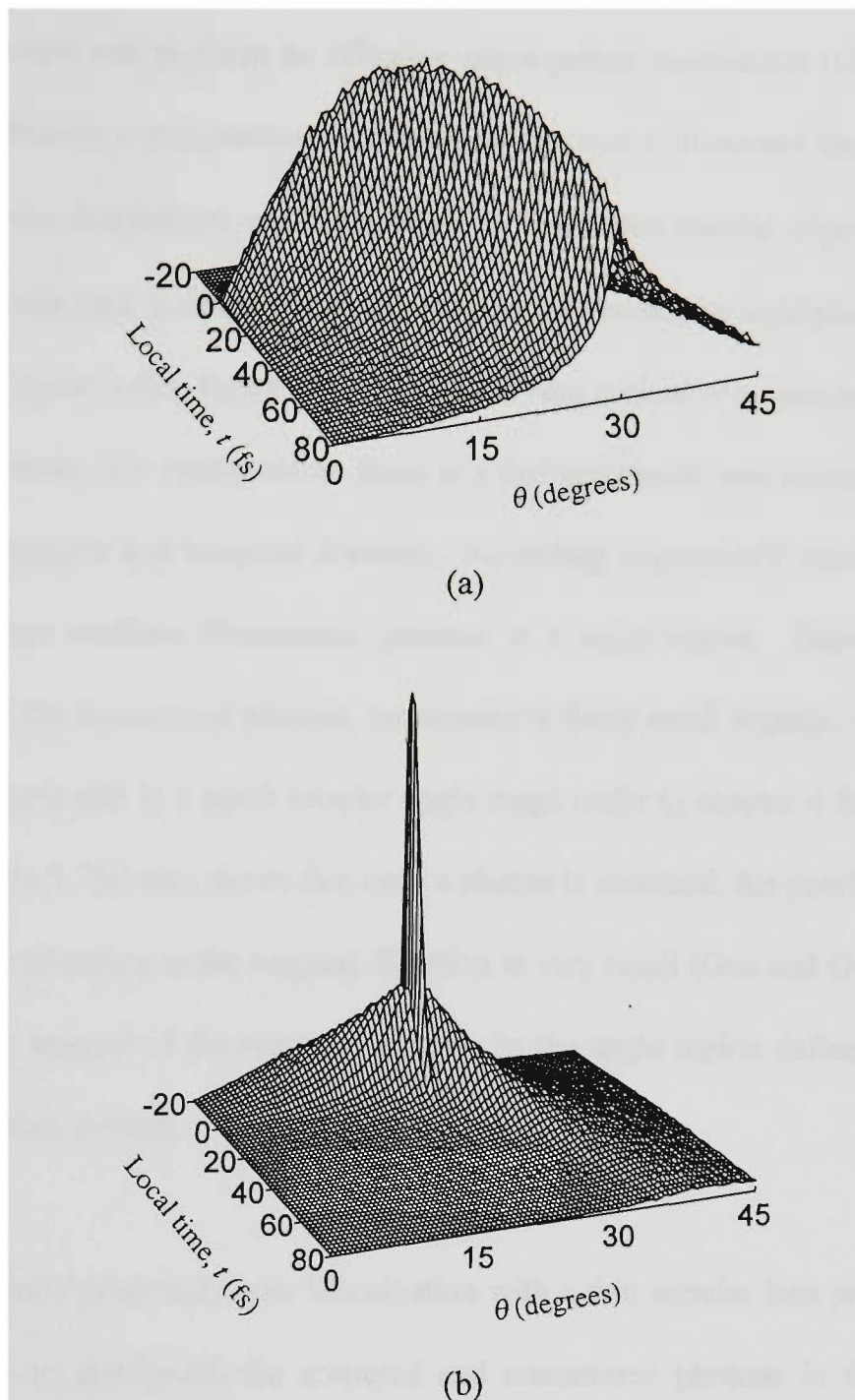


Figure 3.7: Angular-temporal photon distribution of a 20-fs ultrashort pulsed beam propagating through a turbid slab ( $l_s = 40 \mu\text{m}$ ,  $d/l_s = 4$ ). The time  $t$  is a local time, so  $t = 0$  corresponds to the arrival time of the unscattered pulse peak. (a) illumination with a circular objective; (b) illumination with an annular objective. These two curves were calculated by Dr. X. Gan.

It has been proposed and theoretically demonstrated that the use of an annular imaging objective can perform an effective angle-gating mechanism (Gan *et al.*, 1997). This feature is demonstrated in figure 3.7(b) which illustrates the angular-temporal photon distribution under illumination with a thin annular objective ( $\varepsilon = 0.9$ ). An annular lens is simulated in the Monte-Carlo model by confining the x-y coordinate of point A (see figure 3.3) to a circular ring instead of a circular area. It is noted that under this configuration there is a distinguishable unscattered photon peak in both angular and temporal domains. According to geometric optics, a thin annular aperture confines illumination photons to a small region. Therefore the exit angles of the unscattered photons can remain in these small regions, while the scattered photons exit in a much broader angle range (refer to chapter 4 for further details). Figure 3.7(b) also shows that once a photon is scattered, the possibility for such a photon returning to the original direction is very small (Gan and Gu, 1998). Therefore, the amount of the scattered photons in the angle region defined by the annular objective is small.

This phenomenon produced under illumination with a thin annular lens provides a physical basis to distinguish the scattered and unscattered photons in the angle domain in a microscopic imaging system. The use of an annular lens as an angle-gating mechanism is discussed in more detail in chapter 4. Chapter 4 presents an experimental evaluation into the effect of annular imaging objectives on image performance.

### 3.5 Summary

This chapter presents the methodology and functional formula required in developing the Monte-Carlo simulation model. This Monte-Carlo model is based on Mie scattering theory and therefore ignores diffraction phenomena. The principle underlying the use of polarisation and pulse propagation in a microscopic imaging system has been presented in detail. It has also been demonstrated with the use of the developed Monte-Carlo simulation model that the efficiency of time-of-flight mechanisms can be reduced in microscopic imaging systems.

It should be noted that the development of the Monte-Carlo simulation model for microscopic imaging systems has been conducted by other researchers in the Optoelectronic Imaging Group (Gu and Gan, 1997; Gan *et al.*, 1997; Gan and Gu, 1998; Gan *et al.*, 1998) and therefore is not within the main scope of this thesis. However, the use of the modified Monte-Carlo model in the remainder of this thesis helps to confirm experimental data trends and gives guidance to experiments.

# Chapter 4

## Angle-gating in turbid media

### 4.1 Introduction

Reported in this chapter is a new method for microscopic imaging of an object embedded in turbid media. The new method is based on the angle-gating mechanism achieved by the utilisation of polarised annular objectives in the illumination and collection beam paths of microscopic imaging systems (Gan *et al.*, 1997; Schilders *et al.*, 1998a; 1998b; 1998c). A detailed experimental study regarding the effects of the size of annular obstructions and the numerical aperture of an objective on image quality is presented when turbid media including polystyrene microspheres and semi-skimmed milk suspensions are used.

This chapter is organised into the following sections: Section 4.2 qualitatively illustrates the principle of angle-gating and theoretically re-confirms the photon distribution achieved with the utilisation of an annular objective. The performance of annular objectives in a transmission optical microscope is presented in section 4.3, while section 4.4 demonstrates the performance of an annular objective in a reflection optical microscope. Both section 4.3 and section 4.4 also contain numerical results and images to demonstrate both qualitatively and quantitatively

the performance of the angle-gating mechanism. A self contained discussion regarding the experimental and theoretical results is also presented in both sections 4.3 and 4.4. Finally a general discussion and a conclusion are presented in sections 4.5 and 4.6, respectively.

## 4.2 Principle of angle-gating in microscopic imaging

The ability of an annular objective to separate unscattered and scattered photons in the angular domain has been briefly demonstrated in section 3.4 (refer to figure 3.7) with the aid of the Monte-Carlo simulation method. This section describes the angle-gating mechanism in more detail and illustrates how the angle-gating mechanism can be implemented into a microscopic imaging system to suppress unwanted scattered photons.

Without losing generality, a transmission optical microscope is adopted. Figure 4.1 shows the principle of angle-gating in a transmission optical microscope, where a darker region includes more unscattered photons. When one employs a pair of circular objectives ( $O_1$  and  $O_2$ ) in a transmission optical imaging system (figure 4.1(a)), there is no physical way to separate scattered photons in the angle domain of the second (collection) objective  $O_2$ .

In order to separate these two types of photons, it has been proposed by Gu and Gan (1997) that an annular objective (an annular objective can be achieved by placing an annular filter  $F$  in the front focal plane of an objective in a  $4f$  system

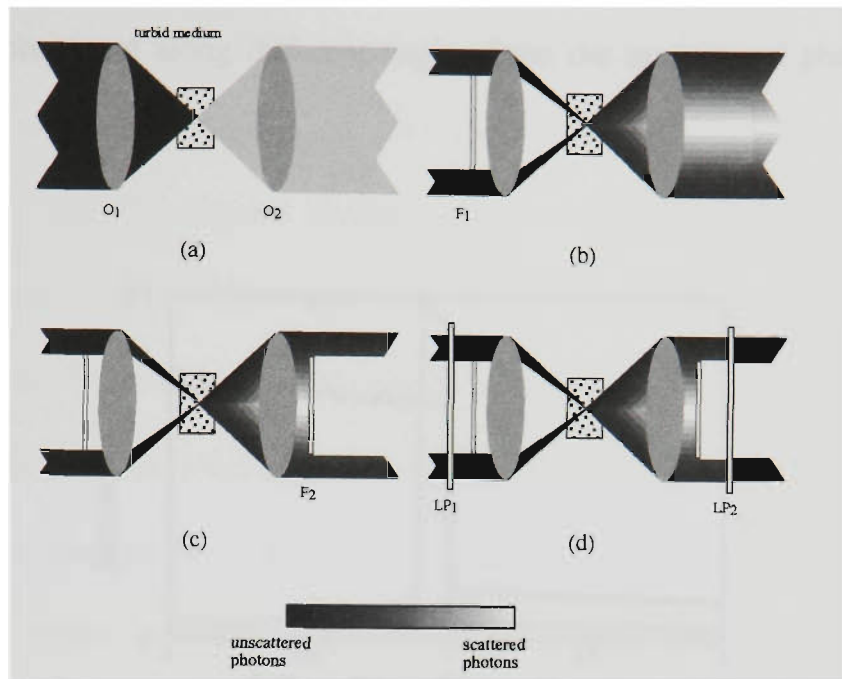


Figure 4.1: Schematic diagram for demonstrating the principle of angle-gating in a transmission microscopic imaging system when, (a) a pair of circular objectives, (b) an illumination annular objective and a collection circular objective, (c) a matching pair of annular objectives and (d) a matching pair of annular objectives employing polarisation-gating are employed.

(Gan *et al.*, 1997) rather than a circular objective is needed for illumination. The size of an annular objective,  $\varepsilon$ , is defined as the ratio of the central obstruction radius to the objective aperture radius. In this chapter,  $\varepsilon_{in}$  and  $\varepsilon_{out}$  are used to define annular objectives in the illumination and collection paths, respectively. It should be noted that the range of the illumination angles for an annular objective is reduced but the numerical aperture of the objective does not change since the maximum aperture of the objective does not change. As expected, with the introduction of an illumination annular objective it is possible to separate the scattered and unscattered photons from each other since the scattered photons

statistically propagate along different angles from the unscattered photons (figure 4.1(b)).

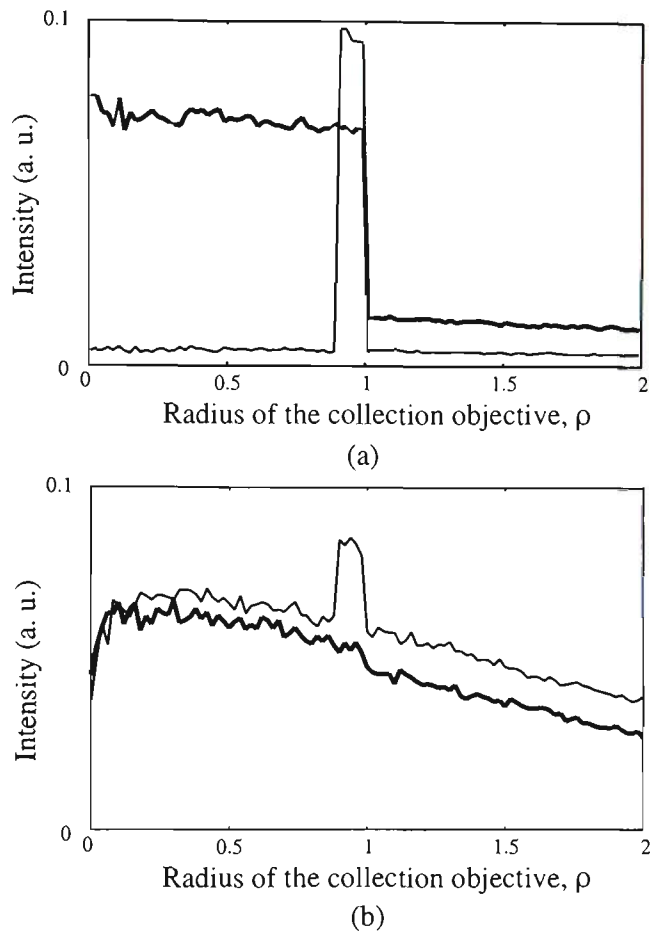


Figure 4.2: Simulated photon distribution along the radial direction of the collection objective for illumination with a circular objective ( $\varepsilon = 0$ , bold) or an annular objective ( $\varepsilon = 0.9$ ). (a) sample3 (a turbid medium consisting of  $0.202 \mu\text{m}$  microspheres, see table 4.1); (b) sample5 (a turbid medium consisting of  $0.48 \mu\text{m}$  microspheres, see table 4.1). Here  $\rho$  is the radial co-ordinate of the collection objective, normalised by the maximum radius of the objective. These two curves were calculated by Dr. X. Gan.

To re-confirm the angle-gating mechanism, the intensity distribution over the collection objective aperture  $O_2$  for a continuous wave beam, has been calculated using the Monte-Carlo program (section 3.3), for sample3 and sample5 (see table 4.1) which will be used in the experiments. Illustrated in figure 4.2 is the intensity distribution, normalised by the incident intensity, along the radial direction of the collection objective,  $\rho$ , when a circular ( $\varepsilon = 0$ ) or an annular objective ( $\varepsilon = 0.9$ ) is employed for illumination. It can be seen from figure 4.2 that an unscattered photon peak appears near the edge of the collection objective aperture only when an annular objective is used for illumination. This result confirms that the thin illumination annular objective confines the unscattered photons to a small angular region on the collection objective plane. The unscattered photon peak in the case of sample5 (figure 4.2(b)) is not as strong as that for sample3 (figure 4.2(a)) due to the significant difference in the average number of scattering events (see table 4.1).

To make use of this unscattered photon peak for high quality microscopic imaging, one can employ another thin annular filter  $F_2$  (i.e.  $\varepsilon \rightarrow 1$ ) to collect the signal originating from the object embedded in turbid media, as depicted in figure 4.1(c). Although a pair of annular objectives can eliminate scattered photons which do not travel along the same direction of the illumination beam, there are still photons which are multiply scattered and finally travel along the same direction as the illumination beam. These scattered photons are superimposed on top of the unscattered photons (see figure 4.2), and they can lead to a reduction of image quality (resolution and contrast) even when annular objectives are employed, since multiply scattered photons carry less information of an object embedded in a turbid

medium. These scattered photons do not possess the same polarisation state as the incident beam because of the scattering process (refer to section 2.2.3). Therefore to suppress them, one can insert a polariser  $LP_1$  in front of or after the illumination annular filter (figure 4.1(d)), so that unscattered photons coming from the sample have the same polarisation state as the illumination while the scattered photons travelling along the illumination direction are depolarised. The amount of diffusing photons can be appreciably reduced by using another polariser  $LP_2$ , (figure 4.1(d)) which has the same polarisation direction as the incident beam and is placed in the back focal plane of the collection objective. As a result of incorporating a polarisation detection mechanism image quality (resolution and contrast) can be further improved. The usefulness of employing polarisation-gating and angle-gating mechanisms simultaneously has been theoretically demonstrated by Gan *et al.* (1997).

### **4.3 Angle-gating in a transmission optical microscope**

The experimental results presented in this section were obtained in a transmission scanning microscope. Consequently, the results regarding contrast and resolution can be easily compared with those obtained in a transillumination imaging system where there is no objective involved.

#### **4.3.1 Experimental details**

##### 4.3.1.1 Experimental set-up

The scanning optical microscope using two polarised annular objectives, as depicted in figure 4.3, was set-up on an optical table. The physical scanning

optical microscope setup, and the schematic diagram of the experimental setup are shown in figures 4.3(a) and 4.3(b), respectively. A 7 mW Melles Griot (model No. 05-LHP-153) He-Ne laser ( $\lambda = 632.8$  nm) was used as the light source. The beam from the laser source was expanded and collimated by an objective  $O_1$  (numerical aperture, NA = 0.25) and a lens  $L_1$  (focal length,  $f = 200$  mm, diameter,  $D = 25$  mm). The illumination objective  $O_2$  (Zeiss FLUAR 20 $\times$ /0.75  $\infty$ /0.17) and the collection objective  $O_3$  (Zeiss PLAN-NEOFLUAR 40 $\times$ /0.75  $\infty$ /0.17) formed a symmetric system around a turbid sample since they had an identical numerical aperture. Scattered and unscattered photons coming from the collection objective were focused via lens  $L_2$  ( $f = 200$  mm,  $D = 25$  mm) onto a Silicon ( $\rho = 0.4$  A/W) large area detector ( $1$  cm<sup>2</sup>) DT which recorded a time-averaged signal. Large area detectors were used to collect a large proportion of photons origination from turbid media. However a photosensitive area of  $1$  cm<sup>2</sup> would contribute substantially greater noise through its higher capacitance and lower dynamic resistance than similar small detectors. Therefore the choice of a detector limits the image quality achievable in this thesis.

All images were recorded with an acquisition time of 27 seconds for a  $200 \times 200$  pixel image. In addition all images were normalised before any data analysis was performed.

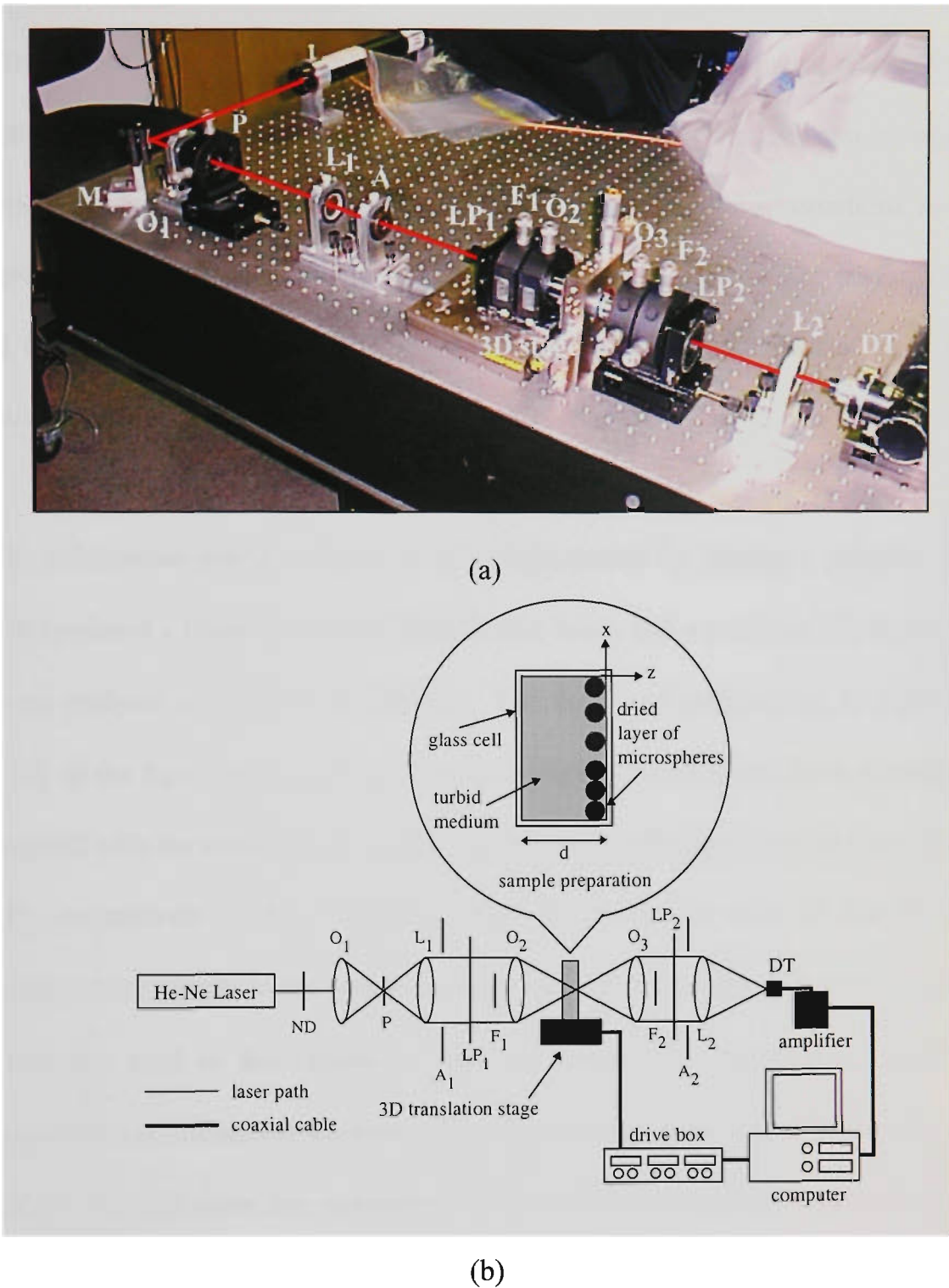


Figure 4.3: Experimental transmission scanning optical microscope with angle-gating and polarisation-gating mechanisms. (a) Photograph of the physical system; (b) Schematic diagram of the system. A: aperture; DT: detector; F: central obstruction; L: lens; LP: polariser; ND: neutral density filter; O: objective; P: pinhole.

Annular objectives were achieved by placing coaxially opaque circular disc obstructions  $F_1$  and  $F_2$  in the illumination and detection beam paths, respectively. Extreme care should be taken when the focal position of the imaging and collection objectives is overlapped and when the position of the central obstructions in the aperture of the illumination and collection objectives is aligned. The performance of the angle-gating mechanism depends on the successful alignment of these two parameters.

The polarisation-gating mechanism was implemented by placing a polariser  $LP_1$  that produced a linearly polarised illumination beam, and a polariser  $LP_2$  that acted as an analyser in front of the detector. The degree of polarisation,  $\gamma$ , (equation 3.39) of the light passing through a turbid sample was measured from the signals detected with the analyser  $LP_2$  parallel ( $I_p$ ) and perpendicular ( $I_s$ ) to the direction of  $LP_1$ , respectively. The polarisation intensity ratio, the ratio of the parallel polarisation intensity to the perpendicular polarisation intensity,  $I_p/I_s$ , (where  $I_p/I_s \geq 1$ ) is also used in this chapter to help demonstrate the contribution made by unscattered and scattered photons. Therefore a large polarisation intensity ratio,  $I_p/I_s$ , is desirable since this represents the situation when more unscattered photons are collected than scattered photons.

Sample number	Scattering medium	Cell thickness, $d$ ( $\mu\text{m}$ )	smfp length, $l_s$ ( $\mu\text{m}$ )	Anisotropy value, $g$	Optical thickness, $n$ ( $d/l_s$ )
1	distilled water	100	-	-	-
2	0.107 $\mu\text{m}$ polysty. microsph. in water	120	416.4 <sup>a</sup>	0.076 <sup>a</sup>	0.3
3	0.202 $\mu\text{m}$ polysty. microsph. in water	120	70.2 <sup>a</sup>	0.31 <sup>a</sup>	1.7
4	0.48 $\mu\text{m}$ polysty. microsph. in water	100	19.2 <sup>a</sup>	0.81 <sup>a</sup>	5.2
5	0.48 $\mu\text{m}$ polysty. microsph. in water	120	19.2 <sup>a</sup>	0.81 <sup>a</sup>	6.3
6	semi-skimmed milk	100	30 <sup>b</sup>	< 0.4 <sup>c</sup>	3.3
7	semi-skimmed milk	300	30 <sup>b</sup>	< 0.4 <sup>c</sup>	10

Table 4.1: Parameters for the samples used in the transmission optical microscope. (a) The parameters were determined by Mie theory (section 3.2); (b) The parameters were experimentally determined; and (c) The parameters were determined from the literature (Jensen, 1995).

#### 4.3.1.2 Sample preparation

Seven turbid samples were prepared and their details are summarised in table 4.1. Each sample was placed in an individual glass cell with lateral dimensions of 2 cm  $\times$  1 cm. The geometric thickness of the glass cell,  $d$ , was varied for the different samples. The optical thickness,  $n$ , (i.e. the average number of scattering events

experienced by a given photon) is given by,  $d/l_s$ , for a transmission system, where  $l_s$  is the scattering-mean-free-path (smfp) length (refer to equation 3.11). Sample1 consisted of distilled water and was used to determine the behaviour of the transmission imaging system without scatterers. Sample2, sample3, sample4 and sample5 consisted of polystyrene microspheres suspended in water (refer to table 3.1, for detailed calculations of the scattering parameters for the microspheres), while sample6 and sample7 consisted of standard semi-skimmed milk (fat content 3.6%). Semi-skimmed milk was chosen since it does not include large scatterers ( $> 1 \mu\text{m}$ ), and has been used by Morgan *et al.* (1997) and, Wabnitz and Rinneberg (1997) in transillumination imaging to simulate tissues which do not include large scatterers ( $> 1 \mu\text{m}$ ).

These samples were chosen so that the performance of the angle-gating mechanism can be experimentally investigated in the regimes when scattering is weak and strong.

The diameter of the scattering particles in the milk suspension was assumed to be in the range of  $0.1 - 1.0 \mu\text{m}$ , and the anisotropy value was assumed from the reference by Jensen (1995). The scattering-mean-free-path length,  $l_s$ , for the semi-skimmed milk was experimentally determined with the experimental arrangement shown in figure 4.4 in conjunction with Beers' law (refer to equation 3.13). Rearranging equation 3.13 yields

$$l_s = \frac{-d}{\ln\left(\frac{N(d)}{N(0)}\right)} \quad (4.1)$$

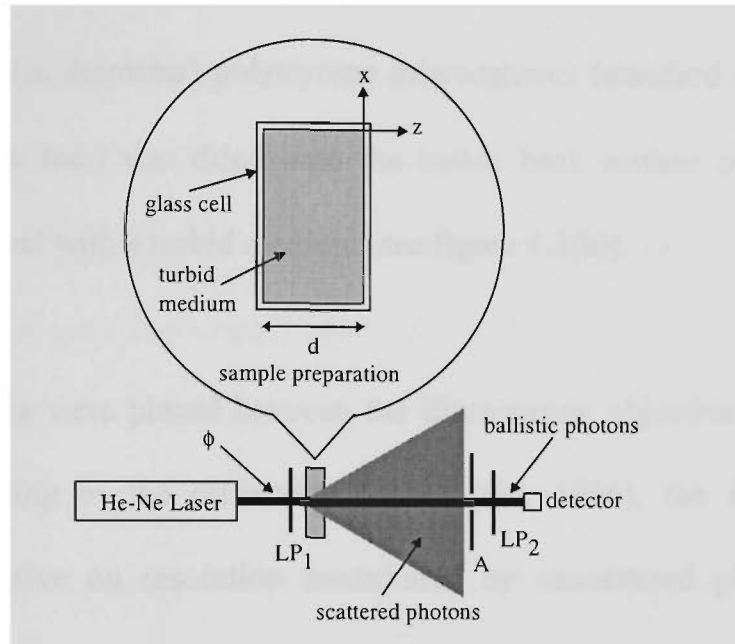


Figure 4.4: Optical system to determine the scattering-mean-free-path length,  $l_s$ , for semi-skimmed milk.  $\phi$ : incident and collection beam diameters; A: aperture; LP: polarisers.

Therefore as long as the incident power, which is proportional to  $N(0)$ , and the turbid medium thickness,  $d$ , are known, the scattering-mean-free-path length,  $l_s$ , can be determined by measuring the transmitted unscattered light intensity, which is proportional to  $N(d)$ , passing through a given turbid medium. The measurement of the transmitted unscattered light intensity was done in the far field region (approximately 1 m away from the turbid sample) to minimise the detection of scattered photons. An aperture in conjunction with a polarisation-gating mechanism was employed in front of the detector to assist in minimising the contribution made by scattered photons, since scattered photons are depolarised

and statistically travel along a different direction from unscattered photons (refer to section 2.3.3).

For evaluating image quality when polarised annular objectives were used a cluster layer of 22  $\mu\text{m}$  (in diameter) polystyrene microspheres (standard deviation 2.593  $\mu\text{m}$ , PolyScience Inc.) was dried onto the inside back surface of the glass cell before it was filled with a turbid medium (see figure 4.3(b)).

The turbid media were placed between the illumination objective and the object because, according to the diffraction theory (Gu, 1996), the function of the collection objective on resolution contributed by unscattered photons may be degraded due to the use of a large area detector. However, the collection objective plays an important role in suppressing diffusing photons.

Prepared samples were mounted on a three-dimensional piezoelectric translation stage (x-y scan directions: Melles Griot NanoFlex™ stage; z scan direction: Melles Griot PowerFlex™ stage) and then placed in the overlapping focal region of the two objectives  $O_2$  and  $O_3$ . The translation stages were controlled via software written in LabVIEW™ 4.1 through a piezoelectric controller with feedback (Melles Griot model No. 17PCZ003). The piezoelectric stages provided 200  $\mu\text{m}$  of traversal with 50 nm and 100 nm resolution in the x-y and z directions, respectively. The overlapping focus of the two objectives  $O_2$  and  $O_3$  was equally spaced in the centre of a turbid sample for the measurements of the degree of polarisation,  $\gamma$ .

The degree of polarisation,  $\gamma$ , for sample1 was measured to be 99.9% for circular imaging objectives ( $\varepsilon = 0$ ), which shows that depolarisation caused by the objectives and other components in this experimental arrangement can be ignored.

### 4.3.2 Effect of annular illumination and collection objectives

#### 4.3.2.1 Effect of an annular illumination objective

In this section only sample4 and sample7 were used, since these two samples can demonstrate the effect of an annular illumination objective when optical scattering is weak and strong (see table 4.1).

The degree of polarisation,  $\gamma$ , with circular illumination and collection ( $\varepsilon_{in} = \varepsilon_{out} = 0$ ) objectives was measured to be 0.574 and 0.118 for sample4 and sample7, respectively. This measurement demonstrates the depolarisation of the incident beam due to the scatterers in the turbid media. Measurements of the degree of polarisation,  $\gamma$ , were then obtained for different central obstruction sizes,  $\varepsilon_{in}$ , placed in the illumination beam path ( $F_1$ ).

Figure 4.5(a) shows the effect of the central obstruction size of the illumination objective,  $\varepsilon_{in}$ , on the degree of polarisation,  $\gamma$ , when a circular collection objective ( $\varepsilon_{out} = 0$ ), were employed for sample4 and sample7. Figure 4.5(b) illustrates the polarisation intensity ratio,  $I_p/I_s$ , for the collected signals under the same conditions. It is seen that as the illumination central obstruction size,  $\varepsilon_{in}$ , increases

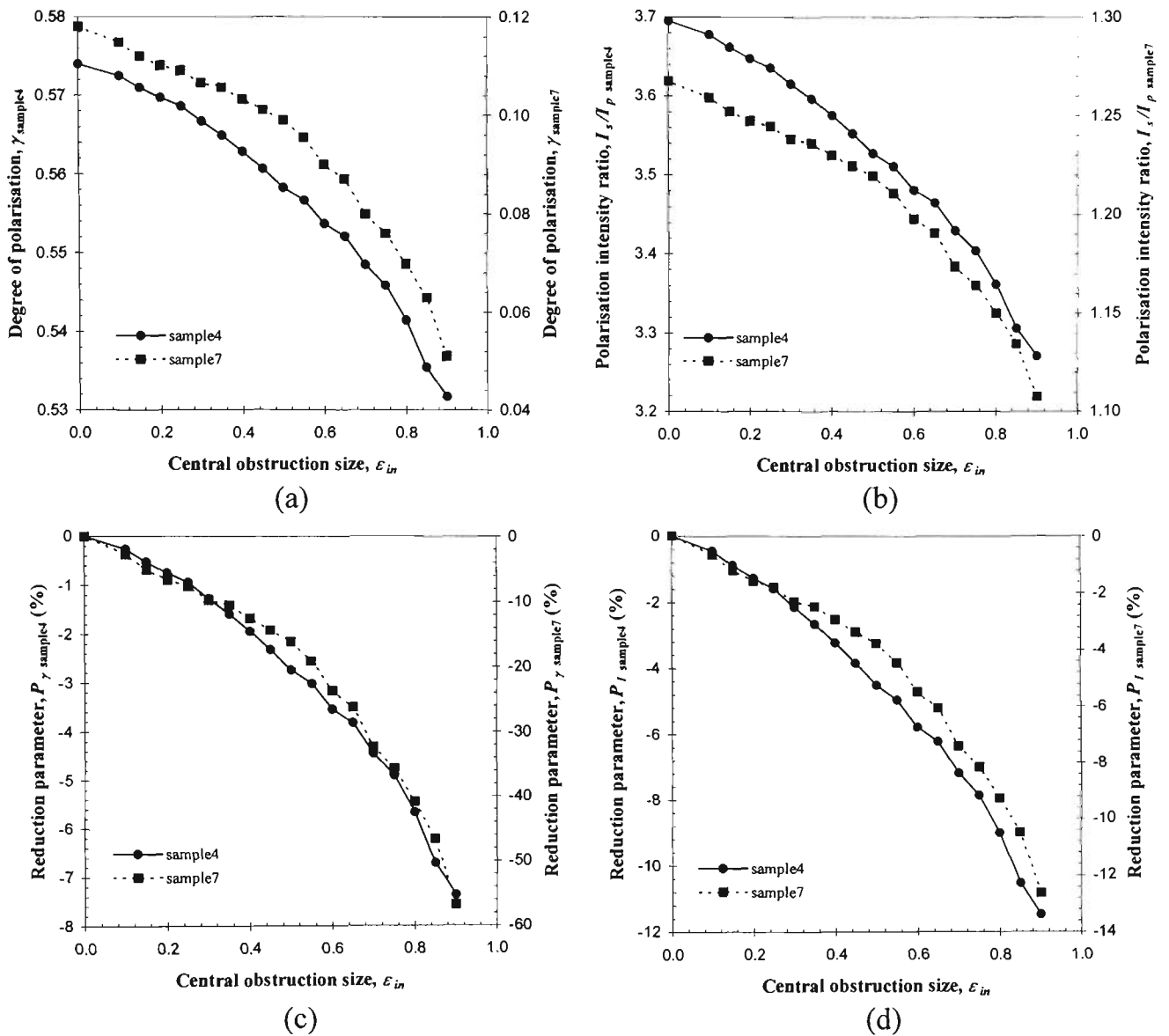


Figure 4.5: Dependence of the degree of polarisation,  $\gamma$  (a), the polarisation intensity ratio,  $I_p/I_s$  (b), and the percentage reduction parameters,  $P_\gamma$  (c) and  $P_I$  (d) on the radius of the central obstruction of the illumination objective,  $\epsilon_{in}$ . The numerical aperture for objectives O<sub>2</sub> and O<sub>3</sub> is 0.6.

from 0 to 0.9, the degree of polarisation,  $\gamma$ , decreases from 0.574 (or  $I_p/I_s = 3.7$ ) to 0.532 (or  $I_p/I_s = 3.3$ ) and from 0.118 (or  $I_p/I_s = 1.3$ ) to 0.051 (or  $I_p/I_s = 1.1$ ) for sample4 and sample7, respectively.

To further help demonstrate the performance of the illumination central obstruction size,  $\varepsilon_{in}$ , on the suppression of scattered photons the following two percentage improvement/reduction parameters were defined

$$P_\gamma = \frac{\gamma_{\varepsilon_{in}} - \gamma_{\varepsilon_{in}=0}}{\gamma_{\varepsilon_{in}=0}} \quad (4.2)$$

and

$$P_I = \frac{\left. \frac{I_p}{I_s} \right|_{\varepsilon_{in}} - \left. \frac{I_p}{I_s} \right|_{\varepsilon_{in}=0}}{\left. \frac{I_p}{I_s} \right|_{\varepsilon_{in}=0}}, \quad (4.3)$$

where  $P_\gamma$  demonstrates the change in the degree of polarisation,  $\gamma$ , and  $P_I$  demonstrates the change in the polarisation intensity ratio,  $I_p/I_s$ .

The parameters  $P_\gamma$  and  $P_I$  as a function of the illumination central obstruction size,  $\varepsilon_{in}$ , for sample4 and sample7 are shown in figures 4.5(c) and 4.5(d), respectively. It is seen that as the illumination central obstruction size,  $\varepsilon_{in}$ , increases from 0 to 0.9,  $P_\gamma$  and  $P_I$  decrease by approximately 7% and 11%, respectively for sample4, while for sample7 the decrease in  $P_\gamma$  and  $P_I$  is approximately 57% and 13%, respectively. This behaviour is because the input annular confines the illumination photons into a high angle region. Incident photons travelling at higher angles through the turbid

samples experience on average more scattering events, leading to a stronger depolarisation effect which is indicated by the lower polarisation intensity ratio,  $I_p/I_s$ , when the illumination central obstruction size,  $\varepsilon_{in}$ , approaches unity (figure 4.5(b)). Since the collection objective collects all the available unscattered and scattered photons within its aperture, scattered photons cannot be further selectively suppressed. Thus the degree of polarisation,  $\gamma$ , and the polarisation intensity ratio,  $I_p/I_s$ , inevitably decrease.

#### 4.3.2.2 Effect of an annular collection objective

This section demonstrates the performance of the central obstruction sizes,  $\varepsilon_{out}$ , placed in the collection beam path ( $F_2$ ), on the degree of polarisation,  $\gamma$ , for fixed values of the central obstruction size,  $\varepsilon_{in}$ , placed in the illumination beam path ( $F_1$ ). Only sample4 is used in this section, since a single turbid sample can demonstrate the effect of the annular collection objective on suppressing scattered photons.

Figure 4.6(a) shows the dependence of the degree of polarisation,  $\gamma$ , on the collection central obstruction size,  $\varepsilon_{out}$ , (used to suppress the scattered photons) when the central obstruction size,  $\varepsilon_{in}$ , of the illumination objective is given, while figure 4.6(b) illustrates the polarisation intensity ratio,  $I_p/I_s$ , for the collected signal.

To help demonstrate the performance of the collection central obstruction size,  $\varepsilon_{out}$ , on the suppression of scattered photons the following two percentage improvement/reduction parameters were defined

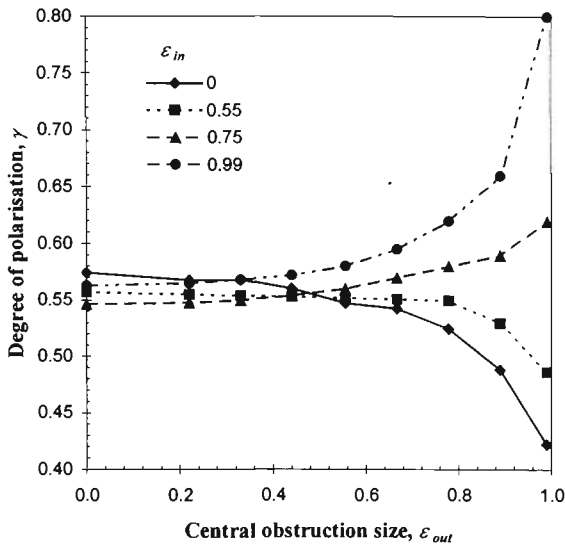
$$P_\gamma = \frac{\gamma_{\varepsilon_{out}, \varepsilon_{in}} - \gamma_{\varepsilon_{out}=0, \varepsilon_{in}}}{\gamma_{\varepsilon_{out}=0, \varepsilon_{in}}}, \quad (4.4)$$

and

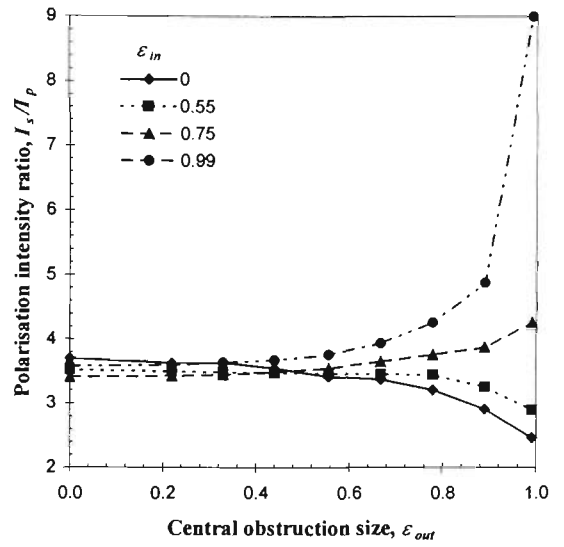
$$P_I = \frac{\left. \frac{I_p}{I_s} \right|_{\varepsilon_{out}, \varepsilon_{in}} - \left. \frac{I_p}{I_s} \right|_{\varepsilon_{out}=0, \varepsilon_{in}}}{\left. \frac{I_p}{I_s} \right|_{\varepsilon_{out}=0, \varepsilon_{in}}}. \quad (4.5)$$

The parameters  $P_\gamma$  and  $P_I$  are plotted in figures 4.6(c) and 4.6(d) for the four cases, respectively.

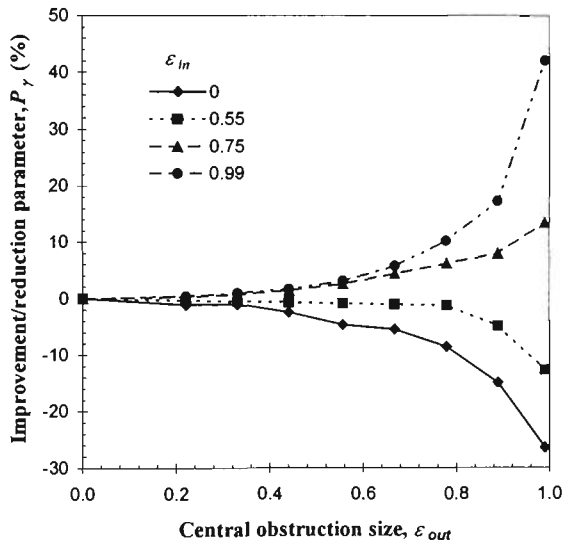
When an annular illumination objective of  $\varepsilon_{in} < 0.75$  is employed there is not enough discrimination of the scattered photons even for a collection central obstruction size,  $\varepsilon_{out}$ , approaching unity. This feature can be further seen from the decreasing values of  $P_\gamma$  and  $P_I$  (i.e. higher contribution of scattered photons) in figures 4.6(c) and 4.6(d), respectively. It can be clearly seen from figure 4.6 that a significant improvement in the degree of polarisation,  $\gamma$ , is made only when both central obstruction sizes,  $\varepsilon_{in}$  and  $\varepsilon_{out}$  are greater than 0.75. For a collection central obstruction size,  $\varepsilon_{out}$ , equal to 0.99 the improvement in the degree of polarisation,  $\gamma$ , is 0.074 (or  $P_\gamma \approx 14\%$ ) and 0.237 (or  $P_\gamma \approx 42\%$ ) when an annular objective with central obstruction size,  $\varepsilon_{in}$ , equal to 0.75 and 0.99, respectively, is used. The improvement in the polarisation intensity ratio,  $I_p/I_s$ , for the same conditions is 0.85 (or  $P_I \approx 25\%$ ) and 5.43 (or  $P_I \approx 152\%$ ), respectively. This result suggests that a pair of annular objectives with a large central obstruction (i.e.  $\varepsilon \rightarrow 1$ ) should be used to efficiently suppress diffusing photons.



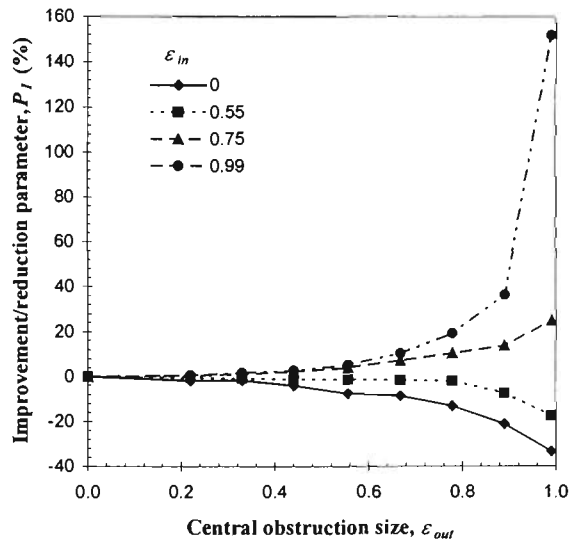
(a)



(b)



(c)



(d)

Figure 4.6: Dependence of the degree of polarisation,  $\gamma$  (a), the polarisation intensity ratio,  $I_p/I_s$  (b), and the percentage improvement/reduction parameters,  $P_\gamma$  (c) and  $P_I$  (d) on the radius of the central obstruction of the collection objective,  $\epsilon_{out}$ , when the central obstruction,  $\epsilon_{in}$ , of the illumination objective is given. The numerical aperture for objective O<sub>2</sub> and O<sub>3</sub> is 0.6.

## 4.3.2.3 Effect of identical annular illumination and collection objectives

This section demonstrates the performance of two equal central obstruction sizes ( $\varepsilon_{in} = \varepsilon_{out} = \varepsilon$ ) placed in the illumination beam path ( $F_1$ ) and collection beam path ( $F_2$ ). In this section sample2, sample3, sample4 and sample7 were used. These four samples were chosen to demonstrate the effect of the angle-gating mechanism on suppression of scattered photons for turbid media with different scattering characteristics.

The dependence of the degree of polarisation,  $\gamma$ , on the central obstruction size,  $\varepsilon$ , for a matching pair of annular objectives is shown in figure 4.7(a), while figure 4.7(b) illustrates the polarisation intensity ratio,  $I_p/I_s$ , for the collected signal.

The following two percentage improvement/reduction parameters were defined to help demonstrate the performance of the central obstruction size,  $\varepsilon$ , on the suppression of scattered photons

$$P_\gamma = \frac{\gamma_\varepsilon - \gamma_{\varepsilon=0}}{\gamma_{\varepsilon=0}}, \quad (4.6)$$

and

$$P_I = \frac{\left. \frac{I_p}{I_s} \right|_\varepsilon - \left. \frac{I_p}{I_s} \right|_{\varepsilon=0}}{\left. \frac{I_p}{I_s} \right|_{\varepsilon=0}}. \quad (4.7)$$

The parameters  $P_\gamma$  and  $P_I$  are plotted in figures 4.7(c) and 4.7(d) for the four samples, respectively.

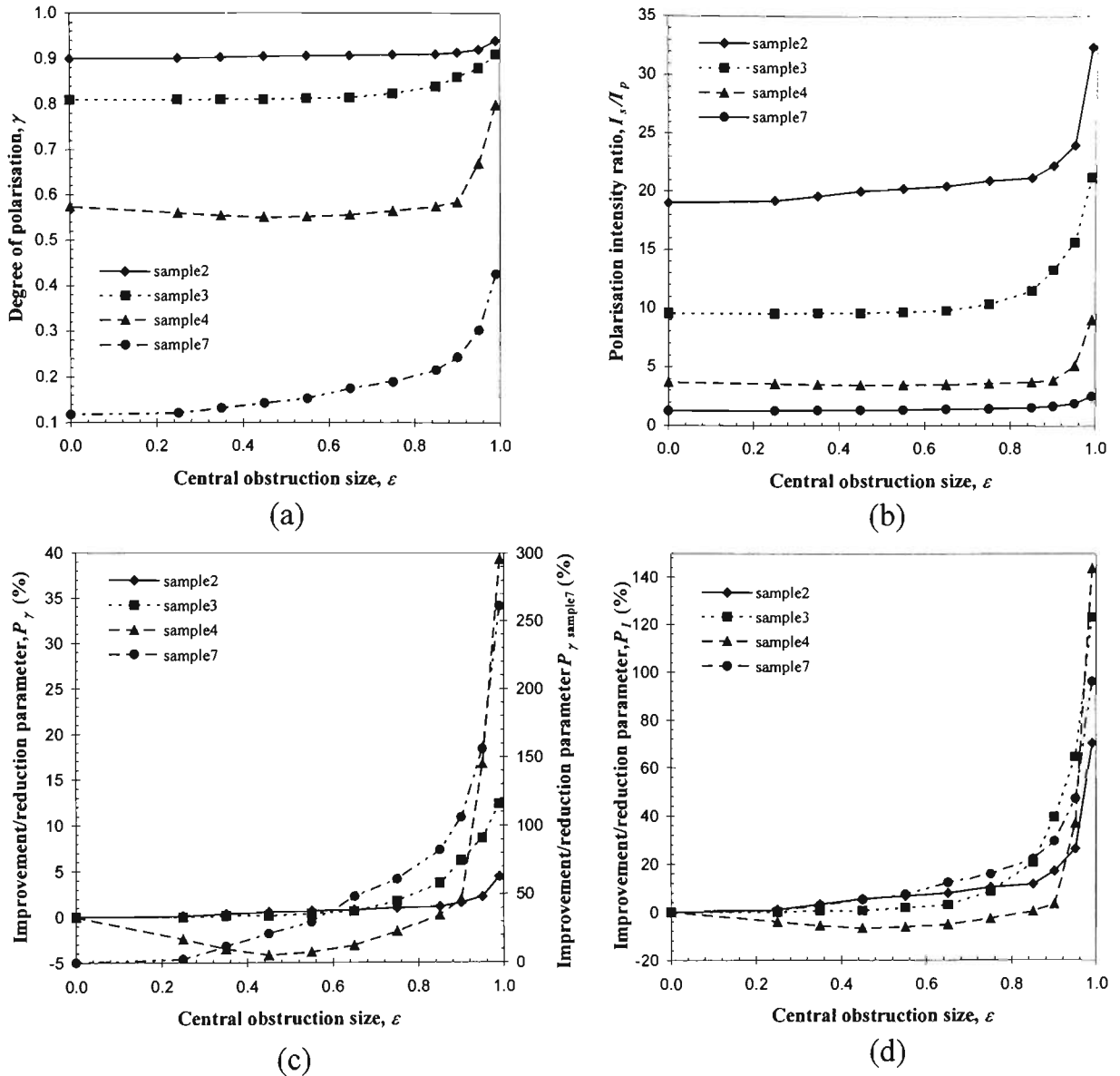


Figure 4.7: Dependence of the degree of polarisation,  $\gamma$  (a), the polarisation intensity ratio,  $I_p/I_s$  (b), and the percentage improvement/reduction parameters,  $P_\gamma$  (c) and  $P_I$  (d) on the radius of the central obstruction of a matching pair of annular objectives,  $\epsilon$ . The numerical aperture for objectives  $O_2$  and  $O_3$  is 0.6.

The measured degree of polarisation,  $\gamma$ , for the four samples was 0.9 (or  $I_p/I_s = 19$ ), 0.81 (or  $I_p/I_s = 9.5$ ), 0.574 (or  $I_p/I_s = 3.7$ ) and 0.118 (or  $I_p/I_s = 1.3$ ), respectively, when circular objectives ( $\varepsilon = 0$ ) were used. The lower degree of polarisation,  $\gamma$ , for sample4 and sample7 results from the fact that the scattering effect is much stronger than that for samples2 and sample3 (see table 4.1).

It is clearly seen from figure 4.6(a) that the degree of polarisation,  $\gamma$ , increases appreciably when the central obstruction size,  $\varepsilon$ , changes from zero to unity. The difference of the degree of polarisation,  $\gamma$ , between the matching pair of circular objectives ( $\varepsilon = 0$ ) and the matching pair of annular objectives ( $\varepsilon \approx 0.99$ ) was 0.04 (or  $P_\gamma \approx 4\%$ ), 0.1 (or  $P_\gamma \approx 12\%$ ), 0.226 (or  $P_\gamma \approx 39\%$ ) and 0.308 (or  $P_\gamma \approx 261\%$ ) for sample2, sample3, sample4 and sample7, respectively. The corresponding improvement in the polarisation intensity ratio,  $I_p/I_s$  is 13.3 (or  $P_I \approx 70\%$ ), 11.7 (or  $P_I \approx 123\%$ ), 5.3 (or  $P_I \approx 144\%$ ) and 1.2 (or  $P_I \approx 96\%$ ) for sample2, sample3, sample4 and sample7, respectively. This result clearly shows that if two thin polarising annular objectives are used diffusing photons can be efficiently suppressed and that the effect of the polarising annular objectives on the suppression becomes more significant when the optical thickness,  $n$ , becomes larger and depolarisation is stronger. The degree of polarisation,  $\gamma$ , increases quickly when the central obstruction size,  $\varepsilon$ , is greater than 0.9, which implies that the improvement in image quality becomes significant in this region. Although an annular objective with the central obstruction size,  $\varepsilon$ , close to unity allows higher suppression of scattered photons, such a large central obstruction size,  $\varepsilon$ , reduces the amount of detectable photons appreciably. Therefore, a trade-off value of the

central obstruction size,  $\varepsilon$ , exists between the signal-to-noise ratio of an image and the ability to suppress scattered photons (i.e. resolution achievable).

The reason for the decreased degree of polarisation,  $\gamma$ , near  $\varepsilon = 0.4$  for sample4 will be discussed in section 4.3.5.

### 4.3.3 Effect of the numerical aperture of the matching objectives

In microscopic imaging the goal is to obtain high resolution. To achieve this one needs to employ a high numerical aperture objective. But there is an inherent problem when a high numerical aperture objective is used to image through a turbid medium. Photons propagating at higher angles in such an objective result in longer path lengths that photons traverse, which effectively increases the average number of scattering events experienced by the photons. Therefore the number of photons maintaining their initial degree of polarisation can be reduced.

The effect of reducing the illumination and collection apertures  $A_1$  and  $A_2$  (see figure 4.3(b)) is shown in figure 4.8. Firstly, reducing the beam diameter of the objective lenses reduces the effective numerical aperture of the objective. Secondly it reduces the angular distribution of illumination and collected photons. In this section only sample4 and sample7 were used.

It is clearly seen from figure 4.8(a) that the degree of polarisation,  $\gamma$ , increases appreciably for both samples when the numerical aperture is decreased, while figure 4.8(b) illustrates the polarisation intensity ratio,  $I_p/I_s$ , for the collected signal.

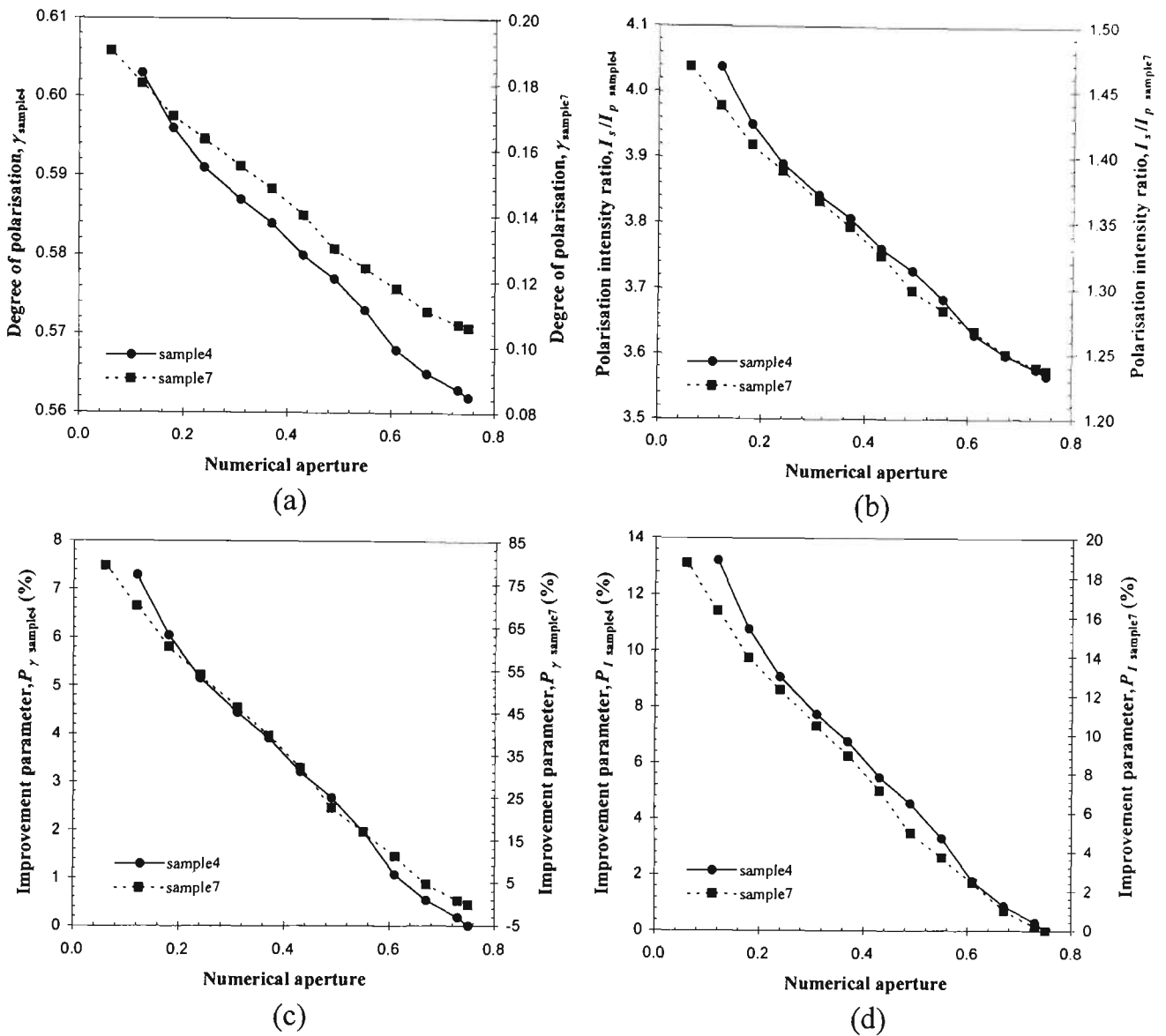


Figure 4.8: Dependence of the degree of polarisation,  $\gamma$  (a), the polarisation intensity ratio,  $I_p/I_s$  (b), and the percentage improvement/reduction parameters,  $P_\gamma$  (c) and  $P_I$  (d) on the numerical aperture of the matched illumination and collection objectives.

The following two percentage improvement parameters were defined to help demonstrate the performance of the numerical aperture (NA) on the suppression of scattered photons

$$P_\gamma = \frac{\gamma_{NA} - \gamma_{NA=0.75}}{\gamma_{NA=0.75}}, \quad (4.8)$$

and

$$P_I = \frac{\left. \frac{I_p}{I_s} \right|_{NA} - \left. \frac{I_p}{I_s} \right|_{NA=0.75}}{\left. \frac{I_p}{I_s} \right|_{NA=0.75}}. \quad (4.9)$$

The parameters  $P_\gamma$  and  $P_I$  are plotted in figures 4.8(c) and 4.8(d) for the two samples, respectively.

The difference in the degree of polarisation,  $\gamma$ , between  $NA = 0.75$  and  $NA = 0.12$  was 0.041 (or  $P_\gamma \approx 7\%$ ) and 0.074 (or  $P_\gamma \approx 70\%$ ) for sample4 and sample7, respectively. For the same conditions the improvement in the polarisation intensity ratio,  $I_p/I_s$  is 0.472 (or  $P_I \approx 13\%$ ) and 0.202 (or  $P_I \approx 16\%$ ) for sample4 and sample7, respectively. The improvement in  $P_\gamma$  and  $P_I$  is due to the suppression of the higher angle photons by reducing the numerical aperture of the objectives. Therefore a trade-off numerical aperture exists between resolution and the ability to efficiently suppress the diffusing photons (i.e. a high degree of polarisation,  $\gamma$ ).

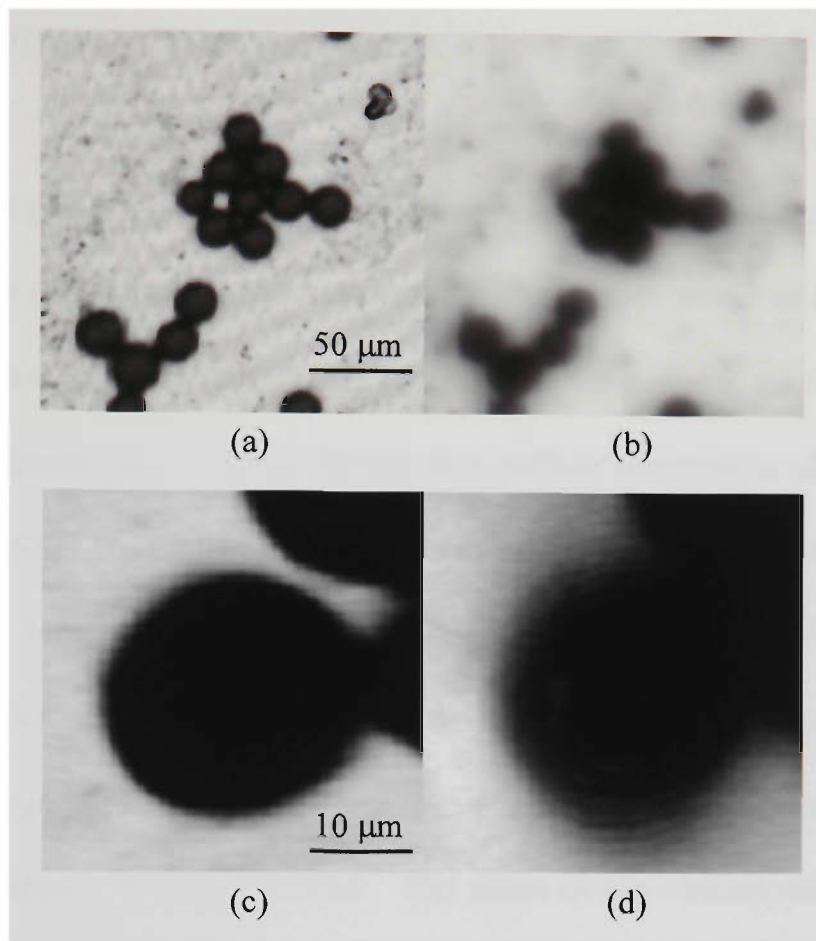


Figure 4.9: Images of a 22  $\mu\text{m}$  polystyrene microspheres embedded within sample1. (a) and (c): circular objectives ( $\varepsilon = 0$ ) with parallel polarisers; (b) and (d): annular objectives ( $\varepsilon \approx 0.93$ ) with parallel polarisers. The intensity of the images was normalised to unity.

#### 4.3.4 Imaging with circular and annular objectives

For a better suppression effect as suggested by figure 4.8, the numerical aperture of the illumination and collection objectives chosen for all imaging (figures 4.9 - 4.13) was 0.25. It should be noted that the detectable signal severely decreases as the central obstruction size,  $\varepsilon$ , approaches unity. An annular objective with  $\varepsilon \approx 0.93$  was therefore chosen to perform all imaging since this annular objective has a

good suppression ability and a high signal-to-noise ratio (the detectable light level is significantly above the noise level of the detector used).

The incident power from the laser was attenuated with the use of a variable neutral density filter (see figure 4.3(b)) such that the illumination power at the focus for a pair of circular objectives ( $\varepsilon = 0$ ) was equivalent to the power at the focus for a pair of annular objectives ( $\varepsilon \approx 0.93$ ). In this way, a direct comparison of the signal-to-noise ratio (SNR is quantified by the ratio of peak-to-peak signal level to peak-to-peak noise level) can be obtained when circular or annular objectives are employed. As a result, the power at the focus was approximately 110  $\mu\text{W}$ . Polarisation-gating was achieved when the polariser  $\text{LP}_1$  and analyser  $\text{LP}_2$  have the same orientation (see figure 4.3(b)). The plane of the overlapped focus for all imaging (unless otherwise stated) was on the surface of the dried bead layer on the turbid medium side. Images were obtained by raster scanning a sample with the aid of a computer.

Figure 4.9 demonstrates the image quality when a dried cluster layer of the 22  $\mu\text{m}$  microspheres embedded within sample1 (see table 4.1) was imaged with two polarising circular objectives (figure 4.9(a) and 4.9(c)) and two polarising annular objectives (figure 4.9(b) and 4.9(d)). Figures 4.9(c) and 4.9(d) have a reduced field of view of figure 4.9(a) and 4.9(b) to demonstrate the image quality for a single 22  $\mu\text{m}$  microsphere. Since an annular objective has a large depth of focus (Gu, 1996), the image formed with annular objectives appears slightly blurred due to the more contribution from the out-of-focus information (figures 4.9(b) and 4.9(d)) when

compared with the images formed with circular objectives (figures 4.9(a) and 4.9(c)). Since the dried microsphere layer is not uniformly dried on the glass surface the microsphere diameter in the case of circular objectives is dependent on the displacement of the focal position relative to the microsphere surface (figure 4.9(a)). In the case of annular objectives (figure 4.9(b)) the imaged microspheres have approximately the same diameter due to the large depth of focus. All images in figure 4.9 are formed by unscattered photons obeying the diffraction theory of light (Wilson and Sheppard, 1984). Therefore blurring caused by diffraction can become more pronounced as the central obstruction size,  $\varepsilon$ , for an annular objective is increased in imaging without turbid media. Image contrast in both cases appears black within the shadow of the microsphere, as may be expected from the diffraction by a spherical microsphere.

To demonstrate the effect of turbid media on image quality, sample4 (see table 4.1) including a cluster layer of 22  $\mu\text{m}$  beads was imaged with circular ( $\varepsilon = 0$ ) and annular ( $\varepsilon \approx 0.93$ ) objectives. Figure 4.10 shows the images recorded at different focal depths in the sample. It is seen that for circular objectives (figures 4.10(a) and 4.10(b)) there is an inversion of image contrast, which is indicated by the white areas in the centre of the microspheres. This inverted contrast can lead to an incorrect interpretation of the information in the image. It is also seen that the image contrast drops dramatically as the focal position moves away from the layer of dried microspheres. In contrast to the case of circular objectives the images obtained by annular objectives (figures 4.10(d), 4.10(e) and 4.10(f)) show the

correct contrast and the ability to image the dried microsphere layer even when the focal position is shifted to  $40\ \mu\text{m}$  above the surface of the dried microsphere layer.

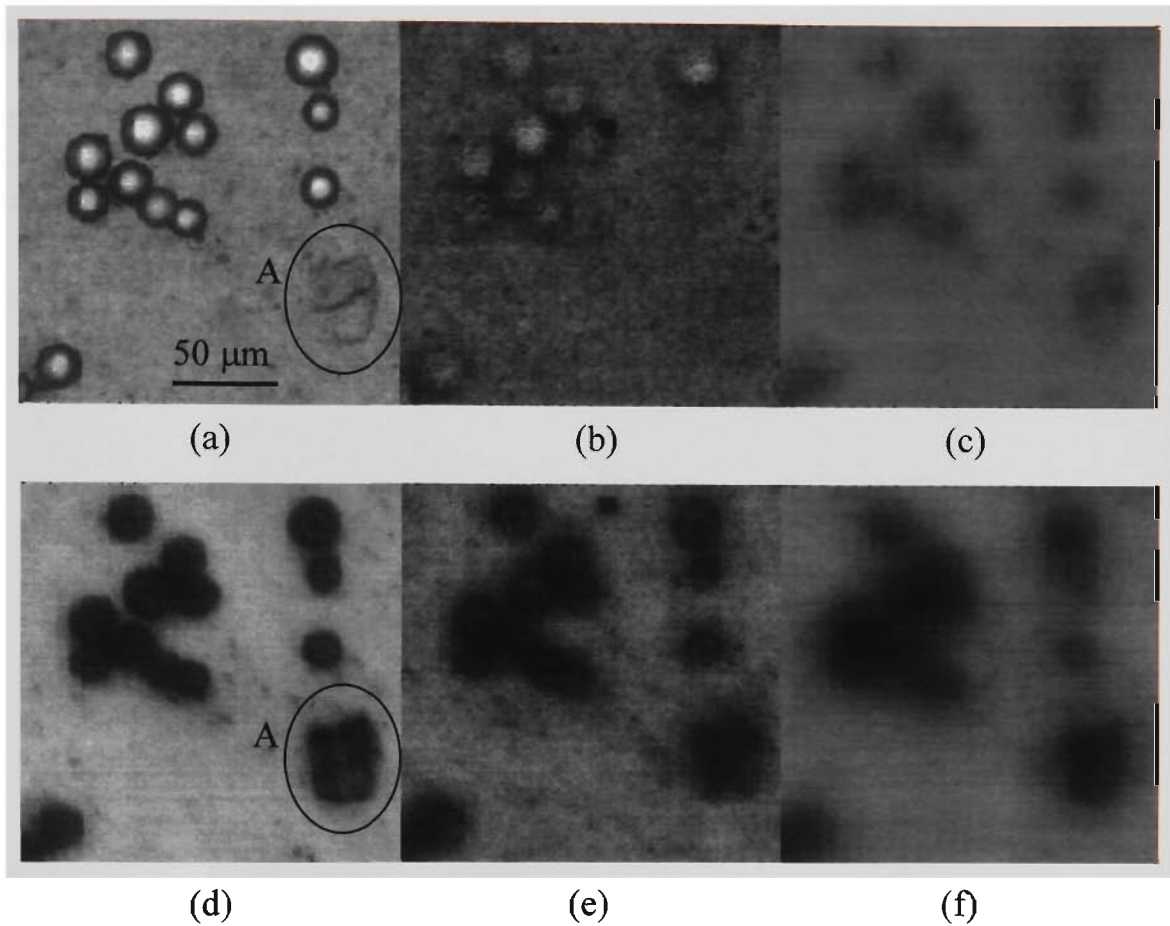


Figure 4.10: Images of a  $22\ \mu\text{m}$  polystyrene microsphere cluster embedded within sample4. (a), (b) and (c): circular objectives ( $\varepsilon = 0$ ) with parallel polarisation; (d), (e) and (f): annular objectives ( $\varepsilon \approx 0.93$ ) with parallel polarisation. In (a) and (d) the focus is on the dried cluster layer, in (b) and (e) the focus is shifted away from the cluster layer by approximately  $20\ \mu\text{m}$ , and in (c) and (f) the focus is shifted away from the dried cluster layer by approximately  $40\ \mu\text{m}$ . The intensity of the images was normalised to unity.

In addition the pair of annular objectives can enhance the contrast of embedded structures within the turbid media. This feature is indicated by the structure marked by 'A' in figure 4.10(d). This embedded structure has strong and equal contrast when imaged with annular objectives, whereas when the embedded structure is imaged with circular objectives (figure 4.10(a)) it is difficult to see due to poor contrast.

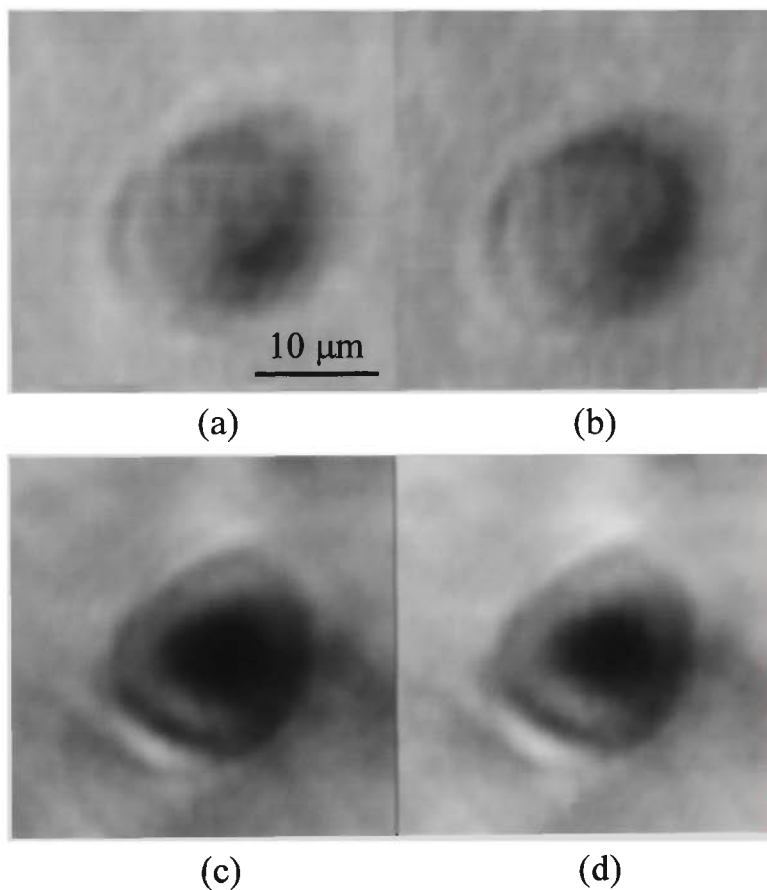


Figure 4.11: Images of a 22  $\mu\text{m}$  polystyrene microsphere embedded within sample5. (a) circular objectives ( $\varepsilon = 0$ ) without polarisers; (b) circular objectives ( $\varepsilon = 0$ ) with polarisers; (c) annular objectives ( $\varepsilon \approx 0.93$ ) without polarisers; (d) annular objectives ( $\varepsilon \approx 0.93$ ) with polarisers. The intensity of the images was normalised to unity.

Figure 4.11 shows images of one 22  $\mu\text{m}$  microsphere embedded in an optically thicker turbid medium (sample5) under different experimental conditions. In figure 4.11(a) two circular objectives ( $\varepsilon = 0$ ) are used. Figure 4.11(b) displays the image when two parallel polarisers are included in the circular objectives ( $\varepsilon = 0$ ). It is seen that the introduction of the polarisers produces a slight improvement in image detail. Both figures 4.11(a) and 4.11(b) reveal a reversion of image contrast near the centre of the microsphere where a dark region should be displayed (see figure 4.9(c)), which as stated earlier may be misleading when the image is interpreted. Figure 4.11(c) shows the image obtained for two annular objectives ( $\varepsilon \approx 0.93$ ). It can be seen that the images recorded with annular objectives have higher resolution, which is indicated by the smaller microsphere size and reduced smearing. In addition the images recorded with annular objectives have a correct image contrast in the centre of the microsphere, resulting from the effective suppression of scattered photons. A further improvement in the image contrast near the surface of the microsphere can be seen in figure 4.11(d) when the parallel polarisers are included.

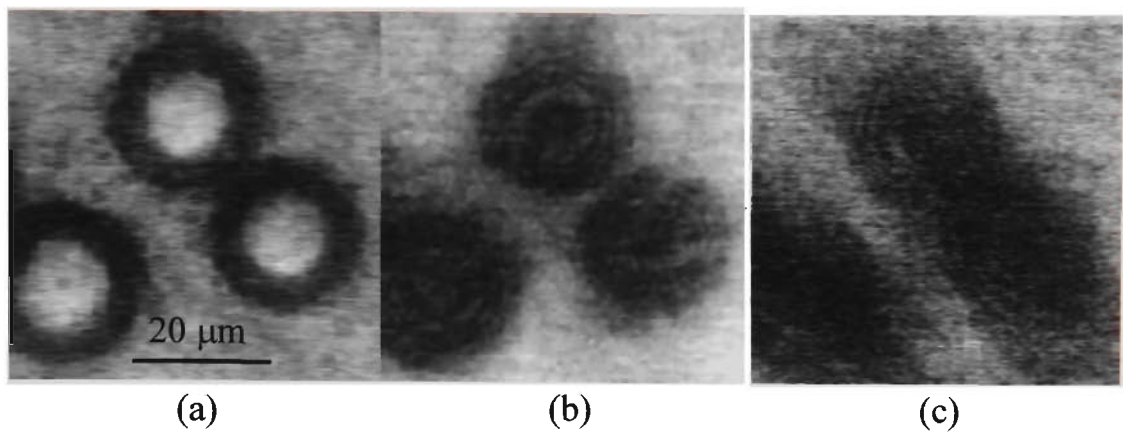


Figure 4.12: Images of 22  $\mu\text{m}$  polystyrene microspheres embedded in sample6. (a) circular objectives ( $\varepsilon = 0$ ) with parallel polarisation; (b) annular objectives ( $\varepsilon \approx 0.93$ ) with parallel polarisation; (c) annular objectives ( $\varepsilon \approx 0.93$ ) with perpendicular polarisation. The intensity of the images was normalised to unity.

The remainder of this section demonstrates the performance of polarising annular objectives on image quality for more realistic samples (i.e. sample6 and sample7, which have a large range of scattering sizes). Figure 4.12 shows the images of a dried cluster layer of microspheres embedded in sample6 recorded with circular (figure 4.12(a)) and annular (figures 4.12(b) and 4.12(c)) objectives. In the case of using circular objectives ( $\varepsilon = 0$ ) an inversion of the image contrast is present, which is indicated by the bright central regions. Figures 4.12(b) and 4.12(c) show the correct image contrast when annular objectives ( $\varepsilon \approx 0.93$ ) are used. It should be noted that figure 4.12(b) is obtained with a parallel analyser  $\text{LP}_2$  with respect to the polariser  $\text{LP}_1$ , (mainly unscattered photons are detected), while figure 4.12(c) is obtained with a perpendicular analyser with respect to  $\text{LP}_1$  (mainly scattered

photons are detected). It is evident that when scattered photons are used to construct an image the resolution drops substantially, which is indicated by the blurring and smearing effects seen in figure 4.12(c).

To demonstrate the ability of annular objectives to select unscattered light in a thick turbid medium, sample7 including the microsphere cluster layer was imaged with circular (figure 4.13(a)) and annular objectives (figure 4.13(b)). The images recorded with circular objectives ( $\varepsilon = 0$ ) again demonstrate an inversion of image contrast near the centre of the microsphere. In addition severe degradation in image quality is seen, as a result of the increased scattering experienced. Once again the correct image contrast is seen when the microsphere is imaged with annular objectives ( $\varepsilon \approx 0.93$ ). However the signal-to-noise ratio of the recorded image (figure 4.13(b)) is degraded due to the reduced number of available unscattered photons. The full-width-at-half-maximum of the imaged microsphere for the annular (figure 4.13(b)) and circular (figure 4.13(a)) objectives is approximately  $39.1 \pm 0.2 \mu\text{m}$  and  $41.8 \pm 0.2 \mu\text{m}$ , respectively. This result further confirms that annular objectives lead to increased resolution in imaging through thick turbid media due to the ability of suppression scattered photons.

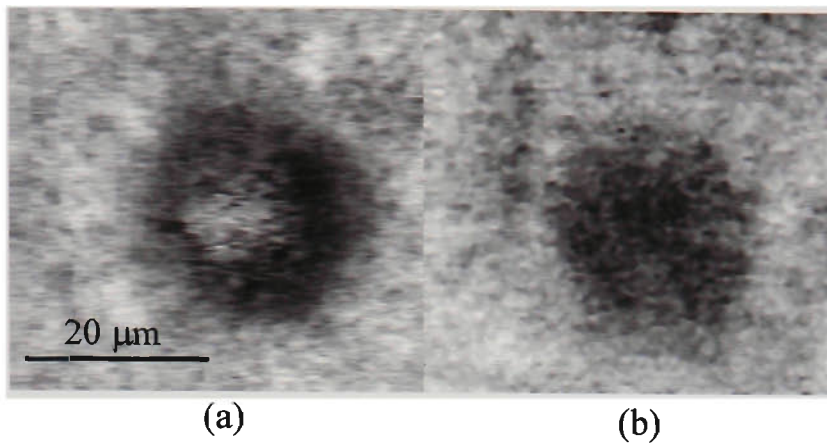


Figure 4.13: Images of a 22  $\mu\text{m}$  polystyrene microsphere embedded in sample 7. (a) circular objective ( $\varepsilon = 0$ ) with parallel polarisation; (b) annular objectives ( $\varepsilon \approx 0.93$ ) with parallel polarisation. The intensity of the images was normalised to unity.

In figures 4.10(a), 4.10(b), 4.12(a) and 4.13(a), the image contrast is inverted within the shadow of microspheres when circular objectives are used. A possible explanation of the contrast inversion is that scattered photons, which cannot be efficiently suppressed by circular objectives, can reach the shadow area of the microspheres thus contributing to a non-zero intensity in this region. These scattered photons are considerably suppressed if annular objectives are used, which gives enhanced and correct image contrast.

#### 4.3.5 Discussion

Although annular objectives achieve the correctly enhanced image contrast (figures 4.11(c), 4.11(d), 4.12(b), 4.12(c) and 4.13(b)), originating from the angle-gating mechanism outlined in section 4.2, there are a number of issues that need to be discussed regarding their performance as a gating mechanism.

#### 4.3.5.1 Diffraction effect

As was illustrated in section 3.3 the Monte-Carlo method, which is based on Mie theory and ignores the diffraction effect, can be mainly used to describe the behaviour of scattered photons in turbid media. That is, the Monte-Carlo model treats the propagation of unscattered photons by ray optics. In fact, the dominant propagation behaviour of unscattered photons in turbid media obeys the prediction by the diffraction theory of light based on Born's approximation (Born and Wolf, 1980) which neglects multiple scattering. These two processes, the multiple-scattering of scattered photons and the diffraction by unscattered photons, exist in imaging through turbid media simultaneously. Scattered photons contribute to an image with low resolution whereas unscattered photons give high resolution. In this section, a pair of annular objectives were used to suppress scattered photons, so that the contribution from unscattered photons is relatively increased with respect to scattered photons when annular objectives are used. As a result, the diffraction effect in the case of imaging in a turbid medium with two annular objectives should be more pronounced, compared with two circular objectives. This property is clearly demonstrated in figures 4.12(b) and 4.12(c) where more diffraction rings are observed.

Another diffraction property associated with an annular objective is that an annular objective can transfer more high transverse spatial frequencies than a circular objective (Wilson and Sheppard, 1984), which consequently leads to improved transverse resolution as observed in the experiments with annular objectives when the contribution from unscattered photons becomes dominant.

An annular objective possesses a weaker optical sectioning property than a circular objective in terms of the diffraction theory (Wilson and Sheppard, 1984). This property is important in achieving angle-gating for a thick object because a longer overlapping focus provided by a pair of annular objectives can efficiently transfer unscattered and less scattered photons from the illumination objective  $O_2$  to the collection objective  $O_3$ . This feature is clearly demonstrated in figure 4.13, in which circular objectives gives a stronger reversion of the image contrast than annular objectives. However, it should be noted that a longer focal depth is disadvantageous for three-dimensional imaging.

#### 4.3.5.2 Polarisation-gating

Employing an analyser with the polarisation direction perpendicular to that of the illumination beam actually suppresses unscattered photons. The resultant image (figure 4.12(c)), constructed mainly by scattered photons, shows low contrast and low resolution. This result confirms that scattered photons can build up an image only with low resolution (Gan *et al.*, 1998).

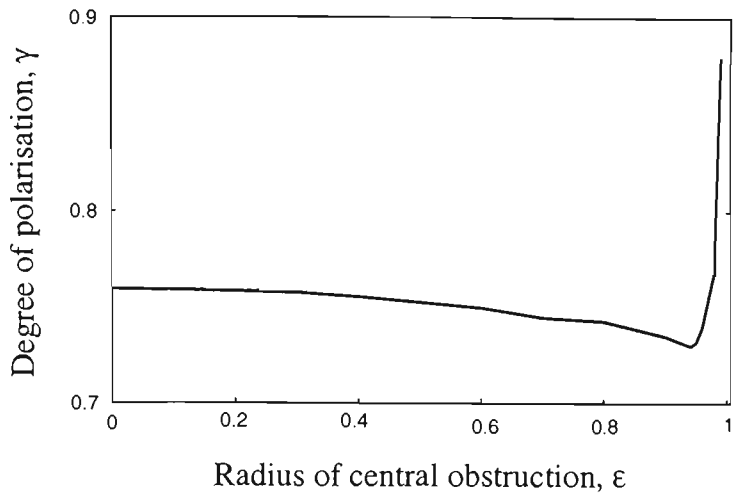
Figures 4.12(b) and 4.13(b) imply that this new method based on polarising annular gating can give tens-of-micrometer image resolution in this application.

The depolarisation of the scattered photons is dependent on the size of scattering particles in turbid media (Gan *et al.*, 1997). Under the condition of figure 4.12 the depolarisation is not so strong that the improvement caused by the polarisers is not significant. However, the image quality could be improved further if the image were constructed by the signal,  $I_p - I_s$ , called the differential polarisation signal (i.e.

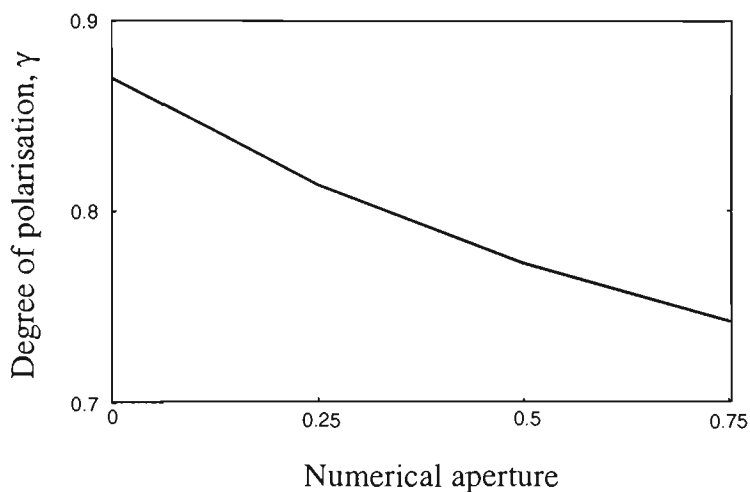
image in figure 4.12(c) is subtracted from the image in figure 4.12(b)). The differential polarisation-gating mechanism is the bases of the study in chapter 5.

#### 4.3.5.3 Theoretical comparison

In figure 4.7(a) sample4 shows that the degree of polarisation,  $\gamma$ , decreases first and then increases when the central obstruction size,  $\varepsilon$ , changes from 0 to 0.9. This phenomenon is caused by the competition between two processes occurring when the central obstruction size,  $\varepsilon$ , increases. The first process is that increasing the central obstruction size,  $\varepsilon_{in}$ , of the imaging objective results in more scattering events due to the longer propagation path of scattered photons and leads to a reduction of the degree of polarisation,  $\gamma$ , as shown in figure 4.5. On the other hand, when a pair of matching annular objectives with a central obstruction size,  $\varepsilon > 0.75$  are used, scattered photons can be suppressed and therefore the degree of polarisation,  $\gamma$ , increases (see figures 4.6 and 4.7). The second process becomes dominant when the central obstruction size,  $\varepsilon$ , approaches unity. As a result, a decreased degree of polarisation,  $\gamma$ , occurs for sample4 when the central obstruction size,  $\varepsilon$ , is not large enough. Once the central obstruction size,  $\varepsilon$ , is large enough, the degree of polarisation,  $\gamma$ , increases appreciably, due to the dominance of the second process. For sample2, sample3 and sample7, it seems that the second process is always dominant (see figure 4.7).



(a)



(b)

Figure 4.14: Simulated dependence of the degree of polarisation,  $\gamma$ , on (a) the radius of the central annular obstruction for a matching pair of annular objectives with a numerical aperture of 0.6 and (b) the numerical aperture of the circular objectives for sample4 in a transmission microscope. These two curves were calculated by Dr. X. Gan.

The behaviour regarding the effect of the size of the central obstruction,  $\epsilon$ , on the degree of polarisation,  $\gamma$ , for sample4 is qualitatively confirmed by the theoretical result in figure 4.14(a), which is based on the Monte-Carlo method (refer to section

3.3). Figure 4.14(b) confirms the dependence of the degree of polarisation,  $\gamma$ , on the numerical aperture, which was also observed in the experiment (figure 4.8).

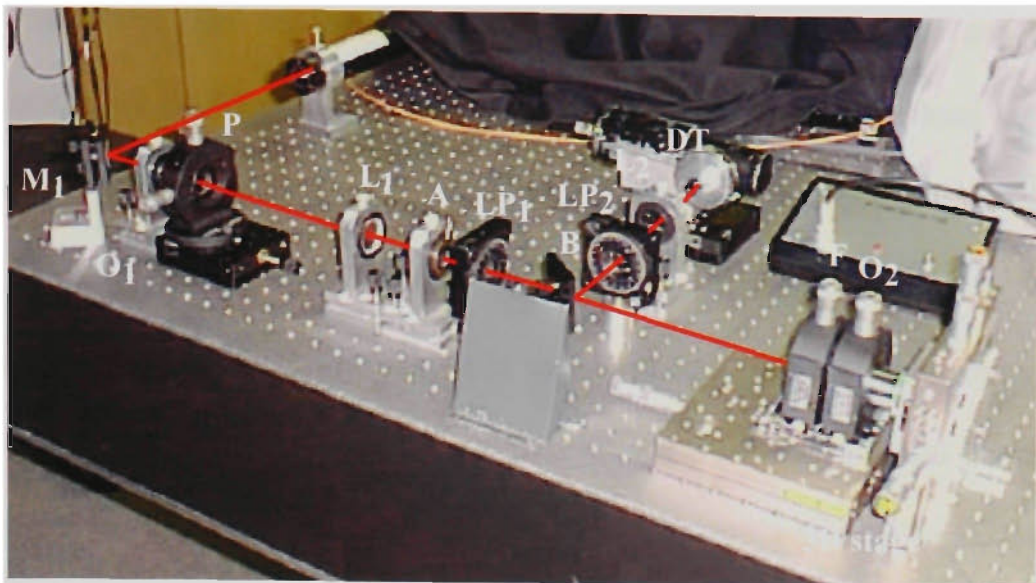
## 4.4 Angle-gating in a reflection optical microscope

It has been demonstrated in the previous section that an angle-gating mechanism can be used as an effective tool in suppressing scattered photons and gives the correct image contrast in a transmission scanning microscope in imaging through turbid media. This section demonstrates the implementation of the angle-gating method for suppressing scattered photons by the use of a polarised annular objective in a reflection scanning microscope. As stated previously this optical arrangement is more applicable for imaging biological tissue *in situ* (i.e. skin biopsy employing an endoscope).

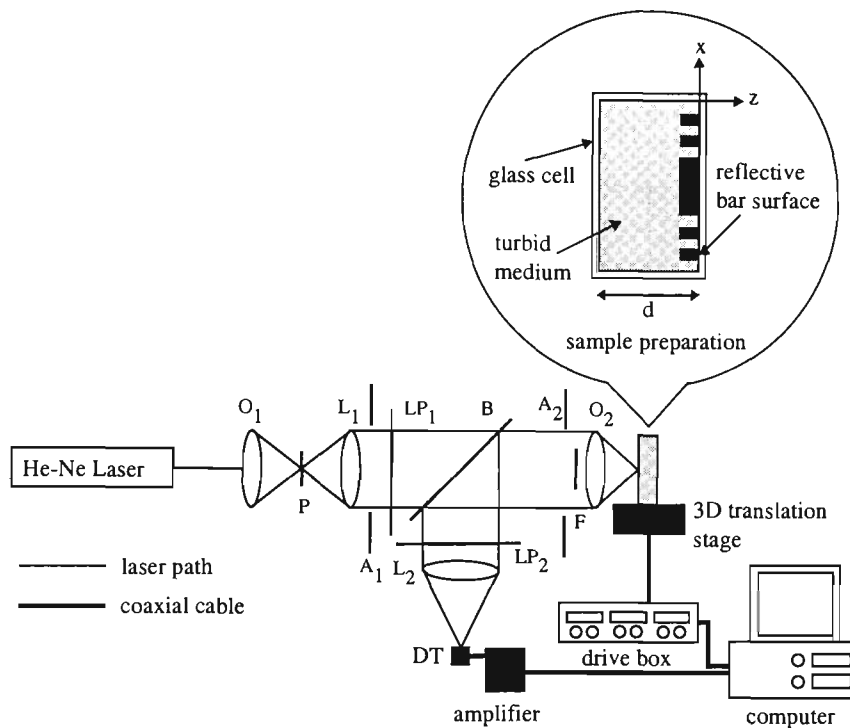
### 4.4.1 Experimental details

#### 4.4.1.1 Experimental set-up

The principle of using a polarising annular objective for angle-gating has been described in detail in sections 4.2 and 4.3. A reflection scanning optical microscope using a polarising annular objectives, as depicted in figure 4.15, was set up on an optical bench. The physical scanning optical microscope set-up, and the schematic diagram of the experimental set-up are shown in figures 4.15(a) and 4.15(b),



(a)



(b)

Figure 4.15: Experimental reflection scanning optical microscope with angle-gating and polarisation-gating. (a) Photograph of the system; (b) Schematic diagram of the system. A: aperture; B: beamsplitter; DT: detector; F: central obstruction; L: lens; LP: polariser; ND: neutral density filter; O: objectives; P: pinhole.

respectively. A 7 mW Melles Griot (model No. 05-LHP-153) He-Ne laser ( $\lambda = 632.8$  nm) was used as the light source. The beam from the laser source was expanded and collimated by an objective  $O_1$  ( $NA = 0.25$ ) and a lens  $L_1$  (focal length,  $f = 200$  mm, diameter,  $D = 25$  mm). In this arrangement a single objective  $O_2$  (Zeiss FLUAR™ 20×/0.75  $\infty$ /0.17, hereafter called the imaging objective) instead of two separate objectives as in the transmission optical arrangement (see figure 4.3) was used to illuminate the object embedded within a turbid sample and to collect the diffuse and unscattered photons originating from a turbid sample. These collected photons were focused via a lens  $L_2$  ( $f = 200$  mm,  $D = 25$  mm) onto a large-area ( $1 \text{ cm}^2$ ) detector DT which recorded a time-averaged signal.

An annular imaging objective was achieved by placing coaxially an opaque central circular disc obstruction F in the illumination/detection beam path. Like in the case of the transmission system, extreme care should be taken in obtaining the correct alignment of the central obstruction in the aperture of the imaging objective, since the performance of the angle-gating mechanism depends on the alignment of the central obstruction.

In order to incorporate the polarisation-gating mechanism into the angle-gating mechanism, a polariser  $LP_1$  was placed such that it produced a linear polarised illumination beam, while the polariser  $LP_2$  acted as an analyser in front of the detector. The degree of polarisation,  $\gamma$ , (equation 3.39) of light passing through a turbid medium is once again measured from the signal detected with the analyser  $LP_2$  parallel ( $I_p$ ) and perpendicular ( $I_s$ ) to the direction of  $LP_1$ , respectively.

## 4.4.1.2 Sample preparation

Three turbid samples (sample8, sample9 and sample10) were prepared and their details are summarised in table 4.2. Each sample was placed in an individual glass cell with lateral dimensions of 2 cm  $\times$  1 cm. The glass cell thickness,  $d$ , was 120  $\mu\text{m}$  for the three samples. It should be noted that the optical thickness,  $n$ , for a reflection microscope is given by,  $2d/l_s$ . Sample8 consisted of distilled water and was used to determine the behaviour of the reflection imaging system without scatterers. Sample9 and sample10 consisted of polystyrene microspheres of diameter 0.48  $\mu\text{m}$  suspended in water (refer to table 3.1 for more detailed calculations of the scattering parameters for the microspheres). It should be noted that, the concentration of polystyrene microspheres for sample9 was diluted by a factor of 2.

Sample number	Scattering medium	Cell thickness, $d$ ( $\mu\text{m}$ )	smfp length, $l_s$ ( $\mu\text{m}$ )	Anisotropy value, $g$	Optical thickness, $n$ ( $2d/l_s$ )
8	distilled water	120	-	-	-
9	0.48 $\mu\text{m}$ polysty. microsph. in water	120	38.4	0.81	6.25
10	0.48 $\mu\text{m}$ polysty. microsph. in water	120	19.2	0.81	12.5

Table 4.2: Parameters for the samples used in the reflection scanning optical microscope. All parameters were determined by Mie theory (refer to section 3.2).

A reflective test bar (geometric thickness  $\sim 3 \mu\text{m}$ ) was embedded within the three samples (refer to figure 4.15(b)) to determine image resolution and contrast achievable when a polarising annular objective was employed.

Prepared samples were mounted onto a three-dimensional translation stage which is the same as that discussed in section 4.3.1.2 and the focus of the imaging objective  $O_2$  was placed on the surface of the test bar.

The degree of polarisation,  $\gamma$ , for sample8 was measured to be 99.9% for a circular imaging objective ( $\varepsilon = 0$ ), which shows that depolarisation caused by the imaging objective and other optical components in this experimental arrangement can be ignored.

#### 4.4.2 Effect of an annular imaging objective

The suppression of diffusing photons by a polarising annular objective can be seen from the measured dependence of the degree of polarisation,  $\gamma$ , on the radius the central obstruction,  $\varepsilon$ , for sample9 and sample10 (figure 4.16(a)), while figure 4.16(b) illustrates the polarisation intensity ratio,  $I_p/I_s$ , for the collected signal. The measured degree of polarisation,  $\gamma$ , for the two samples was 0.52 (or  $I_p/I_s = 3.2$ ) and 0.33 (or  $I_p/I_s = 2.0$ ), respectively, when a circular objective ( $\varepsilon = 0$ ) was used for imaging. The lower degree of polarisation,  $\gamma$ , and polarisation intensity ratio,  $I_p/I_s$ , for sample10 results from its larger optical thickness,  $n$  (see table 4.2). Therefore

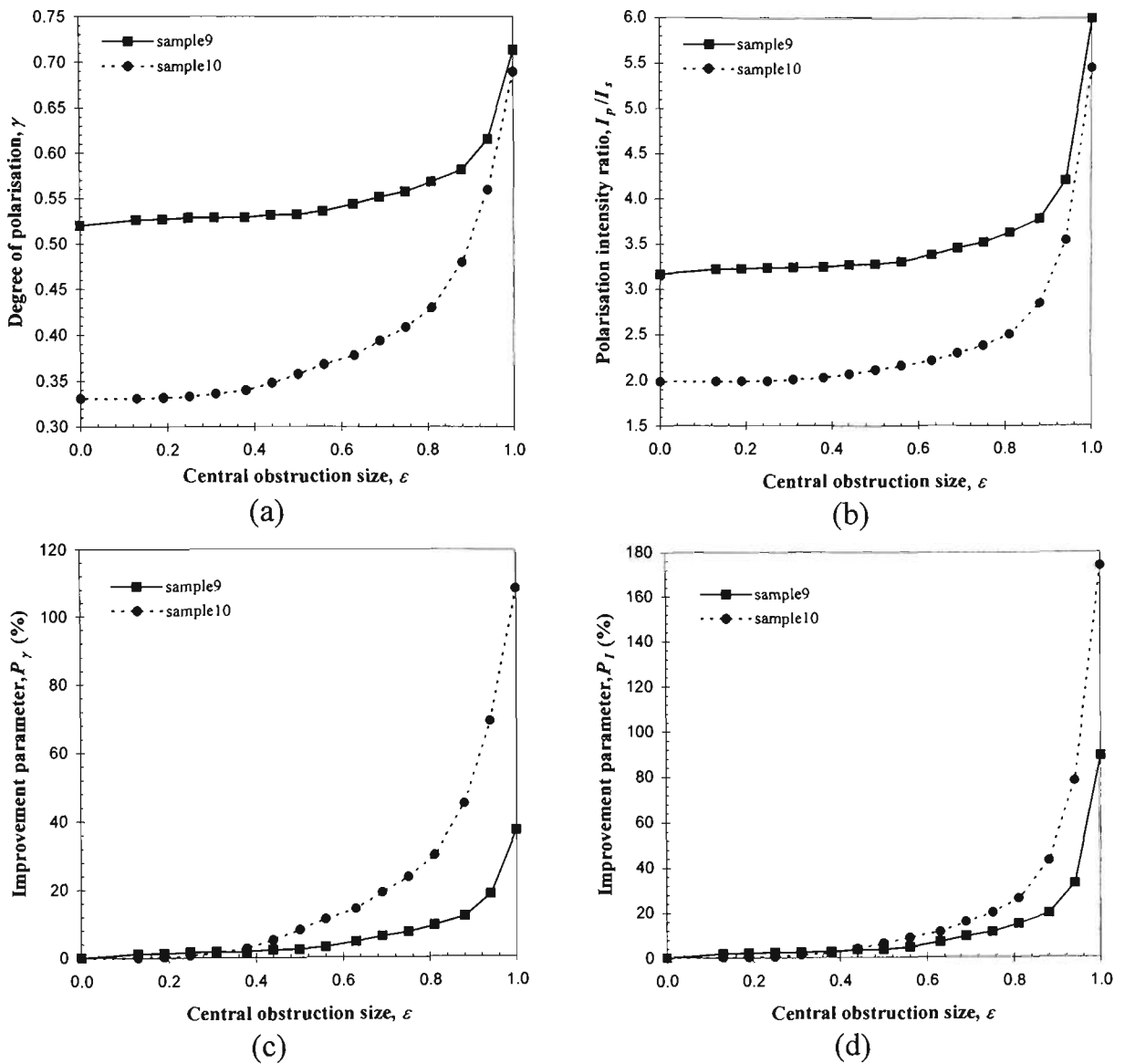


Figure 4.16. Dependence of the degree of polarisation,  $\gamma$  (a), the polarisation intensity ratio,  $I_p/I_s$  (b), and the percentage improvement parameters,  $P_\gamma$  (c) and  $P_I$  (d) on the radius of the central obstruction of an annular imaging objective,  $\varepsilon$ . The numerical aperture for the imaging objective  $O_2$  is 0.75.

each photon propagating through sample10 has experienced on average twice as many scattering events as sample9 and therefore stronger depolarisation than photons propagating in sample9.

To help demonstrate the performance of the central obstruction size,  $\varepsilon$ , on the suppression of scattered photons the percentage improvement parameters,  $P_\gamma$  and  $P_I$ , defined by equations 4.6 and 4.7 were used. The parameters  $P_\gamma$  and  $P_I$  are illustrated in figures 4.16(c) and 4.16(d) for the two samples, respectively.

An appreciable increase in the degree of polarisation,  $\gamma$ , was seen in figure 4.16(a) when a thin polarising annular objective was employed, i.e. when the central obstruction size,  $\varepsilon$ , approaches unity. The degree of polarisation,  $\gamma$ , for an annular objective of  $\varepsilon \approx 0.94$  was 0.62 ( $I_p/I_s = 4.2$ ) and 0.56 ( $I_p/I_s = 3.5$ ) for the two samples, respectively. When compared with the circular objective ( $\varepsilon = 0$ ) the increase in the degree of polarisation,  $\gamma$ , is 0.1 (or  $P_\gamma \approx 19\%$ ) and 0.23 (or  $P_\gamma \approx 70\%$ ) for the two samples, respectively, while the corresponding improvement in the polarisation intensity ratio,  $I_p/I_s$ , is 1.0 (or  $P_I \approx 31\%$ ) and 1.5 (or  $P_I \approx 75\%$ ) for the two samples. This result clearly demonstrates that if a thin polarising annular objectives is used for imaging the weighting of scattered photons is efficiently reduced (i.e.  $I_p/I_s$  increases).

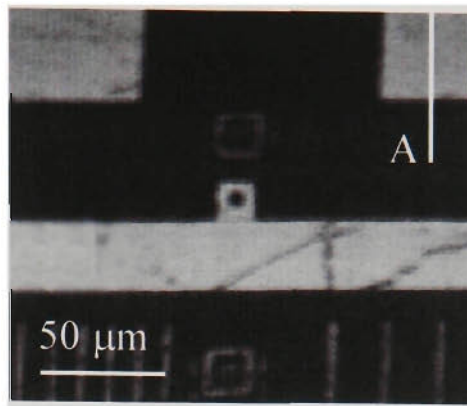


Figure 4.17: Image of a test bar embedded within sample8 (filled with distilled water), when a circular imaging objective ( $\varepsilon = 0$ ) of numerical aperture 0.75 is employed. The intensity of the image was normalised to unity.

#### 4.4.3 Imaging with circular and annular objectives

It should be noted that like in the case for the transmission optical microscope an optimal annular objective with a central obstruction size,  $\varepsilon \approx 0.94$  was chosen to perform all imaging since this annular objective has a good suppression ability and high signal-to-noise ratio. Also like in the case of the transmission optical microscope the incident power from the laser was attenuated with the use of a variable neutral density filter (figure 4.15(b)) for the circular imaging objective ( $\varepsilon = 0$ ) such that the illumination power at the focus was equal to the power at the focus for an annular imaging objective ( $\varepsilon \approx 0.94$ ). The power at the focus was approximately  $110 \mu\text{W}$ . With a fixed incident power at the focus a direct comparison of signal-to-noise ratio could be obtained for the two cases.

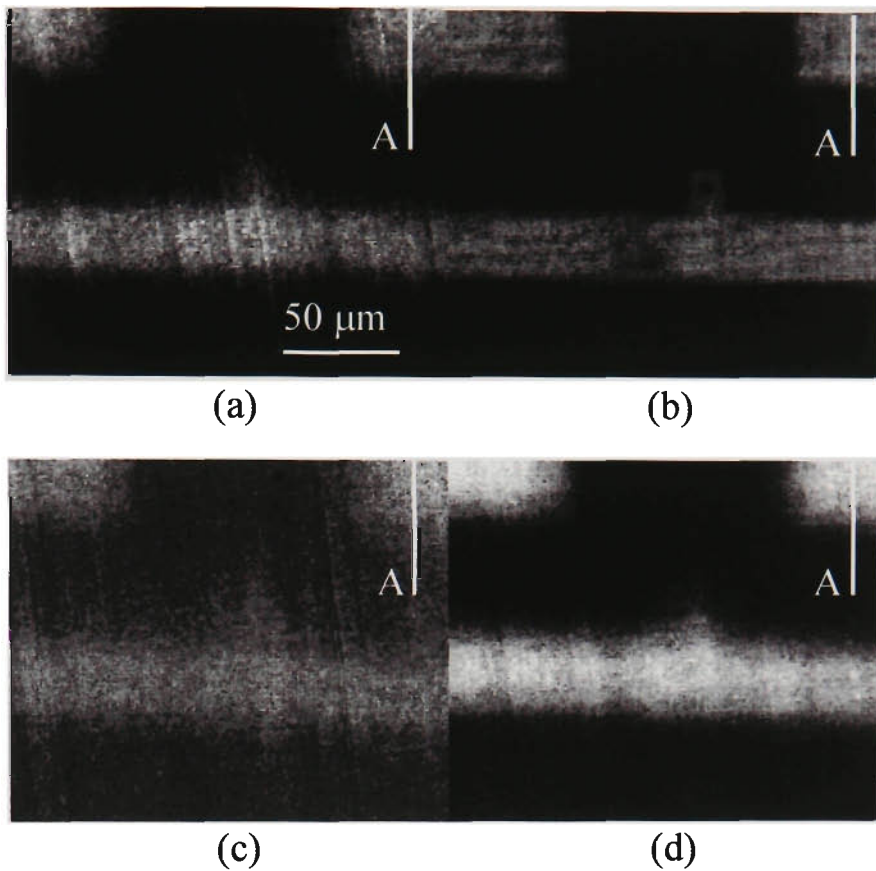


Figure 4.18: Images of a test bar embedded in sample9 ((a) and (b)) and sample10 ((c) and (d)) when a circular imaging objective ( $\varepsilon = 0$ ) with parallel polarisation ((a) and (c)) and an annular imaging objective ( $\varepsilon \approx 0.94$ ) with parallel polarisation ((b) and (d)) are employed. The numerical aperture of the imaging objective in both cases is 0.75. The intensity of the images was normalised to unity.

The test bar embedded within sample8 was imaged with a polarising circular objective ( $\varepsilon = 0$ ) to demonstrate the best image resolution and contrast achievable in our experiment (figure 4.17). The image in this case is constructed purely by unscattered photons obeying the diffraction theory of light (Born and Wolf, 1980). The sharpness of the edge,  $\alpha$ , defined by the distance between 10% and 90% intensity points of a fitted edge response, can be used as a measure of transverse

image resolution. For example at the point 'A' in figure 4.17, the transverse resolution,  $\alpha$ , is approximately 3.1  $\mu\text{m}$ . It is seen from figure 4.17 that the test bar has different linewidths and variable reflectivity indicated by the levels of brightness. These properties can also be used as resolvability markers when the test bar is imaged through sample9 and sample10.

Figure 4.18 shows images of the test bar embedded in sample9 (figures 4.18(a) and 4.18(b)) and sample10 (figures 4.18(c) and 4.18(d)). In figures 4.18(a) and 4.18(c) a polarising circular objective was used, while in figures 4.18(b) and 4.18(d) a polarising annular objective ( $\varepsilon \approx 0.94$ ) was used. The image of the test bar in figure 4.18(a) is smeared and the fine structure of the bar is washed out due to the strong contribution of scattered light. A significant improvement in resolution is seen with the introduction of a polarising annular objectives (figure 4.18(b)), which is indicated by the reduced smearing and finer details (see the small square with a hole). The transverse resolution,  $\alpha$ , in figure 4.18(b) at point 'A' is improved from 23.9  $\mu\text{m}$  to 12.2  $\mu\text{m}$  when compared with that in figure 4.18(a), which corresponds to an improvement in transverse resolution,  $\alpha$ , of approximately 49%. It is noticeably difficult to see the test bar when the optical thickness,  $n$ , is increased (sample10) due to the poor contrast (figure 4.18(c)). This phenomenon can be attributed to the large number of scattered photons collected via the circular objective ( $\varepsilon = 0$ ). Similar to the situation in figure 4.18(b), the introduction of an annular objective ( $\varepsilon \approx 0.94$ ) provides an image with sharper contrast and reduced blurring (figure 4.18(d)). In figure 4.18(d) the transverse resolution,  $\alpha$ , at point 'A' is improved from 46.8  $\mu\text{m}$  to 35.1  $\mu\text{m}$  when compared with that in figure 4.18(c),

which corresponds to an improvement in transverse resolution of approximately 25%. These results quantitatively confirm that a thin imaging annular objective confines unscattered photons to a small region on the objective plane, which has the effect of reducing the weighting of scattered photons that contribute to the image (see figure 4.16).

#### 4.4.4 Discussion

Although it should be noted that two separate central obstructions can be used in the reflection optical microscope depicted in figure 4.15, only one central obstruction has been used in this section. This arrangement is different from the transmission optical microscope (refer to section 4.3) in which two separate central obstructions were placed in the illumination and collection paths respectively. According to the investigation for a transmission optical arrangement (section 4.3) the optimised situation occurs (a maximum improvement in the degree of polarisation,  $\gamma$ ) when the two central obstructions are the same and their size,  $\varepsilon$ , approaches unity.

It has been previously demonstrated from figure 4.8 that there exists a trade-off numerical aperture between the resolution achievable and the ability of the imaging objectives to suppress scattered photons in turbid media with a transmission optical microscope. A significant improvement in the degree of polarisation,  $\gamma$ , has been seen by reducing the numerical aperture of the imaging/collection objective, since a small numerical aperture reduces the path lengths that the photons traverse, which

effectively reduces the average number of scattering events experienced by the photons.

Figure 4.19(a) shows the effect of the numerical aperture on the degree of polarisation,  $\gamma$ , for sample9 and sample10 in the reflection arrangement, while figure 4.19(b) illustrates the polarisation intensity ratio,  $I_p/I_s$ , for the collected signals.

The two percentage improvement parameters,  $P_\gamma$  and  $P_I$ , defined in equations 4.8 and 4.9, were used to help demonstrate the performance of the numerical aperture on the suppression of scattered photons. The parameters  $P_\gamma$  and  $P_I$  are illustrated in figures 4.19(c) and 4.19(d) for the two samples, respectively.

It is clearly seen from figure 4.19 that the degree of polarisation,  $\gamma$ , increases appreciably for both samples when the numerical aperture (NA) is decreased. The difference in the degree of polarisation,  $\gamma$ , between NA = 0.75 and NA = 0.11 is 0.11 (or  $P_\gamma \approx 21\%$ ) and 0.05 (or  $P_\gamma \approx 13\%$ ) for sample9 and sample10, respectively. For the same conditions the improvement in the polarisation intensity ratio,  $I_p/I_s$  is 1.24 (or  $P_I \approx 39\%$ ) and 0.22 (or  $P_I \approx 11\%$ ) for sample9 and sample10, respectively. This result confirms that a trade-off between resolution and suppression ability should also be considered when a reflection optical arrangement is used for imaging through turbid media.

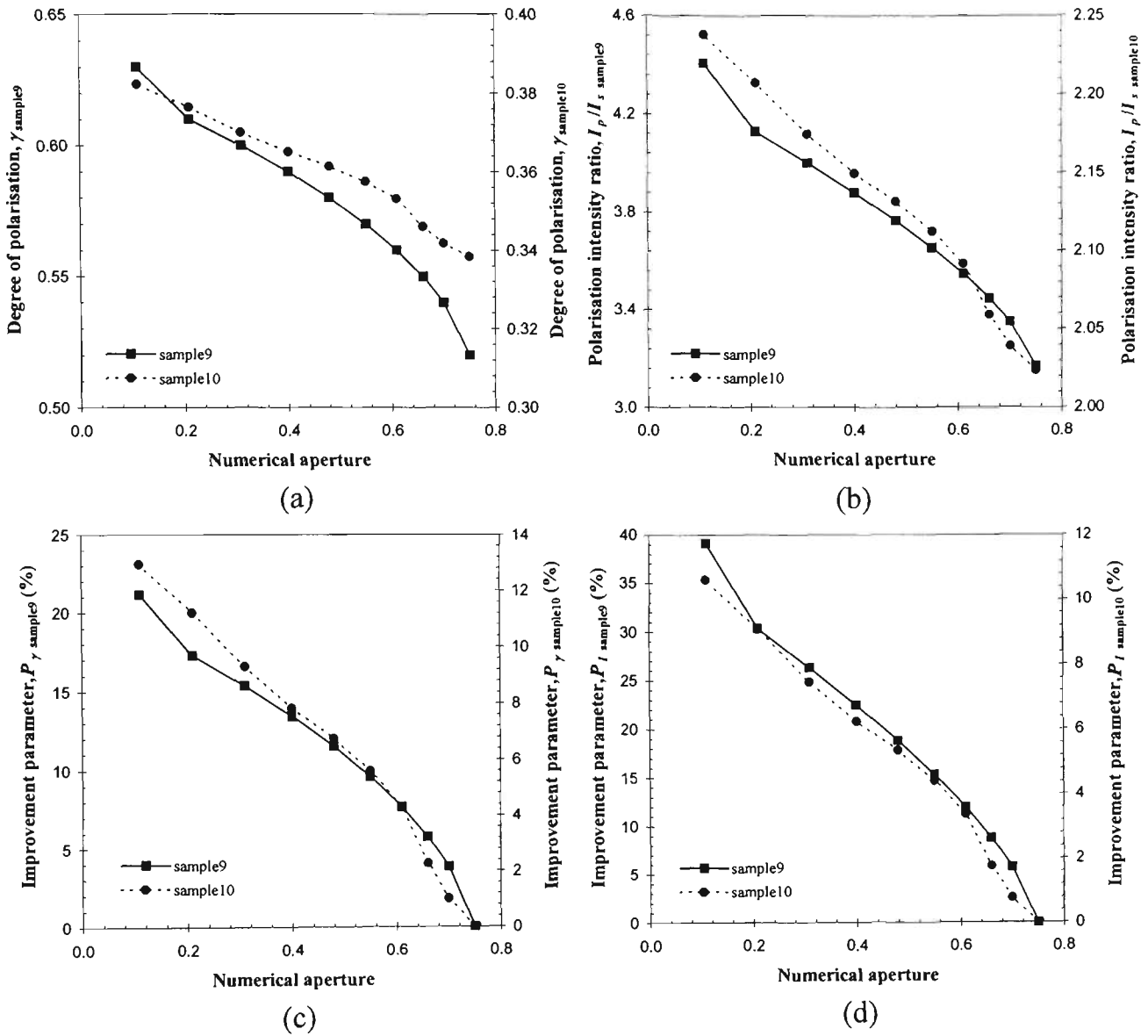


Figure 4.19: Dependence of the degree of polarisation,  $\gamma$  (a), the polarisation intensity ratio,  $I_p/I_s$  (b), and the percentage improvement parameters,  $P_\gamma$  (c) and  $P_I$  (d) on the numerical aperture of the imaging objective  $O_2$ .

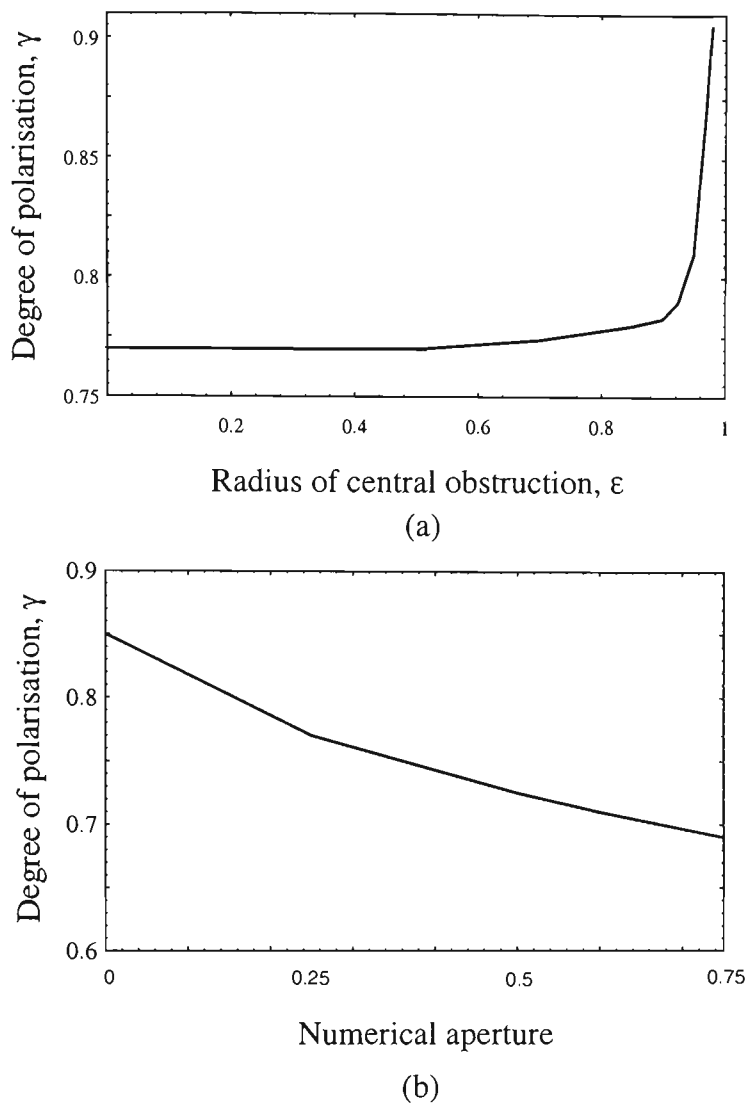


Figure 4.20: Simulated dependence of the degree of polarisation,  $\gamma$ , on (a) the radius of the central annular obstruction for an annular objective with a numerical aperture of 0.6 and (b) the numerical aperture of the circular objectives for sample9 in a reflection microscope. These two curves were calculated by Dr. X. Gan.

In figure 4.16 the degree of polarisation,  $\gamma$ , monotonically increases with the size of the central obstruction,  $\varepsilon$ , unlike the situation in the transmission optical microscope in which case there is a weak dip on the  $\gamma$ - $\varepsilon$  curve (see figure 4.7(a)).

This difference is caused by the larger anisotropy value,  $g$ ; a large anisotropy value,  $g$ , corresponds to the larger proportion of forward diffuse photons (refer to section 3.2.2). As a result, a significant proportion of the forward diffuse photons are scattered out of the collection cone of the imaging objective upon reflection from the test bar surface.

Thus the effect of the polarisation annular objectives on the suppression of scattered photons becomes dominant earlier. This behaviour regarding the effect of the size of the central obstruction,  $\varepsilon$ , on the degree of polarisation,  $\gamma$ , for sample9 is qualitatively confirmed by the theoretical result in figure 4.20(a), which is based on the Monte-Carlo method (refer to section 3.3). Figure 4.20(b) confirms the dependence of the degree of polarisation,  $\gamma$ , on the numerical aperture, which was observed in the experiment (figure 4.19).

## 4.5 General discussion

It is worthwhile to compare, at least qualitatively, the new polarised annular objective gating method with other gating methods currently used in microscopic imaging through turbid media (refer to chapter 2). A confocal pinhole has been proved to be a useful mask to suppress scattered photons (refer to section 2.3.2(a)). It has been demonstrated by Gan *et al.* (1998) that a confocal pinhole also plays an angle-gating role. This feature results from the fact that a scattered photon, which propagates at an angle along a deviated path with respect to an unscattered photon, intersects with a pinhole at a distance from the centre of the pinhole. As a result, the smaller the pinhole size the more scattered photons are suppressed. However,

the signal level in confocal microscopy may be reduced dramatically in imaging through turbid media (Gu *et al.*, 1993). In addition, a small pinhole may lead to pronounced coherent noise due to the purely coherent imaging property in confocal microscopy (Gu *et al.*, 1996). These two problems do not exist in the system discussed in the chapter. In fact, polarised annular objectives combined with a large pinhole could result in a better imaging performance by suppressing scattered photons. In this respect, incorporating polarised annular objectives into optical coherence tomography (OCT) would be another potential method for efficient suppression of scattered photons because OCT is based on the principle of coherence of scattered photons. In addition, since the angle-gating method in this chapter does not involve optical fibres and interference arrangements, the new method may be more easily implemented in a practical microscope than optical coherence microscopy (Hee *et al.*, 1993).

## 4.6 Conclusion

In conclusion, it has been successfully demonstrated (both experimentally and theoretically) that the weighting of scattered photons contributing to an image can be significantly suppressed due to the efficient angle-gating mechanism achieved with the utilisation of annular imaging objectives. For high-quality imaging through a turbid medium,

- (a) there is a trade-off value for the numerical aperture of the objectives between image resolution and image contrast,

- (b) the input annular objective should be as thin as possible (i.e. the central obstruction size,  $\varepsilon$ , should be larger than 0.9),
- (c) the size of the output annular obstruction should be greater than or equal to the input annular size,
- (d) the analyser should have the same polarisation direction of the illumination beam.

For a given sensitivity of a detector,

- (a) there is also a trade-off between the parameters outlined in (a) - (d) and the amount of light that can be detected (signal-to-noise ratio),
- (b) the signal-to-noise ratio also decreases as the scattering increases due to the reduced number of available unscattered photons that can be detected. Therefore the angle-gating mechanism is only useful when a significant number of unscattered photons are available to be detected. Otherwise an averaging process is needed to increase the signal-to-noise ratio.

When a pair of circular objectives ( $\varepsilon = 0$ ) are used to image through a turbid medium in a transmission microscope, an image can be misinterpreted due to an inversion of image contrast. This misinterpretation can be overcome by using a

pair of matching annular objectives ( $\varepsilon > 0$ ) to suppress diffusing photons which are multiply scattered in a turbid medium.

# Chapter 5

## Polarisation-gating in turbid media

### 5.1 Introduction

When some gating methods are applied to microscopic imaging system they may become less efficient due to the wide range of illumination angles produced by a high numerical aperture objective (figure 3.7(a)). The angle-gating mechanism discussed in chapter 4 is one possible method of suppressing scattered photons in imaging through turbid media. However, the limitation of the angle-gating mechanism is that it requires a significant proportion of unscattered photons to be available for detection. Thus, as scattering increases the signal-to-noise ratio of the detected images is substantially reduced.

The polarisation-gating mechanism (refer to section 2.3.3) is one of the methods which can be applied to microscopic imaging for efficiently selecting unscattered or less scattered photons. This feature has been preliminarily shown in the last chapter. Various authors (Morgan *et al.*, 1997; Schmitt and Hiang, 1998; Demos *et*

*al.*, 1998) have demonstrated that further improvement in image quality is possible when differential polarisation-gating is used.

Reported in this chapter is a detailed investigation into the effect of polarisation-gating (conventional and differential) mechanisms used in a reflection optical microscope for imaging through turbid media. The effect of the scattering particle size in turbid media on microscopic imaging is experimentally studied in order to determine the resolution achievable when polarisation-gating mechanisms are employed. Image resolution for a 48  $\mu\text{m}$  wide bar embedded within turbid media is measured as a function of the optical thickness for four different types of polystyrene microspheres suspended in water. To demonstrate the effectiveness of polarisation-gating in more realistic tissue-like turbid media, image resolution of a 48  $\mu\text{m}$  wide bar embedded within semi skimmed-milk suspensions was measured.

This chapter is organised into the following sections: Section 5.2 discusses the principles of polarisation-gating. The performance of the polarisation-gating mechanisms on image quality for different sized scatterers is experimentally presented for a reflection optical microscope in section 5.3 (Schilders *et al.*, 1998d; 1998e; Gan *et al.*, 1999). This section also illustrates the dependence of the degree of polarisation on the optical thickness of turbid media. With the use of the Monte-Carlo simulation model the polarisation-gating performance illustrated in section 5.3 is compared in section 5.4. Finally a conclusion is presented in sections 5.5.

## 5.2 Principle of polarisation-gating

Unscattered or less scattered photons maintain the same or similar state of incident polarisation, and carry more information of an object embedded within turbid media than multiply scattered photons (see section 2.3.3). It is therefore possible to separate the unscattered or less scattered photons with a polarisation detection mechanism.

Image quality can be further improved if the differential polarisation-gated intensity, which can be derived by subtracting the perpendicular polarisation-gated intensity from the parallel polarisation-gated intensity, is used to construct an image. This mechanism is based on the fact that depolarised scattered photons contribute to both the perpendicular polarisation-gated intensity and the parallel polarisation-gated intensity. Although differential polarisation-gating can significantly improve image resolution, it might be at the cost of greatly reduced signal-to-noise.

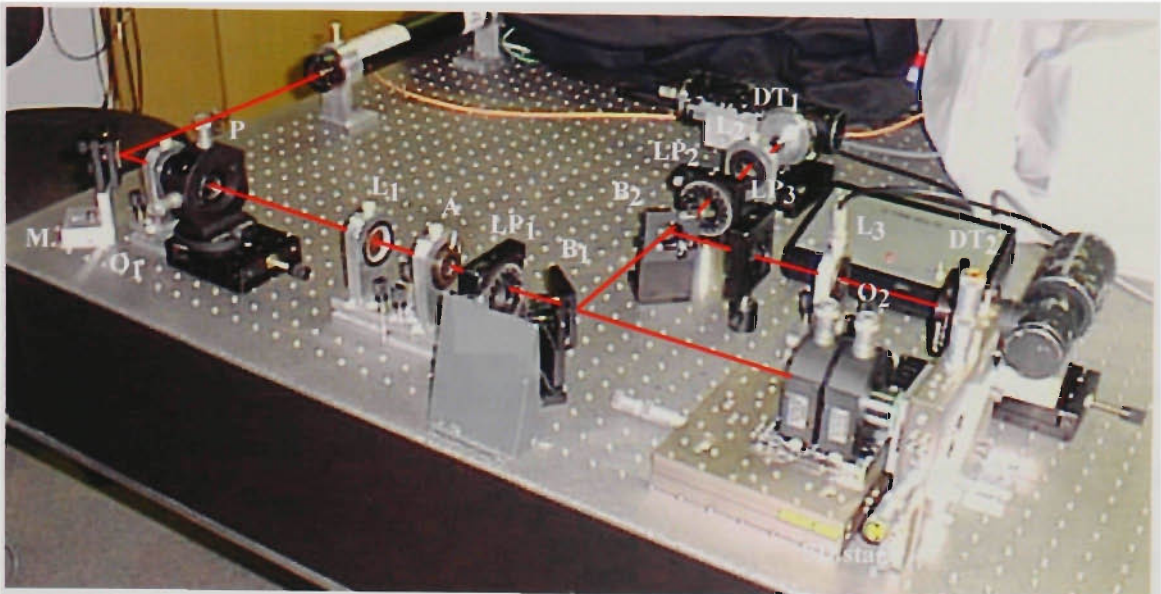
For a transillumination imaging system Morgan *et al.* (1994) demonstrated that the performance of differential polarisation-gating depends on the characteristics of turbid media, such as the size of scatterers and the thickness of turbid media. The scatterer size determines the speed of depolarisation, while the sample thickness determines the magnitude of the depolarisation.

It has been demonstrated that image resolution of 0.7 mm, for an edge object embedded within a semi-skimmed milk suspension (optical thickness  $\approx 18$ ), can be

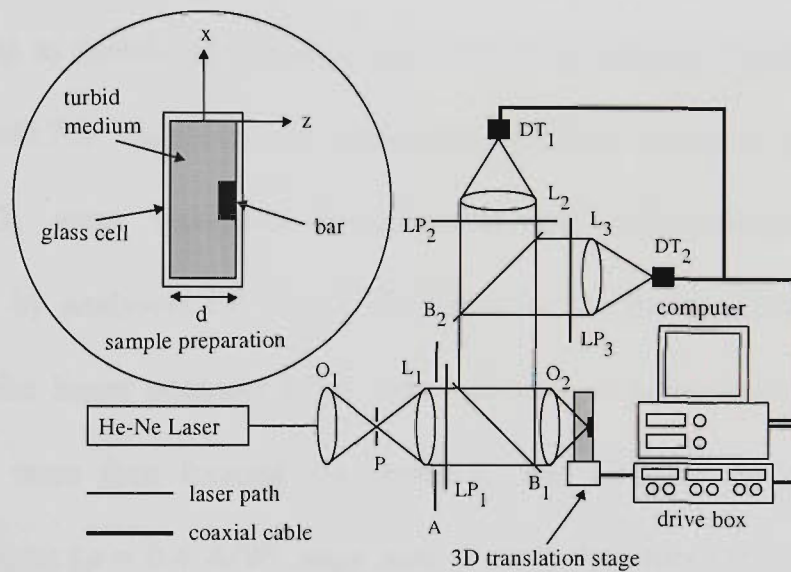
obtained with differential polarisation-gating when a parallel beam probe of approximately 1 mm in diameter is used in a transillumination imaging system (Morgan *et al.* 1997).

The speed of depolarisation of scattered photons is related to the directional change of the incident light upon scattering and is determined by the anisotropy value,  $g$ . For small scattering particles the directional change of scattered photons is large due to the small anisotropy value,  $g$ , which results in a significant change in the polarisation state. Therefore polarisation-gating and in particular differential polarisation-gating is more effective when turbid media with small scattering particles are imaged.

In the transillumination optical arrangement the image resolution is determined by the size of the parallel beam probe. Therefore to improve image resolution further, it is necessary to employ a microscope objective (Schmitt and Hiang, 1998; Schilders *et al.*, 1998d; 1998e). As yet there has been no experimental investigation that demonstrates the dependence of resolution on scattering events and scattering anisotropy in a microscopic imaging system employing conventional polarisation-gating and differential polarisation-gating.



(a)



(b)

Figure 5.1: Experimental reflection scanning optical microscope with differential polarisation-gating mechanism. (a) Photograph of the system, with the beam path shown in red; (b) Schematic diagram of the system. A: aperture; B: beamsplitter; DT: detector; L: lens; LP: polariser; O: objective; P: pinhole.

## 5.3 Polarisation-gating in a reflection optical microscope

### 5.3.1. Experimental details

#### 5.3.1.1 Experimental set-up

A reflection scanning optical microscope employing differential polarisation-gating, as depicted in figure 5.1, was set-up on an optical bench. The physical scanning optical microscope set-up, and the schematic diagram of the experimental set-up are shown in figures 5.1(a) and 5.1(b), respectively. A 7 mW Melles Griot (model No. 05-LHP-153) He-Ne laser ( $\lambda = 632.8$  nm) was used as the light source. The beam from the laser source was expanded and collimated by an objective  $O_1$  (numerical aperture NA = 0.25) and a lens  $L_1$  (focal length,  $f = 200$  mm; diameter,  $D = 25$  mm) to match the entrance aperture of an imaging objective  $O_2$  (Zeiss FLUAR 20 $\times$ /0.75). Scattered and unscattered photons collected via the imaging objective  $O_2$  were separated into parallel and perpendicular polarisation components by analysers  $LP_2$  and  $LP_3$  relative to the incident polarisation state defined by the linear polariser  $LP_1$ . The parallel and perpendicular polarisation components were then focused via lenses  $L_2$  and  $L_3$  ( $D = 25$  mm) onto two identical Silicon ( $\rho = 0.4$  A/W) large area ( $1$  cm<sup>2</sup>) detectors  $DT_1$  and  $DT_2$  which recorded time-averaged signals,  $I_p$  (termed the conventional polarisation-gated intensity) and  $I_s$  (termed the perpendicular polarisation-gated intensity), respectively. The no-gated intensity,  $I_p + I_s$ , and the differential polarisation-gated intensity,  $I_p - I_s$ , were calculated with the aid of a computer. The degree of polarisation,  $\gamma$ , of the light reflected from a turbid sample was calculated with the aid of equation 3.39.

All images were recorded with an acquisition time of 27 seconds for a  $200 \times 200$  pixel image. In addition all images were normalised before any data analysis was performed.

Sample set	Scattering medium	Cell thickness, $d$ ( $\mu\text{m}$ )	smfp length, $l_s$ ( $\mu\text{m}$ )	Anisotropy value, $g$	Optical thickness, $n(2d/l_s)$
A	0.107 $\mu\text{m}$ polysty. microsph. in water	100 - 600	416.4 <sup>a</sup>	0.076 <sup>a</sup>	0.5 - 2.8
B	0.202 $\mu\text{m}$ polysty. microsph. in water	100 - 600	70.2 <sup>a</sup>	0.31 <sup>a</sup>	2.8 - 17.1
C	0.48 $\mu\text{m}$ polysty. microsph. in water	25 - 300	19.2 <sup>a</sup>	0.81 <sup>a</sup>	2.6 - 31.3
D	1.053 $\mu\text{m}$ polysty. microsph. in water	25 - 300	10.8 <sup>a</sup>	0.92 <sup>a</sup>	4.6 - 55.6
E	semi-skimmed milk	50 - 300	30 <sup>b</sup>	<0.4 <sup>c</sup>	3.3 - 20

Table 5.1: Parameters for the sample sets used in the reflection scanning optical microscope. (a) The parameters were determined by Mie theory (refer to section 3.2); (b) The parameters were determined experimentally (refer to section 4.3.1(b)); and (c) The parameters were determined from the literature (Jensen, 1995).

### 5.3.1.2 Sample preparation

Four types of polystyrene microspheres suspended in water (refer to table 3.1 for detailed calculations of the scattering parameters for the microspheres) were respectively used as scattering particles in a turbid medium. A number of samples

were prepared for each type of polystyrene microspheres. The samples produced with each polystyrene microsphere size are grouped into sample sets A-D and their details are listed in table 5.1. The range of the microsphere sizes chosen in this research was consistent with that of scattering particles in real biological samples which do not include large scatterers ( $> 1 \mu\text{m}$ ) (Morgan *et al.*, 1997; Hielscher *et al.*, 1997).

Since real tissue-like samples consist of scatterers of different sizes it is important to demonstrate the effect of the polarisation-gating mechanisms on image quality in such a turbid medium. To demonstrate image quality in a more realistic turbid medium a sample set of semi-skimmed milk was prepared (i.e. sample set E, table 5.1). Semi-skimmed milk (fat content 3.6%) was chosen since it does not include large scatterers ( $> 1 \mu\text{m}$ ), and has been used in transillumination imaging to simulate tissues which do not include large scatterers ( $> 1 \mu\text{m}$ ) (Morgan *et al.*, 1997; Hielscher *et al.*, 1997). If tissue includes large scatterers polarisation-gating may not be efficient as large scatterers (high anisotropy value,  $g$ ) result in highly forward scattering without appreciably changing the degree of polarisation,  $\gamma$ , of the incident beam. The size of scattering particles in the milk suspension is approximately in a range of  $0.1 \mu\text{m}$  to  $1 \mu\text{m}$ , which is similar to that used in the case of polystyrene microspheres (samples sets A-D). According to Beer's law the scattering-mean-free path length,  $l_s$ , of the semi skimmed-milk was measured to be approximately  $30 \mu\text{m}$  (refer to section 4.3.1.2). The anisotropy value,  $g$ , for the semi-skimmed milk suspension was assumed from the literature (Jensen, 1995).

Each type of polystyrene microsphere was placed in a glass cell with lateral dimensions of 2 cm × 1 cm. The thickness of the glass cell,  $d$ , was varied between 25  $\mu\text{m}$  and 600  $\mu\text{m}$ , producing an optical thickness of a turbid sample,  $n$ , of  $2dl_s$ , for the reflection microscope. It should be noted that the maximum optical thickness,  $n$ , achievable for a given turbid medium set is determined by the working distance of the imaging objective  $O_2$  used.

Sample number	Scattering medium	Cell thickness, $d$ ( $\mu\text{m}$ )	smfp length, $l_s$ ( $\mu\text{m}$ )	Anisotropy value, $g$	Optical thickness, $n$ ( $2dl_s$ )
1	distilled water	100	-	-	-
2	0.107 $\mu\text{m}$ polysty. microsph. in water	600	416.4 <sup>a</sup>	0.076 <sup>a</sup>	2.8
3	0.202 $\mu\text{m}$ polysty. microsph. in water	100	70.2 <sup>a</sup>	0.31 <sup>a</sup>	2.8
4	semi-skimmed milk	100	30 <sup>b</sup>	<0.4 <sup>c</sup>	6.7
5	semi-skimmed milk	300	30 <sup>b</sup>	<0.4 <sup>c</sup>	20
6	1.056 $\mu\text{m}$ polysty. microsph. in water	100	10.8 <sup>a</sup>	0.92 <sup>a</sup>	18.5

Table 5.2: Parameters for the specific samples used in the reflection scanning optical microscope. (a) The parameters were determined by Mie theory (refer to section 3.2); (b) The parameters were determined experimentally (refer to section 4.3.1(b)); and (c) The parameters were determined from the literature (Jensen, 1995).

It should be pointed out that the value of the optical thickness,  $n$ , can be altered by changing either the geometric cell thickness,  $d$ , of a sample or the concentration of scatterers or both. For a given scatterer size, the time-averaged angular distribution of scattered photons is dependent only on the value of the optical thickness,  $n$ , although their spatial distribution is determined by both the optical thickness,  $n$ , and the scattering-mean-free-path length,  $l_s$  (Gan and Gu, 1998). The spatial distribution of scattered photons together with a finite-sized detector and collection objective used in this experimental investigation introduces additional gating. As a result, increasing the geometric thickness,  $d$ , of a turbid medium affects the image resolution more appreciably than increasing the concentration of scatterers. In addition increasing the sample thickness,  $d$ , is more realistic since it represents an increase in the penetration depth for a biological sample.

For the evaluation of image quality a 48  $\mu\text{m}$  wide metallic reflective bar (reflectivity  $\approx 70\%$  @  $\lambda = 632.8 \text{ nm}$ ) was embedded within one of the turbid media described above (see figure 5.1(b)). Prepared samples were mounted onto a three-dimensional translation stage (as discussed in section 4.3.1.2). The sample cell was scanned along the x-direction with the focus of the imaging objective  $O_2$  on the surface of the bar. Transverse resolution of the scanned bar image,  $\alpha$ , is defined as the distance between the 10% and 90% intensity points, measured from the responses after they are fitted using a symmetric-double-sigmoidal (SDS) method (TableCurve™ 2D, 1996).

To qualitatively demonstrate the image performance of polarisation-gating a selected set of six samples were imaged in this chapter. The detailed parameters of the six samples (numbered 1 to 6) are illustrated in table 5.2.

The transverse resolution of the bar image,  $\alpha$ , and the degree of polarisation,  $\gamma$ , for sample1 were measured to be  $0.7 \mu\text{m}$  and 99.9%, respectively, for an imaging objective,  $O_2$ , of numerical aperture 0.75. The image in this case is constructed purely by unscattered photons obeying the diffraction theory of light and therefore demonstrates the maximum image resolution achievable in this experimental arrangement.

### **5.3.2 Effect of the optical thickness and scatterer size on resolution**

#### **5.3.2.1 Scattering suspension of $0.107 \mu\text{m}$ polystyrene microspheres**

Figure 5.2 shows typical images of a  $48 \mu\text{m}$  bar embedded in sample2 (see table 5.2) when conventional polarisation-gating (CPG), perpendicular polarisation-gating (PPG) and differential polarisation-gating (DPG) techniques were employed (see figures 5.2(a), 5.2(b) and 5.2(c), respectively). It can be seen that the image constructed by differential polarisation-gating (figure 5.2(c)) has more detail when compared with the image constructed by conventional polarisation-gating (figure 5.2(a)), which implies the effectiveness of differential polarisation-gating over conventional polarisation-gating in suppressing scattered photons. It should also be noted that an image can be constructed with mainly scattered photons (figure 5.2(b)), although its resolution is lower than that of the images formed with conventional polarisation-gating and differential polarisation-gating techniques.

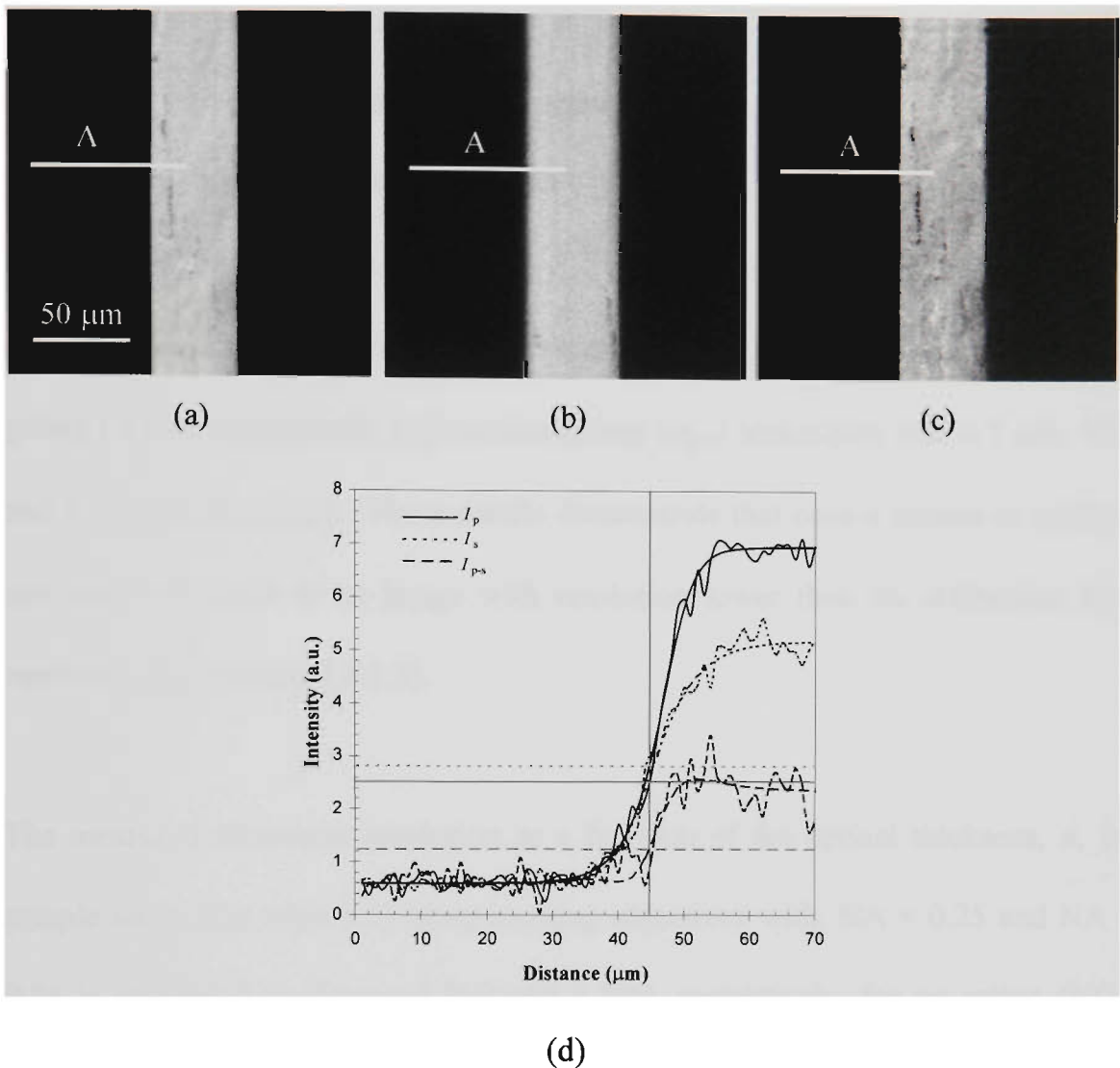


Figure 5.2: Measured images for sample2 (table 5.2) when CPG (a), PPG (b) and DPG (c) techniques are employed. The intensity of the images is normalised to unity. (d) includes the measured edge responses corresponding to CPG ( $I_p$ ), PPG ( $I_s$ ) and DPG ( $I_{p-s}$ ) techniques. The horizontal grey lines represent the intensity for  $I_p$  (solid),  $I_s$  (dot) and  $I_{p-s}$  (dashed), at the bar edge position indicated by the vertical grey line. The numerical aperture of the imaging objective is 0.25.

This feature is illustrated more clearly in figure 5.2(d) which shows typical edge responses (at the position marked by 'A') of the embedded bar and corresponding fitted SDS curves recorded with conventional polarisation-gating ( $I_p$ ), perpendicular polarisation-gating ( $I_s$ ) and differential polarisation-gating ( $I_{p-s}$ ), for the images illustrated in figures 5.2(a), 5.2(b) and 5.2(c), respectively. The measured transverse resolution,  $\alpha$ , for conventional polarisation-gating ( $\alpha_p$ ), perpendicular polarisation-gating ( $\alpha_s$ ) and differential polarisation-gating ( $\alpha_{p-s}$ ) techniques was  $6.7 \mu\text{m}$ ,  $9.2 \mu\text{m}$  and  $4.0 \mu\text{m}$  respectively. These results demonstrate that once a photon is scattered it can only contribute to an image with resolution lower than the diffraction limited resolution (see section 5.3.1.2).

The measured transverse resolution as a function of the optical thickness,  $n$ , for sample set A (see table 5.1) using imaging objectives with,  $\text{NA} = 0.25$  and  $\text{NA} = 0.75$  is illustrated in figures 5.3(a) and 5.3(b), respectively, for no-gating (NG), ( $\alpha_{p+s}$ ), conventional polarisation-gating ( $\alpha_p$ ), perpendicular polarisation-gating ( $\alpha_s$ ) and differential polarisation-gating ( $\alpha_{p-s}$ ) techniques. It is evident from figures 5.3(a) and 5.3(b) that using conventional polarisation-gating ( $\alpha_p$ ) is better than no-gating ( $\alpha_{p+s}$ ) and that differential polarisation-gating ( $\alpha_{p-s}$ ) is superior to conventional polarisation-gating ( $\alpha_p$ ).

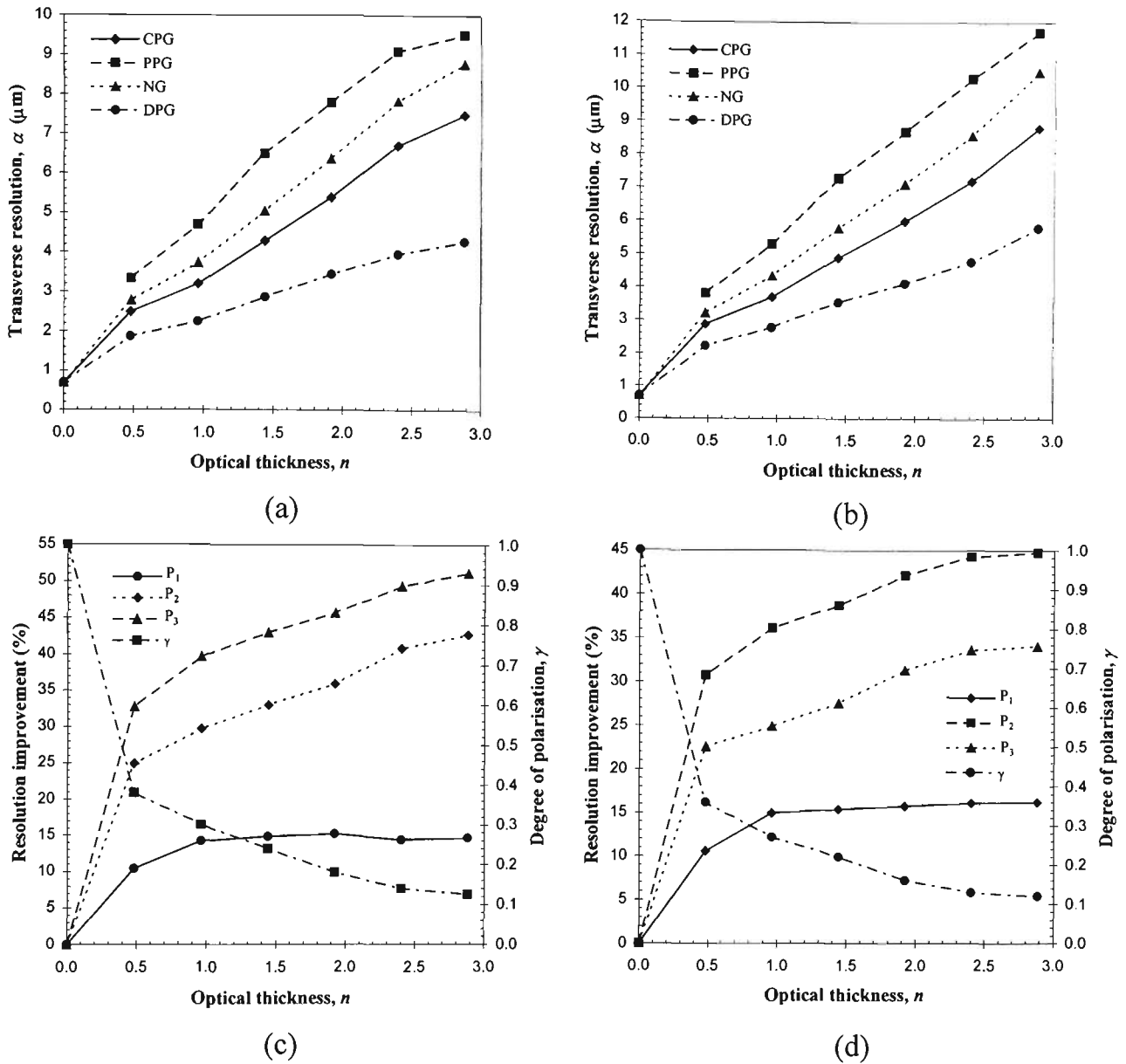


Figure 5.3: Resolution performance for sample set A at  $\text{NA} = 0.25$  ((a) and (c)) and  $\text{NA} = 0.75$  ((b) and (d)). (a) and (b) are the measured transverse resolution as a function of the optical thickness,  $n$ , for NG ( $\alpha_{p+s}$ ), CPG ( $\alpha_p$ ), PPG ( $\alpha_s$ ) and DPG ( $\alpha_{p-s}$ ). (c) and (d) are the resolution improvement and the degree of polarisation,  $\gamma$ , as a function of the optical thickness,  $n$ . A comparison is given between CPG and NG ( $P_1$ ), DPG and NG ( $P_2$ ) and DPG and CPG ( $P_3$ ).

To help illustrate the improvement in transverse resolution achieved with the implementation of a particular polarisation-gating method the following three improvement parameters were defined. The improvement in transverse resolution between conventional polarisation-gating ( $\alpha_p$ ) and no-gating ( $\alpha_{p+s}$ ) is defined as

$$P_1|_n = \frac{\alpha_{p+s}|_n - \alpha_p|_n}{\alpha_{p+s}|_n}, \quad (5.3)$$

the improvement in transverse resolution between differential polarisation-gating ( $\alpha_{p-s}$ ) and no-gating ( $\alpha_{p+s}$ ) is defined as

$$P_2|_n = \frac{\alpha_{p+s}|_n - \alpha_{p-s}|_n}{\alpha_{p+s}|_n}, \quad (5.4)$$

and the improvement in transverse resolution between conventional polarisation-gating ( $\alpha_p$ ) and differential polarisation-gating ( $\alpha_{p-s}$ ) is defined as

$$P_3|_n = \frac{\alpha_p|_n - \alpha_{p-s}|_n}{\alpha_p|_n}, \quad (5.5)$$

where  $n$  is the optical thickness.

The improvement in resolution is illustrated more clearly in figures 5.3(c) and 5.3(d), which show the percentage improvement in transverse resolution between conventional polarisation-gating and no-gating ( $P_1$ ), differential polarisation-gating and no-gating ( $P_2$ ), and differential polarisation-gating and conventional polarisation-gating ( $P_3$ ). It is clearly seen from figures 5.3(c) and 5.3(d) that the improvement in resolution becomes large as the optical thickness,  $n$ , is increased. Differential polarisation-gating has a strong effect when applied to this turbid

medium because scattered photons are depolarised fast when the optical thickness,  $n$ , increases, as shown by the degree of polarisation,  $\gamma$  (figures 5.3(c) and 5.3(d)), and because there is still a significant proportion of unscattered light detectable (i.e. the optical thickness,  $n$ , is small). The reason for the higher improvement in resolution and a higher degree of polarisation,  $\gamma$ , for,  $NA = 0.25$ , compared with those for  $NA = 0.75$ , is due to the stronger suppression of multiply scattered photons when the acceptance angle of an imaging objective is reduced (refer to figure 4.19). However, a higher numerical aperture imaging objective may be more effective for differential polarisation-gating, in terms of the percentage improvement in transverse resolution, when the optical thickness,  $n$ , is large and/or when the depolarisation of each scattering event is weak. This effect will be discussed in more detail in section 5.3.4.

### 5.3.2.2 Scattering suspensions of 0.202 $\mu\text{m}$ polystyrene microspheres

Images of an embedded bar in sample3 (the optical thickness,  $n$ , for this sample is equivalent to the images of sample2 (see table 5.2) shown in figure 5.2) are shown in figures 5.4(a), 5.4(b) and 5.4(c) for conventional polarisation-gating, perpendicular polarisation-gating and differential polarisation-gating, respectively. A comparison of figures 5.2 and 5.4 demonstrates that the resolution for the latter case is significantly poorer, which is indicated by the lack of detail, by smearing and by noise. The degradation in resolution is firstly due to the increase in forward propagation of the scattered photons as a result of the larger anisotropy value,  $g$ , and secondly due to the collection of more scattered photons as a result of the larger numerical aperture (refer to figure 4.19).

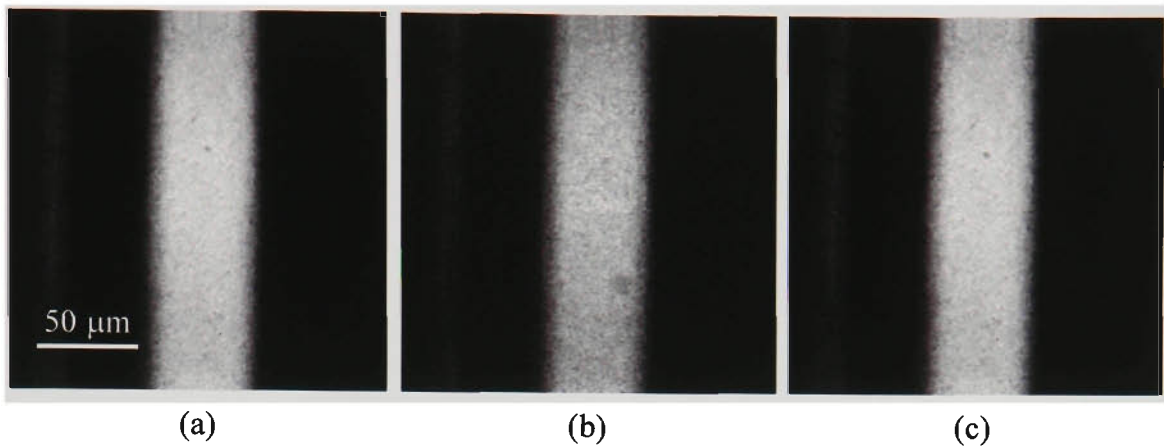
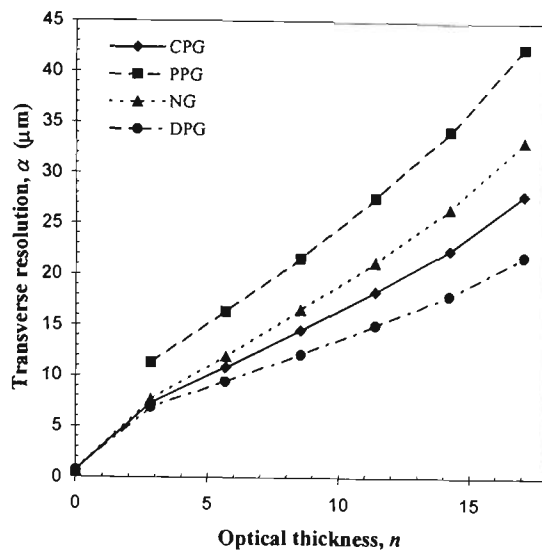
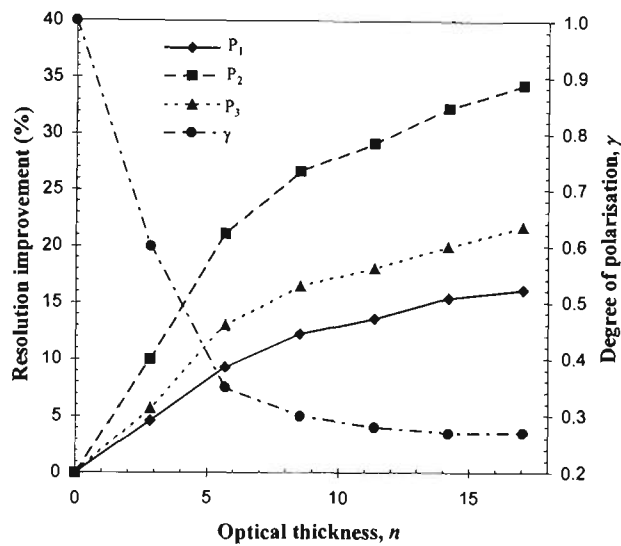


Figure 5.4: Measured images for sample3 (table 5.2) for CPG (a), PPG (b) and DPG (c) techniques. The intensity of the images is normalised to unity. The numerical aperture of the imaging objective is 0.75.

Figure 5.5(a) illustrates the measured transverse resolution as a function of the optical thickness,  $n$ , for no-gating ( $\alpha_{p+s}$ ), conventional polarisation-gating ( $\alpha_p$ ), perpendicular polarisation-gating ( $\alpha_s$ ) and differential polarisation-gating ( $\alpha_{p-s}$ ) techniques when sample set B (see table 5.1) and an imaging objective of numerical aperture 0.75 is used. It is evident from figure 5.5(a), and has already been seen in figures 5.3(a) and 5.3(b), that differential polarisation-gating ( $\alpha_{p-s}$ ) is superior to no-gating ( $\alpha_{p+s}$ ) and conventional polarisation-gating ( $\alpha_p$ ). This improvement is illustrated more clearly in figures 5.5(b), which shows the percentage improvement in transverse resolution between conventional polarisation-gating and no-gating ( $P_1$ ), differential polarisation-gating and no-gating ( $P_2$ ), and differential polarisation-gating and conventional polarisation-gating ( $P_3$ ). A comparison of figures 5.3(d) and 5.5(b)

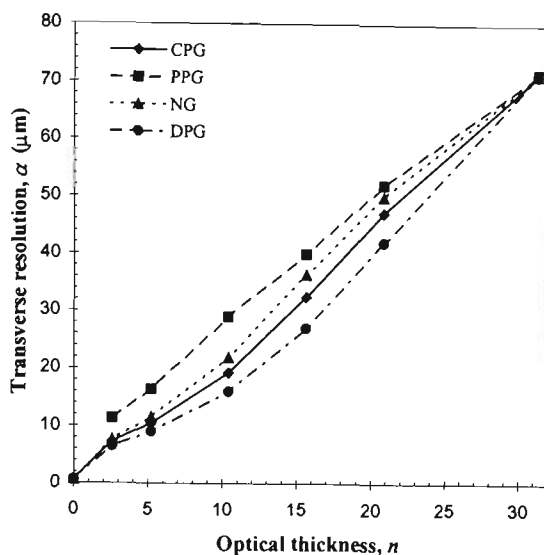


(a)

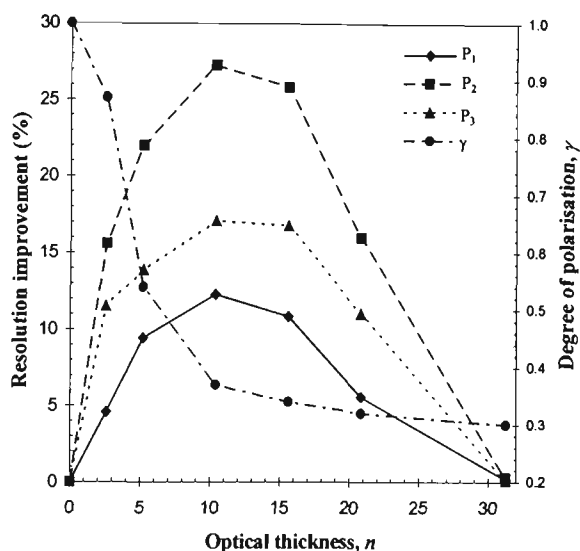


(b)

Figure 5.5: Resolution performance for sample set B at  $\text{NA} = 0.75$ . (a) is the measured transverse resolution as a function of the optical thickness,  $n$ , for NG ( $\alpha_{p+s}$ ), CPG ( $\alpha_p$ ), PPG ( $\alpha_s$ ) and DPG ( $\alpha_{p-s}$ ). (b) is the resolution improvement and the degree of polarisation,  $\gamma$ , as a function of the optical thickness,  $n$ . A comparison is given between CPG and NG ( $P_1$ ), DPG and NG ( $P_2$ ) and DPG and CPG ( $P_3$ ).



(a)



(b)

Figure 5.6: Resolution performance for sample set C at  $\text{NA} = 0.75$ . (a) is the measured transverse resolution as a function of the optical thickness,  $n$ , for NG ( $\alpha_{p+s}$ ), CPG ( $\alpha_p$ ), PPG ( $\alpha_s$ ) and DPG ( $\alpha_{p-s}$ ). (b) is the resolution improvement and the degree of polarisation,  $\gamma$ , as a function of the optical thickness,  $n$ . A comparison is given between CPG and NG ( $P_1$ ), DPG and NG ( $P_2$ ) and DPG and CPG ( $P_3$ ).

shows that the improvement in transverse resolution between differential polarisation-gating and no-gating ( $P_2$ ), in the latter case increases with the optical thickness,  $n$  (i.e. no steady state value is reached). This phenomenon is because the depolarisation of scattered photons in figure 5.5(b) is slower than that in figure 5.3(d), when the optical thickness,  $n$ , increases, due to the larger anisotropy value,  $g$ , for the former case.

### 5.3.2.3 Scattering suspension of 0.48 $\mu\text{m}$ polystyrene microspheres

In this section sample set C was used. Under the same experimental condition as figures 5.3(b), 5.3(d) and 5.5, transverse resolution as a function of the optical thickness,  $n$ , was measured for no-gating ( $\alpha_{p+s}$ ), conventional polarisation-gating ( $\alpha_p$ ), perpendicular polarisation-gating ( $\alpha_s$ ) and differential polarisation-gating ( $\alpha_{p-s}$ ) techniques (figure 5.6(a)). It can be seen from figure 5.6(a) that differential polarisation-gating ( $\alpha_{p-s}$ ) is superior to no-gating ( $\alpha_{p+s}$ ) and conventional polarisation-gating ( $\alpha_p$ ) only when the optical thickness,  $n$ , is less than 30. This property is illustrated more clearly in figure 5.6(b), which shows the percentage improvement in resolution between conventional polarisation-gating and no-gating ( $P_1$ ), differential polarisation-gating and no-gating ( $P_2$ ), and differential polarisation-gating and conventional polarisation-gating ( $P_3$ ). It is noted from figure 5.6(b) that the resolution improvement by using any polarisation-gating method becomes weaker as the optical thickness,  $n$ , becomes larger than 12. This feature is caused by the reduced number of less scattered photons which can be detected and by the fact that at each scattering event depolarisation is weak due to

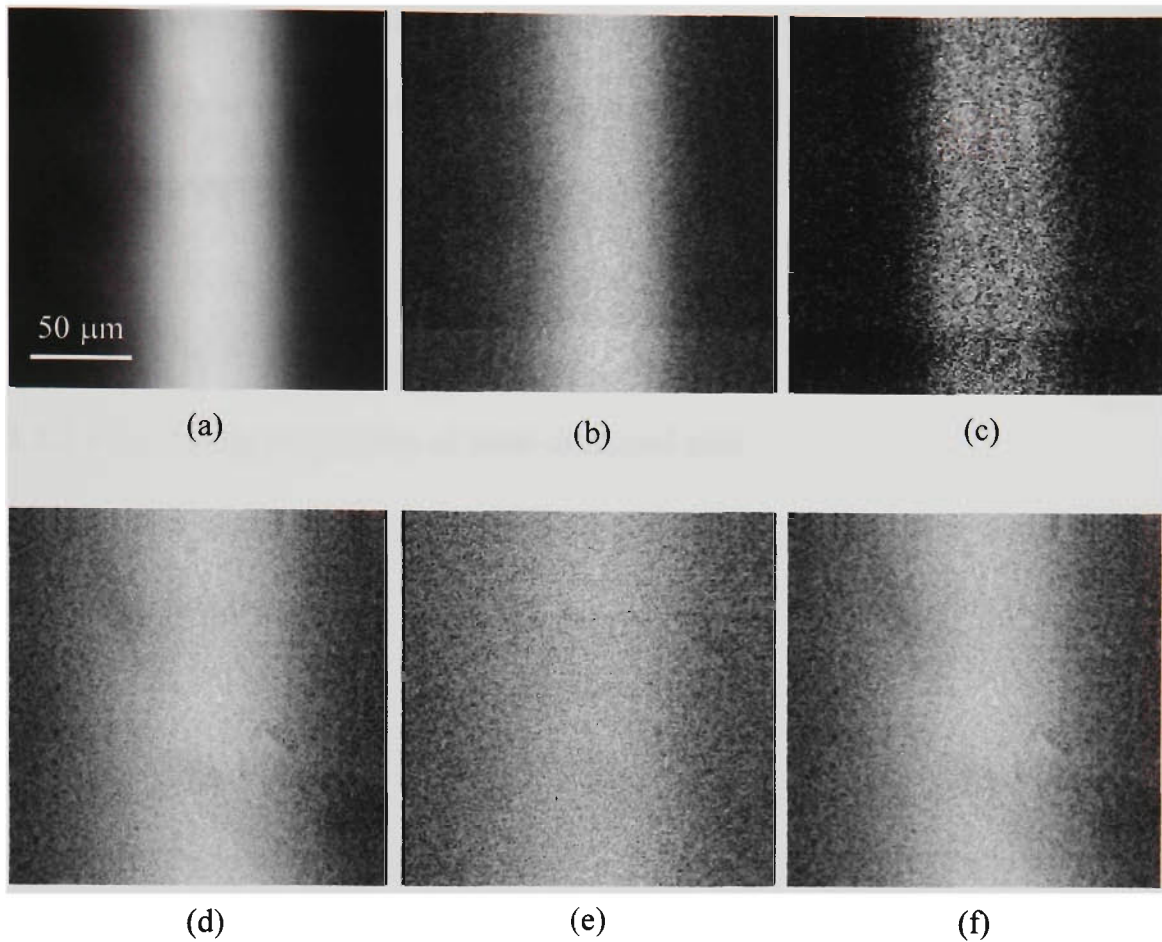


Figure 5.7: Measured images ((a), (b) and (c)) for sample4 (table 5.2). and measured images ((d), (e) and (f)) for sample5 (table 5.2). ((a) and (d)), ((b) and (e)), and ((c) and (f)) correspond to CPG, PPG and DPG techniques, respectively. The intensity of the images is normalised to unity. The numerical aperture of the imaging objective is 0.75.

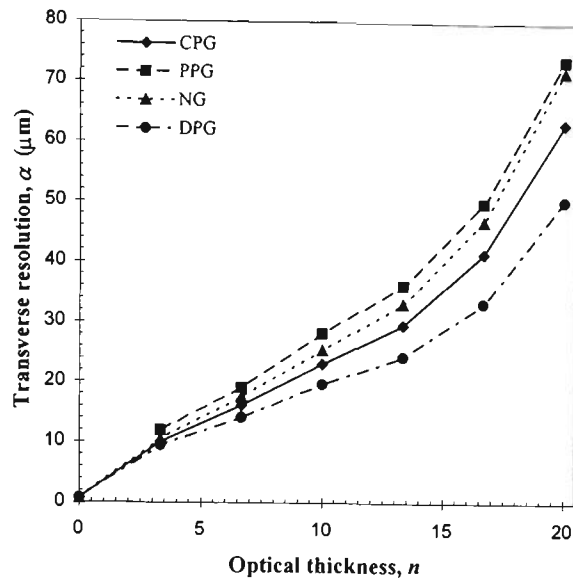
the large anisotropy value,  $g$ , of the scatterers in the turbid media. The latter feature can be seen from figure 5.6(b); photons scattered between 15 and 30 times have similar depolarisation (degree of polarisation,  $\gamma$ ). Therefore it is difficult for polarisation-gating to selectively suppress the highly scattered photons. Since

polarisation-gating is based on the number of detectable unscattered or less scattered photons which maintain the initial degree of polarisation (Morgan *et al.*, 1997), the transverse resolution is eventually degraded to that of the no-gating technique as the optical thickness,  $n$ , increases, which is clearly illustrated in figures 5.6(a) and 5.6(b).

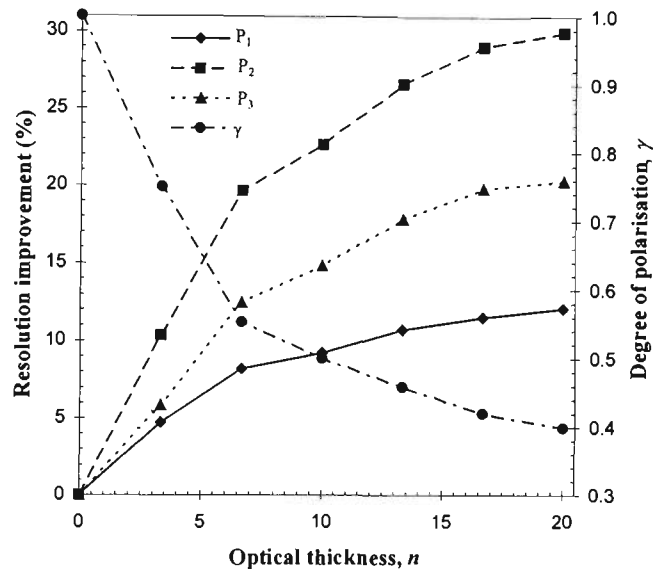
#### 5.3.2.4 Scattering suspension of semi-skimmed milk

This section demonstrates the effect of polarisation-gating in a more realistic tissue-like sample, which consists of scatterers of different sizes.

To demonstrate the effect of the polarisation-gating mechanisms on image quality in tissue-like turbid media, sample4 and sample5 (see table 5.2) were used to form images of an embedded bar. Figure 5.7 shows typical images of a 48  $\mu\text{m}$  bar embedded in sample4 (figures 5.7(a), 5.7(b) and 5.7(c)) and sample5 (figures 5.7(d), 5.7(e) and 5.7(f)) when conventional polarisation-gating, perpendicular polarisation-gating and differential polarisation-gating techniques were employed. Clearly, there is an improvement in the edge sharpness for differential polarisation-gating (figure 5.7(c)) when compared with conventional polarisation-gating (5.7(a)), indicated by the reduced smearing at the edges of the image. As the turbid sample becomes thicker (figure 5.7(d), 5.7(e) and 5.7(f)) it is visually difficult to see the improvement in image quality between conventional polarisation-gating (figure 5.7(d)) and differential polarisation-gating (figure 5.7(f)). This result suggests that at an optical thickness,  $n$ , of 20 for the semi-skimmed milk



(a)



(b)

Figure 5.8: Resolution performance for sample set E at  $\text{NA} = 0.75$ . (a) is the measured transverse resolution as a function of the optical thickness,  $n$ , for NG ( $\alpha_{p+s}$ ), CPG ( $\alpha_p$ ), PPG ( $\alpha_s$ ) and DPG ( $\alpha_{p-s}$ ). (b) is the resolution improvement and the degree of polarisation,  $\gamma$ , as a function of the optical thickness,  $n$ . A comparison is given between CPG and NG ( $P_1$ ), DPG and NG ( $P_2$ ) and DPG and CPG ( $P_3$ ).

suspension, the number of less scattered photons is low. Therefore the effect of polarisation-gating is diminished. From the results presented for polystyrene microspheres the average particle size for the milk suspension may be inferred to be between 0.2-0.5  $\mu\text{m}$ .

The measured transverse resolution as a function of the optical thickness,  $n$ , for no-gating ( $\alpha_{p+s}$ ), conventional polarisation-gating ( $\alpha_p$ ), perpendicular polarisation-gating ( $\alpha_s$ ) and differential polarisation-gating ( $\alpha_{p-s}$ ) techniques when an imaging objective of numerical aperture 0.75 is used, is illustrated in figure 5.8(a). It is evident from figure 5.8(a) that using conventional polarisation-gating ( $\alpha_p$ ) is still superior than no-gating ( $\alpha_{p+s}$ ) in microscopic imaging. Figure 5.8(a) also demonstrates that differential polarisation-gating ( $\alpha_{p-s}$ ) is superior to conventional polarisation-gating ( $\alpha_p$ ) in microscopic imaging. Image resolution using this technique is 10 times better than that achieved in transillumination imaging for a similar turbid medium (Morgan *et al.*, 1997). This improvement is illustrated more clearly in figure 5.8(b), which shows the percentage improvement in resolution between conventional polarisation-gating and no-gating ( $P_1$ ), differential polarisation-gating and no-gating ( $P_2$ ), and differential polarisation-gating and conventional polarisation-gating ( $P_3$ ).

It should be noted that the improvement in resolution between differential polarisation-gating and conventional polarisation-gating ( $P_3$ ) is more pronounced when the optical thickness,  $n$ , is larger ( $> 10$ ). In this range the amount of unscattered light detected is significantly reduced, and furthermore, the

depolarisation of scattered photons becomes pronounced, as is illustrated in the degree of polarisation,  $\gamma$ , in figure 5.8(b). It can be seen that even at an optical thickness of  $n = 20$  unscattered or less scattered photons can be extracted using the differential polarisation-gating method, although the number of these photons are low. In other words high sensitivity detectors (ie. the use of a photomultiplier tube or avalanche photodiode) are needed to produce an image of high resolution without further signal processing.

### 5.3.3 Effect of pinhole-gating and polarisation-gating

Section 2.3.3 illustrated that polarisation-gating can be used in conjunction with spatial-gating and temporal-gating techniques, since these gating methods are based on different aspects of randomisation of the incident light. An example of this principle was illustrated in chapter 4, which involved using the polarisation-gating mechanism to further suppress unwanted scattered photons in the angle-gating mechanism.

Various authors have demonstrated that a finite sized pinhole placed in front of the detector (i.e. weak confocal arrangement) can effectively reduce the contribution of scattered photons which have propagation paths not intersecting at the entrance aperture (Schmitt *et al.*, 1993; Gan *et al.*, 1998; 1999).

In this section the effect of additional spatial filtering on image resolution is experimentally investigated for sample set C, when a pinhole of 150  $\mu\text{m}$  (in diameter) is placed in front of the detectors  $\text{DT}_1$  and  $\text{DT}_2$  (see figure 5.1). It should

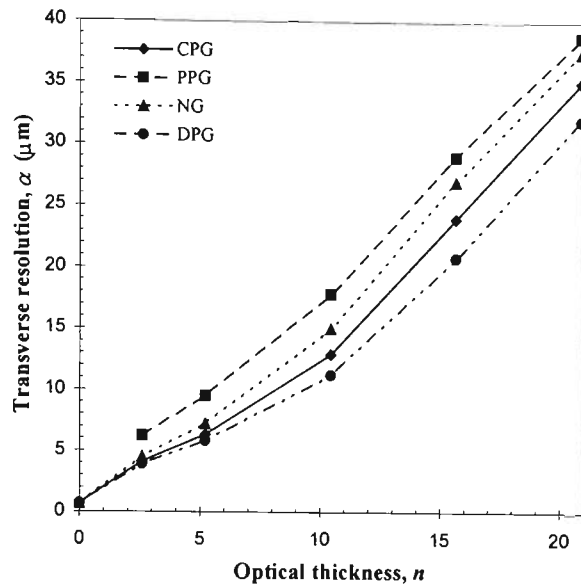
be noted that the maximum optical thickness for this set of results is limited to 20, due to the reduced signal-to-noise ratio for the detected signal when pinholes are employed.

The measured transverse resolution as a function of the optical thickness,  $n$ , for no-gating ( $\alpha_{p+s}$ ), conventional polarisation-gating ( $\alpha_p$ ), perpendicular polarisation-gating ( $\alpha_s$ ) and differential polarisation-gating ( $\alpha_{p-s}$ ) techniques, is illustrated in figure 5.9(a) when a pair of 150  $\mu\text{m}$  pinholes are used. Comparing figures 5.6(a) and 5.9(a) demonstrates that using the additional pinhole filtering significantly increases the transverse resolution for all polarisation-gating mechanisms. The transverse resolution improvement for polarisation-gating with and without pinholes is defined as

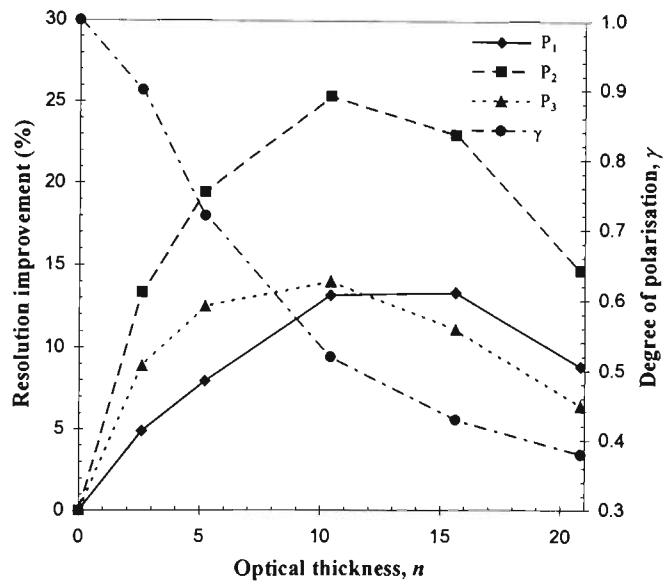
$$P_4|_n = \frac{\alpha_\zeta|_n - \alpha_{\zeta+pinhole}|_n}{\alpha_\zeta|_n} \quad (5.4)$$

where  $\zeta$  represents polarisation gating mechanisms used.

At an optical thickness,  $n$ , of 20, the transverse resolution without the pinholes (refer to figure 5.6(a)) is, 47.2  $\mu\text{m}$ , 52.1  $\mu\text{m}$ , 49.9  $\mu\text{m}$ , 42.1  $\mu\text{m}$  for conventional polarisation-gating, perpendicular-polarisation-gating, no-gating and differential polarisation-gating, respectively. With the addition of the 150  $\mu\text{m}$  pinholes the transverse resolution is improved to (see figure 5.9(a)) 35.1  $\mu\text{m}$  (or  $P_4 \approx 26\%$ ), 38.8  $\mu\text{m}$  (or  $P_4 \approx 26\%$ ), 37.5  $\mu\text{m}$  (or  $P_4 \approx 25\%$ ), and 32.0  $\mu\text{m}$  (or  $P_4 \approx 24\%$ ), for



(a)



(b)

Figure 5.9: Resolution performance for sample set C at  $NA = 0.75$  and with a pinhole of diameter  $150 \mu\text{m}$ . (a) is the measured transverse resolution as a function of the optical thickness,  $n$ , for NG ( $\alpha_{p+s}$ ), CPG ( $\alpha_p$ ), PPG ( $\alpha_s$ ) and DPG ( $\alpha_{p-s}$ ). (b) is the resolution improvement and the degree of polarisation,  $\gamma$ , as a function of the optical thickness,  $n$ . A comparison is given between CPG and NG ( $P_1$ ), DPG and NG ( $P_2$ ) and DPG and CPG ( $P_3$ ).

conventional polarisation-gating, perpendicular-polarisation-gating, no-gating and differential polarisation-gating, respectively. This result demonstrates that scattered photons, which are not suppressed in polarisation-gating, may be removed by a pinhole in terms of their path deviation.

Figure 5.9(b) illustrates the percentage improvement in resolution between conventional polarisation-gating and no-gating,  $P_1$ , differential polarisation-gating and no-gating,  $P_2$ , and differential polarisation-gating and conventional polarisation-gating,  $P_3$ , when the pinholes are used. A comparison of figures 5.6(b) and 5.9(b) illustrates that the difference between the transverse resolution (i.e. resolution improvement) for all polarisation-gating methods becomes lower when a pinhole is used. This phenomenon is due to the efficient reduction in the number of collected multiply scattered photons which have similar polarisation state, with the use of the pinhole. Therefore when the polarisation-gating methods are applied the resolution improvement is not large. The reduction in the number of collected highly scattered photons is also illustrated by a 19% (optical thickness,  $n \sim 20$ ) increase in the degree of polarisation,  $\gamma$  (see figures 5.6(b) and 5.9(b)) when the pinhole is employed.

### 5.3.4 Discussion

According to diffraction theory (Gu, 1996) the image intensity at a sharp edge is  $1/3$  and  $1/2$  of the intensity far from the edge for partially-coherent and incoherent imaging processes, respectively. In the case of conventional polarisation-gating the image is constructed mainly by unscattered photons and therefore imaging is

partially coherent, since the imaging system uses a large area detector (Gu, 1996). As a result the image intensity at the edge is close to 1/3 of the intensity far from the edge (figure 5.2(d), horizontal grey solid line). For perpendicular polarisation-gating the image is constructed by scattered photons (i.e. the incoherent component) and thus the intensity at the edge is close to 1/2 of the maximum intensity (figure 5.2(d), horizontal grey dotted line). In the differential polarisation-gating process the unscattered component of the intensity is dominant due to the subtraction of the scattered photon component and therefore the intensity at the edge for differential polarisation-gating is close to 1/3 of the intensity far from the edge (figure 5.2(d), horizontal grey dashed line). These three intensity points have been marked at the edge position represented by the vertical grey solid line in figure 5.2(d).

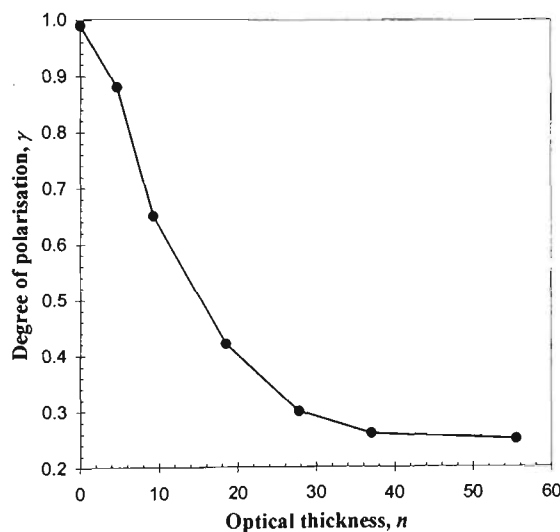


Figure 5.10: Degree of polarisation,  $\gamma$ , for sample set D as a function of the optical thickness,  $n$ . The numerical aperture of the imaging objective is 0.75.

It is seen from figures 5.3(c), 5.3(d), 5.5(b) and 5.6(b) that the degree of polarisation,  $\gamma$ , approaches a non-zero background even when  $n > 20$ . Even in a region where all photons are scattered and are totally depolarised, for example, sample set D illustrated in figure 5.10, the non-zero asymptotic value of the degree of polarisation,  $\gamma$ , is approximately 0.24 at an optical thickness,  $n$ , of 55. The reason for this phenomenon can be explained as follows.

For a reflection scanning microscope with large area detectors the detected signal always includes a contribution from surfaces that are not in the focal volume of the imaging objective. In the case of the sample cells used in this experiment this part of the contribution is primarily due to reflections from the glass cell surfaces. Since the incident light is polarised, the reflected light from the glass cell surfaces has almost the same polarisation direction as the incident beam and only contributes an added offset to the parallel polarisation intensity,  $I_p$ . Thus the degree of polarisation,  $\gamma$ , may be artificially increased, which results in the shifting of the asymptotic value of the degree of polarisation,  $\gamma$ , from zero to a value which depends on the numerical aperture of the imaging objective and the strength of the scattering signal (figure 5.5(b) and 5.6(b)). It should be noted that the effect of the added intensity contribution on the asymptotic value of the degree of polarisation,  $\gamma$ , becomes more pronounced, when the optical thickness,  $n$ , is large and the corresponding intensity originating from the sample is weak. Since this added signal contribution results only in an intensity offset it does not affect the transverse resolution,  $\alpha$ , achievable. This background contribution can be removed

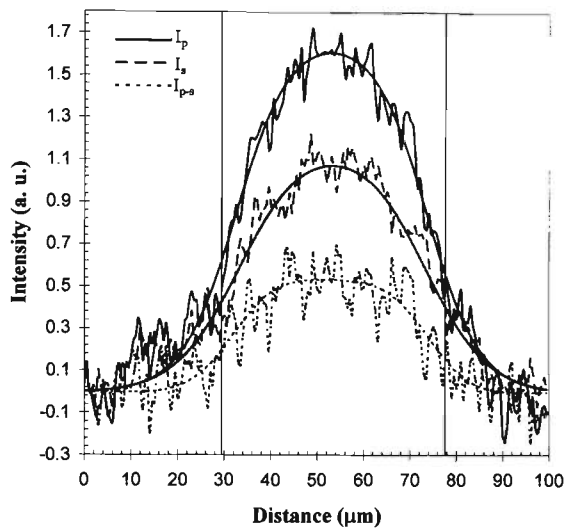
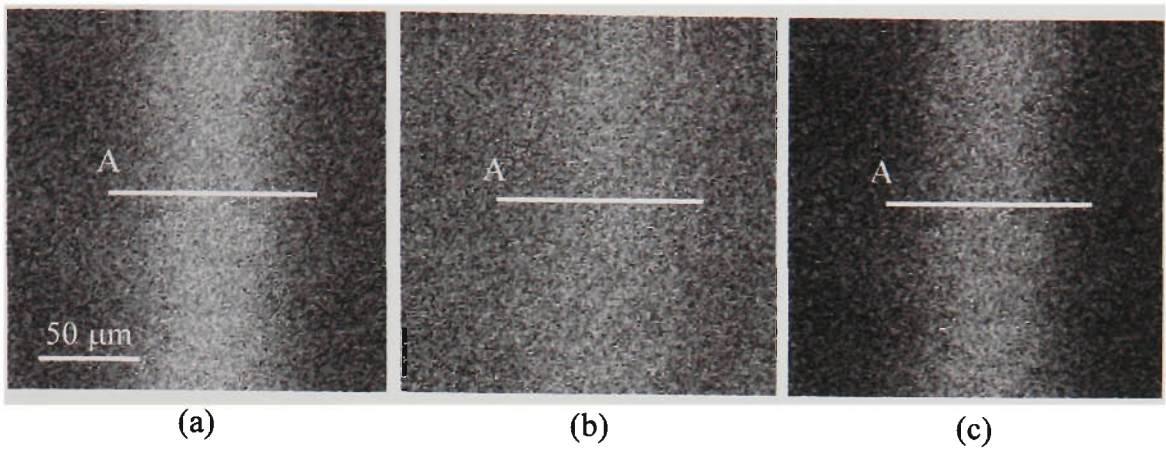
in image processing or reduced to negligible amounts by anti-reflection coating on all surfaces of the glass cell.

The goal of microscopic imaging is to obtain high resolution with a help of a high numerical aperture objective. Although a high numerical aperture objective gives a narrow diffraction spot at its focus, and therefore gives a high-resolution image if scattered photons are negligible, there is a problem when a high numerical aperture objective is used to image through a turbid medium. Scattered photons propagating at higher angles through such an objective result in longer path lengths that the photons traverse, which effectively increases the average number of scattering events,  $n$ , experienced by the photons. Therefore the number of photons maintaining the initial degree of polarisation,  $\gamma$ , can be reduced if a high numerical aperture objective is used (refer to figure 4.19). A lower numerical aperture objective rejects more scattered photons travelling at higher angles. As a result image resolution is higher. Therefore, for a high numerical aperture objective, the degradation of image resolution caused by scattering photons is severe if no other gating mechanism is used.

This effect is further demonstrated in figures 5.3(a) and 5.3(b), which show that an objective of  $NA = 0.25$  gives higher resolution than an objective of  $NA = 0.75$  when the optical thickness,  $n$ , is small and the depolarisation for each scattering event is strong. A comparison of the resolution improvement between differential polarisation-gating and conventional polarisation-gating reveals that

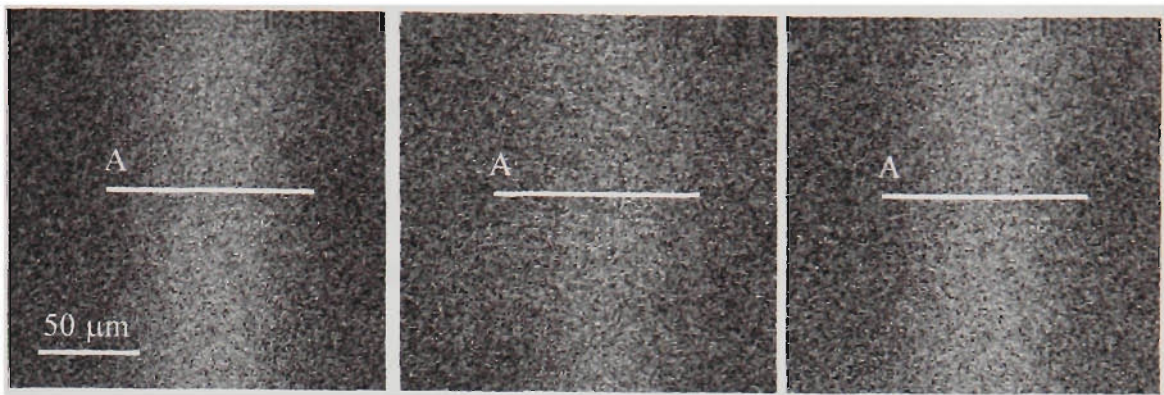
$P_3|_{NA=0.25} > P_3|_{NA=0.75}$ . Thus, using a smaller numerical aperture objective in differential polarisation-gating leads to a stronger improvement.

Another example of demonstrating the effect of the numerical aperture on differential polarisation-gating is depicted in figures 5.11 and 5.12, in which sample 6 (table 5.2) was imaged. Figures 5.11 and 5.12 show typical images of an embedded 48  $\mu\text{m}$  bar for conventional polarisation gating (figures 5.11(a) and 5.12(a)), perpendicular polarisation-gating (figures 5.11(b) and 5.12(b)) and differential polarisation-gating (figures 5.11(c) and 5.12(c)) mechanisms for,  $NA = 0.25$  and  $NA = 0.75$ , respectively. Figures 5.11(d) and 5.12(d) give corresponding cross sections and fitted SDS curves. In this example the depolarisation for each scattering event is weak because the anisotropy value,  $g$ , is 0.92, resulting in the degree of polarisation,  $\gamma$ , of 0.52 and 0.41 for  $NA = 0.25$  and  $NA = 0.75$ , respectively. The measured transverse resolution for  $NA = 0.25$  (figure 5.11(d)) is 46.6  $\mu\text{m}$ , 52.1  $\mu\text{m}$  and 36.6  $\mu\text{m}$  for conventional polarisation-gating ( $\alpha_p$ ), perpendicular polarisation-gating ( $\alpha_s$ ) and differential polarisation-gating ( $\alpha_{p-s}$ ), respectively. The measured transverse resolution of an embedded bar for  $NA = 0.75$  (figure 5.12(d)) is 61.9  $\mu\text{m}$ , 64.4  $\mu\text{m}$  and 47.5  $\mu\text{m}$ , for conventional polarisation-gating ( $\alpha_p$ ), perpendicular polarisation-gating ( $\alpha_s$ ) and differential polarisation-gating ( $\alpha_{p-s}$ ), respectively. It is clearly seen that using an objective of numerical aperture 0.25 gives higher transverse resolution than using an objective of numerical aperture 0.75 for all polarisation-gating mechanisms. In particular, when differential polarisation-gating ( $I_{p-s}$ ) is used, the overall shape of the



(d)

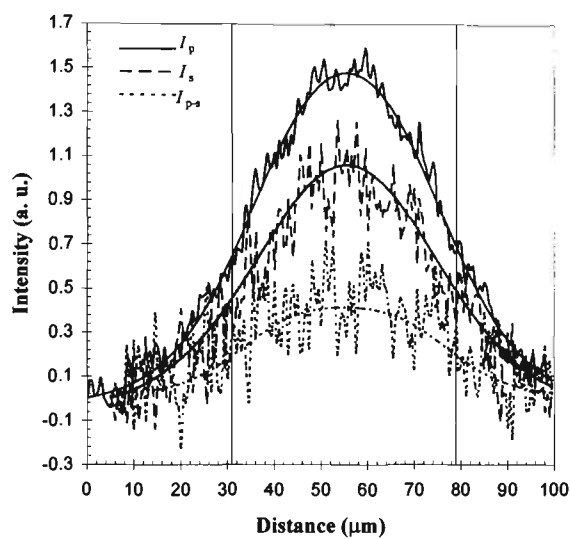
Figure 5.11: Measured images for sample 6 (table 5.2) for CPG (a), PPG (b) and DPG (c) techniques. The intensity of the images is normalised to unity. (d) includes the measured edge responses corresponding to CPG ( $I_p$ ), PPG ( $I_s$ ) and DPG ( $I_{p-s}$ ) techniques. The vertical grey line represents the ideal edge position. The numerical aperture of the imaging objective is 0.25.



(a)

(b)

(c)



(d)

Figure 5.12: Measured images for sample6 (table 5.2) for CPG (a), PPG (b) and DPG (c) techniques. The intensity of the images is normalised to unity. (d) includes the measured edge responses corresponding to CPG ( $I_p$ ), PPG ( $I_s$ ) and DPG ( $I_{p-s}$ ) techniques. The vertical grey line represents the ideal edge position. The numerical aperture of the imaging objective is 0.75.

transverse edge response is closer to that of the embedded bar, which is indicated by the flat top in figure 5.11(d). This property results from the suppression of scattered photons by differential polarisation-gating. Unlike figures 5.3(a) and 5.3(b), it is found that the resolution improvement between differential polarisation-gating and conventional polarisation-gating for a high numerical aperture objective is stronger than that for a low numerical aperture objective, i.e.

$$P_3|_{NA=0.25} < P_3|_{NA=0.75}.$$

It should be also noted the signal-to-noise ratio (SNR) of the edge responses for the objective of numerical aperture 0.25 (figure 5.11(d)) (in this chapter SNR is quantified by the ratio of the peak-to-peak signal level to the peak-to-peak noise level) is clearly higher than that for the objective of numerical aperture 0.75 (figure 5.12(d)). This property is another indication that highly scattered photons are suppressed more efficiently in the former case. Due to the random noise associated with the scattering process the edge response by perpendicular polarisation-gating ( $I_s$ ) has a lower SNR than that by conventional polarisation-gating ( $I_p$ ) since more scattered photons are collected in the former case. Therefore, even though the transverse resolution for differential polarisation-gating ( $\alpha_{p-s}$ ) is higher than conventional polarisation-gating ( $\alpha_p$ ), the differential polarisation-gated signal ( $I_{p-s}$ ) has a lower SNR, since the SNR for the differential polarisation-gated signal ( $I_{p-s}$ ) is mainly determined by that of the signal by perpendicular polarisation-gating ( $I_s$ ). However, this effect can be minimised if an average process is taken over many sample traces for signals obtained by conventional polarisation-gating and

perpendicular polarisation-gating, before the differential polarisation-gated signal is calculated.

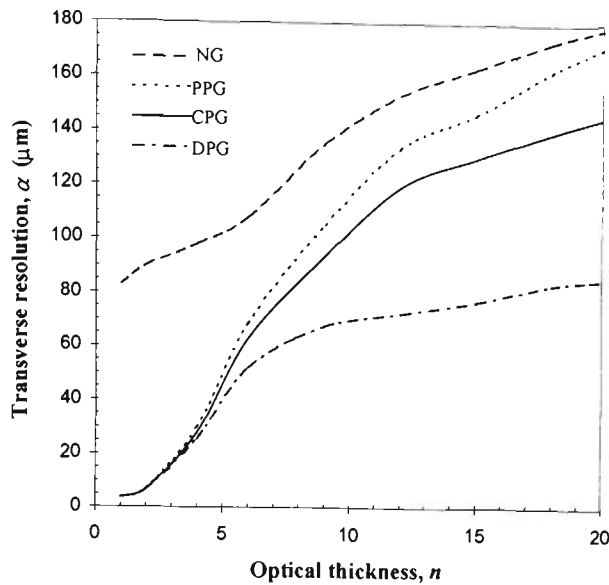
The effectiveness of differential polarisation-gating in suppressing diffusing photons in microscopic imaging depends on a) the number of unscattered photons and b) the degree of polarisation,  $\gamma$ , of the scattered photons. Three working regimes have been introduced according to these two conditions (Morgan *et al.*, 1997), and are characterised as follows: Regime 1: unscattered light is present and scattered light retains polarisation, regime 2: unscattered light is present and scattered light is depolarised or there is no unscattered light but scattered light retains polarisation, and regime 3: there is no unscattered light and scattered light depolarised. Each turbid sample used in this experimental investigation (see table 5.1) experiences 2 or 3 regimes as the optical thickness,  $n$ , is increased. For sample sets A and B regimes 1 and 2 are experienced. In these two cases scattered photons depolarise fast but there is a significant proportion of unscattered photons. In these regimes conventional polarisation-gating is effective but not as effective as differential polarisation-gating as illustrated in figures 5.3 and 5.5. For sample sets C, D and E all 3 regimes are experienced as the optical thickness,  $n$ , is increased. In other words, scattered photons depolarise slower and the number of unscattered or less scattered photons is significantly reduced and eventually they are no longer detectable (figures 5.6 and 5.10). Both conventional polarisation-gating and differential polarisation-gating are thus less effective in regime 3 ( $n > 20$ ) and play no role in improving image resolution as illustrated in figure 5.6.

## 5.4 Theoretical comparison

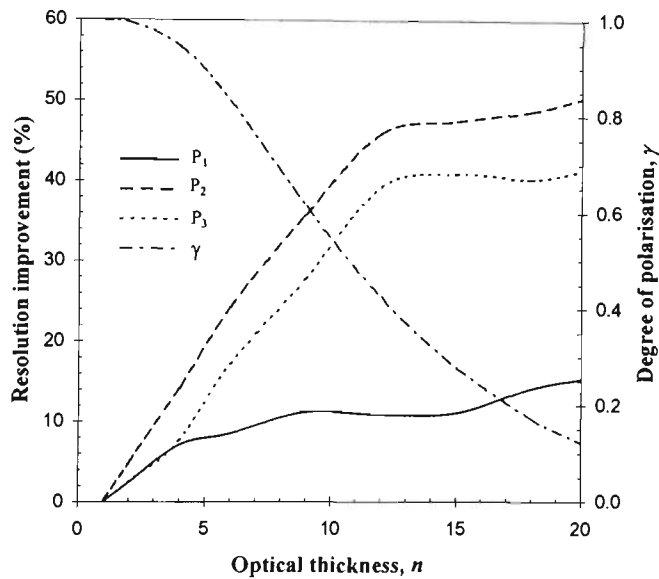
In this section, with the use of the Monte-Carlo simulation model the experimental trends seen for turbid sample set C are qualitatively demonstrated. The theoretical microscope modelled in this section was based on the transmission microscope illustrated in figure 3.4. Theoretically data are presented for a transmission system since at this current time the reflection optical microscope employing polarisation has not been modelled by Dr. X. Gan and Professor M. Gu.

Figure 5.13(a) demonstrates the transverse resolution as a function of the optical thickness,  $n$ , for no-gating ( $\alpha_{p+s}$ ), conventional polarisation-gating ( $\alpha_p$ ), perpendicular polarisation-gating ( $\alpha_s$ ) and differential polarisation-gating ( $\alpha_{p-s}$ ) (Gan *et al.*, 1999). Figure 5.13(b) demonstrates the resolution improvement between conventional polarisation-gating and no-gating ( $P_1$ ), differential polarisation-gating and no-gating ( $P_2$ ) and differential polarisation-gating and conventional polarisation-gating ( $P_3$ ) when an infinitely large detector is employed (Gan *et al.*, 1999).

These results confirm the experimental trends seen in figure 5.6(a), and demonstrate that differential polarisation-gating is the most effective gating mechanism in this regime.



(a)



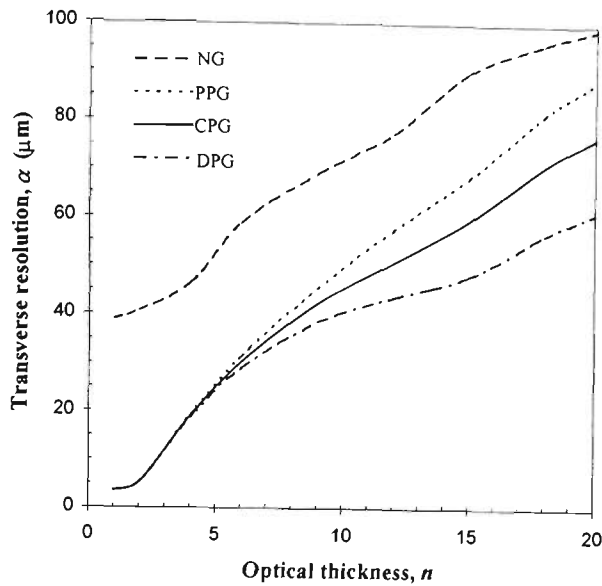
(b)

Figure 5.13. Resolution performance for sample set C at  $NA = 0.25$ . (a) is the calculated transverse resolution as a function of the optical thickness,  $n$ , for NG ( $\alpha_{p+s}$ ), CPG ( $\alpha_p$ ), PPG ( $\alpha_s$ ) and DPG ( $\alpha_{p-s}$ ). (b) is the resolution improvement and the degree of polarisation,  $\gamma$ , as a function of the optical thickness,  $n$ . A comparison is given between CPG and NG ( $P_1$ ), DPG and NG ( $P_2$ ) and DPG and CPG ( $P_3$ ). These curves were calculated by Dr. X. Gan.

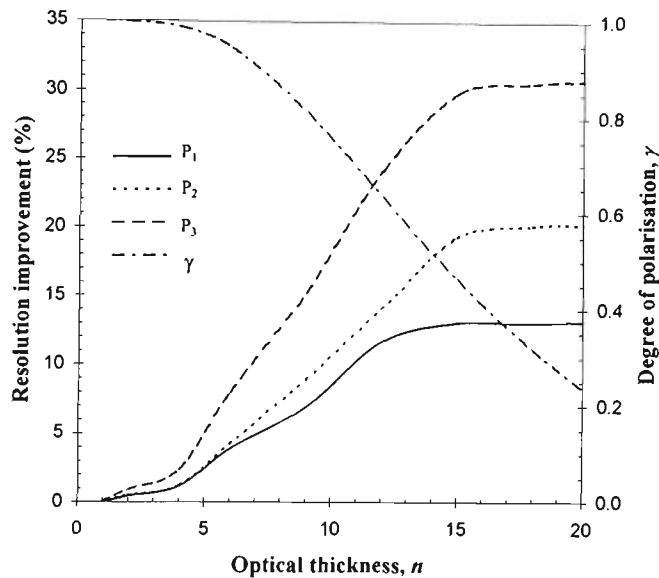
Figure 5.14(a) demonstrates the theoretically improved transverse resolution as a function of the optical thickness,  $n$ , with the introduction of a 100  $\mu\text{m}$  pinhole, for no-gating ( $\alpha_{p+s}$ ), conventional polarisation-gating ( $\alpha_p$ ), perpendicular polarisation-gating ( $\alpha_s$ ) and differential polarisation-gating ( $\alpha_{p-s}$ ). Figure 5.14(b) demonstrates the resolution improvement between conventional polarisation-gating and no-gating ( $P_1$ ), differential polarisation-gating and no-gating ( $P_2$ ) and differential polarisation-gating and conventional polarisation-gating ( $P_3$ ) when a 100  $\mu\text{m}$  pinhole is placed in front of the detector (Gan *et al.*, 1999).

Figure 5.14 theoretically confirms that a finite sized pinhole can significantly improve the transverse resolution,  $\alpha$ , achievable when employed in conjunction with polarisation-gating and that the resolution improvement achieved with polarisation-gating is reduced with the introduction of the spatial pinhole (see figure 5.9).

Figures 5.13(b) and 5.14(b) also confirm the additional suppression of scattered photons with a finite sized pinhole, which is indicated by an increase in the degree of polarisation,  $\gamma$ .



(a)



(b)

Figure 5.14: Resolution performance for sample set C at  $NA = 0.25$  and a pinhole of diameter  $100 \mu\text{m}$ . (a) is the calculated transverse resolution as a function of the optical thickness,  $n$ , for NG ( $\alpha_{p+s}$ ), CPG ( $\alpha_p$ ), PPG ( $\alpha_s$ ) and DPG ( $\alpha_{p-s}$ ). (b) is the resolution improvement and the degree of polarisation,  $\gamma$ , as a function of the optical thickness,  $n$ . A comparison is given between CPG and NG ( $P_1$ ), DPG and NG ( $P_2$ ) and DPG and CPG ( $P_3$ ). These curves were calculated by Dr. X. Gan.

It should be pointed out that the speed of depolarisation of scattered photons in the experimental work (figures 5.6 and 5.9) is faster than that predicted by the Monte-Carlo simulation (see figure 5.13 and 5.14). This phenomenon is caused by the fact that the theoretical results were calculated in a transmission optical microscope and not a reflection optical microscope. In a transmission microscope, backward scattered photons, which have a lower degree of polarisation,  $\gamma$ , than the forward scattered photons are not collected. As a result, for a given optical thickness,  $n$ , the degree of polarisation,  $\gamma$ , in the forward direction (i.e. transmission) is significantly larger than that in the backward (reflection) direction.

## 5.5 Conclusion

In conclusion, the transverse resolution,  $\alpha$ , achievable for an image of a bar embedded within turbid media has been shown to depend directly on the specific characteristics of the turbid media and polarisation-gating techniques employed to suppress unwanted scattered photons. The size of scattering particles (i.e. scattering anisotropy) within turbid media determines the effectiveness of polarisation-gating and therefore the resolution improvement achievable. It has been demonstrated that polarisation-gating is more effective in turbid media consisting of smaller scattering particles (i.e. low anisotropy value). The differential polarisation-gated signal can produce a resolution improvement by up to 50% when compared to the non-gated and conventional polarisation-gated signals, as long as there is a portion of partially polarised light detectable.

# Chapter 6

## Fluorescence imaging in turbid media

### 6.1 Introduction

Fluorescence microscopy and spectroscopy are important tools in medical applications since they allow specific probing of biological characteristics (e.g. cell nuclei, cytoplasm etc., and can be used to distinguish between healthy and unhealthy tissue (Alfano *et al.*, 1984)). Recently multi-photon (in particular two-photon) microscopy (Denk *et al.*, 1990) has been extensively used due to its significant advantages (e.g. reduced scattering, ultra-violet excitation, inherent optical sectioning, reduced photodamage and photon toxicity etc.) over conventional (single-photon) fluorescence microscopy (refer to section 2.3).

Until recently most fluorescence microscopy work has been performed on stained geometrically thin slices (~10-20  $\mu\text{m}$  thick) excised from the specimen under investigation. Thus, optical scattering is minimal which allows high quality image to be obtained. However there is a push towards the development of *in vivo* imaging systems (refer to section 1.1) that are less invasive for the biological

specimen under investigation. It should be noted that most *in vivo* imaging and spectroscopy systems rely on autofluorescence signatures of the biological specimen under investigation (see section 6.3.1).

Since the required information can be at deep depths within the biological specimen under investigation optical scattering can have a significant effect on the image quality achievable. Thus, the effect of optical scattering on fluorescence image quality needs to be understood if high quality images are to be obtained at significant depths into the biological specimen under investigation.

As yet there has been no extensive study into the effect of scattering on two-photon fluorescence image quality except for the recent work on penetration depth of two-photon excitation (Daria *et al.*, 1998; Blanca and Saloma, 1998; Ying *et al.*, 1999). This chapter provides both qualitative and quantitative data to demonstrate the performance of both single-photon and two-photon microscopy in imaging through artificial turbid media with different scattering characteristics (Schilders and Gu, 1999b).

Fluorescence spectroscopy under single-photon excitation has a number of limitations arising from the linear excitation probability (refer to section 2.3.2.2). The non-linear excitation probability of multi-photon excitation (in particular two-photon excitation) provides significant improvement over single-photon excitation since it allows more confined probing of the biological specimen under inspection. As a result, three-dimensional spectroscopy signatures can be obtained at localised areas in thick biological specimens (Schilders and Gu, 1999a).

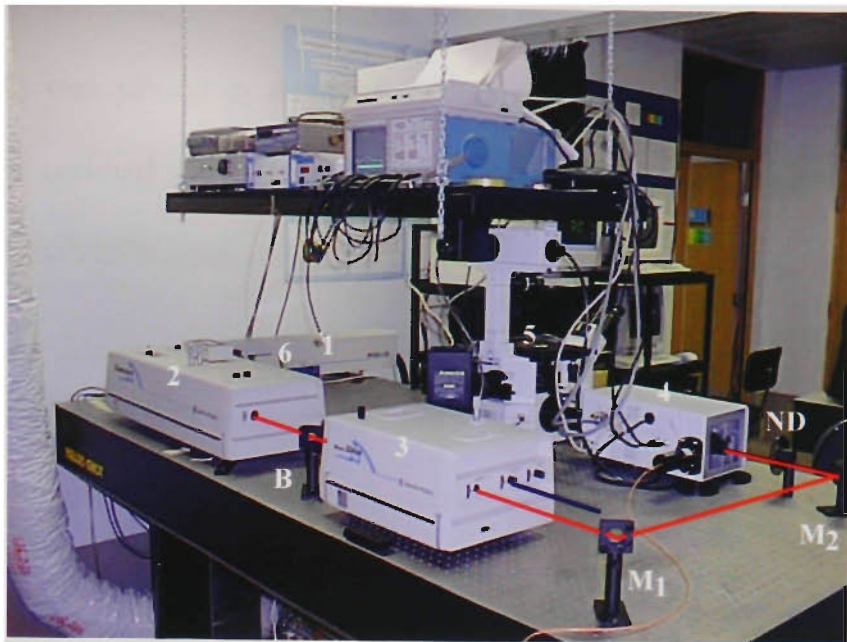
This chapter is organised into the following sections: Section 6.2. demonstrates the performance of single-photon and two-photon microscopy on image quality for different sized scatterers. Section 6.3 demonstrates the advantage of using two-photon excitation to obtain three-dimensional spectroscopic information from biological tissue. Finally a chapter conclusion is presented in section 6.4.

## 6.2 Fluorescence imaging in a reflection optical microscope

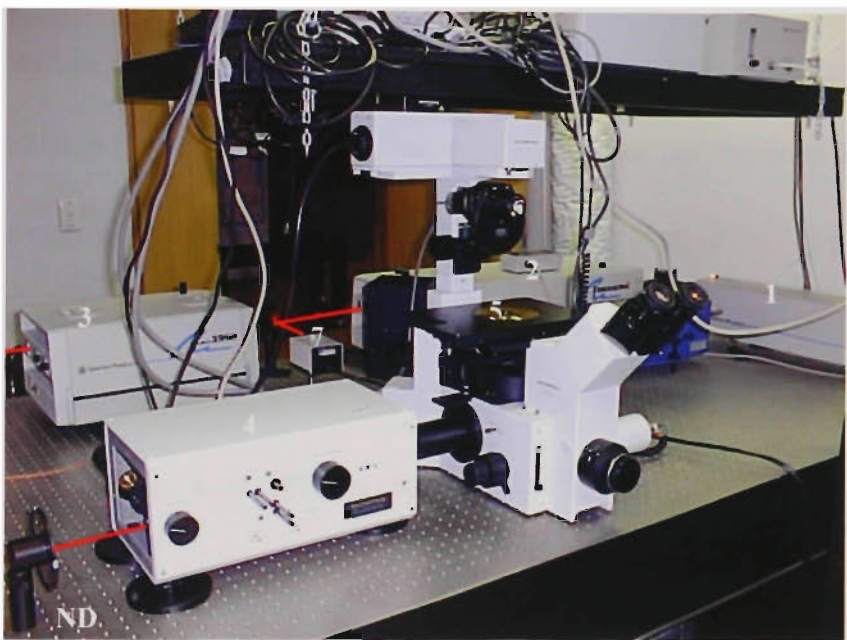
### 6.2.1 Experimental details

#### 6.2.1.1 Experimental setup

The fluorescence work presented in this chapter was performed on the system illustrated in figure 6.1. Figure 6.1(a) illustrates the schematic diagram of the laser system used for two-photon excitation, while figure 6.1(b) illustrates the modified inverted commercial fluorescence confocal microscope (Olympus FluoVIEW™) used for imaging. The FluoVIEW scan unit is designed for single-photon excitation work and has a fibre delivered Ar<sup>+</sup> laser ( $\lambda = 488$  nm) attached. To perform two-photon imaging an ultrashort pulsed Ti:Sapphire laser (Spectra Physics, Tsunami) was coupled via a pair of ultrafast mirrors M<sub>1</sub> and M<sub>2</sub> through a side port of the FluoVIEW scan unit. The laser produced pulses of ~70 fs at wavelengths between 800-900 nm with a repetition rate of 82 MHz. The excitation light was linearly polarized by the insertion of a polariser in the beam path. The original dichroic mirror in the FluoVIEW scan unit (needed for single-photon excitation) was changed to a short-pass dichroic mirror (<1% transmission



(a)



(b)

Figure 6.1: Photographs of the experimental fluorescence scanning optical microscope. (a) laser system and (b) FluoVIEW microscope system. 1: Millennium pump laser; 2: Tsunami; 3: frequency doubler (not used in this work); 4: FluoVIEW scan unit; 5: inverted microscope; 6: autocorrelator; 7: spectrum analyser; B: beamsplitter; M: mirrors; ND: neutral density filter.

efficiency at wavelengths  $> 650$  nm) to allow two-photon excitation. A short pass filter (KG1) was placed in front of the entrance slit of the photomultipliers to remove any residual pump leakage through the dichroic mirror and scattering within the FluoVIEW scan unit.

The fluorescence spectra originating from a sample under inspection was measured by a spectrum analyzer (resolution  $\sim 5$  nm) attached to the FluoVIEW scan unit.

#### 6.2.1.2 Sample preparation

In this work the evaluation of image quality is determined by two objects embedded within turbid media of different characteristics. The first embedded object is a cluster layer of  $10 \mu\text{m}$  (diameter) fluorescent polystyrene microspheres (standard deviation =  $1.028 \mu\text{m}$ ) and the second embedded object is a  $1$  mm wide fluorescent polymer (Cheng, 1996) edge (see section 6.2.3 for further details). The peak fluorescence wavelength in both cases was measured to be  $\sim 520$  nm at excitation wavelengths,  $\lambda$ , of  $488$  nm (single-photon) and  $800$  nm (two-photon).

Due to different wavelengths associated with single-photon excitation ( $\lambda = 488$  nm), two-photon excitation ( $\lambda = 800$  nm) and fluorescence (peak  $\lambda \sim 520$ ), new scattering-mean-free-path lengths,  $l_s$ , and the anisotropy values,  $g$ , need to be calculated for the four sizes of polystyrene microsphere used in this work.

The scattering-mean-free-path lengths,  $l_s$ , and the anisotropy values,  $g$ , for the four types of polystyrene microspheres use in this work for wavelengths,  $\lambda$ , of  $488$  nm,

520 nm and 800 nm are presented in tables 6.1(a), 6.1(b) and 6.1(c), respectively.

Sphere diameter, $\kappa$ ( $\mu\text{m}$ )	Geometric cross-section, $\sigma_g$ ( $\mu\text{m}^2$ )	Concent. $\rho$ (part./ $\mu\text{m}^3$ )	Relative particle size, $A$ ( $a/\lambda$ )	Scattering efficiency, $Q_s = \sigma_s/\sigma_g$	Scattering cross-section, $\sigma_s$ ( $\mu\text{m}^2$ )	smfp length, $l_s$ ( $\mu\text{m}$ )	Anisotropy value, $g$
0.107	0.009	37.11	0.1096	0.0239	$2.16 \times 10^{-4}$	124.9	0.146
0.202	0.032	5.52	0.2069	0.1586	$5.07 \times 10^{-3}$	35.7	0.54
0.48	0.181	0.411	0.4918	1.1896	$2.15 \times 10^{-1}$	11.3	0.86
1.056	0.876	0.038	1.0819	3.4931	3.06	8.6	0.93

(a)

Sphere diameter, $\kappa$ ( $\mu\text{m}$ )	Geometric cross-section, $\sigma_g$ ( $\mu\text{m}^2$ )	Concent. $\rho$ (part./ $\mu\text{m}^3$ )	Relative particle size, $A$ ( $a/\lambda$ )	Scattering efficiency, $Q_s = \sigma_s/\sigma_g$	Scattering cross-section, $\sigma_s$ ( $\mu\text{m}^2$ )	smfp length, $l_s$ ( $\mu\text{m}$ )	Anisotropy value, $g$
0.107	0.009	37.11	0.1029	0.0198	$1.78 \times 10^{-4}$	151.3	0.131
0.202	0.032	5.52	0.1942	0.1356	$4.34 \times 10^{-3}$	41.8	0.482
0.48	0.181	0.411	0.4615	1.0566	$1.91 \times 10^{-1}$	12.7	0.851
1.056	0.876	0.038	1.0154	3.368	2.95	8.9	0.92

(b)

Sphere diameter, $\kappa$ ( $\mu\text{m}$ )	Geometric cross-section, $\sigma_g$ ( $\mu\text{m}^2$ )	Concent. $\rho$ (part./ $\mu\text{m}^3$ )	Relative particle size, $A$ ( $a/\lambda$ )	Scattering efficiency, $Q_s = \sigma_s/\sigma_g$	Scattering cross-section, $\sigma_s$ ( $\mu\text{m}^2$ )	smfp length, $l_s$ ( $\mu\text{m}$ )	Anisotropy value, $g$
0.107	0.009	37.11	0.0669	0.0038	$6.02 \times 10^{-3}$	786.3	0.054
0.202	0.032	5.52	0.1263	0.0389	$1.24 \times 10^{-3}$	145.38	0.20
0.48	0.181	0.411	0.3	0.4197	$7.59 \times 10^{-2}$	32.05	0.73
1.056	0.876	0.038	0.66	1.9937	1.75	15.16	0.90

(c)

Table 6.1: Calculation of the scattering-mean-free-path length,  $l_s$ , and the anisotropy value,  $g$ , for the polystyrene microspheres used in this work for a wavelength,  $\lambda$ , of (a) 488 nm (single-photon excitation), (b) 520 nm (fluorescence) and (c) 800 nm (two-photon excitation).

It should be noted that the ratio of the scattering-mean-free-path length,  $l_s$ , for two-photon (2p) and single-photon (1p) excitation (i.e.  $l_{s(2p)}/l_{s(1p)}$ ) decreases as the polystyrene microsphere size increases i.e.  $l_{s(2p)}/l_{s(1p)}$  equals 6.2, 4.1, 2.8 and 1.8 for microsphere sizes of 0.107, 0.202, 0.48 and 1.056  $\mu\text{m}$ , respectively. This suggests

that the effect of reduced scattering of the illumination source for two-photon excitation is greater for smaller size scattering particles.

A number of samples were prepared for each polystyrene microsphere size. The samples produced by each polystyrene microsphere size are grouped into sample sets A-D and their details are listed in table 6.2. The range of the microspheres sizes chosen in this research was consistent with that of scattering particles in real biological samples which do not include large scatterers ( $>1 \mu\text{m}$ ) (Morgan *et al.*, 1997; Hielsher *et al.*, 1997).

Sample set	Scattering medium	Cell thickness, $d$ ( $\mu\text{m}$ )	Optical thickness, $n$ , single-photon	Optical thickness, $n$ , two-photon	Optical thickness, $n$ , fluorescence
A	0.107 $\mu\text{m}$ polysty. microsph. in water	50 - 300	0.4 - 2.4	0.06 - 0.38	0.33 - 1.98
B	0.202 $\mu\text{m}$ polysty. microsph. in water	50 - 300	1.4 - 8.4	0.34 - 2.1	1.2 - 7.2
C	0.48 $\mu\text{m}$ polysty. microsph. in water	25 - 75	2.2 - 6.6	0.78 - 2.3	2.0 - 5.9
D	1.053 $\mu\text{m}$ polysty. microsph. in water	25 - 50	2.9 - 5.8	1.6 - 3.3	2.8 - 5.6

Table 6.2: Parameters for the specific sample sets used in the fluorescence optical microscope. The parameters were determined from Mie theory (see table 6.1).

Each turbid medium was placed in a glass cell with lateral dimensions of  $2\text{ cm} \times 1\text{ cm}$  (see figure 6.2). The thickness of the glass cell,  $d$ , was varied between  $25\text{ }\mu\text{m}$  and  $300\text{ }\mu\text{m}$ . For a given cell thickness,  $d$ , it is impossible to use a single value of the optical thickness,  $n$ , in single-photon and two-photon imaging, since the optical thickness,  $n$ , for the illumination path is different between single-photon and two-photon excitation (see table 6.2), although the collection optical thickness,  $n$ , is the same because of the same fluorescence wavelengths in both cases. Therefore in this chapter results are presented in terms of the cell thickness,  $d$ . It should be noted that the maximum cell thickness,  $d$ , which can be imaged through for a given scatterer microsphere size is limited by the strength of the detected fluorescence generated from the embedded object.

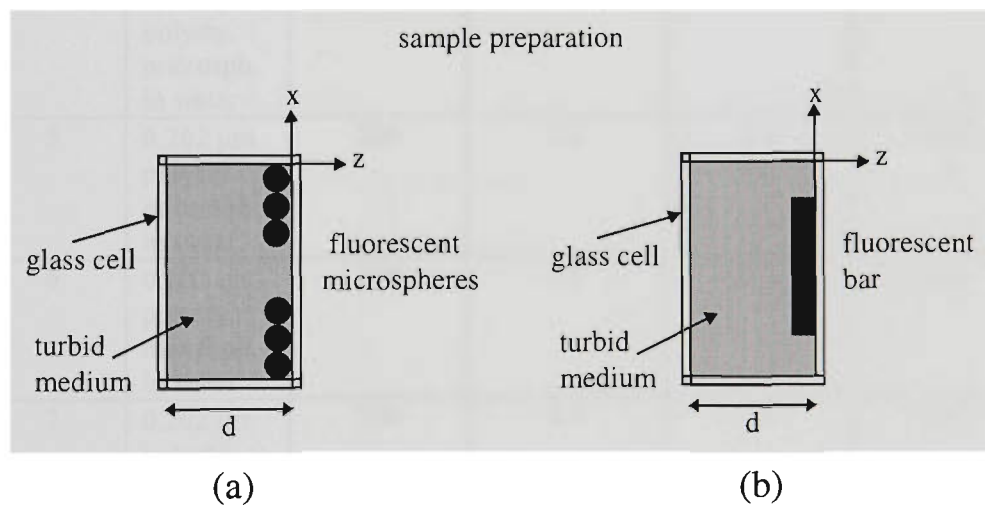


Figure 6.2: Diagram for preparing the samples with a microsphere cluster (a) and a bar embedded object (b).

To qualitatively demonstrate the image performance of single-photon and two-photon imaging in turbid media seven selected samples were imaged. The detailed parameters of the seven samples (numbered 1 to 7) are described in table 6.3.

### 6.2.2 Effect of scatterer size on image quality for fluorescent microspheres

This section qualitatively demonstrates the effect of single-photon and two-photon excitation on image quality for a 10  $\mu\text{m}$  fluorescent polystyrene microsphere embedded in samples 1-7 (see table 6.3). The numerical aperture of the objective used for all imaging in this section was 0.75 (i.e. Zeiss FLUAR 20 $\times$ /0.75  $\infty$ /0.17).

Sample number	Scattering medium	Cell thickness, $d$ ( $\mu\text{m}$ )	Optical thickness, $n$ , single-photon	Optical thickness, $n$ , two-photon	Optical thickness, $n$ , fluorescence
1	distilled water	100	-	-	-
2	0.107 $\mu\text{m}$ polysty. microsph. in water	200	1.6	0.25	1.3
3	0.202 $\mu\text{m}$ polysty. microsph. in water	100	2.8	0.68	2.4
4	0.202 $\mu\text{m}$ polysty. microsph. in water	150	4.2	1.0	3.6
5	0.202 $\mu\text{m}$ polysty. microsph. in water	200	5.6	1.4	4.8
6	0.202 $\mu\text{m}$ polysty. microsph. in water	250	7.0	1.72	6.0
7	0.202 $\mu\text{m}$ polysty. microsph. in water	300	8.4	2.1	7.2

Table 6.3: Parameters for the specific samples used in the fluorescence optical microscope. The parameters were determined by Mie theory (see table 6.1).

Imaging of a spherical microsphere embedded in a turbid medium has practical importance since it can be considered an approximate model of imaging a small tumour embedded in biological tissue. It should be pointed out that this model relies on the tumour being the only fluorescent object within the turbid media. That is, the surrounding tissue does not fluoresce, or the surrounding tissue fluoresces at a wavelength different from the tumour.

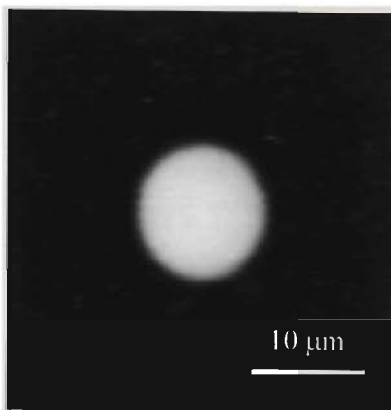


Figure 6.3: Two-photon image of a single 10  $\mu\text{m}$  fluorescence microsphere embedded within sample1 (table 6.3). The intensity of the image was normalised to unity. The numerical aperture of the imaging objective was 0.75.

A single fluorescent microsphere embedded in sample1 was imaged by two-photon excitation (see figure 6.3) to demonstrate the best image resolution and contrast achievable with the optical arrangement in figure 6.1. The image in figure 6.3 is constructed purely by unscattered photons obeying the diffraction theory of light (Born and Wolf, 1980) and therefore represents the best image quality achievable with the imaging system shown in figure 6.1.

### 6.2.2.1 Scattering suspensions of 0.107 $\mu\text{m}$ polystyrene microspheres

Figure 6.4 demonstrates the image quality when a fluorescent microsphere cluster embedded with in sample2 (see table 6.3) is imaged with single-photon (figures 6.4(a) and 6.4(b)) and two-photon (figure 6.4(c)) excitation. Figures 6.4(d), 6.4(e) and 6.4(f) demonstrate the resolution from the two microspheres marked by 'A' in figures 6.4(a), 6.4(b) and 6.4(c), respectively.

A comparison of the fluorescence images recorded for single-photon (figure 6.4(a)) and two-photon (figure 6.4(c)) excitation in a conventional scanning microscope arrangement demonstrates the effectiveness of two-photon excitation over single-photon excitation in imaging through turbid media. The improvement can be clearly seen by comparing figure 6.4(d) with figure 6.4(f), which demonstrate the image cross-section recorded at position 'A', in figures 6.4(a) and 6.4(c), respectively. For single-photon excitation (figure 6.4(d)) it is difficult to resolve the two fluorescent microspheres due to image blurring resulting from scattering. However, the two fluorescence microspheres imaged under two-photon excitation (figure 6.4(f)) can be resolved, which is indicated by the sharper edges and a flat top. The substantial improvement in image quality seen for two-photon excitation (figures 6.4(c) and 6.4(f)) is due to two primary factors. The first factor can be attributed to the smaller optical thickness,  $n$ , for two-photon excitation (see table 6.3), which results in fewer scattering events (i.e. smaller scattering cross-section) experienced by the illumination light. The second factor results from the quadratic dependence of two-photon excitation. That is, two-photon excitation generates less out-of-focus fluorescence that reduces the structural detail and contributes more scattered photons to the image (refer to figure 2.9).

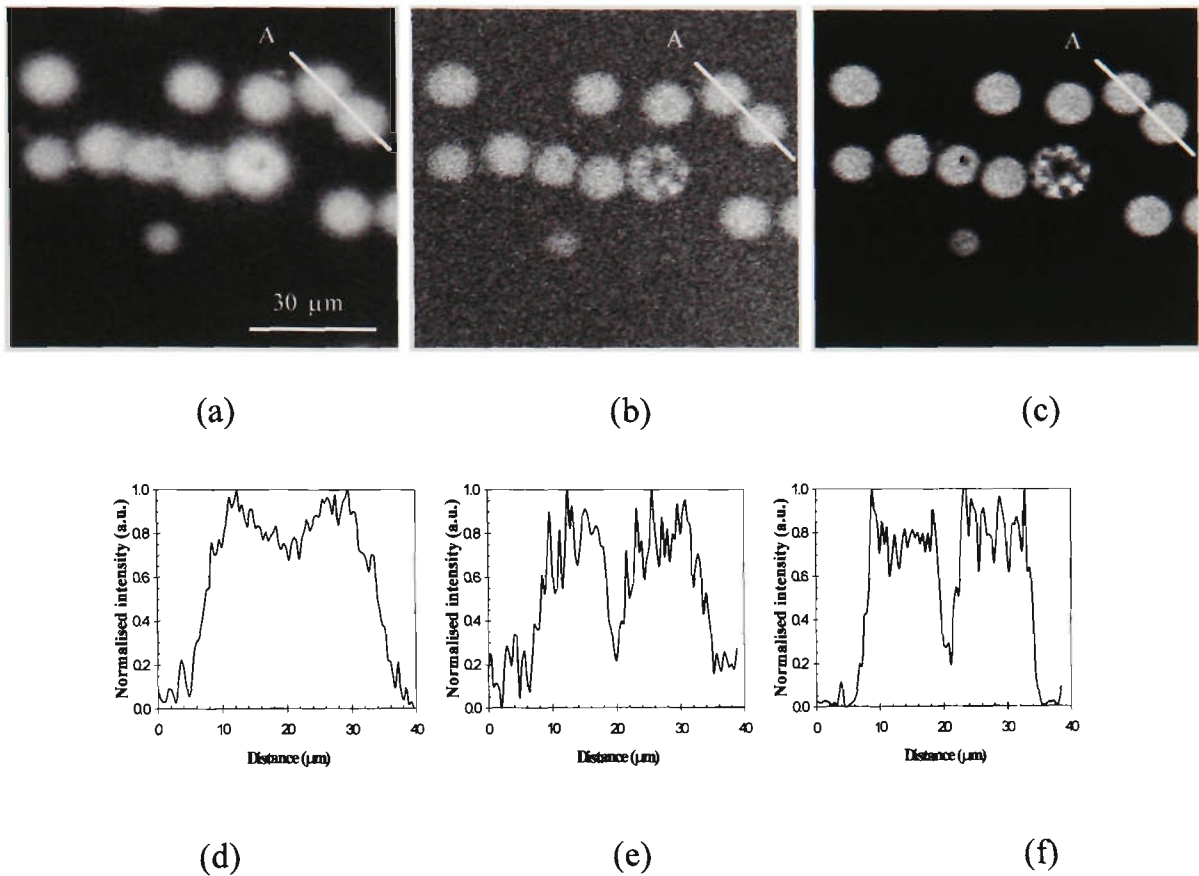


Figure 6.4: Images of a 10  $\mu\text{m}$  polystyrene microsphere cluster embedded within sample2 (table 6.3). The intensity of the images was normalised to unity. (a) Single-photon excitation without a detection pinhole; (b) single-photon excitation with a 300  $\mu\text{m}$  detection pinhole; (c) two-photon excitation without a detection pinhole. (d), (e) and (f) are cross-sections recorded at position 'A' in (a), (b) and (c), respectively. The numerical aperture of the imaging objective is 0.75.

The number of scattered photons contributing to an image can be reduced with the use of a pinhole-filter (refer to 5.3.3), since scattered photons may not intersect with the pinhole aperture due to their path deviation (refer to figure 1.1). A comparison of figures 6.4(a) and 6.4(b) demonstrates that the inclusion of a 300

$\mu\text{m}$  detection pinhole for single-photon excitation reduces the resolution deterioration (compare also figure 6.4(d) with figure 6.4(e)) caused by the out-of-focus information and the number of collected scattered photons. It should be noted that although figure 6.4(b) is imaged with a weak confocal arrangement the signal-to-noise ratio is significantly poorer than that for two-photon excitation (figure 6.4(c)), which is indicated by the noise in figure 6.4(b). This effect primarily demonstrates that even when the out-of-focus fluorescence is suppressed, under single-photon excitation, the limiting factor in obtaining high quality images is scattering of the illumination light, since the fluorescence is the same for single-photon and two-photons excitation, which results in fewer unscattered photons reaching the detector.

#### 6.2.2.2 Scattering suspensions of 0.202 $\mu\text{m}$ polystyrene microspheres

Figure 6.5 primarily demonstrates the effect of two-photon excitation on image quality for different scattering thicknesses of turbid media. A comparison of the images recorded for sample3 (see table 6.3) under single-photon (figure 6.5(a)) and two-photon (figure 6.5(b)) excitation, again confirms the poor imaging performance for single-photon excitation seen in figure 6.4. From this result it can be concluded that image deterioration for single-photon excitation is primarily due to increased scattering of the illumination light (see table 6.3).

Figure 6.5(b) to figure 6.5(f) demonstrate the performance of two-photon excitation for increasing cell thickness,  $d$ . It can be clearly seen from figure 6.5(b) to figure 6.5(f) that the limiting factor on image quality for two-photon excitation is the signal-to-noise ratio of an image, caused by scattering, because the resolution

in figure 6.5(b) to figure 6.5(f) does not change appreciably. That is, the fluorescence signal decreases quicker than the resolution. Further discussion on this issue is presented in section 6.2.4.

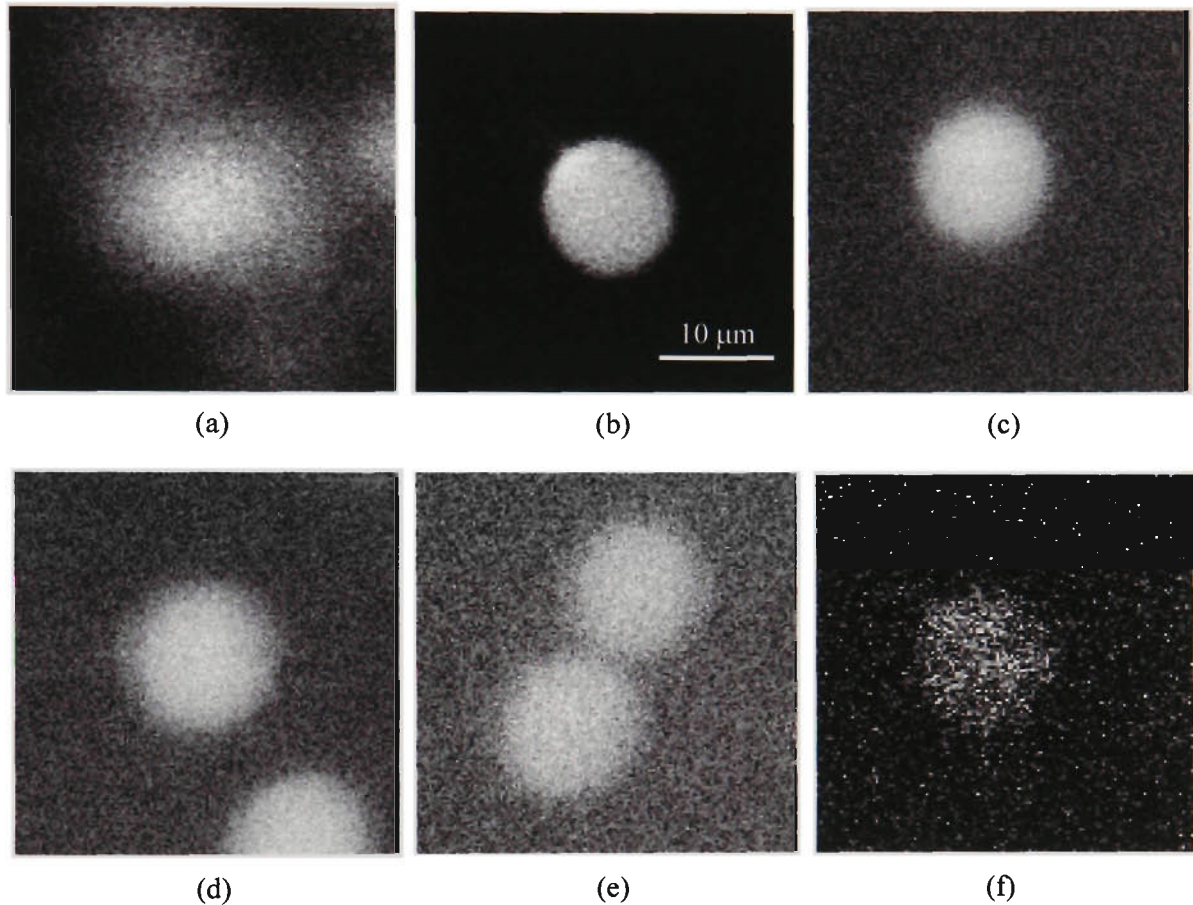


Figure 6.5: Images of 10  $\mu\text{m}$  polystyrene microspheres embedded within sample3 ((a) and (b)), sample4 (c), sample5 (d), sample6 (e) and sample7 (f). Image (a) was recorded with single-photon excitation with a 300  $\mu\text{m}$  detection pinhole. Images (b) to (f) were recorded with two-photon excitation without a detection pinhole. The intensity of the images is normalised to unity. The numerical aperture of the imaging objective is 0.75.

### 6.2.3 Effect of scatterer size on image quality for a fluorescent bar

In the previous section fluorescent microspheres were imaged under single-photon and two-photon excitation to demonstrate the effect of scattering on image quality. Unfortunately due to the fluorescent microspheres having different sizes (standard deviation of approximately 10%) no quantitative data could be obtained since the same fluorescent microsphere could not be imaged in the different turbid samples (see table 6.3). Therefore, this section further demonstrates the effects described in section 6.2.2, and provides quantitative data on the performance of single-photon and two-photon excitation by imaging a single fluorescent polymer bar embedded within the different turbid sample sets (see table 6.2). The numerical aperture of the objective used for all imaging in this section was 0.75 (i.e. Zeiss FLUAR 20×/0.75 ∞/0.17).

Figure 6.6 demonstrates the transverse resolution for a fluorescent bar embedded within sample1 under single-photon and two-photon excitation. The images in this case are constructed purely by unscattered photons obeying the diffraction theory of light (Born and Wolf, 1980) and therefore represent the maximum resolution achievable with the imaging system (figure 6.1).

The transverse resolution,  $\alpha$ , of the imaged fluorescent bar is defined as the distance between to 10% and 90% intensity points, measured from the edge response after they are fitted (TableCurve™ 2D, 1996).

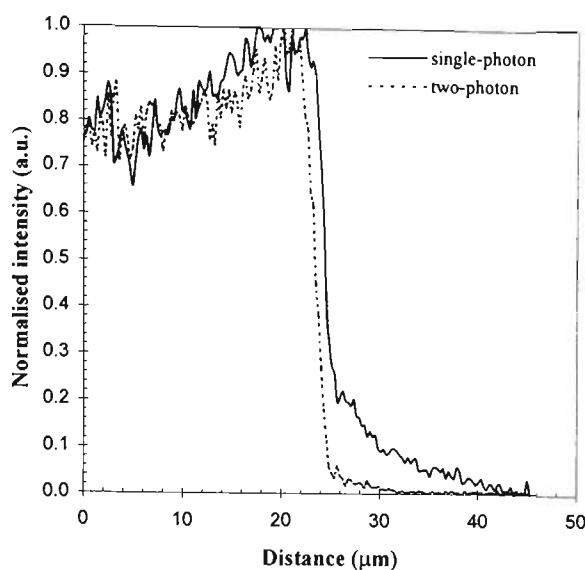
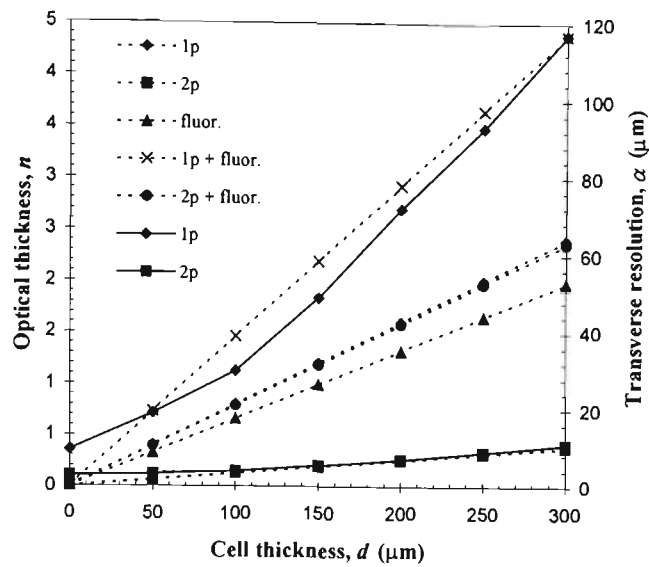


Figure 6.6: Transverse cross-section of the image of a fluorescent bar embedded within sample1 (table 6.1), recorded with single-photon excitation with a 300  $\mu\text{m}$  detection pinhole and two-photon excitation without a detection pinhole.

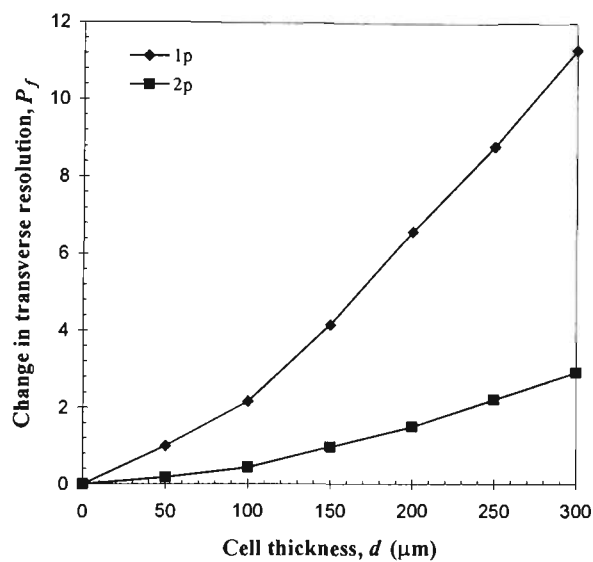
The transverse resolution,  $\alpha$ , of the fluorescent bar recorded with single-photon and two-photon excitation (see figure 6.6) was approximately 9.5  $\mu\text{m}$  and 2.8  $\mu\text{m}$ , respectively. The significant difference in transverse resolution,  $\alpha$ , between single-photon and two-photon excitation is primarily due to the presence of aberration resulting from refractive index mismatches (see section 6.2.4 for further discussion) between the air ( $N = 1$ ), the glass cell ( $N = 1.5$ ) and the distilled water ( $N = 1.33$ ).

#### 6.2.3.1 Scattering suspensions of 0.107 $\mu\text{m}$ polystyrene microspheres

Figure 6.7(a) demonstrates the transverse resolution,  $\alpha$ , and the optical thickness,  $n$ , as a function of geometric cell thickness,  $d$ , for sample set A (see table 6.2). It can be clearly seen that the transverse resolution,  $\alpha$ , for single-photon excitation



(a)



(b)

Figure 6.7: (a) Optical thickness (dashed),  $n$ , and transverse resolution (solid),  $\alpha$ , and (b) the change in transverse resolution,  $P_f$ , as a function of the cell thickness,  $d$ , for sample set A (table 6.2). 1p: single-photon excitation; 2p: two-photon excitation; fluor: fluorescence.

deteriorates significantly faster than the transverse resolution,  $\alpha$ , for two-photon excitation. To help demonstrate the magnitude of the deterioration in transverse resolution,  $\alpha$ , as the cell thickness,  $d$ , and the optical thickness,  $n$ , increase, the following change in fluorescence transverse resolution parameter was defined as follows

$$P_f = \frac{\alpha_d - \alpha_0}{\alpha_0}. \quad (6.1)$$

The change in transverse resolution,  $P_f$ , as a function of the cell thickness,  $d$ , for sample set A (see table 6.2) is illustrated in figure 6.7(b). It is seen from figure 6.7(b) that the resolution deteriorates quickly for single-photon excitation and at a cell thickness,  $d$ , of 300  $\mu\text{m}$  the transverse resolution,  $\alpha$ , is decreased by approximately 12 times compared with that at  $d = 0$ . For two-photon excitation the transverse resolution,  $\alpha$ , is decreased by approximately 5 times for the same comparison. This result confirms that two-photon excitation can significantly improve the transverse resolution,  $\alpha$ , by reducing the amount of scattering experienced by the illumination source, since the optical thickness,  $n$ , for the fluorescence is the same for both single-photon and two-photon excitation.

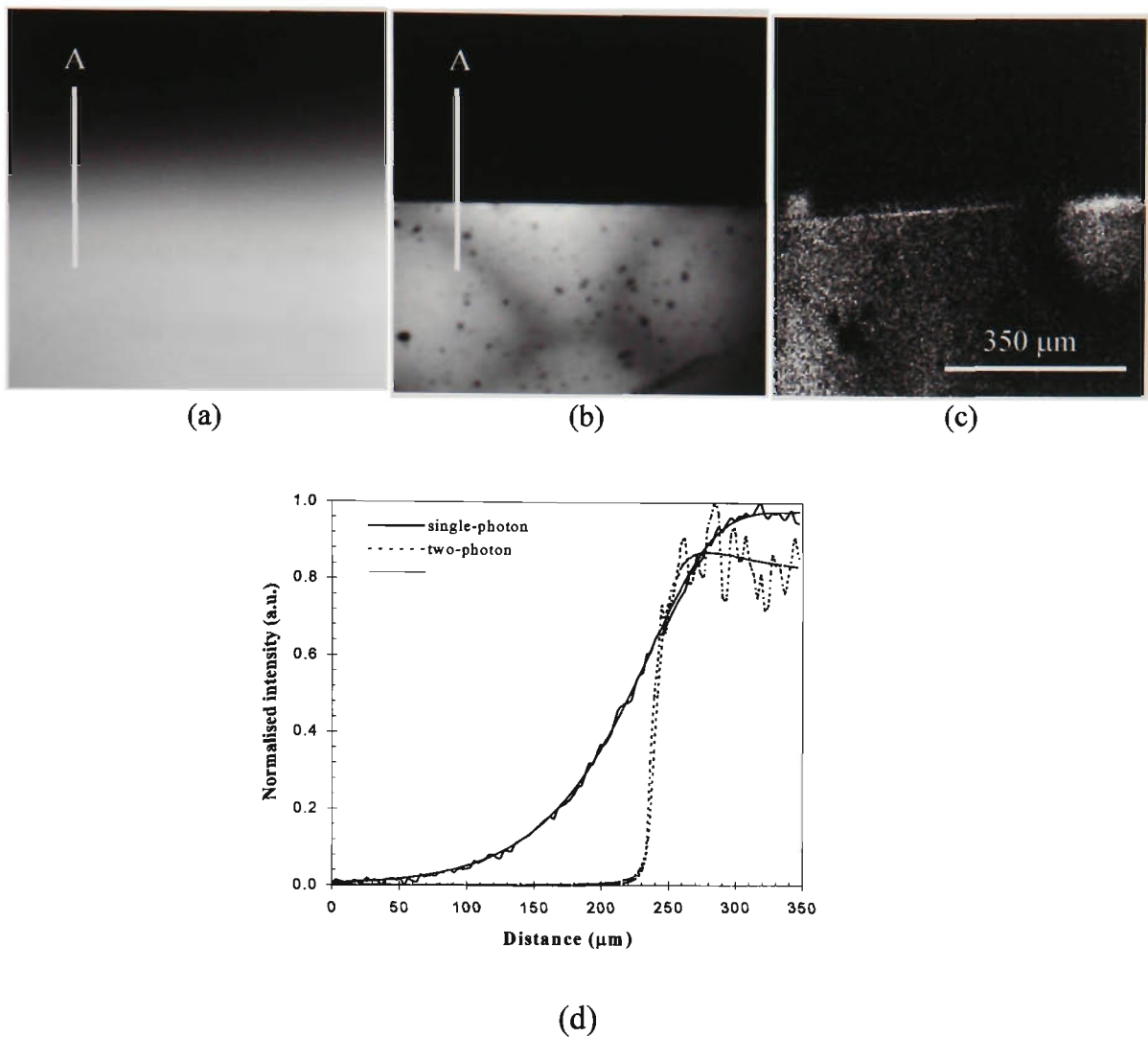


Figure 6.8: Images of a bar embedded within sample3 ((a) and (b)) and sample7 (c). (a) Single-photon excitation with a 300  $\mu\text{m}$  detection pinhole; ((b) and (c)) two-photon excitation without a detection pinhole and (d) cross-section recorded at position 'A' and corresponding fitted curves.

#### 6.2.3.2 Scattering suspensions of 0.202 $\mu\text{m}$ polystyrene microspheres

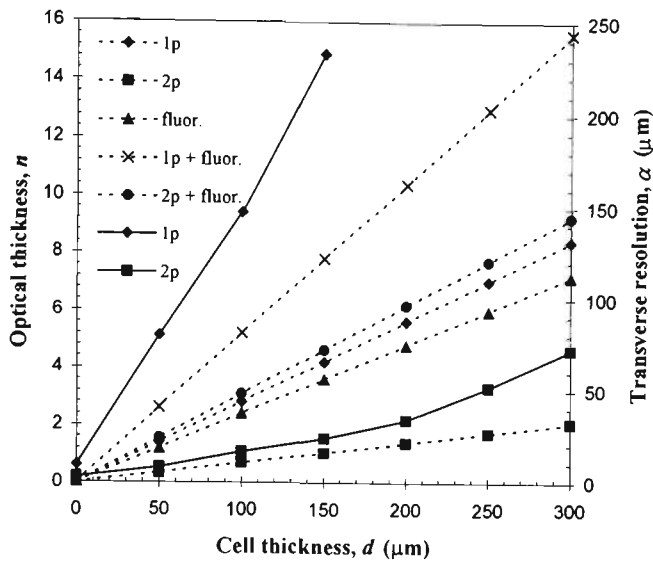
An embedded bar within sample3 (figures 6.8(a) and 6.8(b)) and sample7 (figure 6.8(c)) was imaged with single-photon (figure 6.8(a)) and two-photon (figures

6.8(b) and 6.8(c)) excitation so that the image quality can be compared with that for fluorescent microspheres recorded in the same turbid media (see figure 6.5).

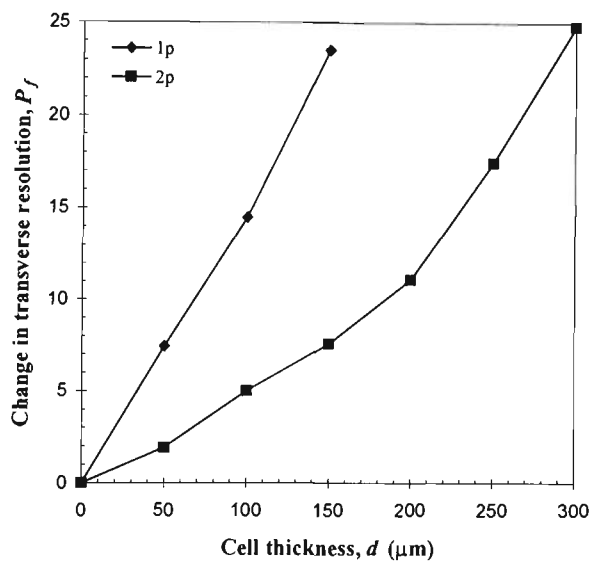
Transverse edge responses and corresponding fitted curves at the position marked by 'A' for single-photon (figure 6.8(a)) and two-photon (figure 6.8(b)) excitation for the fluorescent bar embedded in sample3 is illustrated in figure 6.8(d). The transverse resolution,  $\alpha$ , for single-photon and two-photon excitation was measured to be approximately 147  $\mu\text{m}$  and 17  $\mu\text{m}$ , respectively. This result again confirms the advantage of using two-photon excitation over single-photon excitation in imaging through turbid media.

A comparison of the images recorded for single-photon and two-photon excitation for the embedded fluorescent bar (figures 6.8(a) and 6.8(b), respectively) and fluorescent microsphere (figures 6.5(a) and 6.5(b), respectively) within sample3, shows similar characteristics. That is, the single-photon images (figures 6.5(a) and 6.8(a)) demonstrate significant scattering while the two-photon images (figures 6.5(b) and 6.8(b)) show higher resolution. Figure 6.8(c) confirms that the limiting factor for high quality imaging in sample7 is determined by the signal-to-noise ratio of the image, as was the case for the fluorescent microsphere embedded in sample7 (figure 6.5(f)), since the fluorescence signal attenuates faster than the resolution (compare figures 6.8(c) with 6.8(b)).

Figure 6.9(a) demonstrates the transverse resolution,  $\alpha$ , and the optical thickness,  $n$ , as a function of the cell thickness,  $d$ , for sample set B. As has already been seen



(a)



(b)

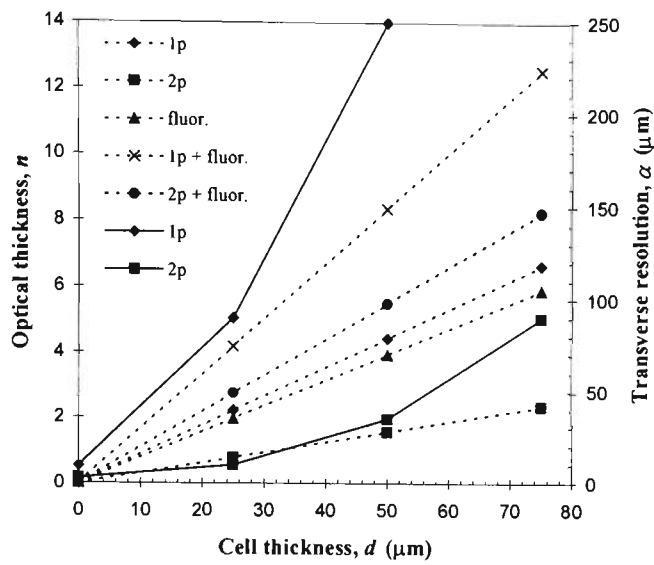
Figure 6.9: (a) Optical thickness (dashed),  $n$ , and transverse resolution (solid),  $\alpha$ , and (b) the change in transverse resolution,  $P_f$ , as a function of the cell thickness,  $d$ , for sample set B (table 6.2). 1p: single-photon excitation; 2p: two-photon excitation; fluor: fluorescence.

for sample set A, the deterioration in transverse resolution,  $\alpha$ , for single-photon excitation is significantly faster than that for two-photon excitation for sample set B. For sample set B single-photon excitation is limited to a cell thickness,  $d$ , of approximately 150  $\mu\text{m}$  due to severe blurring and attenuation of the fluorescence signal, while for two-photon excitation the cell thickness,  $d$ , is limited to approximately 300  $\mu\text{m}$  due primarily to the attenuation of the fluorescence signal (see figure 6.8(c)). Thus no reliable results could be effectively determined beyond these two regions.

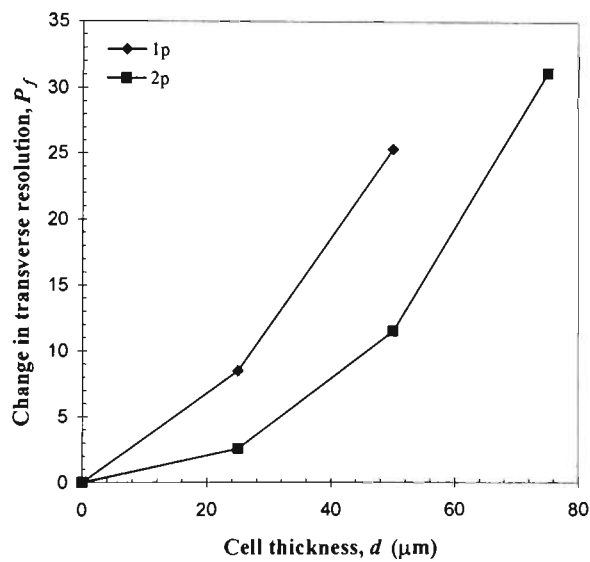
To demonstrate the improved transverse resolution,  $\alpha$ , achieved with two-photon excitation the change in transverse resolution,  $P_f$ , as a function of the cell thickness,  $d$ , for sample set B is illustrated in figure 6.9(b). At a cell thickness,  $d$ , of 150  $\mu\text{m}$  the transverse resolution has decreased by approximately 24 and 8 times compared with that at  $d = 0$ , for single-photon and two-photon excitation, respectively. This result again confirms the advantage of using two-photon excitation over single-photon excitation when imaging through turbid media.

### 6.2.3.3 Scattering suspensions of 0.48 $\mu\text{m}$ polystyrene microspheres

The optical thickness,  $n$ , and transverse resolution,  $\alpha$ , as a function of cell thickness,  $d$ , are illustrated in figure 6.10(a) for sample set C. As has been demonstrated for smaller scatterers (see sections 6.2.3.1 and 6.2.3.2) the degradation of transverse resolution,  $\alpha$ , for single-photon excitation is significantly faster than that for two-photon excitation as the cell thickness,  $d$ , increases due to



(a)



(b)

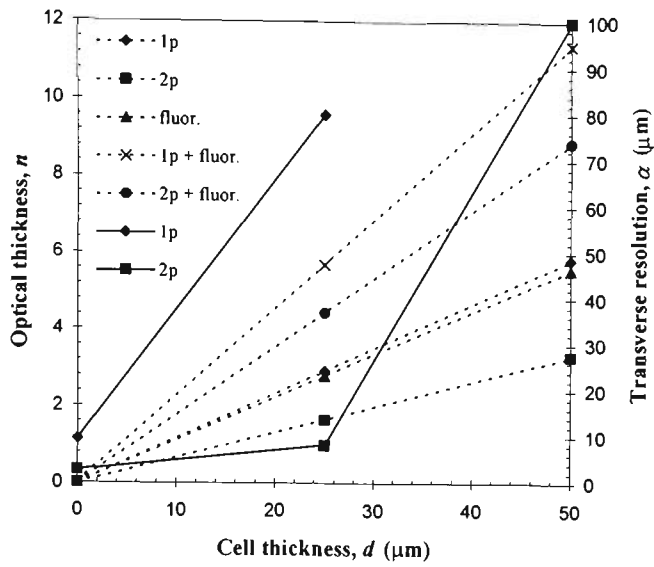
Figure 6.10: (a) Optical thickness (dashed),  $n$ , and transverse resolution (solid),  $\alpha$ , and (b) the change in transverse resolution,  $P_f$ , as a function of the cell thickness,  $d$ , for sample set C (table 6.2). 1p: single-photon excitation; 2p: two-photon excitation; fluor: fluorescence.

the increased scattering experienced by the illumination source. It should be noted that the maximum cell thickness,  $d$ , that can be penetrated through for  $0.48\ \mu\text{m}$  scatterers when two-photon excitation is employed is reduced to  $75\ \mu\text{m}$  due to the inability to generate measurable fluorescence beyond this thickness. This feature results from the increased scattering experienced by the illumination source (see table 6.2).

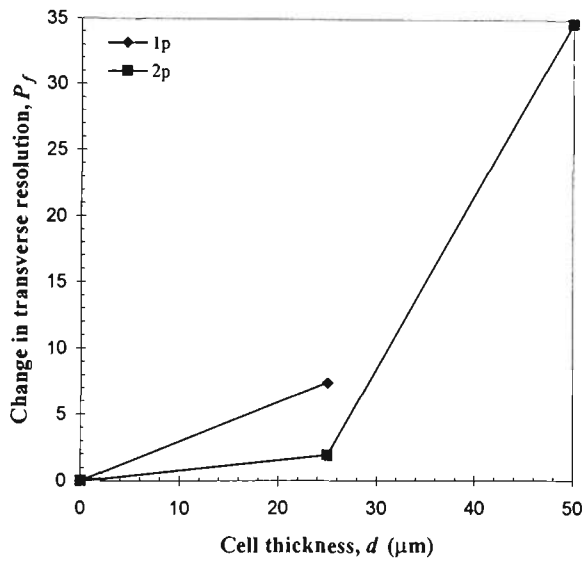
To demonstrate the improved transverse resolution,  $\alpha$ , achieved with two-photon excitation the change in transverse resolution,  $P_f$ , as a function of cell thickness,  $d$ , for sample set C is illustrated in figure 6.10(b). Unlike for the smaller scatterers (see figures 6.7(b)) the transverse resolution,  $\alpha$ , for both single-photon and two-photon excitation in figure 6.10(b) are significantly reduced as the cell thickness,  $d$ , increases. At a cell thickness,  $d$ , of  $75\ \mu\text{m}$  the transverse resolution,  $\alpha$ , is decreased by approximately 32 times for two-photon excitation. This result indicates that scattering of the illumination photons is now strong enough to play a significant role in determining the image quality achievable. This effect is discussed further detail in section 6.2.4.

#### 6.2.3.4 Scattering suspensions of $1.056\ \mu\text{m}$ polystyrene microspheres

To further demonstrate the effect of the scatterer size on transverse resolution,  $\alpha$ , as a function of the cell thickness,  $d$ , sample set D including a fluorescent bar was imaged (figure 6.11(a)). As in the case for  $0.48\ \mu\text{m}$  polystyrene microspheres the limiting cell thickness,  $d$ , is determined by the attenuation of the fluorescence



(a)



(b)

Figure 6.11: (a) Optical thickness (dashed),  $n$ , and transverse resolution (solid),  $\alpha$ , and (b) the change in transverse resolution,  $P_f$ , as a function of the cell thickness,  $d$ , for sample set D (table 6.2). 1p: single-photon excitation; 2p: two-photon excitation; fluor: fluorescence.

generated from the embedded sample, i.e. from the ability to detect generated fluorescence light. For 1.056  $\mu\text{m}$  polystyrene microspheres the cell thickness,  $d$ , was limited to 50  $\mu\text{m}$  for two-photon excitation.

figure 6.11(b) demonstrates the improved transverse resolution,  $\alpha$ , achieved with two-photon excitation and the change in transverse resolution,  $P_f$ , as a function of cell thickness,  $d$ , for sample set D.

Figure 6.11 further demonstrates the advantage of two-photon excitation over single-photon excitation in imaging through turbid media of large scattering particles, although images recorded with two-photon excitation suffer significant resolution deterioration due to substantial scattering of the illumination photons, which results in the poor imaging performance.

#### 6.2.4 Discussion

The results presented for both the fluorescent microspheres and the fluorescent bar demonstrate significant improvement in image quality when imaged with two-photon excitation, compared with those with single-photon excitation. This result is primarily due to reduced scattering (i.e. smaller optical thickness) of the illumination light for two-photon excitation for a given fluorescence wavelength.

The transverse resolution (i.e. image quality) achievable for two-photon excitation is determined by the amount of scattering experienced by the illumination source. When optical scattering is weak, two-photon excitation is dominated by an unscattered component due to the quadratic dependence of the illumination source.

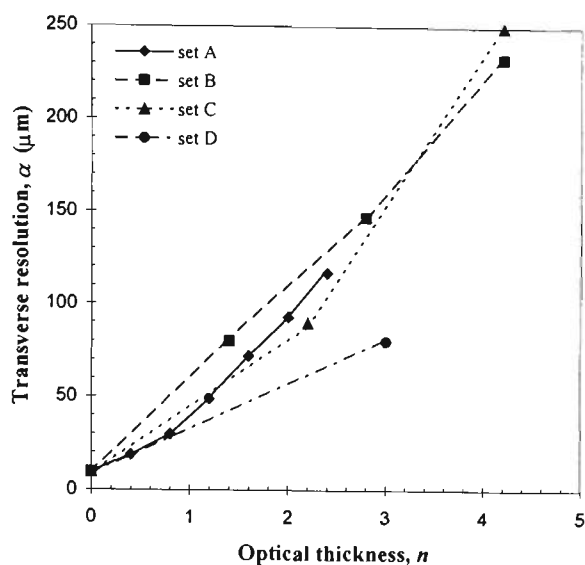
This effect is illustrated in figure 6.7, which shows that when scattering is weak the transverse resolution,  $\alpha$ , achievable is close to that measured without turbid media. As the turbid medium becomes optically thick the unscattered component significantly reduces. Therefore the transverse resolution,  $\alpha$ , deteriorates quickly, since the image is constructed by both unscattered and scattered photons. This feature is illustrated in figures 6.9 which shows that the transverse resolution,  $\alpha$ , decreases at a steady rate until about 200  $\mu\text{m}$ . After a depth of 200  $\mu\text{m}$  the transverse resolution,  $\alpha$ , decreases quickly, indicating that scattering of the illumination source is strong in this region. A similar trend is seen in figures 6.10 and 6.11, although the degradation in transverse resolution,  $\alpha$ , occurs earlier.

As seen in figures 6.5(f) and 6.8(c) the physical limitation in obtaining high contrast and high resolution images is the amount of scattering experienced by the illumination light. It has been found that the fluorescence signal is decreased by 3-4 orders of magnitude if the optical thickness,  $n$ , is up to 10 (Daria, 1998). It should be pointed out that spherical aberration, resulting from the refractive index mismatching between the glass cell, turbid media and the surrounding media also plays a role in determining the image quality achievable (Torok, 1996 ; Day and Gu, 1998). This type of spherical aberration can broaden the point-spread-function of the imaging lens when the penetration depth increases (Day and Gu, 1998). A broadened point-spread-function can reduce the peak power of the illumination pulse by as much as 90% for an interface between water and glass (Day and Gu, 1998). Thus, optical scattering is more dominant than the aberration in decreasing the fluorescence efficiency and resolution achievable under two-photon excitation

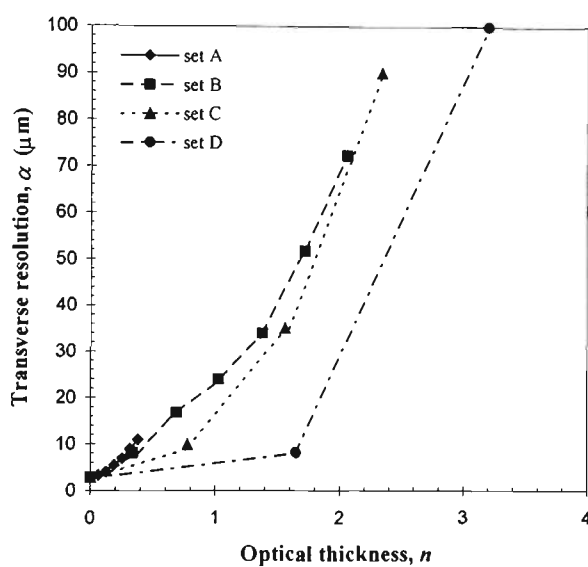
in turbid media (Daria *et al.*, 1998). However, the aberration plays an important role in determining the transverse resolution,  $\alpha$ , achievable in imaging through a non-scattering medium (see figure 6.6). This type of spherical aberration is inversely proportional to illumination wavelength (Torok, 1996); therefore the aberration is stronger for single-photon excitation. Figure 6.6 demonstrates the advantage of using a longer wavelength of excitation (i.e. two-photon excitation) to reduce the amount of the aberration experienced.

Since aberration and scattering are always present a number of techniques have been employed to compensate the reduction in peak power for two-photon excitation. The first technique, which primarily compensates for loss of peak power due to scattering was demonstrated by Daria *et al.* (1998). This technique involves increasing the illumination power with penetration depth, which compensates for the decreased fluorescence intensity. The second technique has been demonstrated by Day and Gu (1998) and involves the correction of the broadened point-spread-function by compensating the aberration through the use of a variable tube length of a lens.

The major physical difference between figures 6.7, 6.9, 6.10 and 6.11 is the scattering anisotropy of the turbid media under inspection (see table 6.2). As the scattering microsphere size increases a larger proportion of scattered photons propagate in the forward (illumination) direction due to their larger anisotropy value,  $g$ . Thus the image quality achievable for a given illumination optical thickness,  $n$ , should be improved as the size of scattering microspheres size



(a)



(b)

Figure 6.12: Transverse resolution,  $\alpha$ , as a function of the illumination optical thickness,  $n$ , for sample sets A to D (table 6.2). (a) single-photon excitation and (b) two-photon excitation.

increases in a reflection fluorescence optical microscope. Figure 6.12 demonstrates the transverse resolution,  $\alpha$ , as a function of the illumination optical thickness,  $n$ , for sample sets A to D, under single-photon (figure 6.12(a)) and two-photon (figure 6.12(b)) excitation. It is seen that at a given illumination optical thickness,  $n$ , the transverse resolution,  $\alpha$ , achievable under two-photon excitation is improved when turbid media with larger scatterers (i.e. sample set D) are used, while such an improvement under single-photon excitation (figure 6.12(a)) is not pronounced because of the poorer resolution which leads to less accurate measurements.

## 6.3 Application of two-photon fluorescence imaging

### 6.3.1 Introduction

The previous section of this chapter has demonstrated the advantage of using two-photon excitation in imaging through turbid media. This section looks further at the advantages of using two-photon excitation, by demonstrating the possible use of two-photon microscopy as a tool in obtaining three-dimensional spectroscopic information from biological tissue (Schilders and Gu, 1999a). The spectroscopic information is obtained from excited autofluorescence signatures within the biological tissue.

### 6.3.2 Imaging with cellular autofluorescence

For many years it has been known that all viable cells exhibit intrinsic fluorescence, i.e. autofluorescence, due to the natural presence of fluorescent molecules inside them (Chance *et al.*, 1962; Aubin, 1979; Benson *et al.*, 1979;

Alfano *et al.*, 1984; Tang *et al.*, 1989). Until recently cellular autofluorescence has been considered a source of unwanted interference; however recently considerable attention has been paid to the cellular autofluorescence due to its potential as a marker to distinguish between healthy and cancerous tissue *in vivo* (Alfano *et al.*, 1984; Tang *et al.*, 1989). Biological tissue is also known to be highly diffusive, which makes it difficult to obtain the information required at a significant depth into tissue and to perform useful microscopic and/or spectroscopic analyses. It has been demonstrated in section 6.2 that two-photon excitation produced by an infrared ultrashort pulsed laser beam (Denk *et al.*, 1990) can reduce multiple scattering, which improves resolution and leads to a deeper penetration depth. In fact, as was illustrated by figure 2.9(a) two-photon excitation can result in an optical sectioning property due to the quadratic dependence of the excitation probability (Denk *et al.*, 1990; Sheppard and Gu, 1990). Therefore, it is possible to perform three-dimensional (3-D) two-photon autofluorescence spectroscopy. Recently, two-photon autofluorescence has been measured from thick native muscle tissue from a chicken (Guo *et al.*, 1997). In this section as an example of two-photon imaging through turbid media, we present 3-D autofluorescence spectroscopic images from native rat muscle tissue under two-photon excitation.

It has been known that cellular autofluorescence in mammalian cells is dominated by two distinct molecular fluorophores, with emission spectra around wavelengths 400-500 nm and 500-600 nm under the excitation at wavelengths 360-365 nm and 440-450 nm, respectively. These spectra indicate the existence of pyridine nucleotides [NAD(P)H] and flavin compounds bound in mitochondria and cytoplasm (Chance *et al.*, 1962; Aubin, 1979; Benson *et al.*, 1979). In this

research we demonstrate that both fluorescence fluophores in rat skeletal muscle tissue can be probed simultaneously by two-photon excitation at a wavelength of 800 nm (Schilders and Gu, 1999a ).

### **6.3.3 Experimental details**

#### **6.3.3.1 Experimental setup**

The experimental system used to perform two-photon autofluorescence spectroscopic imaging is illustrated in figure 6.1 and an in-depth discussion of the system is given in section 6.2.1.1.

The incident light was focused onto a tissue sample through an oil immersion objective (Olympus, UPlanFl 60×/1.25 oil iris ∞/0.17). A short pass filter (KG1) was placed in front of the entrance slit of the photomultiplier to remove any residual pump leakage through the dichroic mirror and scattering within the scan unit. This filter was chosen since it has a uniform transmission efficiency (~85%) in the wavelength region of 350-600 nm.

#### **6.3.3.2 Sample preparation**

The specimen under inspection included fresh skeletal muscle tissue of thickness 60 μm from a single upper thigh of an adult rat (samples supplied by St. Vincent's Institute of Medical Research). The sample was placed on a glass slide and fixed with a layer of wax for preservation. The average power incident upon the rat skeletal muscle tissue was 10 mW to avoid photodamage.

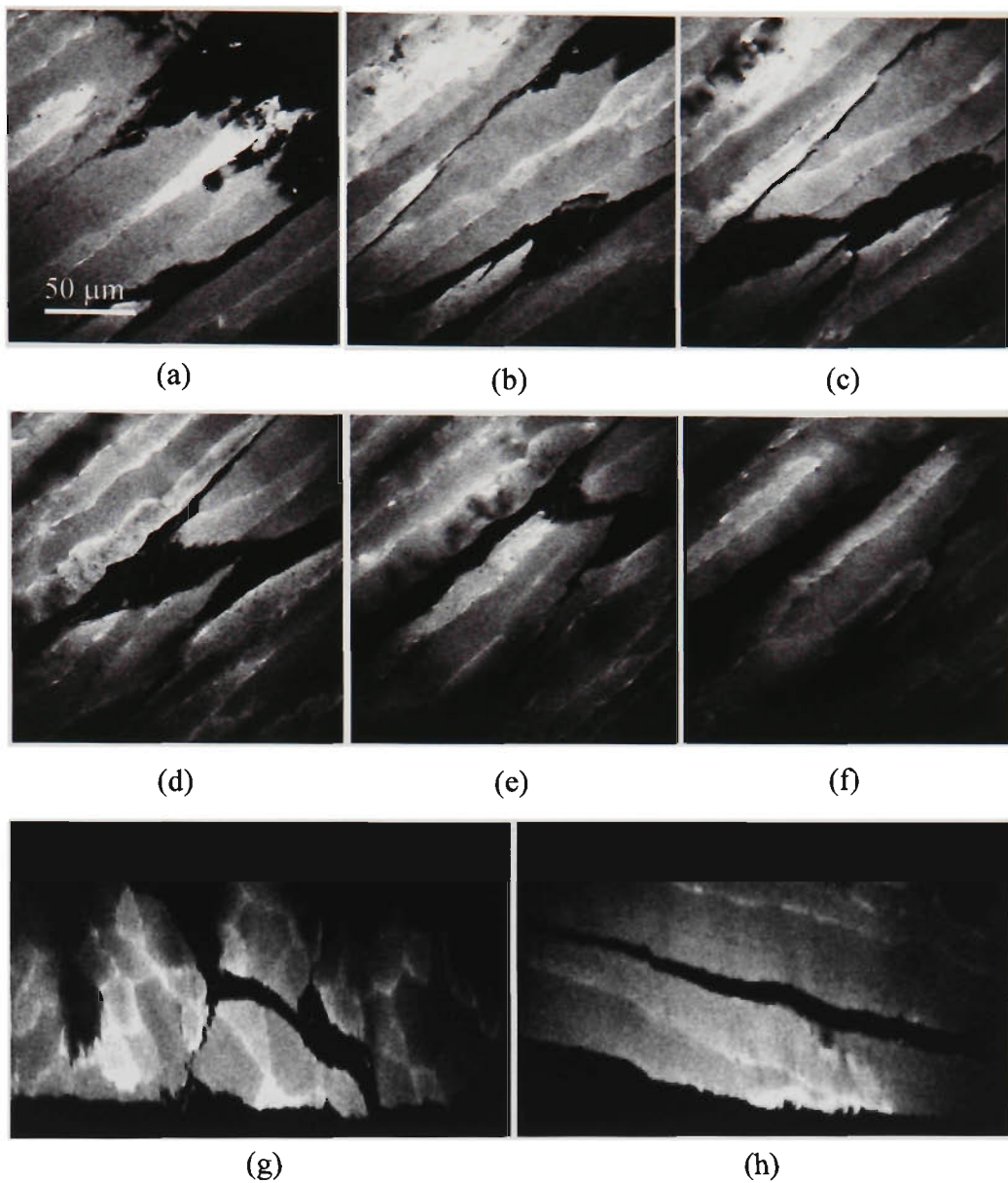


Figure 6.13: Transverse autofluorescence image sections of the rat skeletal muscle tissue recorded at different depths ((a) to (f)). The depth spacing is  $6\ \mu\text{m}$ . Vertical image slices cut from the recorded stack at  $45^\circ$  from left to right (g) and from right to left (h).

### **6.3.4 Three-dimensional microscopy and spectroscopy**

Illustrated in figures 6.13(a) to 6.13(f) are the autofluorescence images recorded at various depths within the rat skeletal muscle tissue, while figures 6.13(g) and 6.13(h) are slices cut at apposite 45° angles through the recorded stack. Each of the images in figure 6.13 clearly show light and dark longitudinal sections which can be attributed to Type I (slow twitch), Type IIA (aerobic and anaerobic) or Type IIB (fast twitch) muscle fibres (Krause, 1994). This result confirms that each muscle fibre type has a different chemical composition and concentration of the autofluorescence fluophores (Krause, 1994). Otherwise the muscle fibre types could not be visually separated. Figures 6.13(d) and 6.13(e) demonstrate the ability of skeletal muscle to contract and relax as a result of contractile protein filaments.

Figure 6.14 illustrates the 3-D image reconstructed from the sections in figure 6.13, demonstrating the structure of the skeletal muscle. It is clear that skeletal muscle fibres are grouped into fascicle structures (Krause, 1994). As expected, no connective tissue or muscle fibre nuclei are visible in the reconstructed image.

Figure 6.15 shows autofluorescence spectra obtained at selected points within the skeletal muscle tissue. It is seen in figures 6.15(a), 6.15(b) and 6.15(c) that two peaks are present with emission maxima approximately at wavelengths 450 nm and 550 nm, respectively, while in figure 6.15(d) only one peak approximately at wavelength 550 nm is present.

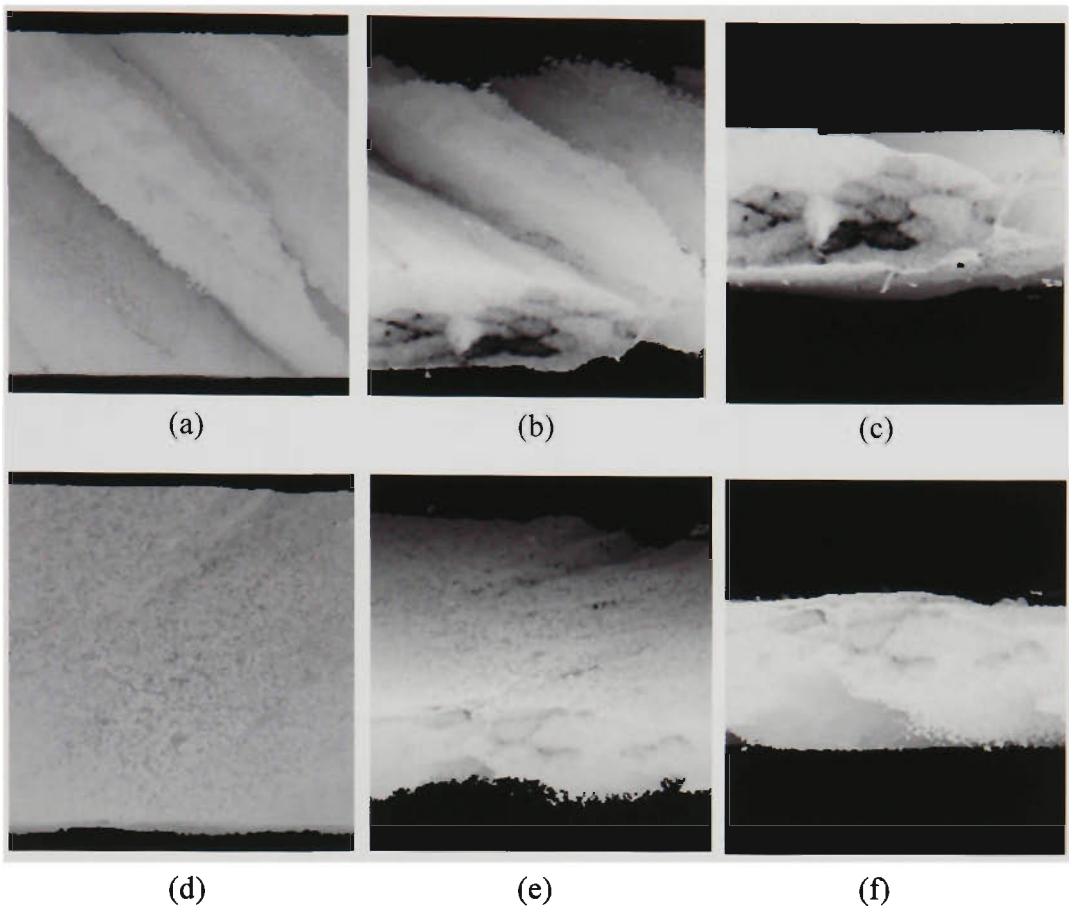
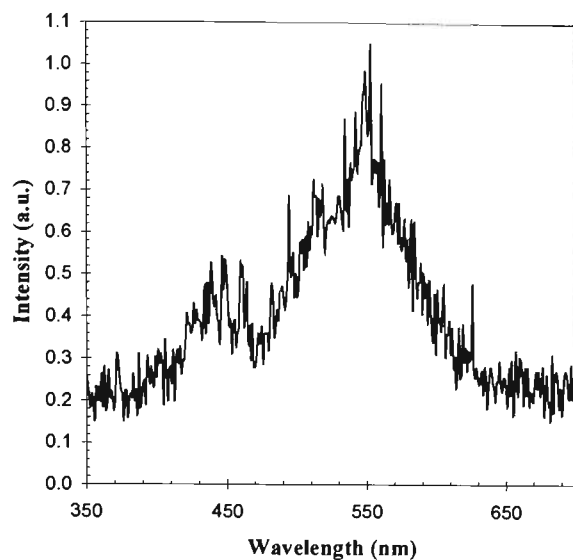
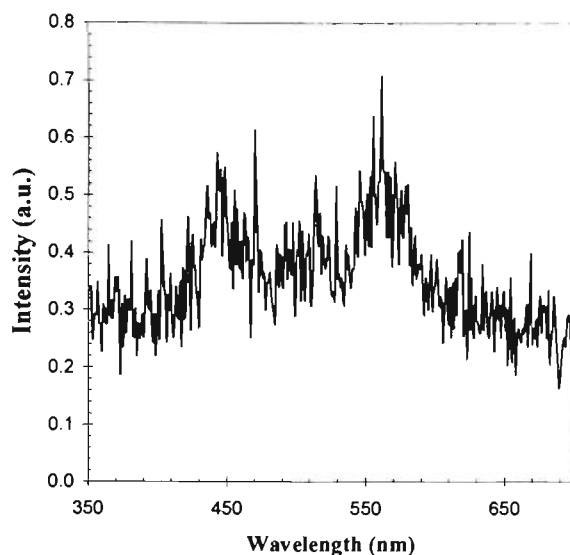


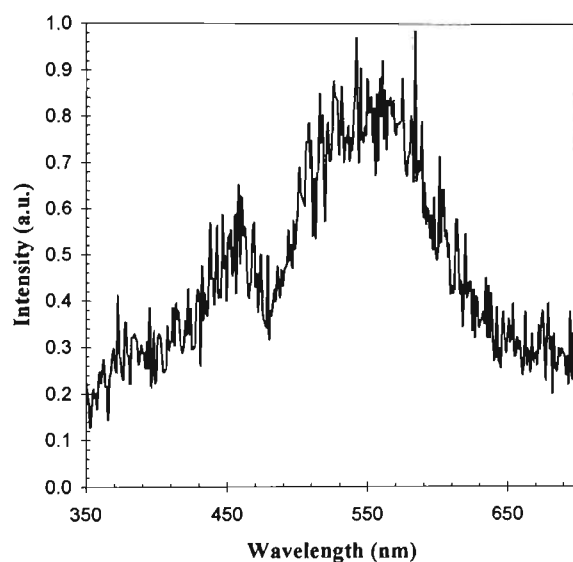
Figure 6.14: Reconstructed three-dimensional autofluorescence image of the rat skeletal muscle tissue at different rotation view angles: (a)  $0^\circ$ , (b)  $45^\circ$ , (c)  $90^\circ$ , (d)  $180^\circ$ , (e)  $225^\circ$  and (f)  $270^\circ$ .



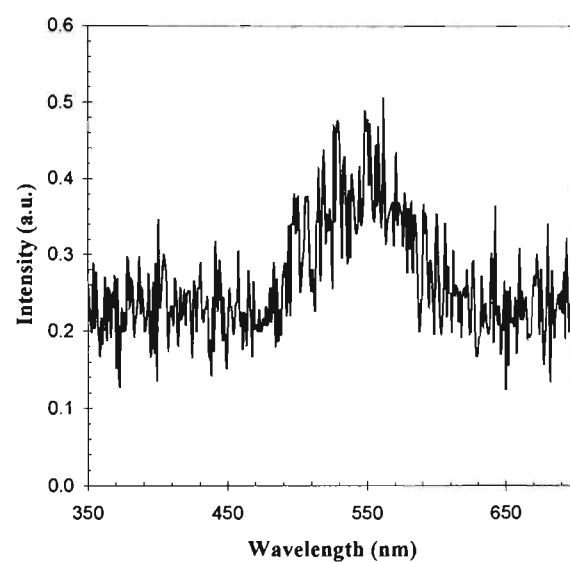
(a)



(b)



(c)



(d)

Figure 6.15: Autofluorescence spectra from different points within the rat skeletal muscle tissue.

The intensity at these peaks can be used to determine the local concentration of the two autofluorescence fluorophores within the muscle tissue. These autofluorescence peaks can most likely be attributed to NADH and riboflavin which are concentrated to mitochondria and cytoplasm (Aubin, 1979; Benson, *et*

*al.*, 1979). It should also be noted that although the relative intensity of the two peaks changes from point to point within the skeletal muscle tissue, there is no change in the position of the fluorescence maxima. Therefore these fluorescence maxima could be used as a marker for healthy muscle tissue to discriminate against cancerous tissue.

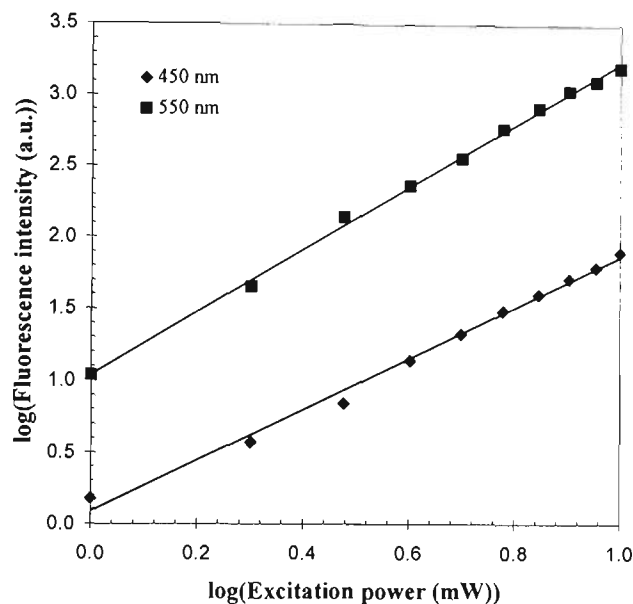


Figure 6.16: Autofluorescence intensity as a function of the excitation laser power at two fluorescence peaks.

Figure 6.16 shows the dependence of the fluorescence intensity on the incident power at the two autofluorescence peaks. The slope of the curves after regression analysis is 1.9 and 2.2 for the 450 nm and 550 nm peaks, respectively, which confirms the two-photon excitation process at these wavelengths.

The degree of polarisation,  $\gamma$ , defined by equation 3.39, where  $I_p$  and  $I_s$  are the fluorescence intensities in the parallel and perpendicular directions, was 0.12 and

0.16 at wavelengths 450 nm and 550 nm, respectively (Demos *et al.*, 1998) . The lower degree of polarisation,  $\gamma$ , for the autofluorescence peak at wavelength 450 nm may be due to the higher scattering of photons at this wavelength within the skeletal muscle tissue.

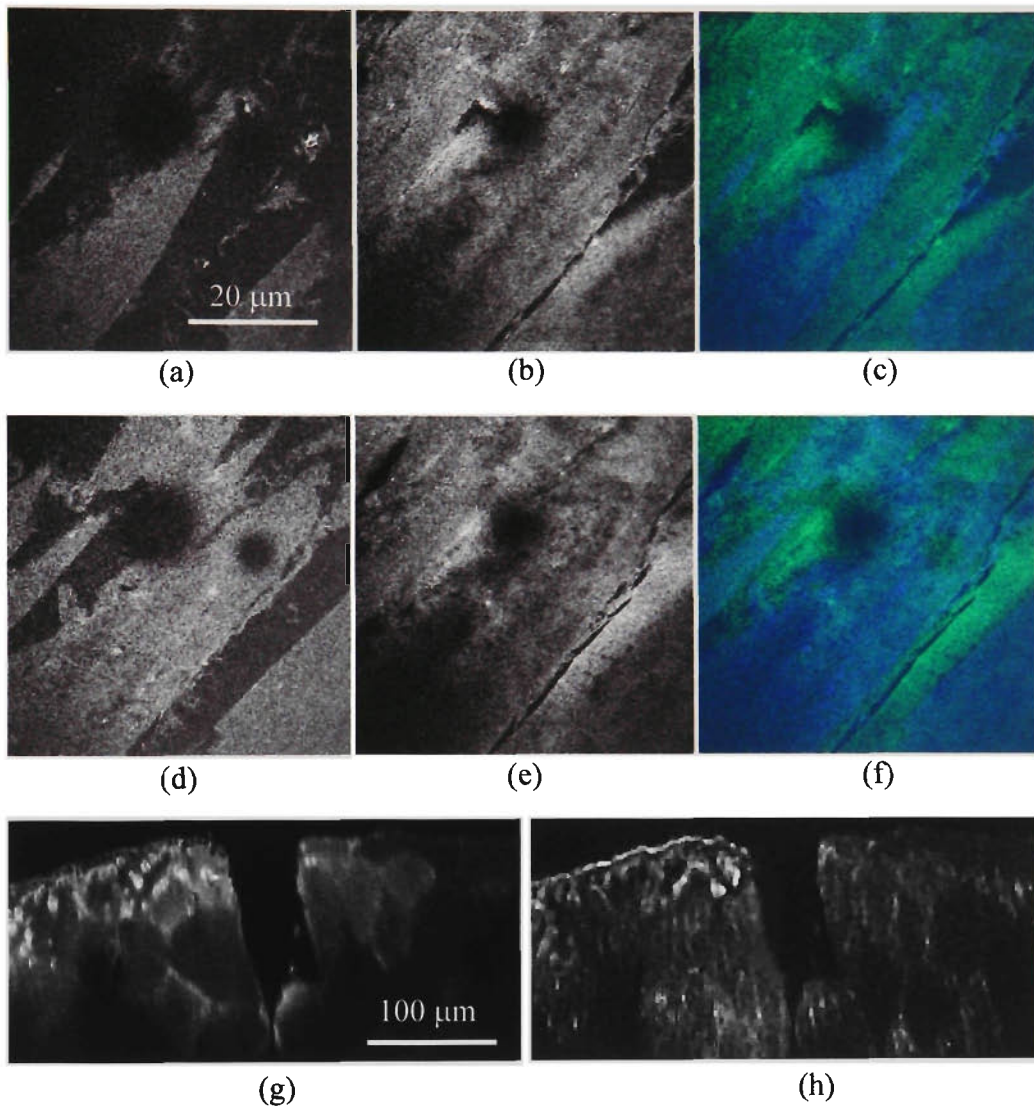


Figure 6.17: Transverse ((a), (b), (c), (d), (e) and (f)) and vertical ((g) and (h)) image sections of the rat skeletal muscle tissue recorded at autofluorescence wavelengths 450 nm ((a), (d) and (g)) and 550 nm ((b), (e) and (h)). Images (c) and (f) are a superposition of images ((a) and (b)) and ((d) and (e)), respectively.

With the help of the appropriate bandpass (BG12) and long pass (GG495) filters, the two autofluorescence peaks can be separated and used to form three-dimensional images respectively. Figure 6.17 displays two transverse image sections and two vertical image sections at the two autofluorescence peaks. It is seen that each autofluorescence fluorophore gives different three-dimensional information about the skeletal muscle tissue, which means that the three-dimensional spectroscopic images can be used to locate the chemical compounds. This result has practical importance in physiology.

### 6.3.5 Discussion

It has been shown that healthy rat skeletal muscle tissue can be probed with a single infrared wavelength through two-photon excitation, which results in the simultaneous excitation of two unique fluorescence fluorophores. The autofluorescence from the two fluorophores exhibit different three-dimensional information about the muscle fibres. It is hopeful that two autofluorescence peaks may be used as a marker to discriminate between healthy and cancerous muscle tissues, since their positions are fixed within the muscle tissue.

Due to the different selection rules followed by two-photon excitation (Shen, 1984), different electronic states may be probed when compared with single-photon excitation. This property may lead to the different spectral peaks and signal strengths of the two-photon autofluorescence from those under single-photon excitation (Aubin, 1979; Benson *et al.*, 1979). Further work is needed to confirm this possibility.

## **6.4 Conclusion**

This chapter has demonstrated the effect of optical scattering on image quality and transverse resolution achievable in imaging through turbid media under single-photon and two-photon excitation. It has been demonstrated that the images recorded with two-photon excitation show higher transverse resolution than those recorded with single-photon excitation. Further two-photon excitation allows deeper penetration due to reduced scattering of the illumination light.

The performance of single-photon excitation in terms of image quality and penetration depth is determined primarily by the amount of scattering experienced by the illumination light. The image quality achievable for two-photon excitation depends primarily on the generation of enough fluorescence light to be detected. i.e. on the signal-to-noise ratio of an image, although scattering still plays an important role in determining the resolution achievable.

# Chapter 7

## Conclusion

### 7.1 Thesis conclusion

Imaging within turbid media is an extremely complex problem, due to the nature of the detected illumination photons once they have propagated through turbid media. Detected photons can be broken down into three classes; they are the unscattered, snake and scattered photons (refer to section 1.2.1). To obtain high quality images of objects embedded within turbid media it is necessary to suppress the scattered photons, since they contribute less information about the embedded object. Thus gating methods that suppress scattered photons need to be implemented in imaging through turbid media. All gating methods rely on the characteristic differences between unscattered and scattered photons (refer to section 1.2.2). However most current gating methods (e.g. ones based on time-of-flight) designed for transillumination imaging systems may not be efficient in microscopic imaging systems, due to the wide range of illumination angles produced by the imaging lens (refer to figure 3.7).

Therefore this thesis has concentrated on the understanding of photon propagation within turbid media so that effective gating mechanisms can be developed for

microscopic imaging systems. Two gating mechanisms have been extensively studied; they are the angle-gating mechanism (refer to chapter 4) which relies on the path deviation of scattered and unscattered photons, and the polarisation-gating mechanism (refer to chapter 5) which relies on the polarisation difference between scattered and unscattered photons. These two gating mechanisms have been chosen since they are easy to implement into microscopic imaging systems and can be combined to further enhance the image quality.

The angle-gating mechanism developed (Gan *et al.*, 1997; Schilders *et al.*, 1998a; 1998b; 1998c) relies on the ability to separate unscattered and scattered photons based on their path deviation after propagating through turbid media (refer to figure 4.1). The gating mechanism is achieved by the utilisation of annular objectives in the illumination and collection beam paths. It should be noted that the conventional polarisation-gating mechanism has also been implemented with the angle-gating mechanism to further suppress unwanted scattered photons that propagate along the same path as the unscattered photons (refer to figure 4.1).

An extensive study into the performance of the angle-gating mechanism for a transmission and a reflection microscopic imaging system has been performed to demonstrate the effective suppression of scattered photons that contribute to an image. Due to the suppression of scattered photons a substantial improvement in image quality has been demonstrated (refer to figures 4.11, 4.12, 4.13 and 4.18). The criterion to obtain the best working performance for angle-gating has also been established (refer to section 4.6). The performance of the angle-gating mechanism

has also been theoretically validated with the aid of Monte-Carlo simulation (refer to figures 4.2, 4.14 and 4.20).

The angle-gating mechanism, although very effective in suppressing unwanted scattered photons, has a severe limitation. That is, the angle-gating mechanism relies on the detection of unscattered photon. Therefore the signal-to-noise ratio of the recorded image is substantially degraded when a turbid medium becomes optically thicker (i.e. optical thickness,  $n > 10$ ), due to the reduced number of available unscattered photons that can be collected.

Due to the need to develop gating mechanisms that can be implemented with optically thick turbid media polarisation-gating mechanisms (in particular the differential polarisation-gating mechanism) has been studied (Gan *et al.*, 1999; Schilders *et al.*, 1998d; 1998e). Polarisation-gating can be effective in imaging through optically thick turbid media because the change in polarisation is slower than the directional change when photons are scattered.

The performance of polarisation-gating mechanisms (i.e. conventional polarisation-gating, perpendicular polarisation-gating and differential polarisation-gating), when compared with no-gating, in terms of image quality and transverse resolution,  $\alpha$ , for turbid media with different characteristics has been experimentally investigated for a reflection optical microscope (refer to section 5.3.2). The criterion and regimes for which the polarisation-gating mechanisms are most effective have also been experimentally determined for the reflection optical microscope. The results

presented for polarisation-gating mechanism demonstrate the effectiveness of using polarisation-gating in imaging through optically thick turbid media ( $n > 10$ ).

The effect of employing an additional pinhole-filter, placed in front of the detector, on the performance of the polarisation-gating mechanisms has also been experimentally investigated (refer to section 5.3.3). An added pinhole-filter further improves the transverse resolution of the recorded images, since the pinhole-filter applies a directional selectivity to scattered photons that have similar depolarisation, and sneak through a polarisation gate (refer to figures 5.6(a) and 5.9(a)). It has been noticed that the improvement in transverse resolution is lower when additional pinhole-filtering is employed (refer to figures 5.6(b) and 5.9(b)).

As in the case of the angle-gating mechanism, polarisation-gating mechanisms with and without the additional pinhole-filter, placed in front of the detector, are theoretically validated with the aid of a Monte-Carlo simulation (refer to figures 5.13 and 5.14, respectively).

The results presented in chapter 5 for polarisation-gating suggest that the size of the scatterers in the turbid media determine the effectiveness of the polarisation-gating mechanism and therefore the resolution achievable. That is, polarisation-gating is more effective in turbid media consisting of smaller scattering particles i.e. the resolution improvement achieved is larger.

The use of fluorescence in biological imaging is an important tool, since it allows spectroscopic information and different structural details to be separated. Typically fluorescence imaging of biological samples is done through staining with dyes or by the use of autofluorescence signatures. Until recently most fluorescence imaging in microscopic systems has been done on optically thin slices of biological tissue excised from the sample under inspection. In this situation optical scattering is negligible and therefore can be ignored. However, if less invasive *in vivo* microscopic imaging systems are used, optically scattering plays a significant role in determining the image quality attainable. Recently multi-photon (in particular two-photon) microscopy has been used due to its significant advantage of reducing scattering over single-photon microscopy (refer to section 2.3).

The performance of fluorescence microscopy (single-photon and two-photon) on image quality and transverse resolution for turbid media with different characteristics has been experimentally investigated for a reflection optical microscope (refer to section 6.2). The results presented illustrate that significant improvement in image quality and transverse resolution is achievable when two-photon excitation is used.

It has been found that the limiting factor for obtaining high quality images for single-photon excitation is the quick degradation of resolution, while for two-photon excitation the limiting factor is the reduction of signal-to-noise ratio of images (Schilders and Gu, 1999b).

The results presented in chapter 6 for fluorescence imaging through turbid media suggest that the scattering particle size plays an important role in determining the image quality achievable. That is, for a given optical thickness,  $n$ , larger sized scatterers give the improved image quality due to the increase in forward propagating of scattered photons.

With the knowledge of the scattering effects on two-photon excitation the imaging principle has been applied to a more realistic application. Muscle samples have been imaged by their autofluorescence to demonstrate the advantage of using two-photon excitation to obtain spectroscopic signatures (Schilders and Gu, 1999a). A further advantage of using two-photon excitation has been found when imaging the muscle samples; two-photon excitation allows multiple fluorophore excitation with a single wavelength of illumination. This feature is different from single-photon excitation, which requires dual wavelengths to excite the same fluorophores in the muscle samples. This finding has practical importance in imaging live samples since it allows the simultaneous and exact mapping of multiple pieces of information embedded within a biological sample.

In conclusion, the work presented in this thesis has systematically shown for the first time the effect of scattering on image quality in microscopic imaging systems employing angle-gating (achieved with the utilisation of an annular objective), polarisation-gating (conventional and differential) and fluorescence (single-photon and two-photon excitation) in imaging through turbid media with different characteristics.

It is clear from these investigations that image quality in an optical microscope can be improved by use of unscattered photons and less scattered photons. However then number of these photons is too low for an optically thick turbid medium. Therefore, it is necessary to develop methods for image reconstruction. The combination of optical gating methods investigated in this thesis with image reconstruction methods may provide a practical solution for imaging through turbid media.

## Future work

The principles and work presented in this thesis can be extensively extended. The following lists some suggested future work:

- Wang *et al.*, (1997) and Demos *et al.*, (1998) demonstrated that differential-polarisation gating can be used to improve the image quality of a fluorescent object embedded within turbid media. Therefore, it can be assumed that polarisation-gating (in particular differential polarisation-gating) can be applied to autofluorescence imaging of biological tissue to suppress scattered photons, thereby improving the image quality. For polarisation-gating to be effective the autofluorescence signatures originating from biological tissue must maintain some degree of the initial polarisation (i.e. fluorescence not totally depolarised).
- If the power loss of single-photon and two-photon fluorescence caused by scattering is compensated by the methods proposed by Daria *et al.* (1998), a further compensation for aberration caused by the mismatch of refractive indices between the sample and its immersion material is needed. The aberration can be compensated by inducing a change in tube length of an imaging objective (Day and Gu, 1998).
- A formal study into the autofluorescence signatures generated from two-photon excitation of healthy and cancerous tissue cultures should be carried out.

- \* Undertake a physiological study of exercised muscle fibres *in situ* using two-photon microscopy to more accurately determine change in chemical compositions.
  
- \* Undertake an in-depth study into multiple fluorophore excitations with two-photon excitation as has been demonstrated in the rat skeletal muscle fibres.

## References

- "1990 Recommendations of the International Commission on Radiological Protection," ICRP Publication 60, Pergamon: New York (1991).
- Alfano R. R., Tang G. C., Pradhan A., Lam W., Choy D. S. J. and Opher E. "Fluorescence spectra from cancerous and normal human breast and lung tissues," *IEEE J. Quan. Elect.* **23**, 1806-1811 (1987).
- Alfano R. R., Tata D. B., Cordero J. C., Tomashefsky P., Longo F. W. and Alfano M. A. "Laser induced fluorescence spectroscopy from native cancerous and normal tissue," *IEEE J. Quan. Elect.* **20**, 1507-1511 (1984).
- Anderson G. E., Liu F. and Alfano R. R., "Microscope imaging through highly scattering media," *Opt. Lett.* **19**, 981-983 (1994).
- Anderson S. G., "Confocal laser microscopes see a wider field of application," *Laser Focus World*, 83-86 (1994).
- Andersson-Engels S., Berg R., Persson A. and Svanberg S., "Multispectral tissue characterisation with time resolved detection of diffusely scattered light," *Opt. Lett.* **18**, 1697-1699 (1993).
- Aubin J., "Autofluorescence of viable cultured mammalian cells," *J. Histochem. Cytochem.* **27**, 36-41 (1979).
- Baltes H. P. "Inverse Source Problems in Optics," Springer-Verlag: Berlin (1978).
- Benson H. C., Meyer R. A. and Zaubas M. E., "Cellular autofluorescence - is it due to flavins?," *J. Histochem. Cytochem.* **27**, 44-48 (1979).
- Blanca C. M. and Saloma C., "Monte Carlo analysis of two-photon fluorescence imaging through a scattering medium," *Appl. Opt.* **37**, 8092-8102 (1998).
- Bohem C. F. and Huffman D. R., "Absorption and Scattering of Light by Small Particles," J. Wiley & Sons: New York (1983).
- Born M. and Wolf E., "Principles of Optics," Pergamon Press (1980).
- Bouma B., Tearney G. J., Boppart S. A., Hee M. R., Brezinski M. E. and Fujimoto J. G., "High-resolution optical coherence tomographic imaging using a mode-locked Ti:Al<sub>2</sub>O<sub>3</sub> laser source," *Opt. Lett.* **20**, 1486-1488 (1995).
- Bruce N. C., Schmidt F. E. W., Dainty J. C., Barry N. P., Hyde S. C. W. and French P. M. W., "Investigation of the temporal spread of an ultrashort light pulse on transmission through a highly scattering medium," *Appl. Opt.* **34**, 5823-5828 (1995).

- Bruscaglioni P., Zaccaniti G. and Wei Q., "Transmission of pulsed polarised light beam through thick turbid media: numerical results," *Appl. Opt.* **32**, 6142-6150 (1997).
- Chance B., Cohen P., Jobsis F. and Schoener B., "Intracellular oxidation states *in vivo*," *Science* **137**, 499-502 (1962).
- Cheng P. C., Bhawalkar J. D., Pan S. J., Wiatakiewicz J., Samarabandu J. K., Liou W. S., He G. S., Ruland G. E., Kumar N. D. and Prasad P. N., "Two-photon generated three-dimensional photon bleached patterns in polymer matrix," *Scanning* **18**, 129-131 (1996).
- Daria V., Blanca C. M., Nakamura O., Kawata S. and Saloma C., "Image contrast enhancement for two-photon fluorescence microscopy in a turbid medium," *Appl. Opt.* **37**, 7960-7967 (1998).
- Day D. and Gu M., "Effects of refractive-index mismatch on three-dimensional optical data storage density in a two-photon bleaching polymer" *Appl. Opt.* **37**, 6299-6304 (1998).
- de Boer J. F., Miller T. E., van Gemert M. J. C. and Nelson J. S., "Two-dimensional birefringence imaging in biological tissue by polarisation-sensitive optical coherence tomography," *Opt. Lett.* **22**, 934-936 (1997).
- de Haller E. B. "Time-resolved transillumination and optical tomography," *J. Biomed. Opt.* **1**, 7-17 (1996).
- Demos S. G., Wang W. B. and Alfano R. R., "Imaging objects hidden in scattering media with fluorescence polarisation preservation of contrast agents," *Appl. Opt.* **37**, 792-797 (1998).
- Denk W., Strickler J. H. and Webb W. W., "Two photon laser scanning fluorescence microscopy," *Science* **248**, 73-76 (1990).
- Dilworth D. S., Leith E. N. and Lopez J., "Three-dimensional confocal imaging of objects embedded within thick diffusing media," *Appl. Opt.* **30**, 1796-1803 (1991).
- Faris G. W. and Banks M., "Upconverting time gate for imaging through highly scattering media," *Opt. Lett.* **19**, 1813-1815 (1994).
- Flock S. T., Patterson M. S., Wilson B. C. and Wyman D. R., "Monte Carlo modeling of light propagating in highly scattering tissues - I: model predictions and comparison with diffusion theory," *IEEE Trans. Biomed. Eng.* **36**, 1162-1173 (1989).

- Flock S. T., Wilson B. C. and Patterson M. S., "Total attenuation coefficients and scattering phase functions of tissue and phantom materials at 633 nm," *Med. Phys.* **14**, 835-841 (1987).
- Fujimoto J. G., De Silvestri S., Ippen E. P., Puliafito C. A., Margolis R. and Oseroff A., "Femtosecond optical ranging in biological systems," *Opt. Lett.* **11**, 150-152 (1986).
- Gan X. and Gu M., "Modified Monte Carlo simulation of multi-dimensional photon distribution for microscopic imaging," *Optik* **108**, 129-136 (1998).
- Gan X., Schilders S. and Gu M., "Combination of annular aperture and polarisation gating methods for efficient microscopic imaging through a turbid medium: theoretical analysis," *Microsc. and Microanal.* **3**, 495-503 (1997).
- Gan X. S., Schilders S. P. and Gu M., "Image formation in turbid media under a microscope," *J. Opt. Soc. Am. A* **15**, 2052-2058 (1998).
- Gan X., Schilders S. P. and Gu M., "Image enhancement through turbid media under a microscope using polarisation gating methods," *J. Opt. Soc. Am. A* **16**, 2177-2184 (1999).
- Graff R., Koelink M. H., de Mul F. F. M., Zijlstra W. G., Dassel A. C. M. and Aarnoudse J. G., "Condensed Monte Carlo simulation for the description of light transport," *Appl. Opt.* **32**, 426-434 (1993).
- Gu M., "Principles of Three-Dimensional Imaging in Confocal Microscopes," World Scientific: Singapore (1996).
- Gu M. and Gan X. S., "Effect of the detector size and the fluorescence wavelength on the resolution of three- and two-photon confocal microscopy," *Bioimaging* **4**, 129-137 (1996).
- Gu M. and Gan X. S., "Monte Carlo Simulation for confocal imaging through highly scattering media," *Scanning* **19**, 148-149 (1997).
- Gu M., Schilders S. P. and Gan X., "Two-photon fluorescence imaging of microspheres embedded in turbid media," *J. Modern Optics* (1999) – in press.
- Gu M., Sheppard C. J. R. and Zhou H., "Optimisation of axial resolution in confocal imaging using annular pupils," *Optik* **93**, 87-90 (1993).
- Gu M., Tannous T. and Sheppard C. J. R., "Effect of an annular pupil on confocal imaging through highly scattering media," *Opt. Lett.* **21**, 312-314 (1996).

- Guo Y., Wang Q. Z., Zhadin N., Liu F., Demos S., Calistru D., Tirkšliunas A., Katz A., Bunansky Y., Ho P. P. and Alfano R. R., "Two-photon excitation of fluorescence from chicken tissue," *Appl. Opt.* **36**, 968-970 (1997).
- Hanninen P. E., Soini E. and Hell S. W., "Continuous wave excitation two-photon fluorescence microscopy," *J. Microsc.* **176**, 222-225 (1994).
- Hasegawa Y., Yamada Y., Tamura M. and Nomura Y., "Monte Carlo simulation of light transmission through living tissue," *Appl. Opt.* **30**, 4515-4520 (1991).
- Hebden J. C. and Kruger R. A., "Transillumination imaging performance: a time-of-flight imaging system," *Med. Phys.* **17**, 351-356 (1990).
- Hebden J. C. and Wong K. S., "Time-resolved optical tomography," *Appl. Opt.* **32**, 372-380 (1993).
- Hebden J. C., "Time-resolved imaging of opaque and transparent spheres embedded in a highly scattering medium," *Appl. Opt.* **32**, 3837-3841 (1993).
- Hebden J. C., Kruger R. A. and Wong K. S., "Time resolved imaging through a highly scattering medium," *Appl. Opt.* **30**, 788-794 (1991).
- Hee M. R., Izatt J. A., Swanson E. A. and Fujimoto J. G., "Femtosecond transillumination tomography in thick tissues," *Opt. Lett.* **18**, 1107-1109 (1993).
- Hell, S. W., "Special Issue on Nonlinear Optical Microscopy," *Bioimaging* **4**, 121-215 (1996).
- Hielscher A. H., Mourant J. R. and Bigio I. J., "Influence of particle size and concentration on the diffuse backscattering of polarised light from tissue phantoms and biological cell suspensions," *Appl. Opt.* **36**, 125-135 (1997).
- Ho P. P., Baldeck P., Wong K. S., Yoo K. M., Lee D. and Alfano R. R., "Time dynamics of photon migration in semiopaque random media," *Appl. Opt.* **28**, 2304-2310 (1989).
- Horinaka H., Hashimoto K., Wada K., Cho Y. and Osawa M., "Extraction of quasi-straightforward-propagating photons from diffused light transmitting through a scattering medium by polarisation modulation," *Opt. Lett.* **20**, 1501-1503 (1995).
- Indebetouw G., Kim T., Poon T.-C. and Schilling B., "Three-dimensional location of fluorescent inhomogeneities in turbid media using scanning heterodyne holography," *Opt. Lett.* **23**, 135-137 (1998).

- Izatt J. A., Hee M. R., Owen G. M., Swanson E. A. and Fujimoto J. G., "Optical coherence microscopy in scattering media," *Opt. Lett.* **19**, 590-592 (1994).
- Jensen R. G., "Handbook of milk composition," Academic Press: San Diego (1995).
- Kalpaxis L. L., Wang L. M., Galland P., Liang X., Ho P. P. and Alfano R. R., "Three-dimensional temporal image reconstruction of an object hidden in highly scattering media by time-gated optical tomography," *Opt. Lett.* **18**, 1691-1693 (1993).
- Kempe M. and Rudolph W., "Scanning microscopy through thick layers based on linear correlation," *Opt. Lett.*, 1919-1921 (1994).
- Kempe M., Rudolph W. and Welsch E., "Comparative study of confocal and heterodyne microscopy for imaging through scattering media," *J. Opt. Soc. Am. A* **13**, 46-52 (1996).
- Kempe M., Thorn A. and Rudolph W., "Resolution limits of microscopy through scattering layers," *Opt. Comm.* **110**, 492-496 (1994).
- Key H., Davis E. R., Jackson P. C. and Wells P. N. T., "Monte Carlo modeling of light propagating in breast tissue," *Phys. Med. Biol.* **36**, 591-602 (1991).
- Kino G. S. and Corle T. R., "Confocal scanning optical microscope," *Physics Today*, 55-62 (1989).
- Krause W. J., "Essentials of Human Histology," Little, Brown and Company (inc.): Boston (1994).
- Liang X., Wang L., Ho P. P. and Alfano R. R., "Time-resolved polarisation shadowgrams in turbid media," *Appl. Opt.* **36**, 2984-2989 (1997).
- Liu F., Yoo K. M. and Alfano R. R., "Speed of the coherent component of femtosecond laser pulses propagating through random scattering media," *Opt. Lett.* **16**, 351-353 (1991).
- Liu F., Yoo K. M. and Alfano R. R., "Transmitted photon intensity through biological tissues within various time windows," *Opt. Lett.* **19**, 740-742 (1994).
- Lohmann W., Mußmann J., Lohmann C. and K $\text{\textcircled{O}}$ nzl W. "Native fluorescence of the cervix uteri as a marker for dysplasia and invasive carcinoma," *Eur. J. Obst. Gyn. Rep. Bio.* **31**, 249-253 (1989).
- MacKintosh F. C., Zhu J. X., Pine D. J. and Weitz D. A., "Polarisation memory of multiple scattered light," *Phys. Rev. B* **40**, 9342-9345 (1989).

- Martin J. L., Lecarpentier Y., Antonetti A. and Grillon G., "Picosecond laser stereometry light scattering measurements on biological material," *Med. Biol. Eng. Comput.* **18**, 250-252 (1980).
- Masters B. R. "Confocal microscopy: history, principles, instruments and some applications to the living eye," *Comm. Mol. Cell. Biophys.* **8**, 243-271 (1995).
- Masters B. R. "Three-dimensional confocal microscopy of human skin in vivo: autofluorescence of normal skin," *Bioimages* **4**, 13-19 (1996).
- Masters B. R., So P. T. C. and Gratton E. "Multiphoton excitation fluorescence microscopy of in vivo human skin," *Biophys. J.* **72**, 2405-2412 (1997).
- McCormick M. J., "Particle-size-distribution retrieval from backscattered polarised radiation measurements: a proposed method," *J. Opt. Soc. Am. A* **7**, 1811-1816 (1990).
- Minsky M., "Memoir on inventing the confocal scanning microscope," *Scanning* **10**, 128-138 (1988).
- Moore J. V., West C. M. L. and Whitehurst C. "The biology of photodynamic therapy," *Phys. Med. Biol.* **42**, 913-935 (1997).
- Morgan S. P., Appel R. K. and Somekh M. G., "Experimental studies of the factors affecting spatial resolution in continuous wave transillumination through scattering media (medical application)," *Bioimaging* **2**, 163-173 (1994).
- Morgan S. P., Khong M. P. and Somekh M. G., "Effects of polarisation state and scatterer concentration on optical imaging through scattering media," *Appl. Opt.* **36**, 1560-1565 (1997).
- Pan Y., Birngruber R. and Engelhardt R., "Contrast limits of coherence-gated imaging in scattering media," *Appl. Opt.* **36**, 2979-2983 (1997).
- PolyScience Inc. Polybead Catalogue, pg 9 (1998).
- Rajadhyaksha M., Grossman M., Esterowitz D., Webb R. H. and Anderson R. R., "In vivo confocal scanning laser microscopy of human skin: melanin provides strong contrast," *J. Invest. Derm.* **104**, 946-952 (1995).
- Saloma C., Palmes-Saloma C. and Kondoh H., "Site-specific confocal fluorescence imaging of biological microstructures in a turbid medium". *Phys. Med. Biol.* **43**, 1741-1759 (1998).
- Schilders S. P., Gan X. S. and Gu M., "Efficient suppression of diffusing photons using polarising annular objectives for microscopic imaging through turbid media". *Bioimaging* **6**, 92-97 (1998a).

- Schilders S. P., Gan X. S. and Gu M., "Microscopic imaging through a turbid medium by use of annular objectives for angle-gating". *Appl. Opt.* **37**, 5320-5326 (1998b).
- Schilders S. P., Gan X. S. and Gu M., "Image enhancement in a reflection optical microscope by suppression of diffusing photons using polarising annular objectives". *Microsc. and Microanal.* **4**, 415-419 (1998c).
- Schilders S. P., Gan X. S. and Gu M., "Resolution improvement in microscopic imaging through turbid media based on differential polarisation-gating". *Appl. Opt.* **37**, 4300-4302 (1998d).
- Schilders S. P., Gan X. S. and Gu M., "Effect of scatterer size on microscopic imaging through turbid media based on differential polarisation-gating". *Opt. Comm.* **157**, 238-248 (1998e).
- Schilders S. P. and Gu M., "Three-dimensional fluorescence spectroscopy of rat skeletal muscle under two-photon excitation". *Appl. Opt.* **38**, 720-723 (1999a).
- Schilders S. P. and Gu M., "Limiting factors on resolution in imaging through turbid media under single-photon and two-photon excitation". *Microsc. and Microanal.* (1999b) – in press.
- Schmidt A., Corey R. and Saulnier P., "Imaging through random media by use of low-coherence optical heterodyning," *Opt. Lett.* **20**, 404-406 (1995).
- Schmitt J. M. and Ben-Letaief K., "Efficient Monte Carlo simulation of confocal microscopy in biological tissue," *J. Opt. Soc. Am. A* **13**, 952-961 (1996).
- Schmitt J. M. and Hiang S. H., "Cross-polarised backscatter in optical coherence tomography of biological tissue," *Opt. Lett.* **23**, 1060-1062 (1998).
- Schmitt J. M., Gandjbakhche A. H. and Bonner R. F., "Use of polarised light to discriminate short-path photons in a multiply scattering medium," *Appl. Opt.* **31**, 6535-6546 (1992).
- Schmitt J. M., Knuttel A. and Yadlowsky M., "Confocal microscopy in turbid media," *J. Opt. Soc. Am. A* **11**, 2226-2235 (1994).
- Schmitt J. M., Lee S. L. and Yung K. M., "An optical coherence microscope with enhanced resolving power in thick tissue," *Opt. Comm.* **142**, 203-207 (1997).
- Schmitt J. M., Yadlowsky M. and Bonner R. F., "Subsurface imaging of living skin with optical coherence microscopy," *Dermatology* **191**, 93-98 (1995).

- Schomacker K. T., Frisoli J. K., Compton C. C., Flotte T. J., Richter J. M., Nishioka N. S. and Deutsch T. F. "Ultraviolet laser-induced fluorescence of colonic tissue," *Las. Sur. Med.* **12**, 63-78 (1992).
- Shen Y. R., "Principles of Nonlinear Optics," Wiley: New York (1984).
- Sheppard C. J. R. and Gu M., "Image formation in two-photon fluorescence microscopy," *Optik* **86**, 104-106 (1990).
- Smithpeter C. L., Dunn A. K., Welch A. J. and Richards-Kortum R., "Penetration depth limits of *in vivo* confocal reflectance imaging," *Appl. Opt.* **37**, 2749-2754 (1998).
- So, P. T. C., "Focus Issue: New trends in biomedical microscopy," *Opt. Exp.* **3**, 311-355 (1998).
- Swanson E. A., Izatt J. A., Hee M. R., Huang D., Lin C. P., Schuman J. S., Puliafito C. A. and Fujimoto J. G., "In *vivo* retinal imaging by optical coherence tomography," *Opt. Lett.* **18**, 1864-1866 (1993).
- Tang G. C., Pradhan A. and Alfano R. R., "Spectroscopic differences between human cancer and normal lung and breast tissues," *Lasers Surg. Med.* **9**, 290-295 (1989).
- Tatterson, "Researches study two-photon technique to treat early-onset cancer," *Biophotonics News*, (1997).
- Torok P., Verga P., Laczik Z. and Booker G. R., "Electromagnetic diffraction of light focused through a planar interface between materials of mismatched refractive indices: an integration representation," *J. Opt. Soc. Am. A* **12**, 325-332 (1996).
- Wabnitz H. and Rinneberg H., "Imaging in turbid media by photon density waves: spatial resolution and scaling relations," *Appl. Opt.* **36**, 64-74 (1997).
- Wang L. M., Ho P. P. and Alfano R. R., "Double-stage picosecond Kerr gate for ballistic time-gated optical imaging in turbid media," *Appl. Opt.* **32**, 535-539 (1993a).
- Wang L., Ho P., Liu C., Zhang G. and Alfano R. R., "Ballistic 2-D imaging through scattering walls using an ultrafast Kerr gate," *Science* **253**, 769-771 (1991).
- Wang L., Ho P. P. and Alfano R. R., "Time-resolved Fourier spectrum and imaging in highly scattering media," *Appl. Opt.* **32**, 5043-5048 (1993b).
- Wang L., Ho P. P., Liang X., Dai H. and Alfano R. R., "Kerr-Fourier imaging of hidden objects in thick turbid media," *Opt. Lett.* **18**, 241-243 (1993c).

- Wang Q. Z., Liang X., Wang L., Ho P. P. and Alfano R. R., "Fourier spatial filter acts as a temporal gate for light propagating through a turbid medium," *Opt. Lett.* **20**, 1498-1500 (1995).
- Wang W. B., Demos S. G., Ali J. and Alfano R. R., "Imaging fluorescent objects embedded inside animal tissues using polarisation difference techniques," *Opt. Comm.* **142**, 161-166 (1997).
- Watson J., Georges P., Lepine T., Alonzi B. and Brun A., "Imaging in diffuse media with ultrafast degenerate optical parametric amplification," *Opt. Lett.* **20**, 231-233 (1995).
- Wilson T. and Sheppard C., "Theory and Practice of scanning Optical Microscopy," Academic Press: London (1984).
- Xiang Y., Raphan T., Liang X., Wang L., Ho P. P. and Alfano R. R., "Image-quality enhancement in turbid media by use of a combined computational-photonics approach," *Appl. Opt.* **36**, 1045-1053 (1997).
- Yadlowsky M., Schmitt J. M. and Bonner R. F., "Multiple scattering effects in optical coherence microscopy," *Appl. Opt.* **34**, 5699-5707 (1995).
- Ying J., Liu F., Alfano R. R., "Spatial distribution of two-photon-excited fluorescence in scattering media," *Appl. Opt.* **38**, 224-229 (1999).
- Yoo K. M. and Alfano R. R., "Time-resolved coherent and incoherent components of forward light scattering in random media," *Opt. Lett.* **15**, 320-322 (1990).
- Yoo K. M. and Alfano R. R., "Time-resolved depolarisation of multiple backscattered light from random media," *Phys. Lett. A* **142**, 531-536 (1989).
- Yoo K. M., Xing Q. and Alfano R. R., "Imaging objects hidden in highly scattering media using femtosecond second-harmonic-generation cross-correlation time gating," *Opt. Lett.* **16**, 1019-1021 (1991).
- Zaccanti G. and Donelli P., "Attenuation of energy in time gated transillumination imaging: numerical results," *Appl. Opt.* **33**, 7023-7030 (1994).

## List of symbols

$a$	radius of particle
$A$	relative particle size
$\alpha$	transverse resolution
$a_i$	Mie theory scattering coefficient
$\alpha_p$	parallel polarisation-gated transverse resolution
$\alpha_{p+s}$	no polarisation-gating transverse resolution
$\alpha_{p-s}$	differential polarisation-gated transverse resolution
$\alpha_s$	perpendicular polarisation-gated transverse resolution
$\beta$	random number between 0 and 1
$b_i$	Mie theory scattering coefficient
$D$	aperture diameter
$d$	penetration depth
$\delta$	random number between 0 and 1
$d'$	imaginary penetration depth
$\Delta g$	difference in anisotropy value
$\Delta Q_s$	difference in scattering efficiency
$\Delta \tau_0$	pulse width
$\Delta \Omega$	spectral width
$\varepsilon$	normalised central obstruction size
$\varepsilon_{in}$	normalised central obstruction size for the illumination objective
$\varepsilon_{out}$	normalised central obstruction size for the collection objective
$E_x$	incident electric field in the x-direction

---

$E_x^*$	conjugate of the incident electric field in the x-direction
$E_y$	incident electric field in the y-direction
$E_y^*$	conjugate of the incident electric field in the y-direction
$\phi$	azimuth angle
$f$	focal length
$f(t_0)$	Gaussian pulse profile
$f_p$	Fresnel weighting factor
$g$	asymmetry parameter (anisotropy value)
$\gamma$	degree of polarisation
$h_n^{(1)}(x)$	spherical Bessel function of the third kind
$i$	expansion term number
$I'_{inc}$	Stokes polarisation vector after propagation through a lens
$I_i$	Stokes vector parameter of the incident light
$I_{inc}$	Stokes polarisation vector of the incident light
$I_p$	parallel polarisation intensity
$I_s$	perpendicular polarisation intensity
$I_{scat}$	Stokes polarisation vector after scattering
$j_n(x)$	spherical Bessel function of the first kind
$\kappa$	diameter of microsphere particles
$k$	wave vector
$\lambda$	wavelength
$\lambda_0$	central wavelength
$l_s$	scattering-mean-free-path length
$l_t$	scattering interaction length

$m$	relative refractive index
$M$	scattering matrix
$n$	optical thickness
$N$	refractive index
$N(0)$	number of incident photons
$N(d)$	number of unscattered photons at depth $d$
$NA$	numerical aperture
$p$	density
$P(d)$	probability of photon propagation at depth $d$
$P_1$	change in transverse resolution between CPG and NG
$P^1_i$	Legendre function
$P_2$	change in transverse resolution between DPG and NG
$P_3$	change in transverse resolution between CPG and DPG
$P_4$	change in transverse resolution with and without pinhole
$P_f$	change in transverse resolution for fluorescence excitation
$P_\gamma$	change in degree of polarisation
$\pi_i$	angle dependent function
$P_I$	change in polarisation intensity ratio
$p_\theta(\theta)$	Henyeey-Greenstein probability distribution
$\theta$	polar angle
$\theta_i$	imaginary polar angle
$Q_i$	Stokes vector parameter of the incident light
$\theta_s$	scattering angle
$Q_s$	scattering efficiency

---

$\rho$	concentration
$R_p$	Fresnel reflection coefficient for parallel polarised light
$R_s$	Fresnel reflection coefficient for perpendicular polarised light
$S(\theta)$	scattering coefficient
$\sigma_g$	geometric cross-section
$\sigma_s$	scattering cross-section
$t$	local time co-ordinate
$T$	period of oscillation
$\tau_i$	angle dependent function
$T_p$	Fresnel transmission coefficient for parallel polarised light
$T_s$	Fresnel transmission coefficient for perpendicular polarised light
$U_0(t)$	Gaussian-shaped pulse in the time domain
$U_i$	Stokes vector parameter of the incident light
$V_0(\Delta\Omega)$	Gaussian shaped pulse in the spectral domain
$V_i$	Stokes vector parameter of the incident light
$\omega$	angular frequency
$W$	weight of particles
$\omega_0$	central angular frequency
$x$	particle size
$x$	x-axis spatial co-ordinate of simulated photon
$y$	y-axis spatial co-ordinate of simulated photon
$y_n(x)$	spherical Bessel function of the second kind
$z$	z-axis spatial co-ordinate of simulated photon

# List of figures

## Chapter 1

- Fig. 1.1: Photon propagation within a turbid medium. For a clear description, the three components are depicted separately: (a) unscattered photons; (b) snake photos; (c) multiply scattered photons..... 5
- Fig. 1.2: Four physical effects of photons propagating through a turbid media: (a) spectral shift; (b) spatial broadening; (c) temporal broadening; (d) polarisation degradation..... 6

## Chapter 2

- Fig. 2.1: Schematic diagram for an imaging system employing a streak camera..... 18
- Fig. 2.2: Schematic diagram for an imaging system employing the optical cross-correlation technique..... 20
- Fig. 2.3: Schematic diagram for an imaging system employing a Kerr cell ..... 22
- Fig. 2.4: Schematic diagram of an imaging system employing a fibre optic coherence-gate..... 24
- Fig. 2.5: Schematic diagram of a reflection confocal scanning optical microscope..... 25
- Fig. 2.6: (a) Confocal image sections of the letter 'A' recorded from the surface of an integrated circuit; (b) three-dimensional reconstruction of the letter 'A' from the image sections shown in (a)..... 27
- Fig. 2.7: Energy level diagram for (a) single-photon and (b) two-photon excitation..... 32
- Fig. 2.8: Focal volume under single-photon (a) and two-photon (b) excitation..... 35

- Fig. 2.9: Images of rat skeletal muscle tissue recorded from autofluorescence excited by (a) two-photon ( $\lambda = 800$  nm) and (b) single-photon ( $\lambda = 488$  nm) excitation in a conventional scanning optical microscope. The numerical aperture of the imaging objective is 0.75..... 36
- Fig. 2.10: Transverse ((a) and (b)) and vertical ((c) and (d)) image section of rat lung tissue recorded from autofluorescence excited by single-photon ( $\lambda = 488$  nm) with a 100  $\mu\text{m}$  pinhole ((a) and (c)) and two-photon ( $\lambda = 900$  nm) without a pinhole ((b) and (d)). The numerical aperture of the imaging objective is 0.9 (water immersion)..... 38
- Chapter 3**
- Fig. 3.1: Scattering efficiency,  $Q_s$ , (solid curve) and anisotropy value,  $g$ , (dashed curve) as a function of the relative particle size,  $A$ ..... 47
- Fig. 3.2: Scattering by a spherical particle..... 50
- Fig. 3.3: Geometric arrangement for a lens system. (a) Three-dimensional view and (b) two-dimensional view in the meridian plane. The full projection space for photons is illustrated in black, while the incident projection of a single-photon is given in grey. The figure illustrates the case when  $N_1 > N_2$ ..... 52
- Fig. 3.4: Schematic diagram of the modelled transmission scanning optical microscope..... 55
- Fig. 3.5: Schematic diagram of the modelled reflection scanning optical microscope..... 57
- Fig. 3.6: Difference of the scattering efficiency,  $\Delta Q_s$ , (solid curve) and the difference in the anisotropy value,  $\Delta g$ , (dashed curve) as a function of the pulse width,  $\Delta\tau_0$  ( $N_1 = 1.33$  and  $N_2 = 1.59$ )..... 65
- Fig. 3.7: Angular-temporal photon distribution of a 20-fs ultrashort pulsed

beam propagating through a turbid slab ( $l_s = 40 \mu\text{m}$ ,  $d/l_s = 4$ ). The time  $t$  is a local time, so  $t = 0$  corresponds to the arrival time of the unscattered pulse peak. (a) illumination with a circular objective; (b) illumination with an annular objective..... 70

## Chapter 4

Fig. 4.1: Schematic diagram for demonstrating the principle of angle-gating in a transmission microscopic imaging system when, (a) a pair of circular objectives, (b) an illumination annular objective and a collection circular objective, (c) a matching pair of annular objectives and (d) a matching pair of annular objectives employing polarisation-gating are employed..... 75

Fig. 4.2: Simulated photon distribution along the radial direction of the collection objective for illumination with a circular objective ( $\varepsilon = 0$ , bold) or an annular objective ( $\varepsilon = 0.9$ ). (a) sample3 (a turbid medium consisting of  $0.202 \mu\text{m}$  microspheres); (b) sample5 (a turbid medium consisting of  $0.48 \mu\text{m}$  microspheres). Here  $\rho$  is the radial co-ordinate of the collection objective, normalised by the maximum radius of the objective..... 76

Fig. 4.3: Experimental transmission scanning optical microscope with angle- and polarisation-gating mechanisms. (a) Photograph of the physical system; (b) Schematic diagram of the system..... 80

Fig. 4.4: Optical system to determine the scattering-mean-free-path length,  $l_s$ , for semi skimmed milk..... 84

Fig. 4.5: Dependence of the degree of polarisation,  $\gamma$  (a), the polarisation intensity ratio,  $I_p/I_s$  (b), and the percentage reduction parameters,  $P_\gamma$  (c) and  $P_I$  (d) on the radius of the central obstruction of the

- illumination objective,  $\varepsilon_{in}$ . The numerical aperture for objective  $O_2$  and  $O_3$  is 0.6..... 87
- Fig. 4.6: Dependence of the degree of polarisation,  $\gamma$  (a), the polarisation intensity ratio,  $I_p/I_s$  (b), and the percentage improvement/reduction parameters,  $P_\gamma$ (c) and  $P_I$ (d) on the radius of the central obstruction of the collection objective,  $\varepsilon_{out}$ , when the central obstruction,  $\varepsilon_{in}$ , of the illumination objective is given. The numerical aperture for objective  $O_2$  and  $O_3$  is 0.6..... 91
- Fig. 4.7: Dependence of the degree of polarisation,  $\gamma$  (a), the polarisation intensity ratio,  $I_p/I_s$  (b), and the percentage improvement/reduction parameters,  $P_\gamma$ (c) and  $P_I$ (d) on the radius of the central obstruction of a matching pair of annular objectives,  $\varepsilon$ . The numerical aperture for objectives  $O_2$  and  $O_3$  is 0.6..... 93
- Fig. 4.8: Dependence of the degree of polarisation,  $\gamma$  (a), the polarisation intensity ratio,  $I_p/I_s$  (b), and the percentage improvement/reduction parameters  $P_\gamma$ (c) and  $P_I$ (d) on the numerical aperture of the matched illumination and collection objectives..... 96
- Fig. 4.9: Images of a 22  $\mu\text{m}$  polystyrene microspheres embedded within sample1. (a) and (c): circular objectives ( $\varepsilon = 0$ ) with parallel polarisers; (b) and (d): annular objectives ( $\varepsilon \approx 0.93$ ) with parallel polarisers. The intensity of the images was normalised to unity..... 98
- Fig. 4.10: Images of a 22  $\mu\text{m}$  polystyrene microsphere cluster embedded within sample4. (a), (b) and (c): circular objectives ( $\varepsilon = 0$ ) with parallel polarisation; (d), (e) and (f): annular objectives ( $\varepsilon \approx 0.93$ ) with parallel polarisation. In (a) and (d) the focus is on the dried cluster layer, in (b) and (e) the focus is shifted away from the cluster layer by approximately 20  $\mu\text{m}$ , and in (c) and (f) the focus is shifted away from the dried cluster layer by approximately 40  $\mu\text{m}$ . The intensity of

the images was normalised to unity.....	101
Fig. 4.11:Images of a 22 $\mu\text{m}$ polystyrene microsphere embedded within sample5. (a) circular objectives ( $\varepsilon = 0$ ) without polarisers; (b) circular objectives ( $\varepsilon = 0$ ) with polarisers; (c) annular objectives ( $\varepsilon \approx 0.93$ ) without polarisers; (d) annular objectives ( $\varepsilon \approx 0.93$ ) with polarisers. The intensity of the images was normalised to unity.....	102
Fig. 4.12:Images of 22 $\mu\text{m}$ polystyrene microspheres embedded in sample6. (a) circular objectives ( $\varepsilon = 0$ ) with parallel polarisation; (b) annular objectives ( $\varepsilon \approx 0.93$ ) with parallel polarisation; (c) annular objectives ( $\varepsilon \approx 0.93$ ) with perpendicular polarisation. The intensity of the images was normalised to unity.....	104
Fig. 4.13:Images of a 22 $\mu\text{m}$ polystyrene microsphere embedded in sample7. (a) circular objective ( $\varepsilon = 0$ ) with parallel polarisation; (b) annular objectives ( $\varepsilon \approx 0.93$ ) with parallel polarisation. The intensity of the images was normalised to unity.....	106
Fig. 4.14:Simulated dependence of the degree of polarisation, $\gamma$ , on (a) the radius of the central annular obstruction for a matching pair of annular objectives with a numerical aperture of 0.6 and (b) the numerical aperture of the circular objectives for sample4 in a transmission microscope.....	110
Fig. 4.15:Experimental reflection scanning optical microscope with angle-gating and polarisation-gating. (a) Photograph of the system; (b) Schematic diagram of the system.....	112
Fig. 4.16:Dependence of the degree of polarisation, $\gamma$ (a), the polarisation intensity ratio, $I_p/I_s$ (b), and the percentage improvement parameters, $P_\gamma$ (c) and $P_I$ (d) on the radius of the central obstruction of an annular imaging objective, $\varepsilon$ . The numerical aperture for the imaging objective $O_2$ is 0.75.....	116

- Fig. 4.17: Image of a test bar embedded within sample8 (filled with distilled water), when a circular imaging objective ( $\varepsilon = 0$ ) of numerical aperture 0.75 is employed. The intensity of the image was normalised to unity..... 118
- Fig. 4.18: Images of a test bar embedded in sample9 ((a) and (b)) and sample10 ((c) and (d)) when a circular imaging objective ( $\varepsilon = 0$ ) with parallel polarisation ((a) and (c)) and an annular imaging objective ( $\varepsilon \approx 0.94$ ) with parallel polarisation ((b) and (d)) are employed. The numerical aperture of the imaging objective in both cases is 0.75. The intensity of the images was normalised to unity..... 119
- Fig. 4.19: Dependence of the degree of polarisation,  $\gamma$  (a), the polarisation intensity ratio,  $I_p/I_s$  (b), and the percentage improvement parameters,  $P_\gamma$  (c) and  $P_I$  (d) on the numerical aperture of the imaging objective  $O_2$ ..... 123
- Fig. 4.20: Simulated dependence of the degree of polarisation,  $\gamma$ , on (a) the radius of the central annular obstruction for an annular objective with a numerical aperture of 0.6 and (b) the numerical aperture of the circular objectives for sample9 in a reflection microscope..... 124

## Chapter 5

- Fig. 5.1: Experimental reflection scanning optical microscope with differential polarisation-gating mechanism. (a) Photograph of the system, with the beam path shown in red; (b) Schematic diagram of the system..... 133
- Fig. 5.2: Measured images for sample2 (table 5.2) when CPG (a), PPG (b) and DPG (c) techniques are employed. The intensity of the images is normalised to unity. (d) includes the measured edge responses corresponding to CPG ( $I_p$ ), PPG ( $I_s$ ) and DPG ( $I_{p-s}$ ) techniques. The

horizontal grey lines represent the intensity for  $I_p$  (solid),  $I_s$  (dot) and  $I_{p-s}$  (dashed), at the bar edge position indicated by the vertical grey line. The numerical aperture of the imaging objective is 0.25..... 140

Fig. 5.3: Resolution performance for sample set A at NA = 0.25 ((a) and (c)) and NA = 0.75 ((b) and (d)). (a) and (b) are the measured transverse resolution as a function of the optical thickness,  $n$ , for NG ( $\alpha_{p+s}$ ), CPG ( $\alpha_p$ ), PPG ( $\alpha_s$ ) and DPG ( $\alpha_{p-s}$ ). (c) and (d) are the resolution improvement and the degree of polarisation,  $\gamma$ , as a function of the optical thickness,  $n$ . A comparison is given between CPG and NG ( $P_1$ ), DPG and NG ( $P_2$ ) and DPG and CPG ( $P_3$ )..... 142

Fig. 5.4: Measured images for sample3 (table 5.2) for CPG (a), PPG (b) and DPG (c) techniques. The intensity of the images is normalised to unity. The numerical aperture of the imaging objective is 0.75..... 145

Fig. 5.5: Resolution performance for sample set B at NA = 0.75. (a) is the measured transverse resolution as a function of the optical thickness,  $n$ , for NG ( $\alpha_{p+s}$ ), CPG ( $\alpha_p$ ), PPG ( $\alpha_s$ ) and DPG ( $\alpha_{p-s}$ ). (b) is the resolution improvement and the degree of polarisation,  $\gamma$ , as a function of the optical thickness,  $n$ . A comparison is given between CPG and NG ( $P_1$ ), DPG and NG ( $P_2$ ) and DPG and CPG ( $P_3$ )..... 146

Fig. 5.6: Resolution performance for sample set C at NA = 0.75. (a) is the measured transverse resolution as a function of the optical thickness,  $n$ , for NG ( $\alpha_{p+s}$ ), CPG ( $\alpha_p$ ), PPG ( $\alpha_s$ ) and DPG ( $\alpha_{p-s}$ ). (b) is the resolution improvement and the degree of polarisation,  $\gamma$ , as a function of the optical thickness,  $n$ . A comparison is given between CPG and NG ( $P_1$ ), DPG and NG ( $P_2$ ) and DPG and CPG ( $P_3$ )..... 147

Fig. 5.7: Measured images ((a), (b) and (c)) for sample4 (table 5.2). and measured images ((d), (e) and (f)) for sample5 (table 5.2). ((a) and (d)), ((b) and (e)), and ((c) and (f)) correspond to CPG, PPG and DPG

techniques, respectively. The intensity of the images is normalised to unity. The numerical aperture of the imaging objective is 0.75..... 149

Fig. 5.8: Resolution performance for sample set E at NA = 0.75. (a) is the measured transverse resolution as a function of the optical thickness,  $n$ , for NG ( $\alpha_{p+s}$ ), CPG ( $\alpha_p$ ), PPG ( $\alpha_s$ ) and DPG ( $\alpha_{p-s}$ ). (b) is the resolution improvement and the degree of polarisation,  $\gamma$ , as a function of the optical thickness,  $n$ . A comparison is given between CPG and NG ( $P_1$ ), DPG and NG ( $P_2$ ) and DPG and CPG ( $P_3$ )..... 151

Fig. 5.9: Resolution performance for sample set C at NA = 0.75 and with a pinhole of diameter 150  $\mu\text{m}$ . (a) is the measured transverse resolution as a function of the optical thickness,  $n$ , for NG ( $\alpha_{p+s}$ ), CPG ( $\alpha_p$ ), PPG ( $\alpha_s$ ) and DPG ( $\alpha_{p-s}$ ). (b) is the resolution improvement and the degree of polarisation,  $\gamma$ , as a function of the optical thickness,  $n$ . A comparison is given between CPG and NG ( $P_1$ ), DPG and NG ( $P_2$ ) and DPG and CPG ( $P_3$ )..... 155

Fig. 5.10: Degree of polarisation,  $\gamma$ , for sample set D as a function of the optical thickness,  $n$ . The numerical aperture of the imaging objective is 0.75. 157

Fig. 5.11: Measured images for sample 6 (table 5.2) for CPG (a), PPG (b) and DPG (c) techniques. The intensity of the images is normalised to unity. (d) includes the measured edge responses corresponding to CPG ( $I_p$ ), PPG ( $I_s$ ) and DPG ( $I_{p-s}$ ) techniques. The vertical grey line represents the ideal edge position. The numerical aperture of the imaging objective is 0.25..... 161

Fig. 5.12: Measured images for sample 6 (table 5.2) for CPG (a), PPG (b) and DPG (c) techniques. The intensity of the images is normalised to unity. (d) includes the measured edge responses corresponding to CPG ( $I_p$ ), PPG ( $I_s$ ) and DPG ( $I_{p-s}$ ) techniques. The vertical grey line represents the ideal edge position. The numerical aperture of the

- imaging objective is 0.75..... 162
- Fig. 5.13:Resolution performance for sample set C at NA = 0.25. (a) is the calculated transverse resolution as a function of the optical thickness,  $n$ , for NG ( $\alpha_{p+s}$ ), CPG ( $\alpha_p$ ), PPG ( $\alpha_s$ ) and DPG ( $\alpha_{p-s}$ ). (b) is the resolution improvement and the degree of polarisation,  $\gamma$ , as a function of the optical thickness,  $n$ . A comparison is given between CPG and NG ( $P_1$ ), DPG and NG ( $P_2$ ) and DPG and CPG ( $P_3$ )..... 166
- Fig. 5.14:Resolution performance for sample set C at NA = 0.25 and a pinhole of diameter 100  $\mu\text{m}$ . (a) is the calculated transverse resolution as a function of the optical thickness,  $n$ , for NG ( $\alpha_{p+s}$ ), CPG ( $\alpha_p$ ), PPG ( $\alpha_s$ ) and DPG ( $\alpha_{p-s}$ ). (b) is the resolution improvement and the degree of polarisation,  $\gamma$ , as a function of the optical thickness,  $n$ . A comparison is given between CPG and NG ( $P_1$ ), DPG and NG ( $P_2$ ) and DPG and CPG ( $P_3$ )..... 168

## Chapter 6

- Fig. 6.1: Photographs of the experimental fluorescence scanning optical microscope. (a) laser system and (b) FluoVIEW microscope system. 1: Millennium pump laser; 2: Tsunami; 3: frequency doubler (not used in this work); 4: FluoVIEW scan unit; 5: inverted microscope; 6: autocorrelator; 7: spectrum analyser; B: beamsplitter; M: mirrors and ND: neutral density filter..... 173
- Fig. 6.2: Diagram for preparing the samples for a microsphere cluster (a) and a bar embedded object (b)..... 177
- Fig. 6.3: Two-photon image of a single 10  $\mu\text{m}$  fluorescence microsphere embedded within sample1 (table 6.3). The intensity of the image was normalised to unity. The numerical aperture of the imaging objective

- was 0.75..... 179
- Fig. 6.4: Images of a 10  $\mu\text{m}$  polystyrene microsphere cluster embedded within sample2 (table 6.3). The intensity of the images was normalised to unity. (a) Single-photon excitation without a detection pinhole; (b) single-photon excitation with a 300  $\mu\text{m}$  detection pinhole; (c) two-photon excitation without a detection pinhole. (d), (e) and (f) are cross-sections recorded at position 'A' in (a), (b) and (c), respectively. The numerical aperture of the imaging objective is 0.75..... 181
- Fig. 6.5: Images of 10  $\mu\text{m}$  polystyrene microspheres embedded within sample3 ((a) and (b)), sample4 (c), sample5 (d), sample6 (e) and sample7 (f). Image (a) was recorded with single-photon excitation with a 300  $\mu\text{m}$  detection pinhole. Images (b) to (f) were recorded with two-photon excitation without a detection pinhole. The intensity of the images was normalised to unity. The numerical aperture of the imaging objective was 0.75..... 183
- Fig. 6.6: Transverse cross-section of the image of a fluorescent bar embedded within sample1 (table 6.1), recorded with single-photon excitation with a 300  $\mu\text{m}$  detection pinhole and two-photon excitation without a detection pinhole..... 185
- Fig. 6.7: (a) Optical thickness (dashed),  $n$ , and transverse resolution (solid),  $\alpha$ , and (b) the change in transverse resolution,  $P_f$ , as a function of the cell thickness,  $d$ , for sample set A (table 6.2)..... 186
- Fig. 6.8: Images of a bar embedded within sample3 ((a) and (b)) and sample7 (c). (a) Single-photon excitation with a 300  $\mu\text{m}$  detection pinhole; ((b) and (c)) two-photon excitation without a detection pinhole and (d) cross-section recorded at position 'A' and corresponding fitted curves..... 188
- Fig. 6.9: (a) Optical thickness (dashed),  $n$ , and transverse resolution (solid),  $\alpha$ ,

and (b) the change in transverse resolution, $P_f$ , as a function of the cell thickness, $d$ , for sample set B (table 6.2).....	190
Fig. 6.10:(a) Optical thickness (dashed), $n$ , and transverse resolution (solid), $\alpha$ , and (b) the change in transverse resolution, $P_f$ , as a function of the cell thickness, $d$ , for sample set C (table 6.2).....	192
Fig. 6.11:(a) Optical thickness (dashed), $n$ , and transverse resolution (solid), $\alpha$ , and (b) the change in transverse resolution, $P_f$ , as a function of the cell thickness, $d$ , for sample set B (table 6.2).....	194
Fig. 6.12:Transverse resolution, $\alpha$ , as a function of the illumination optical thickness, $n$ , for sample sets A to D (table 6.2). (a) single-photon excitation and (b) two-photon excitation.....	198
Fig. 6.13:Transverse autofluorescence image sections of the rat skeletal muscle tissue recorded at different depths ((a) to (f)). The depth spacing is 6 $\mu\text{m}$ . Vertical image slices cut from the recorded stack at 45° from left to right (g) and from right to left (h).....	202
Fig. 6.14:Reconstructed three-dimensional autofluorescence image of the rat skeletal muscle tissue at different rotation view angles: (a) 0°, (b) 45°, (c) 90°, (d) 180°, (e) 225° and (f) 270°.....	204
Fig. 6.15:Autofluorescence spectra from different points within the rat skeletal muscle tissue.....	205
Fig. 6.16:Autofluorescence intensity as a function of the excitation laser power at two fluorescence peaks.....	206
Fig. 6.17:Transverse ((a), (b), (c), (d), (e) and (f)) and vertical ((g) and (h)) image sections of the rat skeletal muscle tissue recorded at autofluorescence wavelengths 450 nm ((a), (d) and (g)) and 550 nm ((b), (e) and (h)). Images (c) and (f) are a superposition of images ((a) and (b)) and ((d) and (e)), respectively.....	207

## List of Tables

### Chapter 3

Table 3.1: Calculation of the scattering-mean-free-path length, $l_s$ , and the anisotropy value, $g$ , for the polystyrene microspheres used in this work for an excitation wavelength, $\lambda$ , of 632.8 nm.....	48
-----------------------------------------------------------------------------------------------------------------------------------------------------------------------------------------------------------------------	----

### Chapter 4

Table 4.1: Parameters for the samples used in the transmission optical microscope.....	82
Table 4.2: Parameters for the samples used in the reflection scanning optical microscope.....	114

### Chapter 5

Table 5.1: Parameters for the sample sets used in the reflection scanning optical microscope.....	135
Table 5.2: Parameters for the specific samples used in the reflection scanning optical microscope.....	137

### Chapter 6

Table 6.1: Calculation of the scattering-mean-free-path length, $l_s$ , and the anisotropy value, $g$ , for the polystyrene microspheres used in this work for a wavelength, $\lambda$ , of (a) 488 nm (single-photon excitation), (b) 520 nm (fluorescence) and (c) 800 nm (two-photon excitation)...	175
--------------------------------------------------------------------------------------------------------------------------------------------------------------------------------------------------------------------------------------------------------------------------------------------------------	-----

Table 6.2: Parameters for the specific sample sets used in the fluorescence  
optical microscope..... 176

Table 6.3: Parameters for the specific samples used in the fluorescence optical  
microscope..... 178

## List of author's publications

\* indicates work related to this thesis.

### Journals

1. 'Optimising the strength of an evanescent wave generated from a prism coated with a double-layer thin-film stack'. Pu Chun Ke, X. S. Gan, Jakub Szajman, S. P. Schilders and M. Gu. *Bioimaging* **5**, 1-8 (1997).
2. 'Imaging concentration profiles of praseodymium-doped optical fibres'. B. P. Petreski, S. P. Schilders, P. M. Farrell and M. Gu. *Elect. Lett.* **33**, 889-891 (1997).
- \*3. 'Combination of annular aperture and polarisation gating methods for efficient microscopic imaging through a turbid medium: Theoretical analysis'. X. Gan, S. Schilders and M. Gu. *Microsc. and Microanal.* **3**, 495-503 (1997).
- \*4. 'Efficient suppression of diffusing photons using polarising annular objectives for microscopic imaging through turbid media'. S. P. Schilders, X. S. Gan and M. Gu. *Bioimaging* **6**, 92-97 (1998).
- \*5. 'Microscopic imaging through a turbid medium by use of annular objectives for angle-gating'. S. P. Schilders, X. S. Gan and M. Gu. *Appl. Opt.* **37**, 5320-5326 (1998).
- \*6. 'Image formation in turbid media under a microscope'. X. Gan, S. Schilders and M. Gu. *J. Opt. Soc. Am. A* **15**, 2052-2058 (1998).
- \*7. 'Resolution improvement in microscopic imaging through turbid media based on differential polarisation-gating'. S. P. Schilders, X. S. Gan and M. Gu. *Appl. Opt.* **37**, 4300-4302 (1998).
- \*8. 'Effect of scatterer size on microscopic imaging through turbid media based on differential polarisation-gating'. S. P. Schilders, X. S. Gan and M. Gu. *Opt. Comm.* **157**, 238-248 (1998).
- \*9. 'Image enhancement in a reflection optical microscope by suppression of diffusing photons using polarising annular objectives'. S. P. Schilders, X. S. Gan and M. Gu. *Microsc. and Microanal.* **4**, 415-419 (1998).
- \*10. 'Three-dimensional fluorescence spectroscopy of rat skeletal muscle under two-photon excitation'. S. P. Schilders and M. Gu. *Appl. Opt.* **38**, 720-723 (1999).

- \*11. 'Image enhancement through turbid media under a microscope using polarisation-gating methods'. X. Gan, S. P. Schilders and M. Gu. Submitted to J. Opt. Soc. Am. A (1999).
- \*12. 'Limiting factors on resolution in imaging through turbid media under single-photon and two-photon excitation'. S. P. Schilders and M. Gu. Submitted to Opt. Lett. (1999).
- \*13. 'Two-photon fluorescence imaging of microspheres embedded in turbid media'. M. Gu, S. P. Schilders and X. Gan. J. Modern Optics (1999) - in press.

### Conference Proceedings

14. 'Determination of the concentration profile of praseodymium doped optical fibre by confocal microscopy'. B. P. Petreski, S. P. Schilders, P. M. Farrell and M. Gu. Proc. 20th International Quantum Electronic Conference, pg. 241 (Sydney, Australia 1996).
15. 'Imaging concentration profiles of rare earth doped optical fibres', B. P. Petreski, S. P. Schilders, P. M. Farrell, and M. Gu. Proc. 21st Australian Conference of Optical Fibre Technology, pg. 113-116 (Goldcoast, Australia 1996).
16. 'Time resolved confocal fluorescence microscopy for determining the concentration in a doped optical fibre'. S. P. Schilders, B. P. Petreski, P. M. Farrell, and M. Gu. Proc. 10th International Conference on 3D image processing in microscopy and the 9th International Conference on confocal microscopy (Cell Vision: Vol. 4), 117 (Buffalo, USA 1997).

### Conference Papers

- \*17. 'Effect of particle and concentration on microscopic imaging through a turbid medium'. S. P. Schilders, X. S. Gan and M. Gu. 11th Conference of the Australian Optical Society, (Adelaide, Australia 1997).
- \*18. 'Use of polarised light to construct high resolution images through a turbid medium'. X. S. Gan, S. P. Schilders and M. Gu. 11th Conference of the Australian Optical Society, (Adelaide, Australia 1997).
- \*19. 'Image formation in turbid media'. M. Gu, X. S. Gan and S. P. Schilders. 11th Conference of the Australian Optical Society, (Adelaide, Australia 1997).

20. 'Rare earth dopant imaging in optical fibres'. P. M. Farrell, G. Baxter, M. Gu, S. P. Schilders, B. Petreski and I. Mitchell. 11th Conference of the Australian Optical Society, (Adelaide, Australia 1997).
21. 'Three-Dimensional Optical Memory in Two-Photon Bleaching Material', D. Day, S. P. Schilders and M. Gu. 11th Conference of the Australian Optical Society, (Adelaide, Australia 1997).
22. 'Construction and characterisation of a fibre-optical double pass confocal scanning microscope', D. Bird, S. P. Schilders and M. Gu. 11th Conference of the Australian Optical Society, (Adelaide, Australia 1997).
- \*23 'Differential polarisation microscopic imaging through turbid media'. S. P. Schilders, X. S. Gan and M. Gu. 11th International Conference on 3D image processing in microscopy and the 10th International Conference on confocal microscopy (Sydney, Australia 1998).
- \*24. 'Microscopic imaging through turbid media'. X. S. Gan, S. P. Schilders and M. Gu. 11th International Conference on 3D image processing in microscopy and the 10th International Conference on confocal microscopy (Sydney, Australia 1998).
- \*25. 'Image formation in tissue-like turbid media under an optical scanning microscope'. M. Gu, X. Gan and S. Schilders. 13th National Congress of the Australian Institute of Physics (Fremantle, Australia 1998).
- \*26. 'Three-dimensional autofluorescence spectroscopy of biological tissue under two-photon excitation'. S. P. Schilders and M. Gu. 4th Australasian Conference on Optics, Lasers and Spectroscopy (Christchurch, New Zealand 1998).
- \*27. 'Fluorescence image formation in turbid media'. X. Gan, S. Schilders and M. Gu. 4th Australasian Conference on Optics, Lasers and Spectroscopy (Christchurch, New Zealand 1998).
- \*28 'High-resolution imaging in tissue-like turbid media under an optical microscope'. X. Gan, S. Schilders and M. Gu. (Mexico)

### **Articles**

29. 'Three dimensional optical data storage'. M. Gu, D. J. Day and S. P. Schilders. Australian Optical Society News Vol 11(4), pg. 1-4, 1997.
- \*30. 'High resolution imaging through tissue-like turbid media'. M. Gu, S. P. Schilders and X. S. Gan. Australian Optical Society News 12(2), 1-6 (1998).